CHALMERS
UNIVERSITY OF TECHNOLOGY

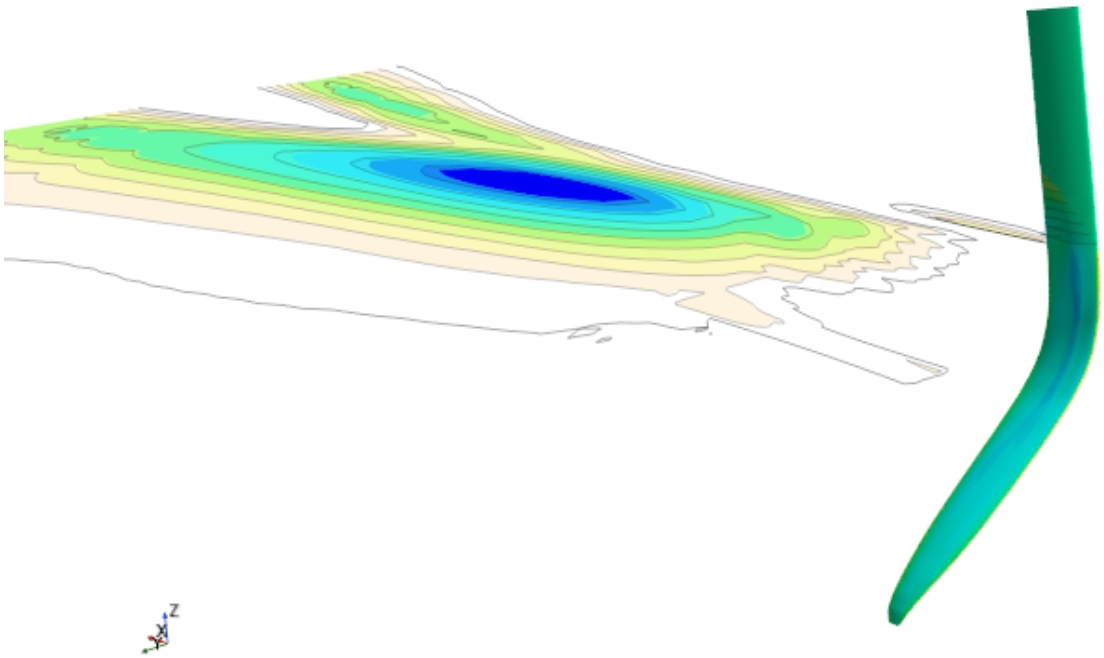

Fluid Structure Interaction of hydrofoils

For the NACRA 17 Olympic class

Master's thesis in Naval Architecture And Ocean Engineering

Fabian M. Ebbesson

Ali M. Farousi

DEPARTMENT OF MECHANICS AND MARITIME SCIENCES

CHALMERS UNIVERSITY OF TECHNOLOGY
Gothenburg, Sweden 2021
www.chalmers.se

Master's thesis 2021

Fluid Structure Interaction of hydrofoils For the NACRA 17 Olympic class

Carried out with numerical simulations and verified with tests in a cavitation tunnel

Fabian M. Ebbesson

Ali M. Farousi

CHALMERS
UNIVERSITY OF TECHNOLOGY

Department of Mechanics and Maritime Sciences
Division of Marine Technology
Chalmers University of Technology
Gothenburg, Sweden 2021

Fluid Structure Interaction of hydrofoils
Carried out with numerical simulations and verified with tests in a cavitation tunnel
Fabian M.Ebbesson
Ali M. Farousi

Supervisor: Alex Abolfazl Shiri, SSPA
Supervisor: Laura Marimon Giovannetti, SSPA
Supervisor and Examiner: Arash Eslamdoost, Department of Mechanics and Maritime Sciences

Master's Thesis 2021:84
Department of Department of Mechanics and Maritime Sciences
Division of Marine Technology
Chalmers University of Technology
SE-412 96 Gothenburg
Telephone +46 31 772 1000

Cover: From STARCCM+ simulation

Typeset in LaTeX
Printed by Chalmers Reproservice
Gothenburg, Sweden 2021

Abstract

The motion of a fluid interacting with a structure has long been a well known phenomena, but up until recently, the motion of the fluid and the structural response of the structure has been treated as two separate problems. This approach works well and gives accurate results when there is a insignificant to no deformation of the structure. However, in the case of a hydrofoil, the deformation is significant, and it will change the flow pattern and subsequently the forces acting on the hydrofoil.

This paper presents the fluid structure interaction of the NACRA 17 hydrofoil, using a isotropic model and a composite model, and subsequently compare the results generated of the two models. During the project experiments are carried out at the facility's of SSPA to validate the models. The paper also presents the reverse engineering of the hydrofoil and the verification process of the reverse engineered geometry.

Acknowledgements

Aloïs Thollot, the effort and time you have spent working with us during the project is truly appreciated, especially in the Computational fluid dynamics (CFD) section. Your input when setting up and creating the numerical module in the cavitation Tunnel has proven invaluable. It allowed us to expand the scope of the project.

A big thank you goes to our examiner and supervisor Arash Eslamdoost, from Chalmers University of Technology, your effort throughout the project were priceless. Following the progress of the project on weekly basis, mentoring, and assisting us to solve problems and obstacles specially when creating the CFD module.

We would like to thank Laura Marimon Giovannetti, from SSPA. We were lucky to have you in this project, supervising and assisting us throughout the project to build up an understanding for the Fluid structure interaction (FSI), and your supervision during the tests at the cavitaion tunnel at SSPA facilities. Your input to the project was invaluable.

We want also to thank Alex Abolfazl Shiri, our supervisor from SSPA, for his efforts spent to prepare for the tests in the cavitaion tunnel at SSPAs facilities, and for his supervision throughout the project.

Rolf Sörmans fond, for the finical contribution that allowed us to carry out the validation and testing at SSPA.

We want to thank Frank Bramkamp at the Tetralith support, who worked tirelessly with us for several weeks, answering multiple emails and making adjustments in the code for ABAQUS to run the CO-Simulation on the cluster. Without your support, the simulations would not have been possible.

We also want to thank Rikard Karlsson from Chalmers and the CASE lab, who was more than willing to help us 3D-scan the foil we acquired for testing at SSPA's facilities. Your contribution ensured that our geometry was true to reality and removed any uncertainty we had about our geometry.

Marcus Dackhammar, thank you for being willing to part with your hydrofoil after we discovered that the delivery time for a new hydrofoil would make it impossible for us to carry out any testing at SSPA. We hope the new one we ordered for you will bring a smile to your face as you fly above the waves once more.

We also want to thank Erik Kling from ReVibe energy for coming to Chalmers to both show us their datalogger ReLog, and for helping us capture the eigenmodes of the hydrofoil

The simulations were performed on high-performance computing resource (Tetralith) at the National Supercomputer Centre at Linköping University (NSC) provided by

the Swedish National Infrastructure for Computing (SNIC).

Fabian M. Ebbesson, Gothenburg,
Ali M. Farousi, Gothenburg,
December, 2021

Contents

List of Figures

List of Tables

Acronyms

ALE	Arbitrary Lagrangian Eulerian formulation
C2C	Cloud To Cloud
C2M	Cloud To Mesh
CAD	Computer Aided Design
CFD	Computational fluid dynamics
CNC CMM	Computer numerically controlled coordinate measuring machine
CPUh	Central processing unit hours
FIA	Fédération Internationale de lAutomobile
DIC	Digital Image Correlation
FEA	Finite element analysis
FSI	Fluid structure interaction
FVM	Finite Volume Method
M2M	Mesh To Mesh
NS	Naiver-Stokes equations
RMS	Root Mean Square
RANS	Reynolds Averaged Naiver-Stokes equations
STL	Stereolithography
VOF	Volume Of Fluid

1
Introduction

Foiling is by no means a new technology but has been developing for the past 100 years. The first foiling sailboat was the foiling trimaran *Williwaw*, built in the '70s. In more modern times, foiling has changed the competitive scene in sailing substantially, with the introduction of *AC72* foiling catamarans in America's cup in 2017 and the increased popularity of the *Moth* class.

The *Nacra 17* made its first appearance in the Olympic games in 2016 and was the first class capable of foiling under some conditions and the only class allowing for a mixed crew. For the world championship of 2017, the class received some upgrades, including the switch from C-foils to Z-foils. The updates made it possible to foil the multi-hull skiff fully. It was scheduled to be the first fully foiling class in the 2020 summer Olympics in Japan. [1] A overview of the *Nacra 17* with rigging is provided in figure 1.1

As stated by the *Nacra 17* class association:
"As in all foiling boats, the daggerboards are the most critical technical element of the boat (Nacra17.org, 2021)."

Given the importance of the daggerboards and the hydrofoils for the performance of the sailboat and the safety of the crew, the design and characteristics of the hydrofoil are important to *get right*, in other words, obtain sufficient and well-balanced lift and sideways force. At the same time, structural soundness must be maintained.

Fluid Structure Interaction (FSI) is still a relatively new area of research, and only in the past four decades have the computational power allowed researchers and engineers to start diverting from experimental approaches to understand the fluid-structure interaction in favor of a numerical approach. With this relatively recent development, the line between the traditional isolation of, for example, fluids and structures have started to be erased, as the new and powerful software's makes it possible to simulate both fields at the same time (Xiaodong (Sheldon) Wang, 2008).

With the advancement in FSI made in recent years and the importance of the design of the hydrofoils, a FSI simulation should be carried out during a design phase of a hydrofoil. Both the bend and the twist of the hydrofoil could dramatically impact the performance of the hydrofoil. The results from such a simulation can be used

[1] Due to the outbreak of covid 19, the summer Olympics of 2020 is postponed to 2021 and pending future feasibility evaluation

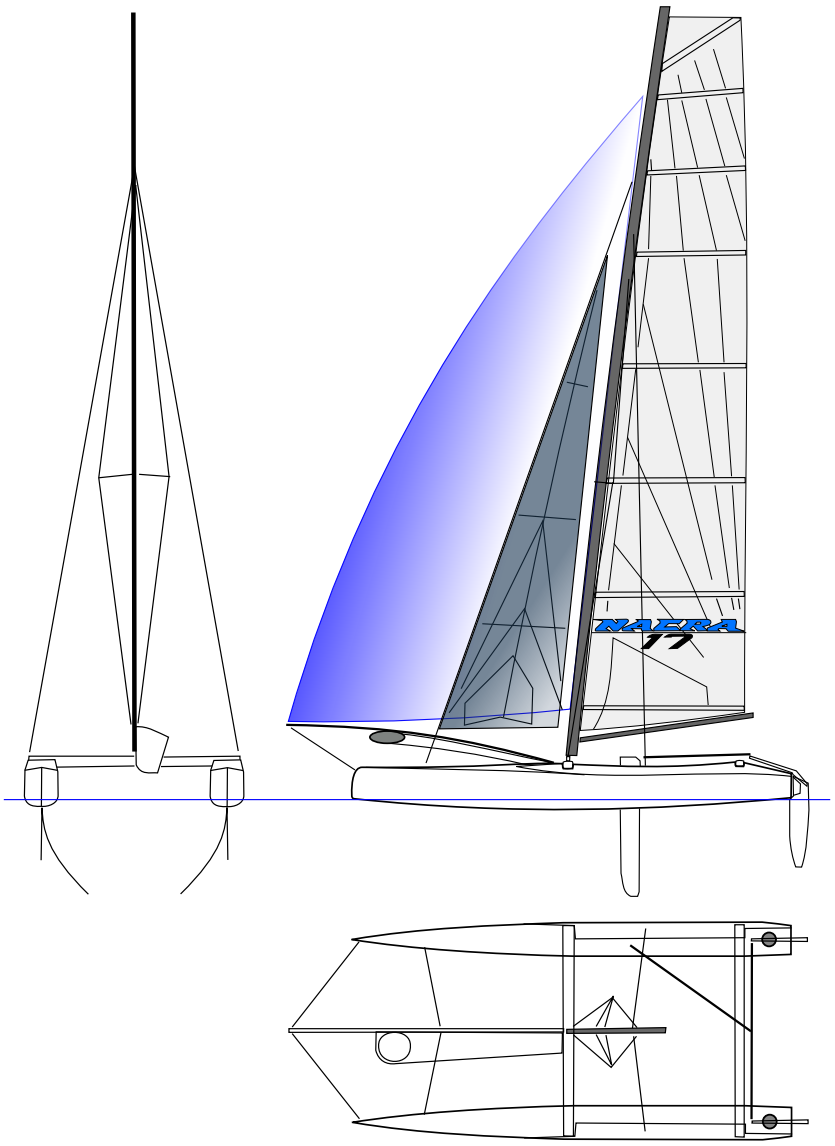

Figure 1.1: Outline of the Nacra 17 class (Wikipedia, 2021).

to optimize the hydrofoil design so that the deformation of the foils changes, for example, lift and drag at a given speed. One example of this being done is in *Formula 1*, where the introduction of flexible body parts was introduced in 1999. Unfortunately, this resulted in a high number of failing rear wings (Lawrence Barretto, 2021). With the high safety requirement posed by the Fédération Internationale de lAutomobile (FIA), the flexible body parts were banned shortly after that and are still banned to this day, as per sections 3.8 and 3.9 in (Fédération Internationale de l'Automobile (FIA), 2020). (Giovannetti, 2017) have explored the possibility of designing a passively adapted foil, achieving the desired response in a wind tunnel. L.Giovannetti concludes her thesis that the next step would be to carry out testing in water rather than air. The Raynold's number[2] in a race is easier to replicate in a test in water since the flow velocity can be reduced substantially.

To avoid the same faith of being banned in sailing competitions due to safety concerns, the structural soundness and robustness must be the main design criteria when designing a hydrofoil. Especially if the intended purpose of the hydrofoil is a commercial application, where failure under extreme or unforeseen conditions may never happen, or offshore racing, where help can be many hours or even days away. In most cases, a hydrofoil for a sailing skiff or boat is made out of some sort of composite material, more often than not, a carbon fiber composite. But even if the designer has no intention of using any other benefits than the high strength and stiffness to weight ratio that a composite offers, there will be some degree of deformation of the hydrofoil when its under load. The change in shape will affect the performance of the hydrofoil, and a understanding of how its affected and by how much is important for the overall performance of the flying vessel.

[2]A dimensionless number used to determine the degree of turbulence, dependent on geometry, fluid properties, and flow velocity

2
Objective

This project intends to acquire a deep understanding of how the NACRA17 hydrofoil is influenced by the FSI effects and how this influences the physical system. the aim will be achieved through the following objectives:

- Define the geometry of the NACRA hydrofoil.
- Define the material properties of the hydrofoil.
- Obtain the CFD domain.
- Define the optimal mesh for the studied case.
- verification and validation for the obtained numerical models.
- Running the co-simulations between the solid solver and the fluid solver to obtain the resulting forces and deformations.

3
Method

The work required to carry out the thesis is defined into discrete sections, where it is divided between the people involved in the project. During this project, an intern worked in close, collaborating with the students carring out the master thesis.

At an early stage of the thesis, an application for the scholarship, Rolf Sörmans fond, was applied for and granted to carry out some testing in the cavitation tunnel at SSPA. A total of 90,000 SEK was provided by Rolf Sörmans fond. The obtained funds were used to purchase a hydrofoil for the *NACRA 17* for 25,000 SEK, and the remainder was used to pay for parts of the tests at SSPA. L.Giovannetti also obtained funds from *Hugo Hammars fond* and *Chalmersska forskningsfonden*, 300,000 SEK and 100,000 SEK respectively, allowing for a full week of tests to be carried out in the cavitation tunnel at SSPA. This allowed the numerical models to be validated from actual test data.

During the project, a collaboration with the manufacturer of the Nacra 17 was desired from the students but not from the manufacturer. Due to the high price of the hydrofoil, a limitation to non-destructive testing was set as a criteria for the project.

In collaboration with the supervisors and Jan Hallander, a Senior specialist in cavitation and Hydro acoustics at SSPA, a test matrix was developed for the tests in the cavitation tunnel. The test matrix is also used for simulations.

The computationally heavy simulations were performed on a high-performance computing resource, Tetralith, at the National Supercomputer Centre at Linköping University (NSC).

3.1 Geometry generation and verification

Computer Aided Design (CAD) is used to generate a geometry based on a 3D scan provided by the supervisor L.Giovannetti. The purchased hydrofoil is 3D-scanned and compared with the generated hydrofoil. From the results of the 3D scan, the geometry is then subsequently refined to match the bought hydrofoil closely.

3.2 Fluid dynamics model

The numerical CFD model needed to carry out the desired simulations is generated in STARCCM+ software. The fluid domain, the physical models, and the mesh were specified and defined for the CFD numerical models. Furthermore, a detailed study for the mesh was preformed, followed by a mesh dependency study to o define the optimal mesh that serves the best for solving the desired problem.

3.3 Structural model

The structural model is generated in the FEA software ABAQUS. A mesh dependency is carried out to determine the most efficient mesh size since the structural model needs to be computed several thousands of times.

The purchased hydrofoil is used in static load testing to obtain the deflection during a known load condition. The results from the static load test are used as a basis when determining the material properties for the hydrofoil. The loads are replicated in ABAQUS and simulated, and the deformed structure is then exported to MATLAB for post-processing and compared with the results for the static load test.

Once a satisfactory model is obtained, input files containing the mesh, material properties and boundary conditions are generated and can be used in the FSI simulations.

3.4 Fluid Structure Interaction

To solve a FSI problem numerically, adaption of the created CFD model to make it solve for a FSI. Therefore, some additional physical models and an extra meshing technique were necessary to add to the CFD model.

During the project, two numerical models were generated in the CFD solver, a cavitation tunnel numerical model and a towing tank numerical model. Creating a cavitation tunnel allows for capturing, but is not limited to lift, drag, side forces, and the deformations of the hydrofoil. Having an additional model in the towing tank will be beneficial not only to capture the forces and deformations but also would allow to capture the performance of the *NACRA 17* hydrofoil, having the chance to include a free surface model and thus simulate the reel conditions more accurately.

3.5 Test results and verification

The deflection of the hydrofoil during testing is captured using Digital Image Correlation (DIC) equipment during the static load test and the tests carried out in the

cavitation tunnel. The deflection is imported to MATLAB together with the deflection from the FSI simulation. The two results are compared to verify the accuracy of the numerical model. The eigen modes of the hydrofoil are also captured from a impact test to compare with the eigen modes in the FEA model.

To determine the accuracy of the CFD numerical models which is important for the accuracy of the results, a validation and verification process needs to be preformed. The results of the experiment preformed in the cavitaion tunnel at SSPA facilities is to be utilized when validating the numerical model in the cavitaion tunnel by comparing lift, drag, and side forces and quantify the difference. The results are post-processed and exported to MATLAB to preform the comparison. In general the same process is to be preformed for the Towing tank, although due to lack of time a verification was carried out together with only a comparison with the results of the experiments.

4

Foil geometry

To be able to carry out the simulations, an accurate CAD model of the geometry must be established. Ideally, the manufacturer of the hydrofoil provides the geometry and material properties. However, there is always some variation in production that needs to be accounted for. so, in practice, the only way to make sure that the numerical models match the real hydrofoil is to reverse engineering the geometry and carry out material testing to obtain the applicable properties of the actual specimen.

Unfortunately, the manufacturer of the *NACRA 17* proved unwilling to provide the CAD geometry of the hydrofoil. This resulted in that a purchased hydrofoil had to be 3D-scanned and subsequently reverse engineered. Difficulties in acquiring a hydrofoil also lead to that an accurate geometry could not be established early on in the project.

4.1 Initial draft

From the start of the project, an old 3D scan of a *NACRA 17* hydrofoil was made available by L. Giovannetti and served as a baseline for an initial draft of the hydrofoil, see figure 4.1.

Figure 4.1: Initial 3D scan used as a starting point for the simulations

The provided 3D scan had some problems, especially along the trailing edge and the tip. Resulting in some uncertainty about the geometry of the hydrofoil. See figure 4.2.

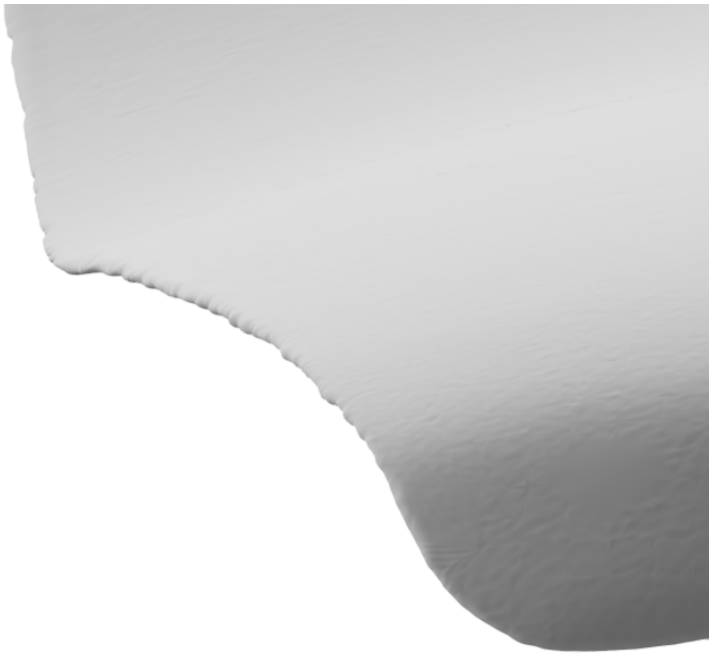

Figure 4.2: The trailing edge of the provided 3D-scan of a NACRA 17 hydrofoil

3D scanners often cannot capture corners of thin geometries and sharp edges, for

instance, hydrofoils trailing edge. Based on Laura's experience with the *NACRA 17* hydrofoil, it is also assumed that there is some variation between different specimens of the hydrofoil. Therefore, the initial draft of the geometry is viewed as a practice geometry used to get familiar with the workflow around setting up an FSI simulation, and that most likely, the geometry would have to be re-worked once a 3D-scan could be performed on the obtained hydrofoil. It is worth mentioning that the *Nacra 17* is a one-type class, and all the race participants are supposed to use identical equipment.

To reverse engineer the hydrofoil, a set of planes perpendicular to the hydrofoil along the length is created. If the curvature and change in cross-section of the hydrofoil was deemed large, the density of the planes is increased, see figure 4.3.

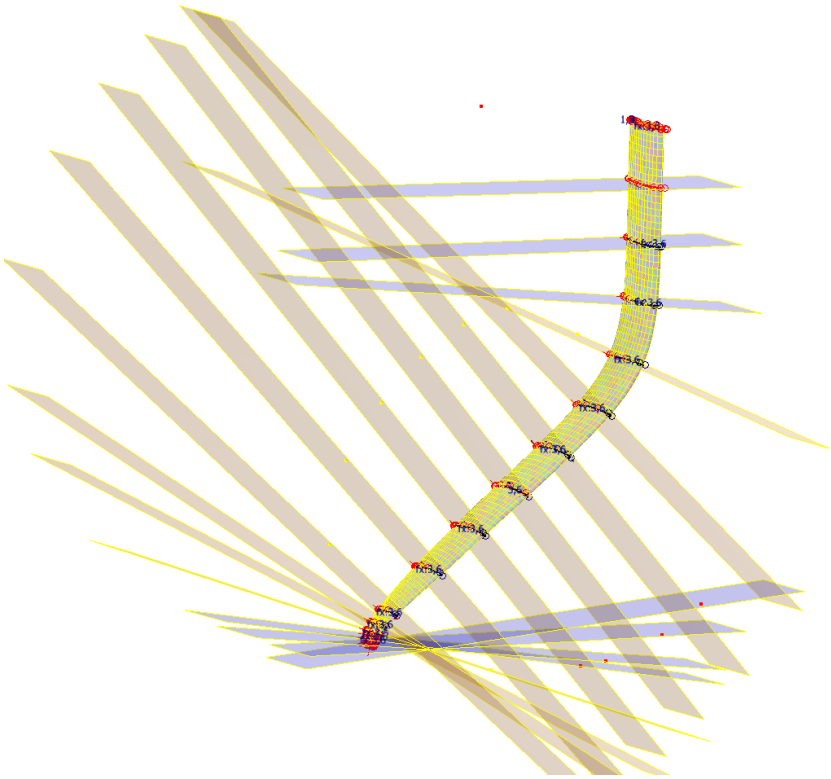

Figure 4.3: Planes used for the initial geometry

On each plane, the cross section of the wing profile was traced manually using a splines with control vertexes, and example of this is presented in figure 4.4.

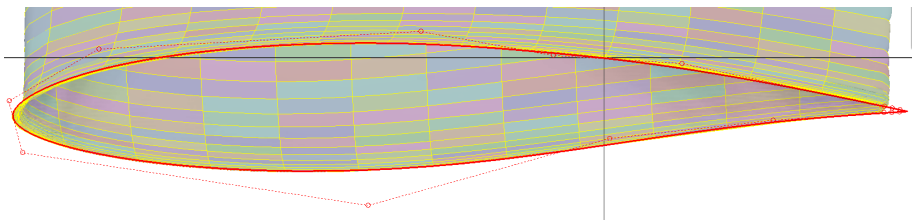

Figure 4.4: Manual tracing of the tracing of the cross-section using splines

Due to the poor quality of the 3D scan around the trailing edge, the splines were allowed to converge to a single point, giving the hydrofoil a sharp trailing edge. Se figure 4.5.

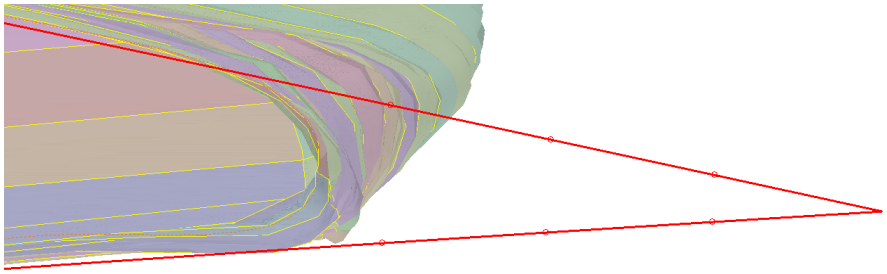

Figure 4.5: Idealized trailing edge of the hydrofoil

The 2D sketches are used to generate the geometry with a loft command. The lofting command creates a solid perpendicular to the 2D sketch planes, with the same cross-section as the sketch. The volume between the planes follows a smooth path, much like a spline using interpolation points would behave. The resulting initial geometry is presented in figure 4.6. As can be seen in figure 4.6b, the trailing edge of the initial geometry has a sharp and well-defined trailing edge.

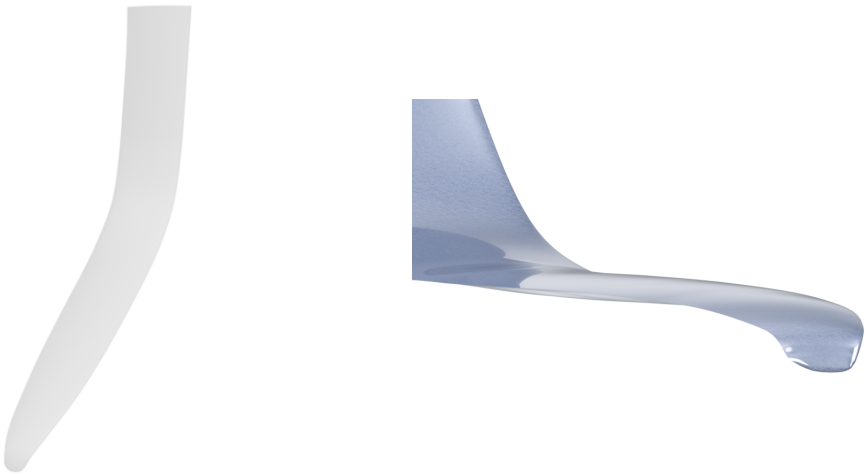

(a) ISO view **(b)** Trailing edge around the tip

Figure 4.6: The initial estimated geometry based on the provided 3D-scan

4.2 Geometry verification

Since it was assumed that the geometry would have to be re-worked once the hydrofoil for the testing is obtained, the geometry of the hydrofoil would have to be

captured and digitized. To measure the hydrofoil by traditional means, for example, ruler, calipers, measuring tape, etc, was deemed almost impossible due to the complex nature of the geometry. To obtain the actual geometry, there are a few techniques available to generate a 3D model from a real-life object.

- Photogrammetry - With the help of a digital camera, multiple photos can be taken of an object, and with the help of specialized software such as *COLMAP*, the geometry generated from the photos. To achieve a good and accurate model, the photos need to be of a high resolution, the camera needs to be calibrated, the angle between points of the image should be low, and points of the model should appear in many photos, to name a few. The accuracy of a photogrammetry model is measured in relative terms, where the largest length of the object being modeled is divided by NNN[1], where NNN ranges from $100 - 30,000+$, depending on the setup. According to (photomodeler.com, 2021). For an average accuracy, NNN can be set to 5000. This would give an accuracy of ± 0.4 mm for the hydrofoil in question, but it could also be as low as ± 20 mm.
  - \+ Relatively cheap, assuming a good camera is already available
  - − A large effort for calibration needed
  - − A high unknown factor of the accuracy of the generated model

- 3D-scanning - the term 3D-scanning is often misused since it only refers to a process of converting a physical object into a computer model. However, the term of 3D-scanning will henceforth describe the process of using a machine intended to generate a computer model of a real object with specialized hardware and software. 3D scanners can be grouped into a few different categories, laser triangulation, structured light, photogrammetry, and laser pulse-based. The cost and accuracy vary widely between make, model, and technique. But in general, an accuracy between ± 0.2 mm and 0.03 mm could be expected.
  - \+ Good and reliable accuracy
  - \+ No calibration needed
  - \+ Easy to use hardware and software
  - − Expensive hardware

- Computer numerically controlled coordinate measuring machine (CNC CMM) uses a probe, typically ruby or ceramic, located on a Cartesian robot equipped with glass scales to track the probe point's position in space. The base of the CNC CMM is often a large granite slab to provide stability. The CNC CMM needs to be kept in a climate-controlled environment to preserve the accuracy of the machine. The probe point can either probe selected points of the geometry to obtain their location or sweep along a patch to define a line in space. The accuracy of a CNC CMM is typically measured in the μm range since intended use is to measure tolerances for machined parts.
  - \+ Extremely high accuracy
  - − Very expensive

[1]NNN is defined from control points in the setup and is a relative accuracy

- Takes a long time to fixture the geometry to prepare the scanning operation

- Highly specialized equipment, expert knowledge is needed to operate the machine.

All the options would, in theory, be possible to carry out, but since a 3D scanner can be provided from the CASE-lab at Chalmers, it is considered to be the best option, striking a decent balance between accuracy, consumed time, and cost.

4.2.1 3D scanning

To verify the geometry, a 3D scan of the acquired foil is performed. The scanning was carried out at SSPA's facilities with the help from a Ph.D. student, Rikard Karlsson, who have access to a *Artec3D-Eva* scanner and knowledge of how to operate the machine and the software. The scanners use a hybrid of geometry and texture tracking for capturing the geometry. According to the manufacturer, it should not have any difficulty capturing shiny or black surfaces. Artec 3D, 2021. The resolution of the handheld 3D scanner is up to 0.1 mm. The full technical specifications of the 3D-scanner can be found in A.1.1.

However, based on Rikards experience and advice, carbon fiber can be tricky to capture accurately with the *Artic3D-Eva* scanner, mainly due to the black and shiny surface. To avoid this shortcoming, a specialized type of spray paint, *AESUB blue*, specially developed to generate a beneficial surface for 3D scanning, can be used to paint the foil. The paint also has the added benefit that it evaporates fully after 1-2 hours without leaving any traces of the paint. The surface treatment leaves the foil with a white and mat surface, more suitable for 3D-scanning. In figure 4.7, only the shiniest parts of the foil have been painted. In figure 4.8 Rikard is trying to 3D-scan the partly painted hydrofoil. This, however, proved to be unsuccessful, and the entire foil had to be painted, as in figure 4.9

Figure 4.7: Parts of the foil painted

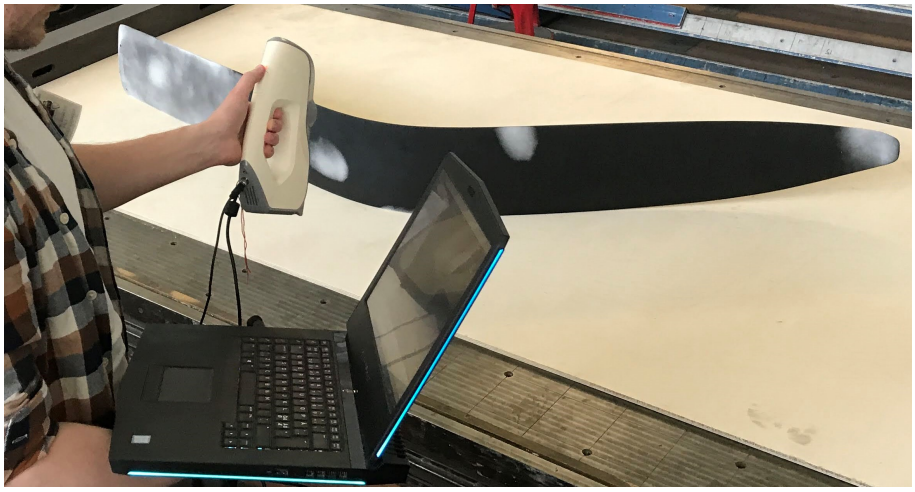

Figure 4.8: Attempted scanning of the partly painted foil

Figure 4.9: The entire foil painted

When the 3D scan is completed, the point cloud is used to generate a Stereolithography (STL) file. This STL file can then be used to compare the generated geometry with the 3D-scanned geometry for verification. The obtained STL file is presented in figure 4.10.

(a) ISO view

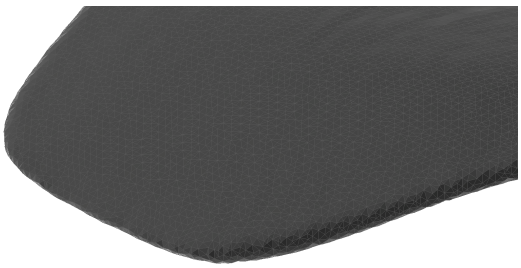

(b) Detail view of the tip with the mesh for from the STL geometry

Figure 4.10: The new geometry obtained from the 3D-scan

4.2.2 CloudCompare and geometry refinement

To compare the scanned geometry with the initial draft, an open-source software is used (CloudCompare, 2021). The software allows the user to align two models and then compare the geometric deviation between the two models. The process of aligning two parts in CloudCompare consists of two steps. First at least three points are selected in each model, with the sets on one of the models and one of the models is set to the the reference model. These points do not have to be exactly in the same spot on the two models since they are only used to ruffly align the parts. Once the parts have been ruffly aligned, the fine alignment algorithm can be initiated. The fine alignment algorithm calculates the shortest distance between Cloud To

Cloud (C2C), Cloud To Mesh (C2M) or Mesh To Mesh (M2M), depending on what type of model is used. The model is then moved to best match reference model, minimizing the Root Mean Square (RMS) value of the distance between the two models. The result of comparing the initial geometry with the obtained geometry from the 3D scan is presented in figure 4.11.

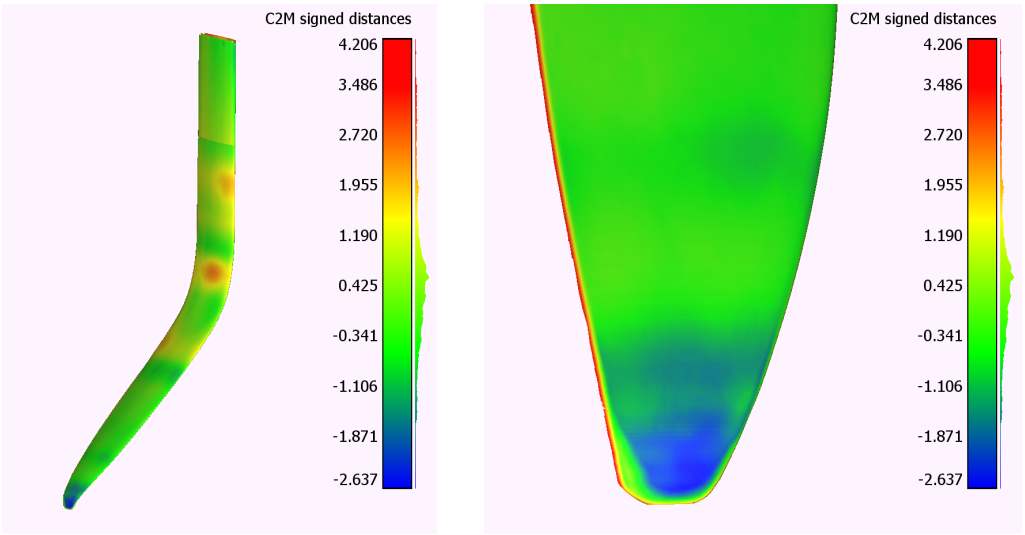

(a) ISO view

(b) Detaild view of the tip and trailing edge

Figure 4.11: The initial draft compared with the 3D-scanned hydrofoil

A histogram over the deviation is generated in CloudCompare to quantify the deviation. The resulting plot is presented in figure 4.12.

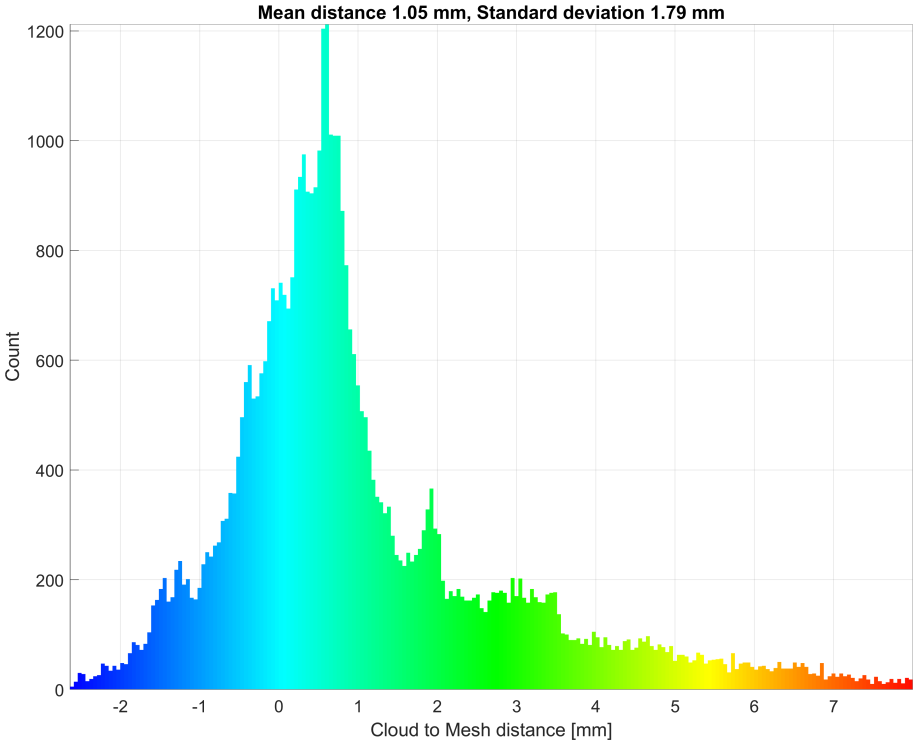

Figure 4.12: Histogram over the deviation of the initial draft when compared with the 3D-scanned hydrofoil

As can be seen in figure 4.12, the deviation is rather large and has a large range. These values are also based on the exclusion of the trailing edge and the top of the hydrofoil, since the length of the hydrofoil was overestimated.

Based on the findings from CloudCompare, it is deemed that the geometry has to be refined. The approach and workflow used to refine the geometry were the same as the one described in section 4.1, with the exception that the trailing edge would not be a single sharp point, but rather a sharp corner, as shown in figure 4.13. The reason to do so is to be able to obtain a good quality mesh easier in STARCCM+. After a discussion with the examiner and the supervisors of the project, the conclusion is that this would not have a significant impact on the performance of the hydrofoil. The length to be chopped from the trailing edge varied along the hydrofoil. The corner thickness defined the shortening length of the trailing edge. The distance is set to 3 mm where the daggerboard is inside the hull of the *NACRA 17*. The part that sticks out of the hull is set to 2 mm. The trailing edge on the part of the hydrofoil that is located inside the hull is thicker.

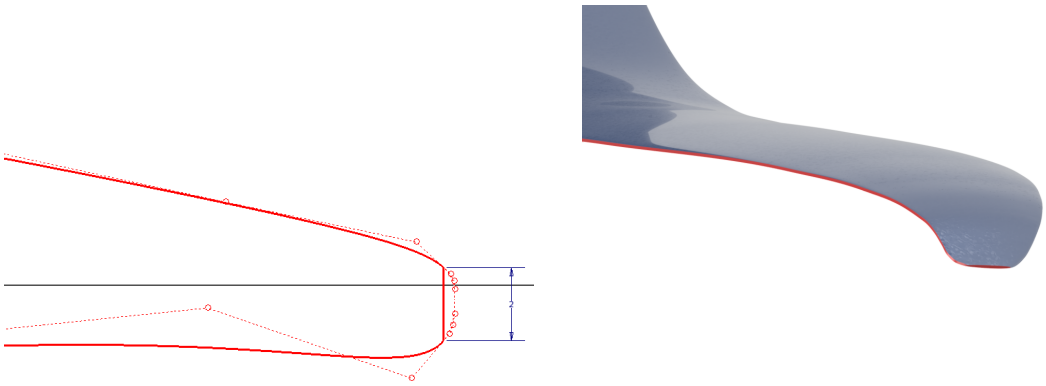

(a) Updated cross section

(b) Excluded trailing edge highlighted in red

Figure 4.13: Simplification of the trailing edge

The new geometry is then imported to CloudCompare to compare it with the 3D-scanned hydrofoil. As expected, there was a large deviation at the top of the hydrofoil since the real hydrofoil has smooth corners. However, those were deliberately chosen not to include in the model, both to keep as a reference surface and to make the meshing process easier. A heat map over the deviation of the new geometry compared with the geometry from the 3D scan was generated in CloudCompare to find potential errors in the new geometry. The result is illustrated in figure 4.14.

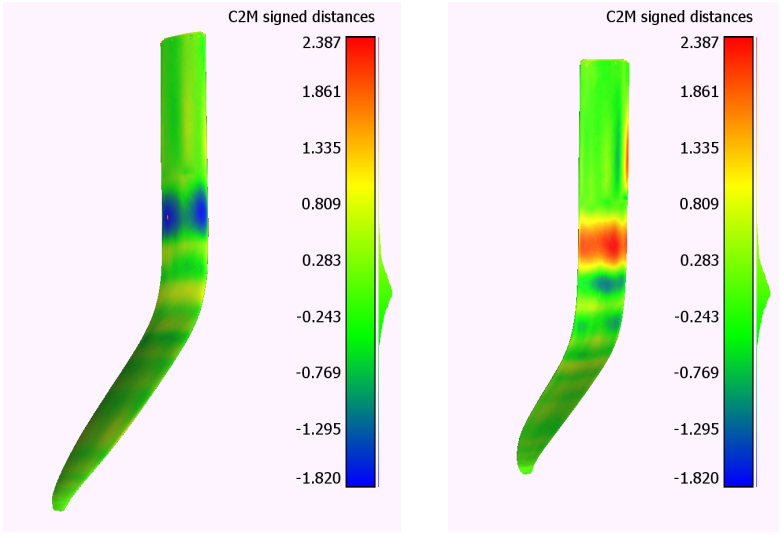

(a) Suction side of the new geometry

(b) Pressure side of the new geometry

Figure 4.14: Deviation of the new geometry compered to 3D-scan

As can be seen in figure 4.14, there is a rather significant difference just above the

knee of the hydrofoil. This is most likely caused by the way the CAD software generates the loft command and the fact that the density of the cross-section 2D sketches is relatively low in that region. Another cross-section 2D sketch is inserted where the deviation was significant in an attempt to minimize the error.

A new heat map was generated to find any hot spots in the deviation between the new geometry and the 3D-scan. The result is presented in figure 4.15. Comparing the new heatmap with the one in figure 4.14, the hot spots above the knee have been eliminated, and the overall deviation seams to be very small.

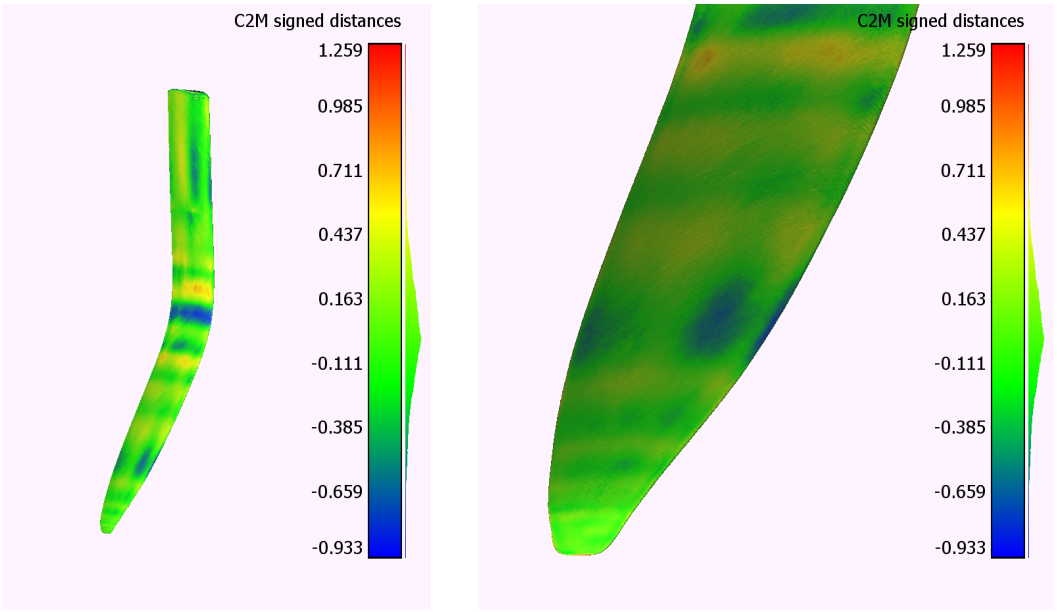

(a) ISO view **(b)** Detailed view of the leading edge

Figure 4.15: Deviation of the new updated geometry compared to 3D-scan

A histogram of the deviation is generated in CloudCompare. Se figure 4.16. As can be seen in the histogram, the deviation from the 3D-scanned geometry compared to the reverse engineered geometry within $\pm 2\sigma$ is about ± 0.5mm. The new geometry is considered to be sufficiently accurate to be used in the CFD and FEA model.

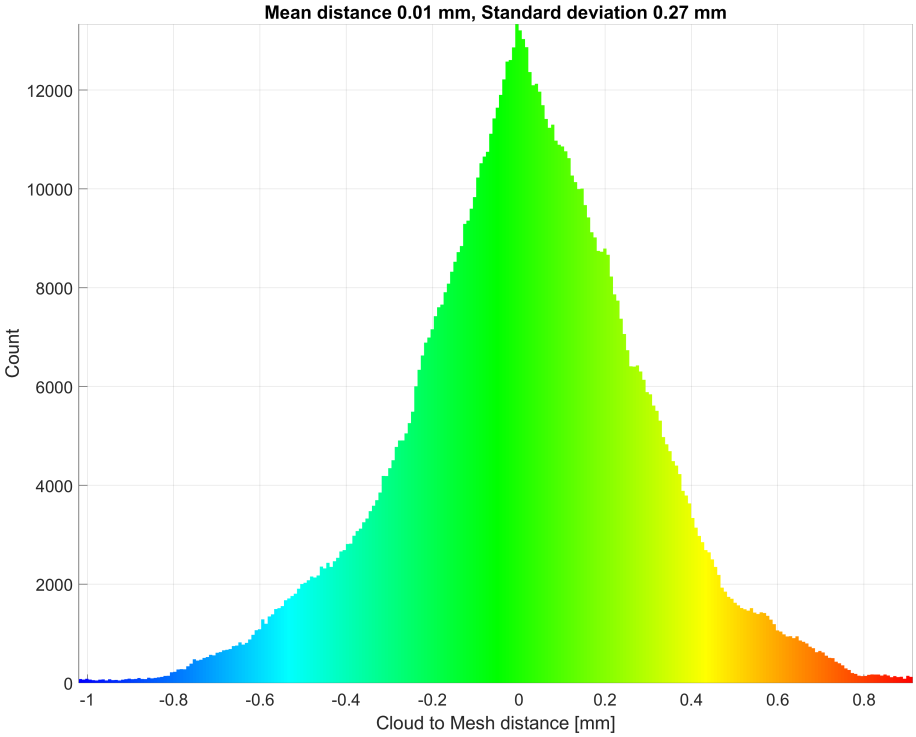

Figure 4.16: Histogram over the deviation of the reverse engineered geometry compared to the 3D-scanned model

If so desired or required, this iterative process could be used to closer match the 3D-scanned geometry, to the point where the surface matches the accuracy of the 3D-scanner. More pictures of the geometry comparison are presented in appendix A.1.2.

4.3 Unknown aspects of the hydrofoil

Despite the accurate surface geometry obtained from the 3D scan, there are still some unknown aspects of the geometry of the hydrofoil, mainly the internal structure. In a composite structure, the skin of the part is considered to be the main load-bearing element. However, a composite typically suffers from poor out-of-plane material properties, and thus an internal structure is needed to keep the faces of the hydrofoil from collapsing. This is done in two ways primarily. The structure could be made with a core, for example, an aluminum honeycomb or a foam core, or an internal stiffener made out of composite or an aluminum beam.

Since the testing of the hydrofoil is limited to non-destructive testing, cutting open the hydrofoil and take a look inside was not possible. This, coupled with the fact that the manufacturer where reluctant to share the drawings for the hydrofoil, meant that the internals of the hydrofoil ended up as a qualified guessing game.

It was, however, know that the foil most likely does not use a core material. This conclusion is based on two findings. On the top of the hydrofoil, there are two drain

plugs, so that the sailor can empty the hydrofoil of water, if any water manages to get inside the hydrofoil. A picture of a broken NACRA 17 hydrofoil is provided by L. Giovannetti, see figure 4.17. Unfortunately, it is tough to draw any other conclusion about the internal structure of the hydrofoil, other than the fact that no core material can be seen in it.

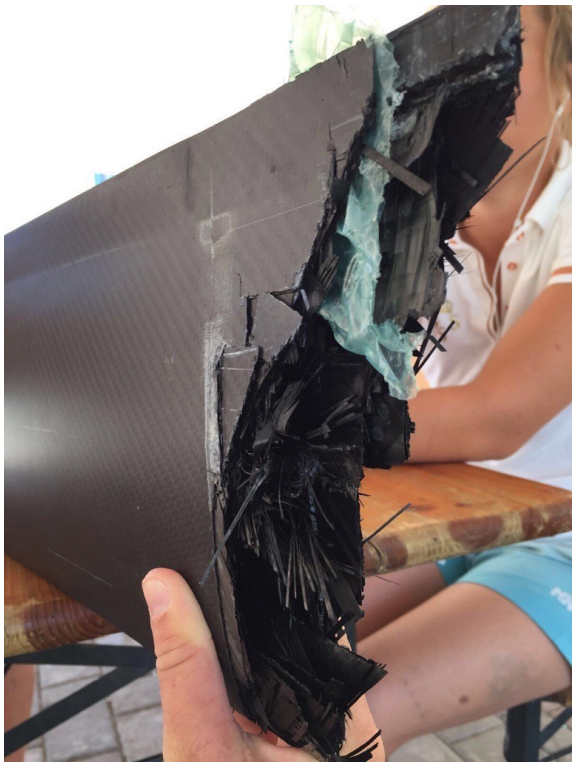

Figure 4.17: A broken NACRA 17 hydrofoil

But with these two findings, some conclusions can be drawn:

- The internal structure divides the void inside the hydrofoil into two separate chambers, creating the need for two drain plugs.
- The foil is most likely equipped with an internal stiffener in the form of a spar.

An attempt to figure out the location of the stiffener was made by knocking on the hydrofoil, listening for a change in the sound generated when knocking on the hydrofoil. A distinct difference in the pitch could be heard at a given point, just before the midpoint of the cord length. The position of the internal stiffener was estimated to be ⅜ of the cord length. Since it will be impossible to determine the geometry of the stiffener, it is assumed that the stiffener is a simple plate, running from the top of the hydrofoil down to the bend at the tip, see figure 4.18 In reality, the cross-section and the span of the stiffener are most likely more complex, for example a U or box shape, but based on what is know, a plate can be considered accurate enough.

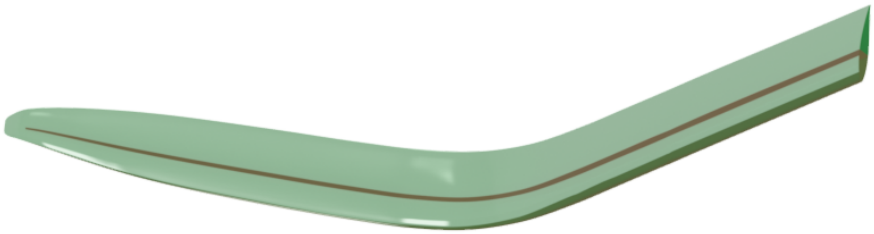

(a) Overview of the internal stiffener

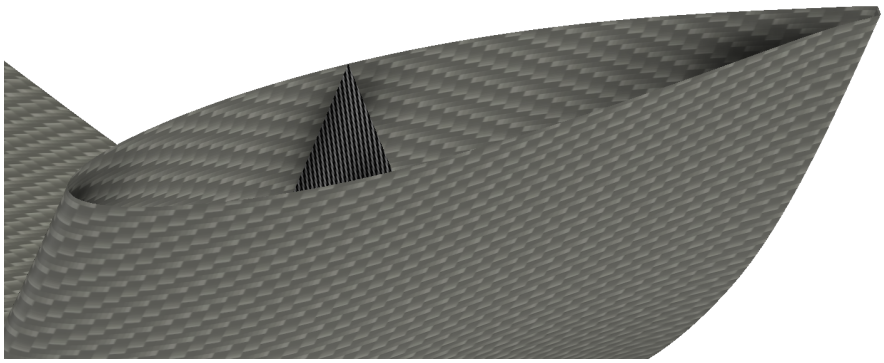

(b) Cross section of the internal stiffener

Figure 4.18: Estimated internal stiffener

5

Numerical method for flow analysis

Utilizing CFD in the field of engineering predictions nowadays has become so vital that it is considered as a new third dimension in the fluid dynamics according to Wendt, 2008. This new dimension will join the other two dimensions represented by the pure theory and the pure experiment. In figure5.1 one can observe the relationship between all three dimensions.

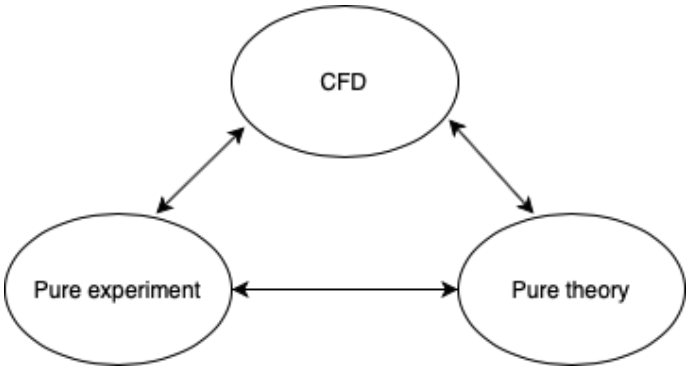

Figure 5.1: Pure experiment, pure theory, and Computational Fluid Dynamics CFD relationship scheme

The importance and the increased interest of utilizing CFD are based on several aspects. One of the main aspects is related to expenses. The costs of the experiments, .i.e, wind and cavitation tunnels, Etc., are relatively high and constantly increase. At the same time, the computation costs are, in general, lower and keep going down. Over time, and simultaneously computers have been improving and evolving, and thus the costs for operating them have reduced while the costs for operating the testing facilities increased. According to Chapman, 1979, the costs have been reduced by order of magnitude almost every eight years, see figure 5.2.

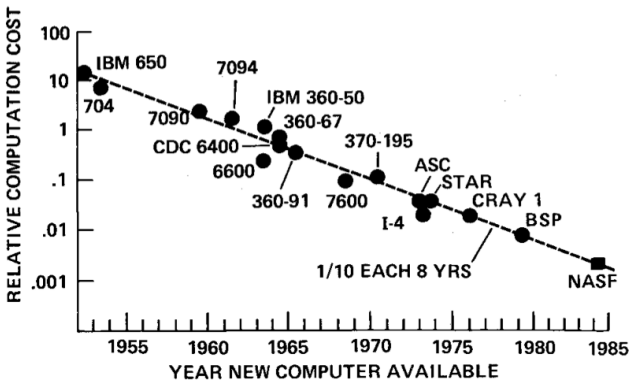

Figure 5.2: Relative computation costs plotted against time Chapman, 1979.

5.1 Computation fluid dynamics CFD Theory

Computation fluid dynamics CFD can be described as a method to solve fluid dynamics governing equations numerically. In this section a short introduction about CFD will be described followed by an introduction for the FSI.

5.1.1 Governing Physics

The base of the CFD according to Wendt, 2008 is the fundamental equations of the fluid dynamics .e.g the continuity, the momentum, and the energy equations. Those equations are based on and derived from the fundamental physical principles:

- Mass is conserved.
- Newtons second law.
- Energy is conserved.

The governing equations of the fluid flow in their simplest form are presented in a partial differential form which is complex, complicated, and are not analytically solved yet. On the other hand, Computational Fluid Dynamics CFD is the magic trick to replace the complexity of the governing partial differential equations with only numbers, where obtaining the numerical description of the fluid flow is through progressing these numbers in space and or in time.

In CFD in order to apply the fundamental physical principles to moving fluid, a Finite region should be defined. Thus, a control Volume V is defined, and a closed (control) surface is defined. The defined control volume can be fixed in space while the fluid is crossing through or can be moved with the fluid so that the fluid particle is always inside the control volume. The fundamental physical principles are applied to the fluid particle that is inside the control volume in both. The approach moves the observer's attention only to the location of the fluid particle inside the finite region. The governing equations of the fluid flow are obtained by applying these fundamental physical principles to a finite control volume. The resulting equations are in the integral form, which can be transformed indirectly to a differential form by

manipulation. Moreover, the governing (partial differential or integral form) equations are considered to be in a conservation mode when the control volume is fixed in space while the fluid is crossing through and in a non-conservation mode when the control volume is moving with the fluid.

Converting the conservation laws to partial differential equations is possible when the additional demands of having enough regularity of the solution are achieved, which is generally not always guaranteed. Discretizing the integral form of the equations instead of the partial form would represent the conservation laws accurately, which is the cornerstone of the Finite Volume Method (FVM). In the FVM the fluid domain is divided into cells, and the conservation laws are applied in some discrete points of these cells to obtain the variables of the flow.

5.1.2 Theory behind Fluid-Structure Interaction

According to Bazilevs et al., 2013, fluid-structure interaction is a type of problem where the fluid and the solid parts influence each other mutually. The flow field around the solid structure is dependant on the shape and the motion of the structure. In contrast, the solid structure's deformation and its motion depend on the resultant pressure and shear forces extracted from the fluid on the structure. Nowadays, and since the reliance among the action and reaction has become more robust, analyzing the Fluid-Structure interaction behavior has become more critical.

From Zienkiewicz et al., 2014 Fluid-structure interaction or FSI problems can be noticed in both nature (e.g., a tree with the wind Etc.) and in the different industrial applications (e.g., marine applications at seas Etc.). However, the type and the level of the interaction in these problems are categorized differently according to the type of coupling.

In general the FSI can be divided into two main categories Zienkiewicz et al., 2014 based on the flow physics to:

- Gas-solid interaction.
- Liquid-solid interaction.

The Liquid-solid interaction is the relevant type in the marine application. Thus, it is to be implemented in this study. According to Siemens, 2020 the fluid-structure interaction can be categorised based on the type of coupling as well to

- One-way or weak coupling.
- Two-way or strong coupling.

These types demonstrate the relationship between the action and reaction of the coupled systems. In one-way coupling, the influence from the flow motion around the solid body is noticeable, causing deformations on its structure. The case is different from the reaction side. When the structure deforms as a resultant of the applied fluid loads, the displacement of the structure influence the fluid flow in

return, although the influence is so slight that the effect could be neglected.
As in the two-way coupling, the case is different. The influence of the pressure and shear forces of the fluid on the structure deforms the structure. Hence, the responses in the solid are significant, which results in an alteration of the flow field.
In this master's thesis, a strong coupling system is to be studied and investigated.

5.1.3 Moving mesh

In general, two approaches are available to address the Naiver-Stokes equations (NS); Lagrangian and Eulerian descriptions. The first one considers a single material particle and follows its motion. The latter is based on fixing a control volume and capturing what is happening inside it. In fluid dynamics, define and follow a fluid particular can be tricky; therefore, the Eulerian approach is more suitable for such problems. The Lagrangian description is the standard approach for structural problems. In FSI simulation another approach is introduced, the Arbitrary Lagrangian Eulerian formulation (ALE) approach developed by Donea et al., 1982. According to Sigrist, 2015 in ALE approach, a combination of the Eulerian which considers writing the equation of motion in a spatial domain where the system moves through a fixed mesh. In the Lagrangian approach, the equation of motion is written in a material domain, tracking the equation of motion through mesh that deforms when the system moves. Stating the equation of motion in a moving frame would be possible when utilizing the ALE, allowing for controlling the mesh geometry independently from the material geometry. According to Zienkiewicz et al., 2014, when FSI problems are introduced, the solid part could be treated using the Lagrangian description. For the fluid domain, the ALE formations are to be considered, which will allow for an independent shift for the mesh from the material points. Hence more beneficial for the mesh quality. In figure 5.3 one could see the difference between the different descriptions and their impact on the grid quality.

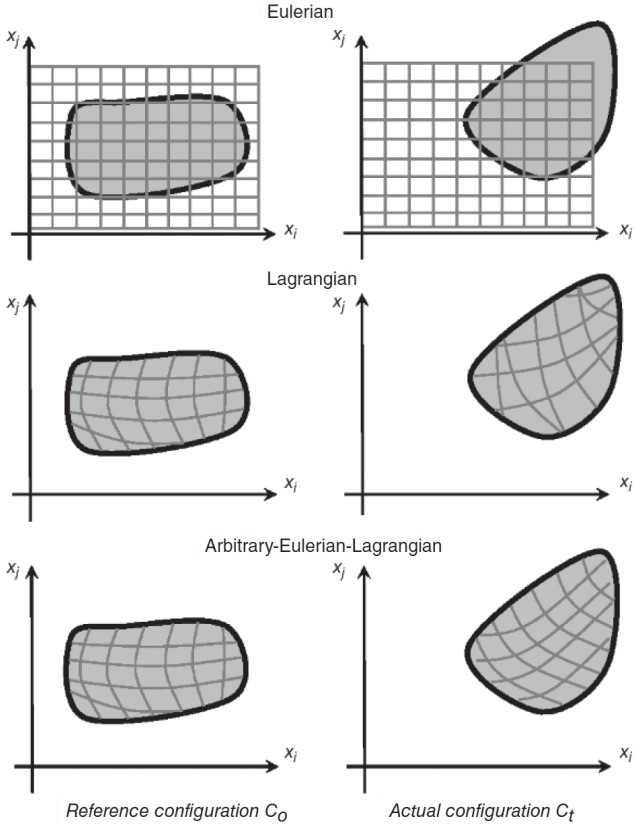

Figure 5.3: Lagrangian, Eulerian, and the Arbitrary Lagrangian Eulerian descriptions Zienkiewicz et al., 2014

5.2 CFD domain

The purpose is to generate a numerical model capable of simulating the actual conditions for a NACRA17 hydrofoil, capture, and analysis its performance. In real life, experiments can be made to simulate the sailing conditions inside testing facilities. Where Testing in a Towing-tank will simulate the desired conditions to some extent since the testing would be limited over a range of speed due to a limited achievable speed. These types of experiments, in general, are costly and require a considerable setup. Another option is the Cavitation tunnel which is less expensive than the previous, although still costly. Nowadays, one can simulate these tests in a CFD numerical model. Although, validation is needed here to make sure that the model is accurate enough and reflects the life conditions.

This project includes two numerical models: a cavitation tunnel model and a towing tank model. The CFD model for the cavitation tunnel is to be verified and then validated based on the results of the experiment at the actual tunnel at SSPA testing facilities. In order to validate the towing tank numerical model, one would base the validation on results obtained from tests performed in a towing tank. In the project, tests were made only at the cavitation tunnel since testing in a towing

tank is relatively costly; thus, it was not possible. In general, validation can be made based on a similar tested case in a towing tank to the studied one; validation was not performed for the towing tank model due to a lack of time. However, a comparison between the results for the lift, drag, side forces of the towing tank numerical model with the forces obtained from the tests in the cavitation tunnel at SSPA testing facilities is performed to determine the accuracy of the results derived from the numerical model.

5.2.1 Cavitation tunnel

The main step is to define the size of the domain where it is defined based on the actual size of the tunnel at SSPA. The tunnel contains three main sections, inlet, outlet, and a middle body section (test section). The total length of the middle section is 8 m, a test section of 2.1×1.22 m^2, and a maximum achievable speed at the tunnel 9.9 m^2. The figures 5.4a, 5.4c, and 5.4b shows the cavitation tunnel geometry; indication the position of the foil at the tunnel.

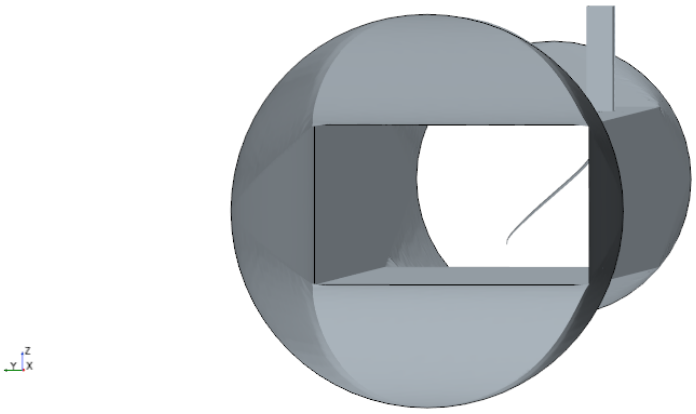

(a) Front view of the cavitation tunnel

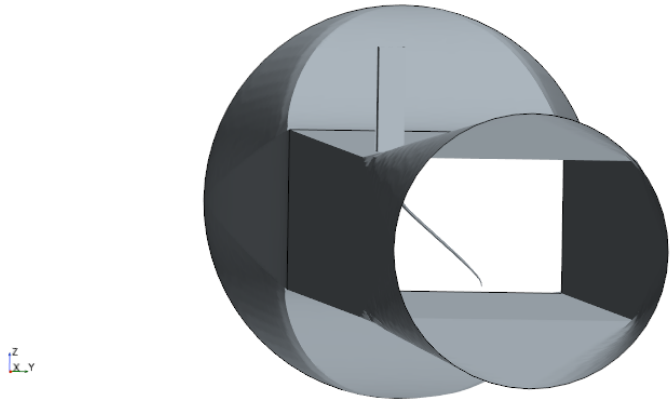

(b) Back view of the cavitation tunnel

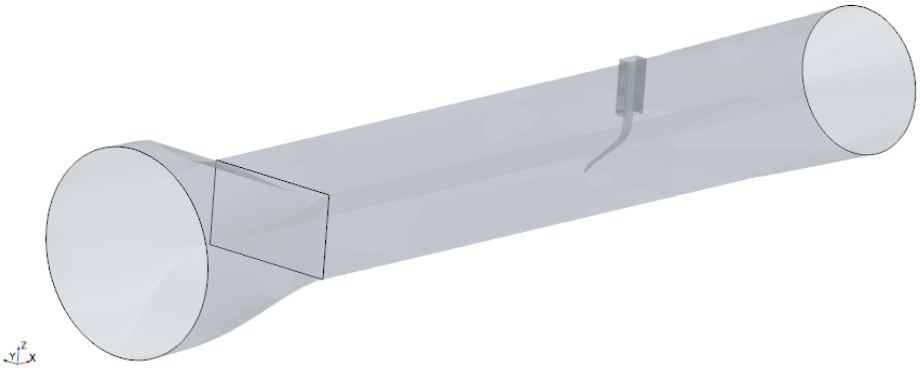

(c) Side view of the cavitation tunnel

Figure 5.4: Fluid domain for the cavitation tunnel domain

It is decided to insert the foil in the last third of the cavitation tunnel by the technicians at SSPA for technical reasons. This section has more apparent windows compared with other sections and has an extra-wide window. Locating the foil at this position would give the cameras and the setups more space and thus allowing for more accuracy while capturing and monitoring the tests.
During testing, the foil is clamped to a fixture and inserted through a hatch at the top of the tunnel. The clamping fixture is located at the same position as the foil will be fixed in the hull to reflects the actual boundary condition.

On the other hand, in the numerical model, one would specify the position of the foil, the dimension of the tunnel, and its boundary conditions. The foil will be located at the same position as in the tests. Hence, the part of the foil that is clamped and located outside should be located outside the flow field inside the domain. Initially, the foil was located to cross the top of the virtual tunnel (fluid domain). However, negative volume cell error occurs after a few time steps disallowing the simulations from continuing. The error occurred due to the boundary conditions (walls) at the top of the domain. The mesh cells at the crossing were trying to deform to follow the displacement of the foil; only the walls of the domain were trying to fix the cells and restricting them from moving. A solution is made to fix the issue by opening at the top of the virtual tunnel then adding an extra small block to close the opening. This approach is beneficial where the foil now is not crossing the top walls of the domain and thus no more negative volume cells. The advantages of having this extra block were not limited only to solving the error. It reduced the number of cells, too, since the prism layer at the opening is removed, and the surface mesh around the foil area inside the block can be reduced.

5.2.1.1 Boundary condition

The boundary conditions are specified in table 5.1. The desired achieved velocity at the foil region is to be 9 m/s. Although, in order to get the desired speed at the foil region, one would calculate the speed that the flow should have at the inlet. Hence, the flow will be fully developed when it reaches the foil position having the desired velocity. One can derive the velocity at the inlet based on the mass conservation as follows in equation 5.1:

$$A_{inlet}\nu_{inlet} = A_{foil}\nu_{foil} \tag{5.1}$$

In the equation, 5.1 the references "foil" and "inlet" stand for the location of the flow. On the right-hand side, A_{foil} is the section area near the foil, which is the same as the section area of the tunnel mid-body 1.22×2.1 m^2. On the left-hand side, A_{inlet} is the area of the circular inlet section $A_{inlet} = \frac{\pi d^2}{4}$ m^2, where d is the diameter 3 m. The resultant velocity one needs to apply at the inlet is v_{inlet}=3.26 m/s.

Table 5.1: Boundaries conditions

Name of the boundary	Type of boundary	Values
Inlet	Velocity Inlet	3.26 m/s
Bottom	wall	no slip
Top	Wall	no slip
Right-side	wall	no slip
Left-side	Wall	no slip
Outlet	Pressure Outlet	0 Pa

5.2.2 Towing tank model in the presence of the free surface model

The second model utilized in this study is the Towing-Tank model, which includes a free surface. A detailed description of this model is defined and described in this section.

Defining the fluid domain is the primary step when building up the numerical model. Unlike the Cavitation tunnel model, the dimensions of the towing tank's fluid domain are not restricted from the size point of view. Thus one can define the dimensions of the domain adaptively to the purpose of this model. Therefore, the influence from the walls on the flow field could be avoided by defining as large a domain as possible, locating the walls far from the flow field region. The flow is in the X-direction, Z-direction is upwards, and the Y-direction is out of the plane. In figure 5.5 a demonstration of the resultant tank can be seen:

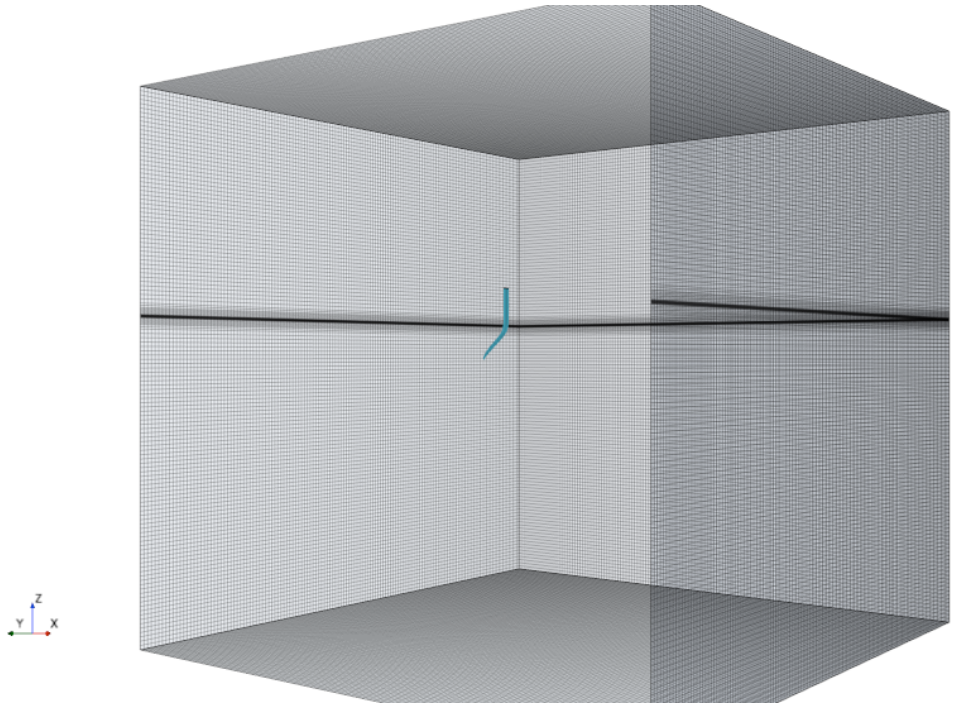

Figure 5.5: View of the Towing tank fluid domain together with the *NACRA17* foil

In STARCCM+ one would define the coordinates of the fluid domain (virtual tank) to obtain its dimensions. The corner coordinates of the fluid domain seen in the figure 5.5 and utilized for the preformed simulations can be seen in table 5.2:

Table 5.2: Corner coordinates of the fluid domain for the towing-tank numerical model

Axis	Size (m)
+ X	-6
- X	8
+ Y	-8
- Y	6
+ Z	-8
- Z	5

5.2.2.1 Boundary conditions

In this model the free surface model is to be included to obtain much closer results to the reality. The inlet speed is a field function of the velocity of flat VOFWave and so the outlet pressure is to be a Hydrostatic pressure of a flat VOFWave. In *STARCCM+* one can utilize VOFWave model to include the effects of the water surface in the simulation. The walls are far enough from the flow region and thus the resultant disruption from the walls on the flow is neglected. Furthermore, Symmetry plane condition is to be used as a boundary condition at the bottom, top, left, and

right side of the fluid domain .e.g the tank for simplicity. The boundary conditions are specified in table 5.1.

Table 5.3: Boundaries conditions

Name of the boundary	Type of boundary	Values
Inlet	Velocity Inlet	Velocity of Flat VofWave 1
Bottom	Symmetry Plane	zero gradient in wall normal direction
Top	Symmetry Plane	zero gradient in wall normal direction
Right-side	Symmetry Plane	zero gradient in wall normal direction
Left-side	Symmetry Plane	zero gradient in wall normal direction
Outlet	Pressure Outlet	Hydrostatic Pressure of Flat VofWave 1

5.2.3 Fluid-Structure Interaction Numerical model

In general, when the interest is to obtain a numerical solution for a case that involves the effects of a fluid, utilizing a CFD solver would be optimal, similarly when having a pure solid case utilizing a FEA solver would be optimal. In a FSI problem, the fluid influence the solid, causing deformation of the structure, then the deformation of the structure is to influence the fluid again Etc. To capture the effects in both the fluid and the structure, utilization of the two solvers is needed.
In this master thesis, $STAR-CCM+$ a CFD numerical solver is used together with ABAQUS a FEA numerical solver. The mechanism of deriving a solution for a typical FSI problem could be seen in figure 5.6.

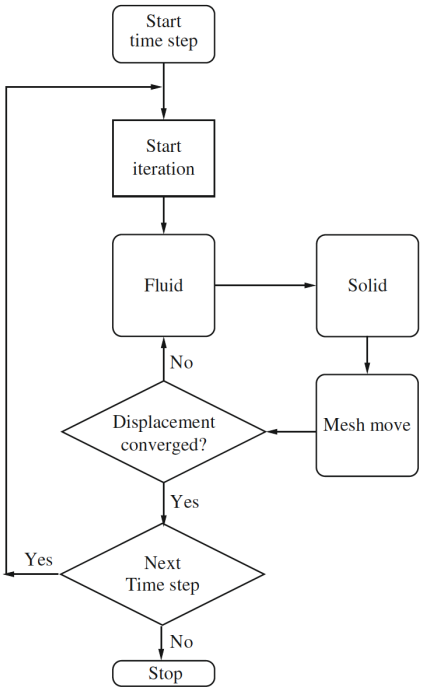

Figure 5.6: Fluid Structure Interaction coupling routine Zienkiewicz et al., 2014

The procedure of a co-simulation when searching for a converged solution contains a sequence of actions that iterates between the two models in the two software. During the co-simulation, the motion, pressure, and shear forces of the fluid flow in STAR-CCM+ will cause the solid to deform and displace in ABAQUS; as a result, the deformation is to influence the flow in turn. The described process runs during a one-time step and until a converged solution for the displacement is obtained. Then the simulation proceeds to the next time step, and the same described process will be repeated. A detailed description of the practical aspects applied in both STAR-CCM+ and ABAQUS are defined and can be found in the appendix E.1

5.3 Computational grid

Creating a mesh in the most straightforward meaning is the act of dividing a domain into small cells where the conservation laws will be applied and solved to obtain the desired results. In general, forming the mesh is the crucial step to obtain results in which its accuracy is related directly to the quality of the mesh; finer mesh yields more accurate results.

Furthermore, in this study, a detailed investigation for the mesh is performed to understand the different aspects of the models, commands, and parameters provided in the software $STARCCM+$.
The process could be divided into two main steps, a generation of the surface mesh and a generation of the volume mesh. The surface mesh is generated on the surfaces

of the studied geometry, e.g., NACRA17, which is vital for generating the volume mesh, where generating the surface mesh would ease generating the volume mesh. The volume mesh can be described as the workbench of the FVM.

5.3.1 In Cavitation Tunnel

A short description of the adopted models in the cavitation tunnel is shown in this subsection :

- Trimmed Cell mesher is to be utilized in the model, according to Siemens, 2020 this model has proven to give more accurate solutions when compared with tetrahedral mesh. Unlike the polyhedral and the tetrahedral, the trimmer mesher is no dependant on the quality of the surface mesh of the initial surface. Therefore, one can always obtain a good quality for the volume mesh.

- A Prism Layer Mesher is essential to resolve the boundary layer near the wall and improve the flow solution's accuracy. The mesh dependency study shows that having six layers for the prism layer is sufficient. It increases the density of the mesh near the wall and allows for more accurate results.

- Surface Remesher is sufficient to include as well, in order to promote the accuracy of the existing surface and optimize it for the volume mesh model.

- Including an Automatic Surface Repair enables an automatic process to resolve various problems that could appear at the re-meshed surface after the surface re-meshing is finished.

- The mesh base size is chosen to be 0.4 m and the first cell thickness near the wall is calculated and defined from the equation 5.2:

$$\mu^+ = \frac{1}{k} ln(y^+) + B \tag{5.2}$$

  where:
  - y^+=50
  - B=5
  - K=0.41
  - ν=1.2×10^{-6} m^2/s
  - u=9 m/s.

$$y^+ = y\frac{\mu_R}{\nu} \tag{5.3}$$

$$\mu_R = \frac{\mu}{u^+} \tag{5.4}$$

  From equations 5.2, 5.3, and 5.4 one can derive:

$$y = \frac{\nu}{u} y^+ (\frac{1}{k} ln(y^+) + B) \tag{5.5}$$

Hence, the first layer thickness near the wall is to be 1.5×10^{-4}m. The set-up for the resultant mesh is shown in tables **??** and 5.5.

Table 5.4: Mesh settings

Default Controls	
Meshing Method	Triangle
Base Size	0.4 m
Target Surface Size	100 %
Minimum Surface Size	60 %
Surface Curvature: Pts/circle	360
Surface Growth rate	1.2
Number of Prism Layers	6
Prism near wall thickness	1.5×10^{-4} m
Prism Layer Total Thickness	4×10^{-3} m
Maximum Core/Prism Transition Ration: Size/Thickness Ration	4
Default and surface growth rate	Both set to Slow
maximum cell size	100 %

Table 5.5: Meshers prism layer mesher settings

Prism Layer Mesher	
Gap Fill Percentage	25
Minimum Thickness Percent	1 %
Layer Reduction Percentage	0 %
Boundary March Angle	85
Concave Angle Limit	0
Convex Angle Limit	360
Near Core layer Aspect Ratio	0.5

- Adding a surface control for different parts will allow for more flexibility and control over the surface mesh. A surface control is added around the foil for further refining, added around the fluid domain to control the number of the prism layer; near wall thickness at the walls of the domain, around the extra added part on top of the tunnel to disable the prism layer since this part is not influencing the flow field, and around the part of the foil that is located inside that extra block to reduce quality of the mesh since this part is away form the flow; not effecting the flow. The setup for the surface refinements are shown in tables 5.6:

Table 5.6: Surface controls for the cavitation tunnel

Around the foil	
Target Surface Size	$4\times10^{-}3$ m
Minimum Surface Size	$5\times10^{-}4$ m
Around the domain	
Number of the prism layers	3
Prism layer near wall thickness	3×10^{-4} m
Around the added extra block	
prism layer	disabled
Around the part of the foil that is inside the extra block	
prism layer	disabled
Target Surface Size	8×10^{-3} m
Minimum Surface Size	1×10^{-4} m

- In addition, three volumetric refinements are used. The first one added around the fluid domain in order to increase the density of the mesh around this region, having a finer mesh and thus more accurate results. The second one added around the foil to capture more accurate results. The first two has a box shape, and last one has a cylindrical shape; added to the region just behind the tip of the foil to capture the vortex shedding more clearly. The setup for the volumetric refinements are shown in table 5.7 :

Table 5.7: Volumetric refinements used in the cavitation tunnel

Around the fluid domain	
Trimmer	Customize Anisotropic size
Costume size	25 % of the base size
Around the foil	
Trimmer	Customize Anisotropic size
Costume size	5 %
Behind the tip	
Trimmer	Customize Anisotropic size
Costume size	5 %

The resultant surface and volume mesh based on the previous described setup in tables 5.4, 5.5, 5.6, and 5.7 can be seen in figures 5.7a, 5.7b, 5.8a, and 5.8b where the total number of cells is $7,1 \times 10^6$ million cells.

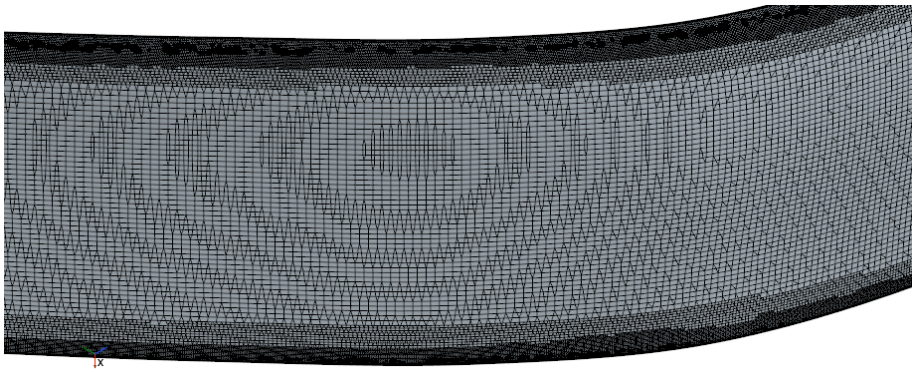

(a) Surface mesh at the pressure side of the foil near the foils knee

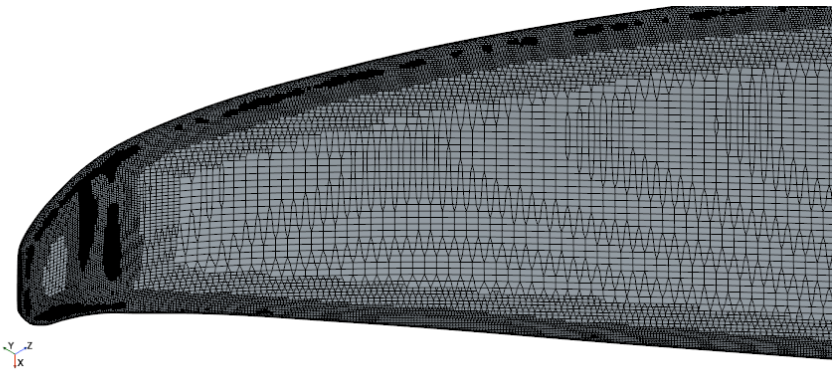

(b) Surface mesh at the pressure side of the foil near the foils tip

Figure 5.7: Resultant surface mesh of the foil on two different positions

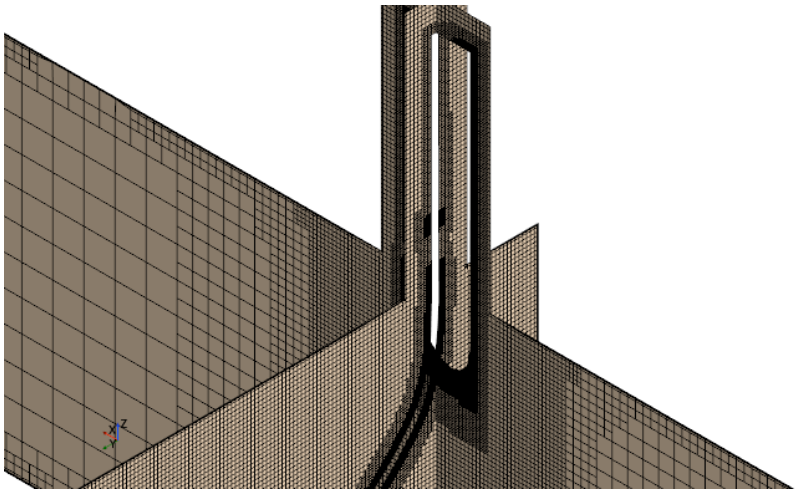

(a) The volume mesh at the upper part of the fluid domain

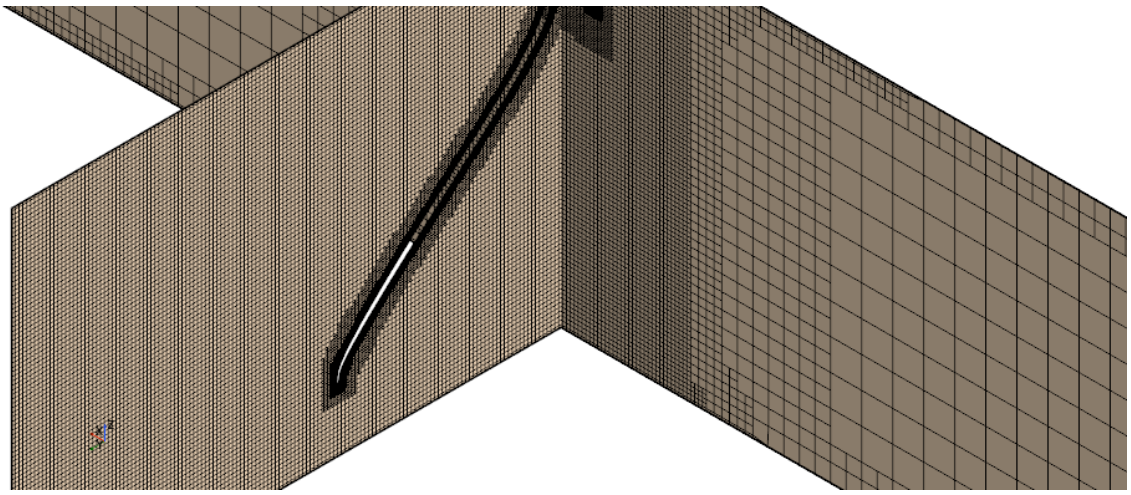

(b) The volume mesh at the lower part of the fluid domain

Figure 5.8: Resultant volume mesh of the fluid domain at the foils location

5.3.2 In the Towing Tank

The authors decide to use a similar approach when generating the mesh in the towing tank model to the cavitation tunnel model. Although, extra modifications are to be added to this model since the model utilizes a free surface model. In the table 5.8 is an indication of the utilized parameters and values when obtaining the model. Likewise, a surface control is used to refine further the surface mesh around the foil, where the setup for the parameters is shown in table 5.9.

Table 5.8: Mesh settings

Default Controls	
Meshing Method	Triangle
Base Size	0.4 m
Target Surface Size	100 %
Minimum Surface Size	60 %
Surface Curvature: Pts/circle	360
Surface Growth rate	1.2
Number of Prism Layers	6
Prism near wall thickness	1.5×10^{-4} m
Prism Layer Total Thickness	4×10^{-4} m
Maximum Core/Prism Transition Ration: Size/Thickness Ration	4
Default and surface Growth rate	Both set to Slow
maximum cell size	100 %

Table 5.9: Surface control around the foil

Surface control around the foil values	
Target Surface Size	4×10^{-3} m
Minimum Surface Size	5×10^{-4} m

Volumetric refinements are also added. A box-shaped refinement around the foil and the flow region to have finer mesh around these volumes, thus capturing more accurate results; a cylindrical shape refinement just behind the tip of the foil at the flow direction to have finer mesh and thus be able to capture for the vortex shedding. Moreover, three extra volumetric refinements are added to the model and generate the free surface region. The setup for the volumetric refinements are shown in tables 5.10, and 5.11:

Table 5.10: Free-surface volumetric refinement thick, thin, and very thin

	Thick	**Thin**	**Very Thin**
Trimmer	Anisotropic size	Anisotropic	Anisotropic size
Relative X and Y size	50 %	50 %	50 %
Relative Z size	25 %	10 %	1 %

Table 5.11: Volumetric refinement around the fluid domain, the foil, and behind the tip at the tip vortex region

	Domain	**Foil and Vortex region**
Trimmer	Isotropic size	Isotropic
size	30 %	5 %

The obtained mesh based on the previous described setup in tables 5.9, 5.10, and 5.11 has 11.9 million cells. The resulting mesh can be seen in figure 5.9.

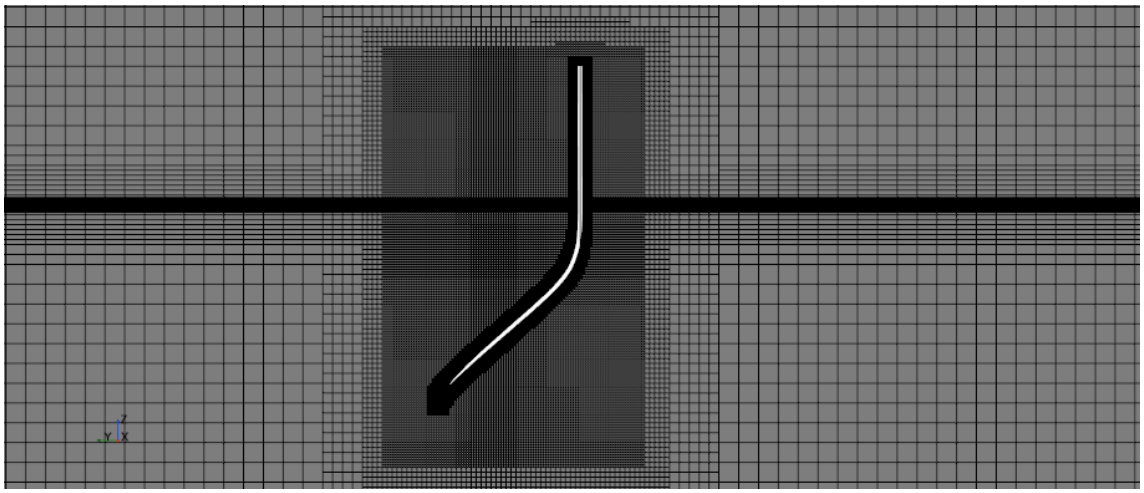

Figure 5.9: Front view of the mesh

5.4 Physical models

To capture good results that reflect reality with minimum uncertainties, One needs to utilize and pick the best suitable models for the studied case. Luckily STAR-CCM+ provides significant variations of different models.

5.4.1 Cavitation tunnel

A description of the models used in the cavitation tunnel model according to Siemens, 2020:

- **Space and Time:** Having a three-dimensional mesh and a co-simulation between STAR-CCM+ and ABAQUS needs a three-dimensional model. The implicit unsteady model is available only when using segregated flow and Segregated Fluid Energy models. The approach utilizes an implicit unsteady solver. It gives a choice to update every time-step in the objects that offer a trigger .i.e monitors, scenes, between iterations time-steps, and allow having a multi-phase flow used in the towing tank model. Wall Distance model is added to account for near-wall effects, which describes the distance from a cell centroid to the nearest wall face considering no-slip boundary conditions.

- **Flow and motion**: The Segregated Flow model is to be used to solve the mass and conservation equations in a sequent mode. This model utilizes a pressure-velocity algorithm, where a pressure-correction equation is to be solved; hence, the relation between the mas conservation and the velocity field is satisfied. Solving all different scales of turbulence in a flow by the NS is possible only if a high-quality mesh is achieved; if such high quality is achieved, high computing power would be needed. Moreover, the computers available today can only solve for low Reynolds numbers. Alternatively, it is essential to employ Reynolds decomposition with turbulence models according to Zienkiewicz et al., 2014 and obtain an approximated solution. Therefore, the Reynolds Averaged Naiver-Stokes equations (RANS) model is used together with the K-Omega turbulence model, where the later model is a two equations model which solves the transport equations for the kinetic energy k and the specific dissipation rate ω. A shear stress transport model $SSTK-\omega$ is used as well. The density is constant, and the fluid is liquid (water).

5.4.2 Towing Tank

The physical models are selected in the Towing tank model to be as similar as possible as in the Cavitation tunnel model. Although, extra adjustments were needed to be applied i.e., to account for the free surface:

- **Multi-phase flow:** The term Multi-phase flow can be explained as the flow and the interaction of several phases in the same system. Utilizing this model is necessary to use multi immiscible fluid phases (e.g., water, air) hence obtaining the free surface in the numerical model.
- **Volume Of Fluid (VOF) Waves:** Having the multi-phase model included would resultant gravity waves at the interface of the light fluid-heavy. Including the VOF waves model will allow taking the surface gravity waves into account during the simulation

5.4.3 Co-simulation

In a stand-alone simulation, the aforementioned models would be sufficient. However, running a co-simulation between STAR-CCM+ and ABAQUS is different and requires several additional models. The extra models added in both numerical models, .e.g Cavitation Tunnel and Towing Tank, are described shortly:

- **Co-simulation:** The model allows for coupling between two simulations, .i.e, Simulations in STAR-CCM+ and ABAQUS, in a co-simulation analysis.
- **ABAQUS implicit coupling:** In general, in the strongly coupled systems, implicit coupling schemes are implemented. These schemes give the chance to exchange data between the coupled software more than once per time-step, which allows for larger time-steps than the explicit coupling scheme.

5.5 Mesh convergence and discretization error

5.5.1 Cavitation tunnel

Good results should be defended and quantified; therefore, a detailed study for the grid refinement was performed for the initial obtained model to define an adequate cell size together with the discretization uncertainty. This grid study included seven grids, where its parameters (the number of layers in the prism layer and the base cell size) vary methodically from one to another. The initial obtained grid size has a total number of 20.8×10^6 million cells, the size of the coarsest grid obtained was 7.1×10^6 million cells, and the finest obtained grid size 49.4 million cells. The lift, drag, and side forces were exported from STARCCM+ for each case after reaching convergence in a stand-alone simulation, a converged solution of the forces coefficients calculated from equation 5.6

$$F_x = \frac{1}{2} C_x \rho V^2 A \tag{5.6}$$

Where:

- F_x is the force .e.g lift, drag, side
- C_x is the force coefficient for lift, drag, and side forces.
- ρ density 1000 $^{kg}/_{m^3}$
- A is the foil area inside the fluid domain.

To define the time-steps for each model (grid case), one needs to consider the Courant-Friedrichs-Lewyor condition/number (CFL). According to Laney, 1998, "*The full numerical domain of dependence must contain the physical domain of dependence.*" Hence, the traveled space on the mesh of any data during the time-step must be lower than the space between the mesh elements Caminha, G., 2019. Since an implicit time-stepping solver is used in the numerical models, a (CFL) number larger than one is allowed. The time-steps is calculated from equation 5.7 for a fixed CFl=10, for the cell size of the cells located just outside the prism layer, and for a 9m/s velocity.

$$\Delta t = C \frac{\Delta x}{u} \tag{5.7}$$

The resultant mesh convergence for Lift-force, drag-force, and side-force coefficients can be seen in the figures 5.10b 5.10a, and 5.10c. The horizontal axis is the number of grid cells obtained from the finest grid to the coarsest one for each case. Moreover, the Least Squares Root method based on Eça and Hoekstra, 2014 is used to perform a systematic verification for the obtained grid and thus derive the numerical uncertainty for the grid see figures 5.11. The method sets values between 1 and 2 for each grid case. The range indicated how fine is the grid and is called the refinement ratioplotting the refinement ratio against the coefficients of the force. The mesh dependency and uncertainty results showed that the 7,1 $\times10^6$ grid has the numerical uncertainties in the drag U_d=9.3, in the lift U_l= 6.2, and the side force U_l= 4.6, is sufficient to carry out the desired simulations.

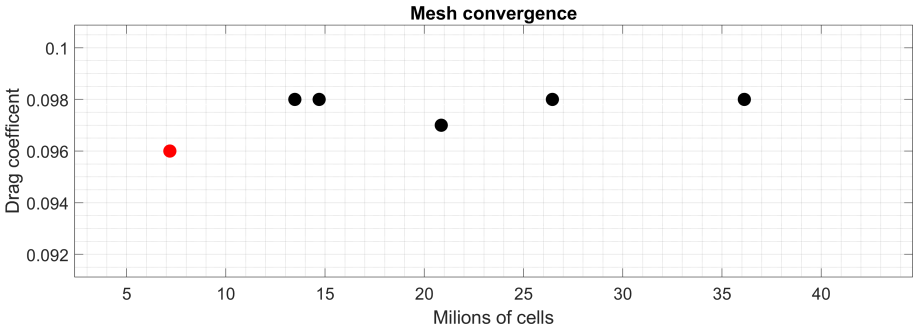

(a) The obtained uncertainty of the grid for the drag force

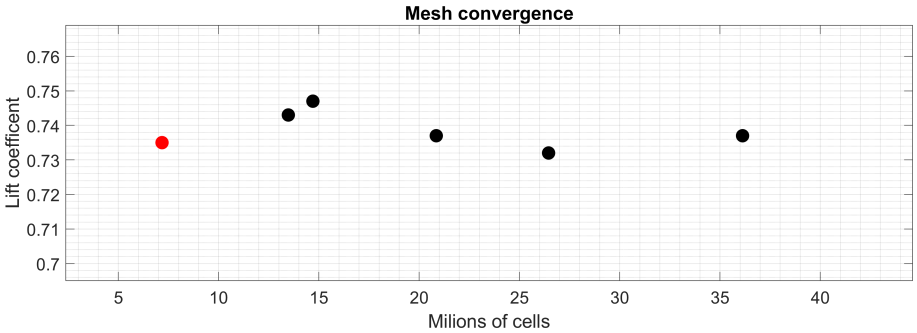

(b) Mesh convergence for the lift-force coefficient

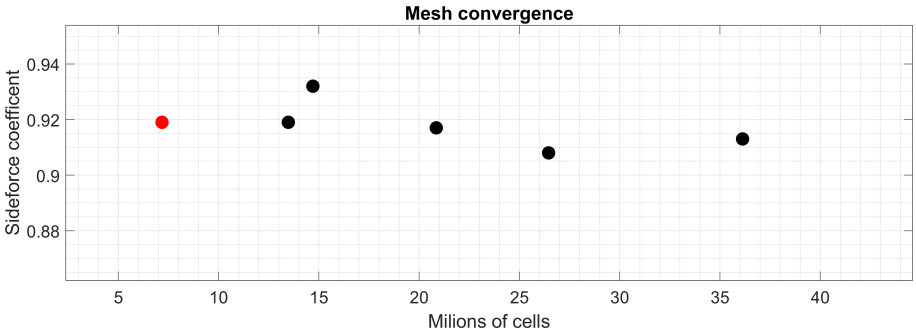

(c) Mesh convergence for the drag-force coefficients

Figure 5.10: Mesh convergence for the side-force coefficients

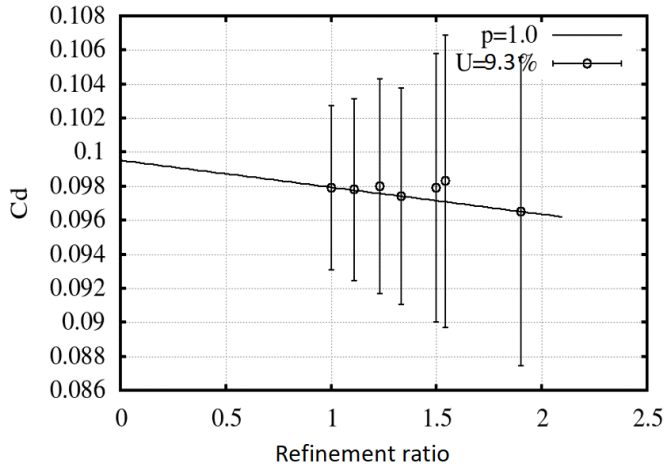

(a) The obtained uncertainty of the grid for the drag force

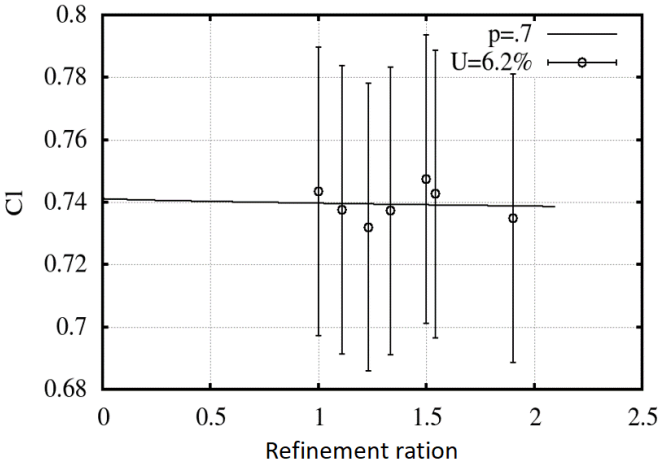

(b) The obtained uncertainty of the grid for the lift force

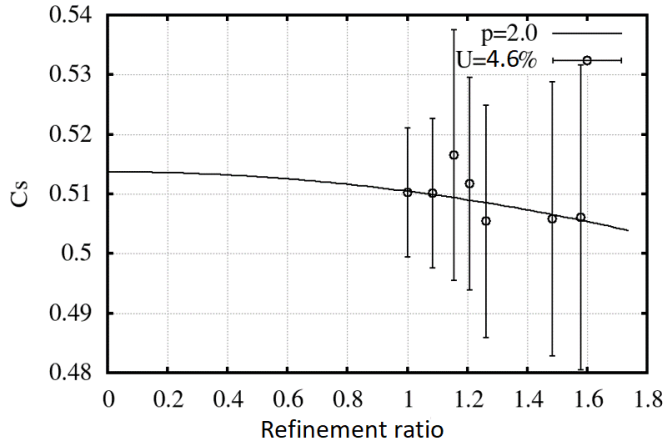

(c) The obtained uncertainty of the grid for the side force

Figure 5.11: Uncertainty plots for the forces in the cavitaion tunnel

5.5.2 Towing Tank

The grid dependence study is carried out Similarly as in section 5.5, where It was performed for seven cases (for different grids), and the initial total number of cells of the numerical model was 46.6 $\times 10^6$ which was the finest mesh obtained, and a total number of 11.8 $\times 10^6$ million cells for the coarsest.

The results of the mesh dependency and uncertainty can be seen in figures 5.12 and in 5.13. Based on the obtained results, it was decided by the authors to utilize the 11.8 $\times 10^6$ grid to carry out the simulations needed in the towing tank model.

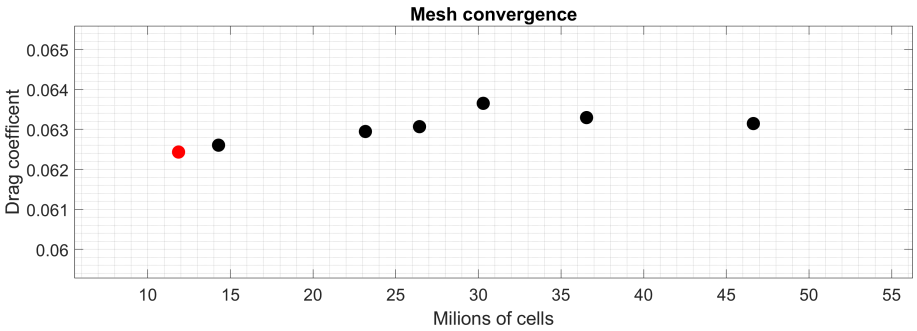

(a) Mesh convergence for the drag-force coefficients

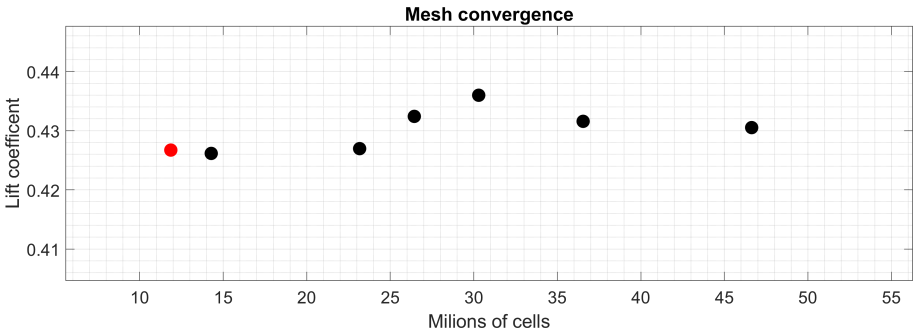

(b) Mesh convergence for the lift-force coefficient

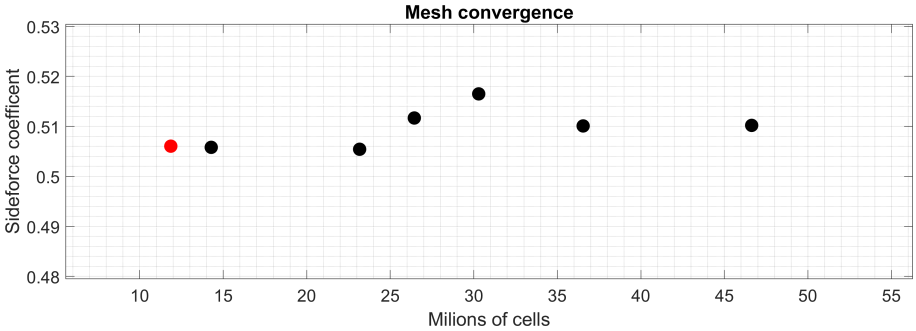

(c) Mesh convergence for the side-force coefficients

Figure 5.12: Mesh convergence for the side-force coefficients

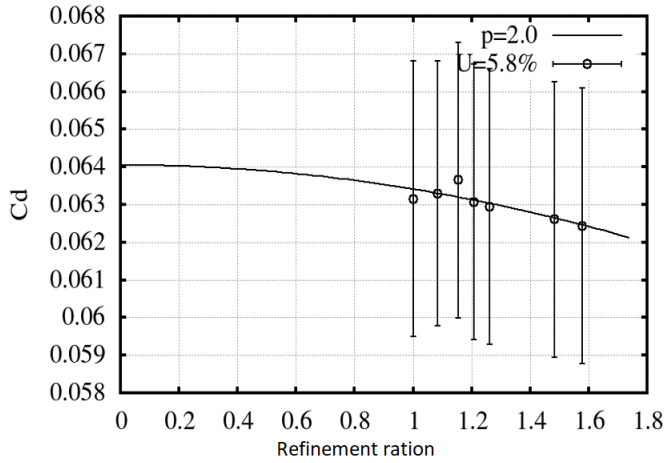

(a) The obtained uncertainty of the grid for the drag force

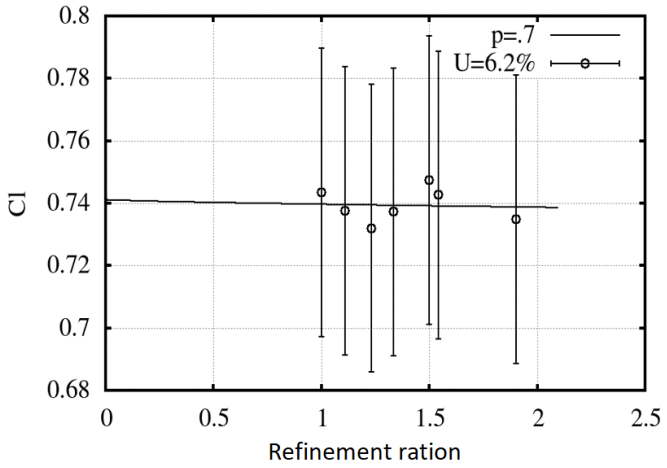

(b) The obtained uncertainty of the grid for the lift force

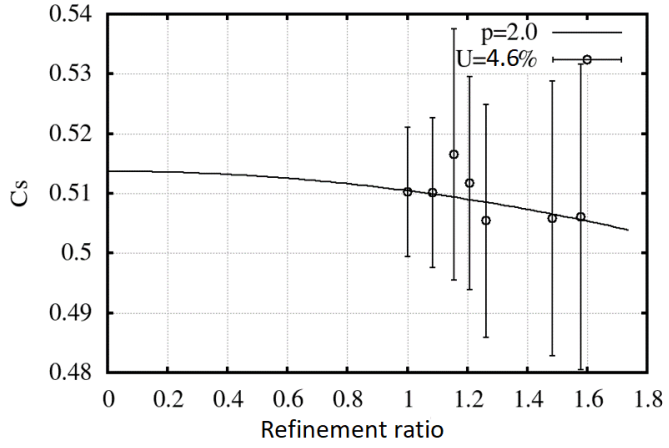

(c) The obtained uncertainty of the grid for the side force

Figure 5.13: Uncertainty plots for the forces in the Towing Tank

5.6 Convergence

In CFD, an iterative procedure will define the solution for the discretized equations; therefore, a solution will be obtained after reaching convergence, monitoring the residual will determine when reaching a converged solution. Residuals can be described as the difference between the external and internal forces. In general, an accurate solution would have zero residuals, Although this is almost unachievable in most cases.

The iterative solution for the non-linear differential equations includes two iterative steps: one solution for every separate equation and another for all equations. A simple description of the process based on Wendt, 2008 can be shown as :

- solving and obtaining a solution for the energy and the momentum equations until reaching convergence.
- Obtaining a solution for the continuity equation.
- Computation of the density
- Since the procedure is to be iterative. The previous steps are to be repeated until reaching a converged solution.
- The solution is to be started at the next downstream position.

6
Structural model

To simulate the structural response of the hydrofoil, a sound structural model must be established. As touched upon in chapter 4, the designers of the *NACRA 17* hydrofoil were not willing to share the design for the hydrofoil. Therefore a significant effort is needed to reverse-engineer the hydrofoil and obtain a structural response deemed to resemble the real hydrofoil with sufficient accuracy. Nevertheless, the material properties and wall thickness in the numerical model will deviate from the actual hydrofoil.

6.1 Composite mechanics

A composite is a material that is made of two or more constituent parts, each with their own set of material properties. This is done to achieve a new set of more desired material properties, more suited for the intended application. Composites also offer a high stiffness and yield strength compared to there weight, as can be seen in figure 6.1. However, the layup of the composite has to be engineered to achieve the desired properties.

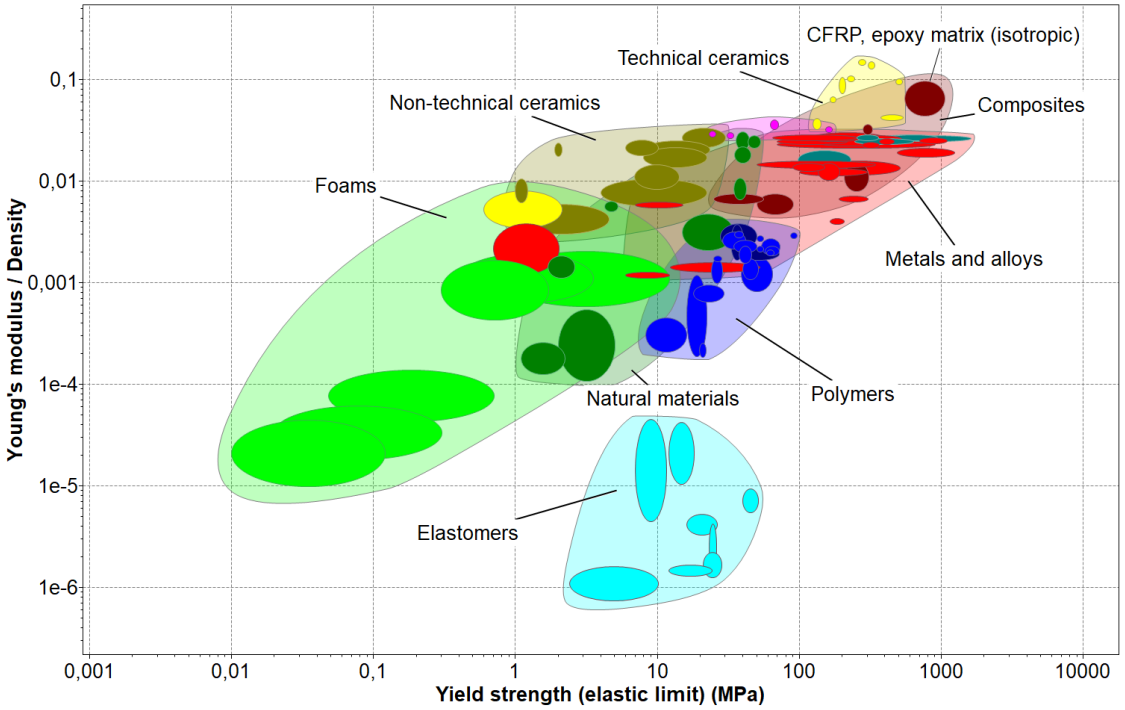

Figure 6.1: Stiffness per unit of weight compared to yield strength for many material families. Figure generated in Granta EduPack 2021 (ANSYS, 2021)

6.1.1 Micromechanics of unidirectional composites

To analyze and engineer the desired material properties, the properties of the isotropic matrix and the anisotropic properties of the fibers need to be combined. The first material property to be determined is the longitudinal stiffness. This is done thru the rules of mixtures according to equation 6.1, E_i and is the Young's modulus for the fibers and the matrix. V_i is the fraction the respective part make up of the composite. The denotation f and M represents the Fibers and the Matrix. This gives a linear relationship between the longitudinal stiffness based on the volume fraction of fibers in the composite (Bhaqwan et al., 2018). The denotation L and T used for the equations represents the Longitudinal and Transverse direction with respect to the fibers, as can be seen in figure 6.3.

$$E_L = E_f V_F + E_M V_M \tag{6.1}$$

For the transverse stiffness, Halpin Tsai (Bhaqwan et al., 2018) used curve fitting methods to establish an easy-to-use formulation for design calculations, presented in equation 6.2 and 6.3. ξ is a measurement of the amount of reinforcements in the composite, how densely they are packed, and the load case. Halpin Tsai suggests that 2 is a good base value for circular fibers and commonly used manufacturing techniques (Bhaqwan et al., 2018). The value of ξ is affected by the fibers used, the manufacturing technique and the tolerances during the manufacturing process.

$$E_T = \left(\frac{1 + \xi \eta V_F}{1 - \eta V_F} \right) E_M \tag{6.2}$$

$$\eta = \frac{(E_F/E_M) - 1}{E_F/E_M) + \xi} \tag{6.3}$$

For a unidirectional composite, Poisson's ratio is defined as in equation 6.4.

$$\nu_{LT} = \nu_F V_F + \nu_M V_M \quad \& \quad \nu_{TL} = \frac{\nu_{LT} E_T}{E_L} \tag{6.4}$$

Halpin Tsai also suggests an empirical model to obtain an estimation of the shear modulus G_{LT}, of a unidirectional composite, shown in equation 6.5, Halpin Tsai suggests that ξ=1.

$$G_{LT} = \left(\frac{1 + \xi\eta V_F}{1 - \eta V_F}\right) G_M \tag{6.5}$$

$$\eta = \frac{(G_F/G_M) - 1}{G_F/G_M) + \xi} \tag{6.6}$$

In the most general case, the stress-strain relationship for a anisotropic material can be described with hooks generalized law, as in equation 6.7 where σ the nine stress components, E is 81 elastic constants and ε is the nine component strain tensor.

$$\sigma_{ij} = E_{ijkl}\varepsilon_{kl} \tag{6.7}$$

6.1.2 Macro mechanics

In (Bhaqwan et al., 2018), it is show that for a orthotropic materials, the stress-strain relationship is simplified to only include nine independent elastic constants, as in equation 6.8.

$$\sigma_i = C_{ij}\varepsilon_j \tag{6.8}$$

Considering a schematic cross-section with the fibers perpendicular to the cross-section, as shown in figure 6.2, it is clear that the material properties in the plane of the cross-section are not orientation dependent. In most structural applications, the laminate is loaded in plane that produces a plane stress condition. With these assumptions the stress-strain relation can be further simplified as shown in equation 6.9

$$\begin{Bmatrix} \sigma_L \\ \sigma_T \\ \tau_{LT} \end{Bmatrix} = \begin{bmatrix} Q_{11} & Q_{12} & 0 \\ Q_{12} & Q_{22} & 0 \\ 0 & 0 & Q_{66} \end{bmatrix} \begin{Bmatrix} \epsilon_L \\ \epsilon_T \\ \gamma_{LT} \end{Bmatrix} \tag{6.9}$$

where Q_{ij} is the stiffness matrix, being defined by the Young's modulus, shear modules and the Poisson's ratio as in equation 6.10 (Bhaqwan et al., 2018).

$$\begin{aligned} Q_{11} &= \frac{E_L}{1 - \nu_{LT}\nu_{TL}} \\ Q_{22} &= \frac{E_T}{1 - \nu_{LT}\nu_{TL}} \\ Q_{12} &= \frac{\nu_{LT} E_T}{1 - \nu_{LT}\nu_{TL}} \\ Q_{66} &= G_{LT} \end{aligned} \tag{6.10}$$

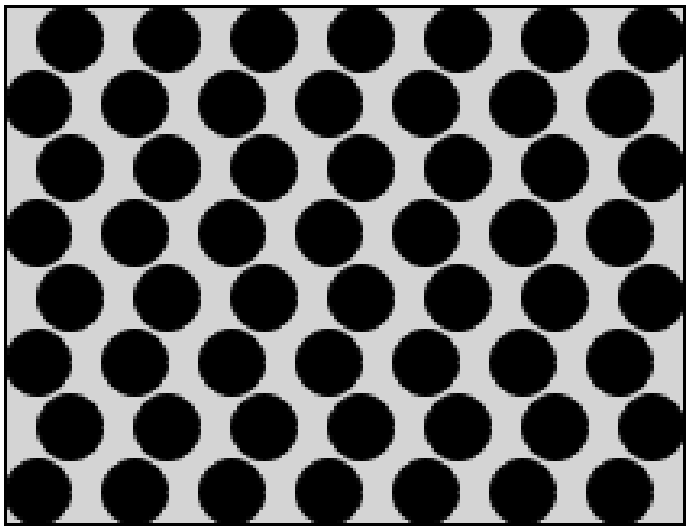

Figure 6.2: Schematic cross section of unidirectional fibers. Black representing the fibers and gray the matrix

However, this stiffness matrix is only applicable in the local coordinate system, with the main principle axis longitudinal to the fibers and the second axis transversely to the fibers, as shown in figure 6.3.

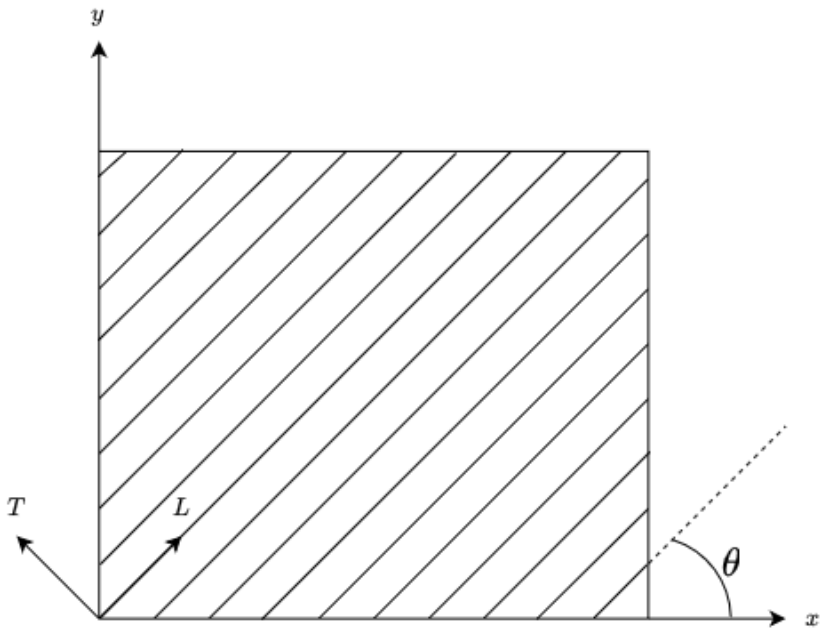

Figure 6.3: Global coordinate system xy and local coordinate system LT

In reality, the fibers will have more than one orientation. Thus a transformation matrix is needed to obtain the material properties in the $x - y$ coordinate system.

The stress transformation can be written as equation 6.11, with T_1 defined as equation 6.12 and the angle ϑ being the positive angle between the x axis and the fibers, as show in figure 6.3.

$$\begin{Bmatrix} \sigma_L \\ \sigma_T \\ \tau_{LT} \end{Bmatrix} = \Big[T_1\Big] \begin{Bmatrix} \sigma_x \\ \sigma_y \\ \tau_{xy} \end{Bmatrix} \tag{6.11}$$

$$[T_1] = \begin{bmatrix} cos^2\vartheta & sin^2\vartheta\vartheta & 2sin\vartheta cos\vartheta \\ sin^2\vartheta & cos^2\vartheta & -2sin\vartheta cos\vartheta \\ -sin\vartheta cos\vartheta & sin\vartheta cos\vartheta & cos^2\vartheta - sin^2\vartheta \end{bmatrix} \tag{6.12}$$

The strain transformation is calculated in a similar manor, according to equation 6.11

$$\begin{Bmatrix} \varepsilon_L \\ \varepsilon_T \\ \gamma_{LT} \end{Bmatrix} = \Big[T_2\Big] \begin{Bmatrix} \varepsilon_x \\ \varepsilon_y \\ \gamma_{xy} \end{Bmatrix} \tag{6.13}$$

$$[T_2] = \begin{bmatrix} cos^2\vartheta & sin^2\vartheta & sin\vartheta cos\vartheta \\ sin^2\vartheta & cos^2\vartheta & -sin\vartheta cos\vartheta \\ -2sin\vartheta cos\vartheta & 2sin\vartheta cos\vartheta & cos^2\vartheta - sin^2\vartheta \end{bmatrix} \tag{6.14}$$

Combining equation 6.9 with 6.11 and 6.13, equation 6.15 is obtained, enabling the calculations of the stress-strain relationship based on the fiber orientation of a single lamina.

$$\begin{Bmatrix} \sigma_x \\ \sigma_y \\ \tau_{xy} \end{Bmatrix} = \Big[T_1\Big]^{-1} \begin{bmatrix} Q_{11} & Q_{12} & 0 \\ Q_{12} & Q_{22} & 0 \\ 0 & 0 & Q_{66} \end{bmatrix} \Big[T_2\Big] \begin{Bmatrix} \varepsilon_x \\ \varepsilon_y \\ \gamma_{xy} \end{Bmatrix} \tag{6.15}$$

To conform to convention, typically $[Q]$ is replace with $\Big[\overline{Q}\Big]$, defined as equation 6.16.

$$\overline{Q}_{ij} = [T_1^{-1}]Q_{ij}[T_2] \tag{6.16}$$

6.1.3 Laminated composites

A single layer fibers in a matrix is refereed to as a lamina, but most composite structures consist of more than one lamina that have been bounded to form a laminate. The laminate has multiple lamina's, all in different orientations to obtain the desired material properties with respect to stiffness and strength. In classical laminate theory, it is assumed that the bond between the lamina's is perfect and that the lamina's are very thin. This allows for the assumption that the displacement can be linked to the midplane at any given point of the laminate.

Since the strain and displacement are linked to the stress in the laminate, a constitutive relations must be calculated across the thickness of the laminate. This is done with the **ABBD** matrix with the respective parts in equation 6.17 to 6.18. In

Layman's terms, the **ABBD** matrix links the individual lamina's together into the laminate.

$$A = \sum_{k}^{n} \left(\overline{Q}_{ij}\right)_k (h_k - h_{k-1}) \tag{6.17}$$

$$B = \frac{1}{2} \sum_{k}^{n} \left(\overline{Q}_{ij}\right)_k (h_k^2 - h_{k-1}^2) \tag{6.18}$$

$$D = \frac{1}{3} \sum_{k}^{n} \left(\overline{Q}_{ij}\right)_k (h_k^3 - h_{k-1}^3) \tag{6.19}$$

The **A** matrix is the extensional stiffness matrix that relates forces to the mid-plane strains, **D** relates the moments to the curvature of the mid-plane, and **B** is the coupling matrix. If a laminate is symmetric around the mid-plane, the **B** matrix will always be zero, and the laminate is considered uncoupled. For an unsymmetrical laminate, any in-plane normal or shear force will cause an in-plane deformation. There is also a link between twists and bending caused by the unsymmetrical laminate (Bhaqwan et al., 2018). This property can be utilized to design structures that change shape when submitted to a predicted load, for example, to increase the performance.

Once the lamina's are linked together with the **ABBD** matrix, the strain and curvature can be linked with to the normal forces and moments, as shown in equation 6.20. The stress can then be calculated from the strain as shown in equation 6.15, and transformed into the local coordinate system with the help of the transformation matrix T_2.

$$\begin{Bmatrix} N \\ ... \\ M \end{Bmatrix} = \begin{bmatrix} A & B \\ B & D \end{bmatrix} \begin{Bmatrix} \epsilon \\ ... \\ k \end{Bmatrix} \tag{6.20}$$

6.2 FEA model

Due to the complex geometry of the hydrofoil, a Finite element analysis (FEA) model is created using ABAQUS, an FEA solver and CAD software. ABAQUS is used due to the possibility to couple it with STARCCM+.

6.2.1 Element types

ABAQUS offers the user a vast selection of elements to use in the FEA model, ranging from simple shell triangles to more complex solid elements. However, it is concluded that using solid elements is not suitable because of the unknown composite design used for the hydrofoil. If solid elements are used, the total thickness of the composite is tied to the thickness of the elements, and the design of the laminate can only be specified as a ratio of the total thickness, limiting the possibility to simulate different laminate thicknesses to the number of solid models generated. This is however also an advantage. Since in some regions, for example, the trailing edge, the thickness of the laminate will most certainly not be as thick as a point

picked in the mid chord length of the hydrofoil due to geometric restrictions. The solid elements can adjust the thickness of the laminate in that region, as shown in figure 6.4a. However, comparing this with a conventional shell model that uses the shell element as either the top, bottom, or midplane of the laminate brings some other problems, especially in the area where two shells merge into a sharp corner. In figure 6.4b the shell element is represented with a solid line, and the dashed line presents the theoretical laminate thickness. As shown in the figure, there is an overlap between the blue and the red laminate, causing the numerical model to contain twice the amount of material in the overlap than would be physically possible, subsequently causing the area to be stiffer and more robust than the real corner.

Nevertheless, according to (ABAQUS documentation, 2021), using a solid element does typically not offer any extra accuracy for modeling composites but is instead an option included for the convenience of the user.

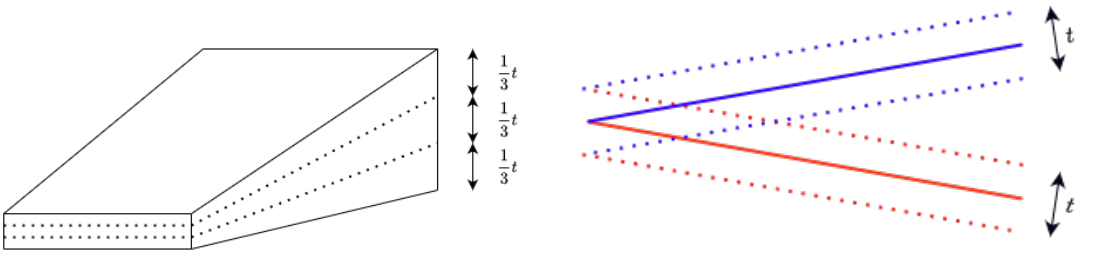

(a) Thickness distribution of a solid element

(b) Thickness distribution around a sharp corner with shell elements

Figure 6.4: Main difference between shell and solid elements

In ABAQUS, two different types of shell elements can be used, either two-dimensional conventional shell elements or continuum shell elements. The continuum offers the advantage that they also define the thickness of the laminate when modeling a composite. The implications are that the bottom and top of the continuum shell element refer to the laminate's bottom and top surface. The drawback of using continuum shell elements is that a new model needs to be generated for each laminate thickness that is to be simulated. For the same reasons mentioned previously when comparing shell and solid elements, it is desired to use conventional shell elements since they offer a higher degree of flexibility when modeling different laminate thicknesses.

6.2.2 FEA mesh generation

To generate the mesh, the surface of the hydrofoil is divided into several different parts. This is to obtain a reasonable level of control when seeding the part and because ABAUQS meshing algorithm fails to generate a mesh for a complex shape.

First, the hydrofoil is divided into the top and bottom surface, commonly reefed to the pressure and suction side on a foil geometry. It is also split into the main

segments, the daggerboard, knee, wing, and tip. See figure 6.5.

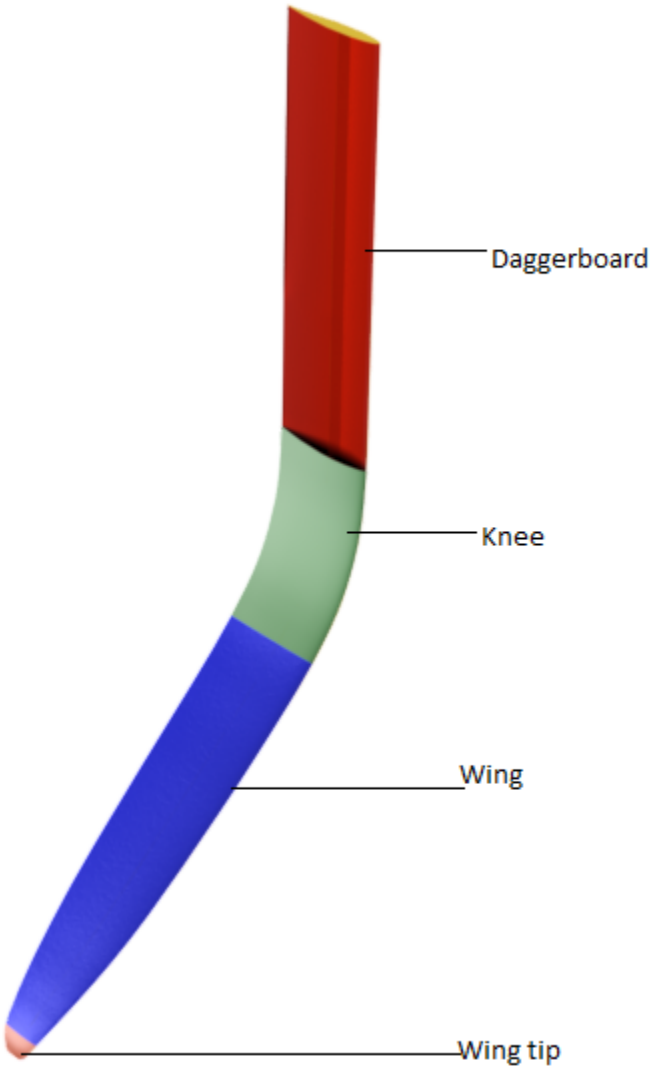

Figure 6.5: Division of sectios for seeding in ABAQUS

The parts are then imported into ABAQUS and seeded for the mesh generation, ensuring that the seeds and nodes at the edge of a part line up with the respective area in the adjacent part to ensure a good mesh once the parts are assembled. The seeds are also given a 50% weight towards the leading edge from the middle to capture the curvature better. The weighed mesh changes the spacing of the seeds so that

the distance between the last and second last seed is half of the distance between the first and the second seed, as shown in the schematic figure 6.6. The blue dots represent the seeds and subsequently element nodes, the thin black lines is the mesh generated between the seeds. The red dots represents the resulting element nodes.

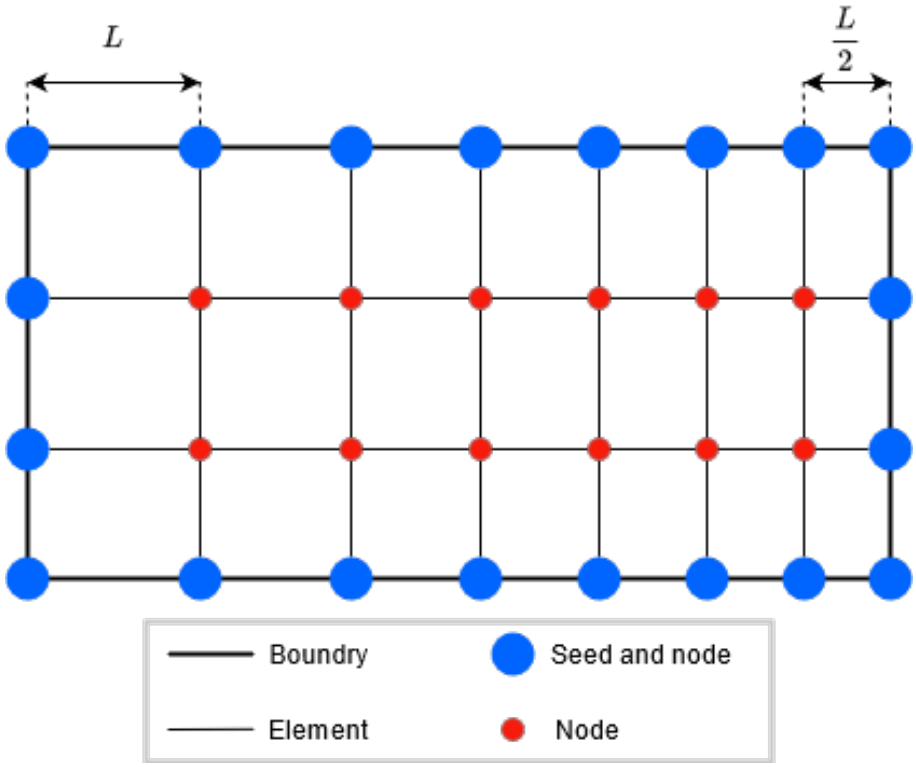

Figure 6.6: Principal of seeds for meshing

For all the parts, a structured quad-dominated structured mesh algorithm is used. The quad-dominated meshing algorithm results in a mix of square and triangle elements but only uses triangles when the number of seeds changes. The reduction or increase in the number of seeds is used to maintain ruffly the same element size when the cord length changes, as can be seen in figure 6.7b.

The described method for generating a mesh is used to generate multiple models with a varying mesh density. The models are then used to carry out a mesh dependency study.

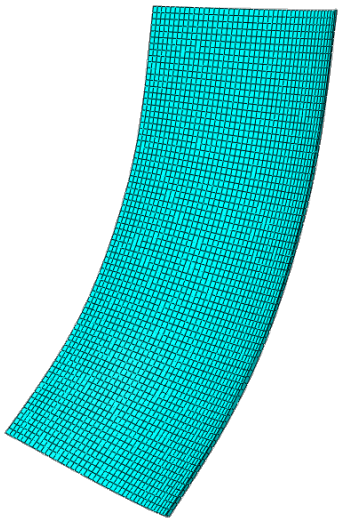

(a) Mesh for the pressure side at the knee

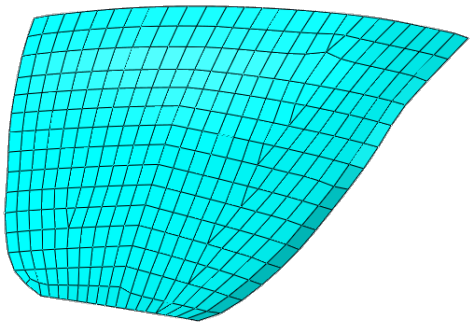

(b) Mesh at the suction side at the tip

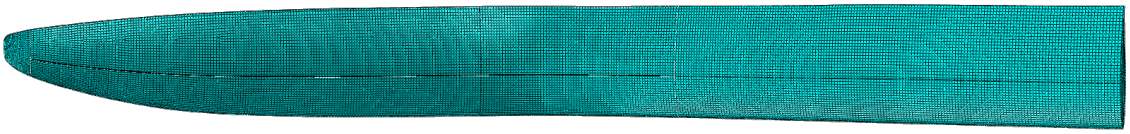

(c) Overview of the mesh at the suction side

Figure 6.7: Mesh generated in ABAQUS

6.2.3 Mesh dependency

In order to obtain accurate and reliable results, the results have to be independent of the mesh used in the FEA model. In theory, the best approach to do this would be to run the co-simulation with varying mesh sizes, element types, and even local mesh refinement. This approach is however not practically feasible due to the long computation time in the co-simulation and the work involved in setting up multiple models with non-2D elements for the reasons stated in section 6.2.1.

The approach chosen to avoid this problem is to set up multiple models with a varying mesh size and compare them with the same boundary conditions and load. Two loads are place close to the tip of the foil, one vertical and one horizontal. Three boundary conditions are placed on the hydrofoil, two sets on the dagger board that mimic the clamps found in the NACRA 17 hull that prevents out of plane movement, spaced 490 mm and with a width of 20 mm for the top and 10 mm for the lower. The vertical movement is prevented by a constraint placed at the top of the hydrofoil, see figure 6.8. The forces and boundary conditions used are presented in table 6.1 It is then assumed that when the results converge, the results are independent on the mesh and that the independence will carry over to the co-simulation.

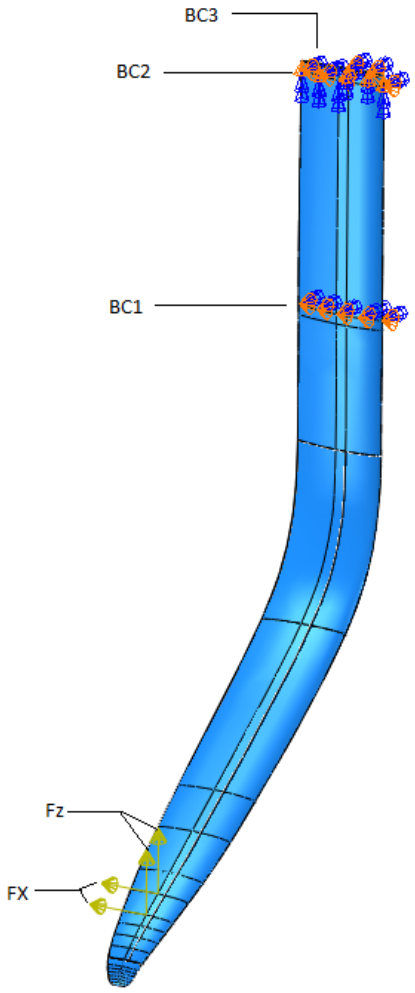

Figure 6.8: Load and boundary conditions for mesh convergence

F_x	700N
F_z	700N
BC 1	U1=0, U2=0, UR1=0, UR3=0
BC 2	U1=0, U2=0, UR1=0, UR3=0
BC 3	U3=0

Table 6.1: Forces and boundary conditions used for the mesh convergence

The mesh sizes used in the study varied from 14mm down to 1mm in average size, in steps of 2mm, except for the finest mesh. The number of elements increased rapidly as the mesh size got smaller resulting in increased computational cost. (see figure 6.9.)

To compare the results from each model, data is extracted along a path on the pressure side of the hydrofoil, see figure 6.10. The variables that are extracted are presented in table 6.2. The data is then exported from ABAQUS using a pre-recorded macro and imported to Python for post-processing.

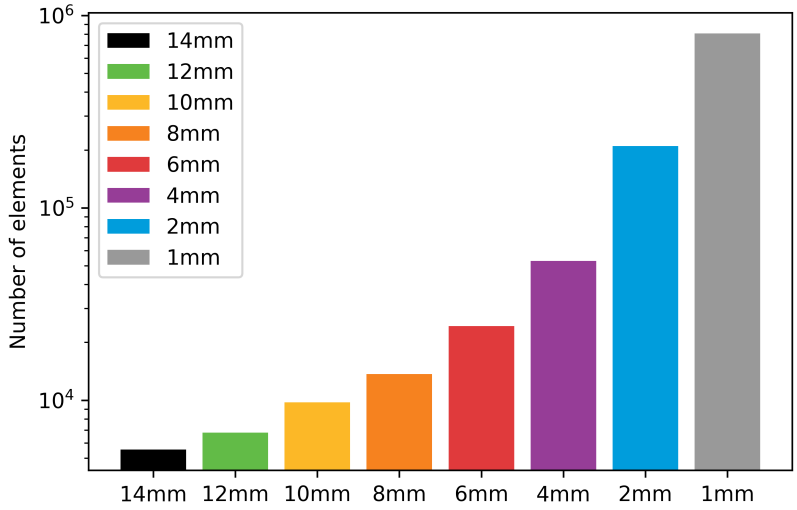

Figure 6.9: Number of elements in the models used in the study

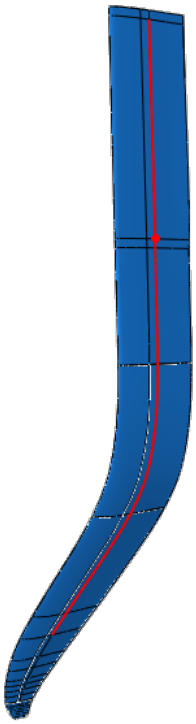

Figure 6.10: Path from where data is extracted

Since the deformation of the foil is a crucial aspect for the co-simulation, conver-

Variable	Ply number
σ_{11}	P1,P2,P3,P4,P5,P6
σ_{12}	P1,P2,P3,P4,P5,P6
σ_{22}	P1,P2,P3,P4,P5,P6
U_{mag}	All
U_1	All
U_2	All
U_3	All
UR_{mag}	All
UR_1	All
UR_2	All
UR_3	All

Table 6.2: Extracted variables along the probed line

gence for the deflection is considered the most crucial parameter. In figure 6.11 the deflection along the probed line is presented for all simulated mesh densities. The extracted data is then plotted for each variable and mesh size to establish where the mesh size converges. All the plots can are included in appendix B.

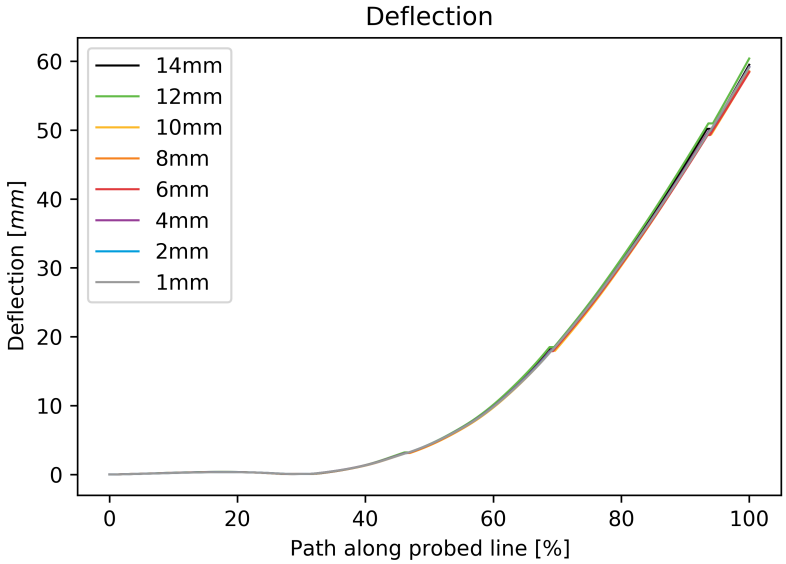

Figure 6.11: Deflection along the probed line

As can be seen in figure 6.11, there is almost no difference in deflection along the probed line for the different mesh sizes. Looking closer at the end of the data set, a very small difference can be spotted between the coarse mesh and the fine mesh, almost after 8 mm mesh size, the computed deflection converges. See figure 6.12.

The principal stress in each ply for a composite model is also investigated. Only the results that have a relatively large difference between the coarse and fine mesh are presented here. All the plots can be found in appendix B. The resulting plots in

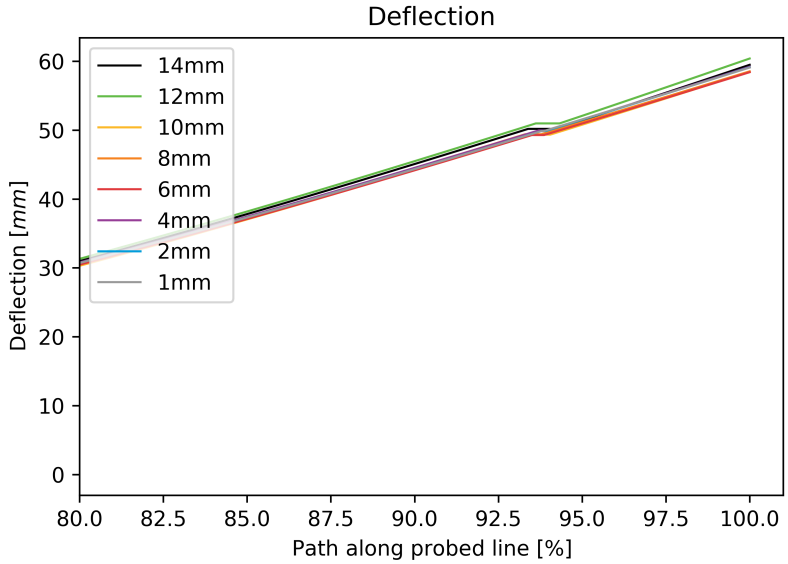

Figure 6.12: Deflection close to the tip

figure 6.13 to 6.16 shows that there is a point of diminishing return for using a finer mesh size, especially when considering computing time. This aspect is even more critical in this case when the FEA model will be used in a co-simulation, and the simulation needs to be carried out several times to complete a single time step.

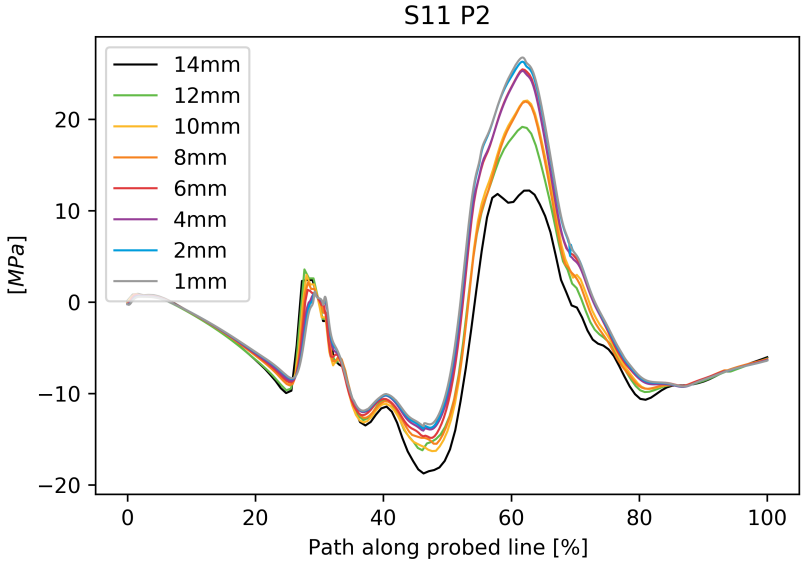

Figure 6.13: First principal stress in the second ply

Based on the mesh convergence investigation, a mesh size of 5 mm is considered suitable for the simulations. Since it yields accurate results for the displacement and the stress in the material is captured reasonably accurately while still keeping the number of elements at a low number compared with the most refined mesh.

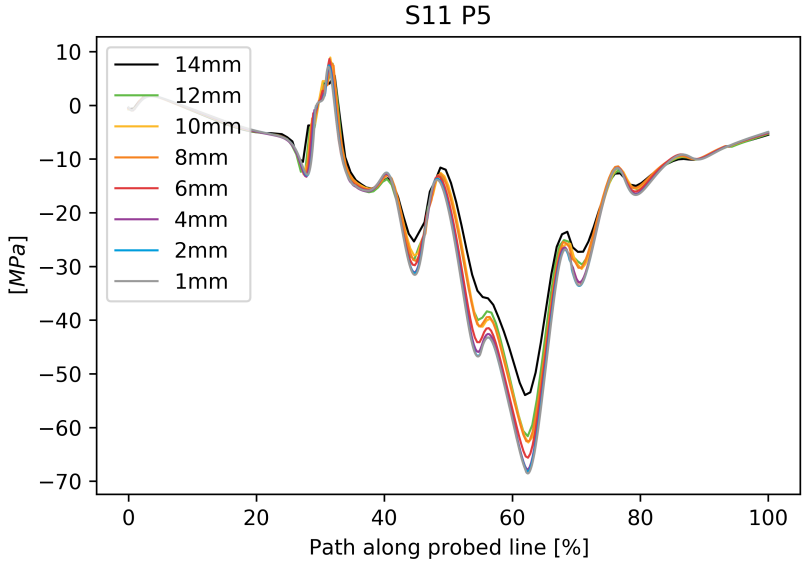

Figure 6.14: First principal stress in the fifth ply

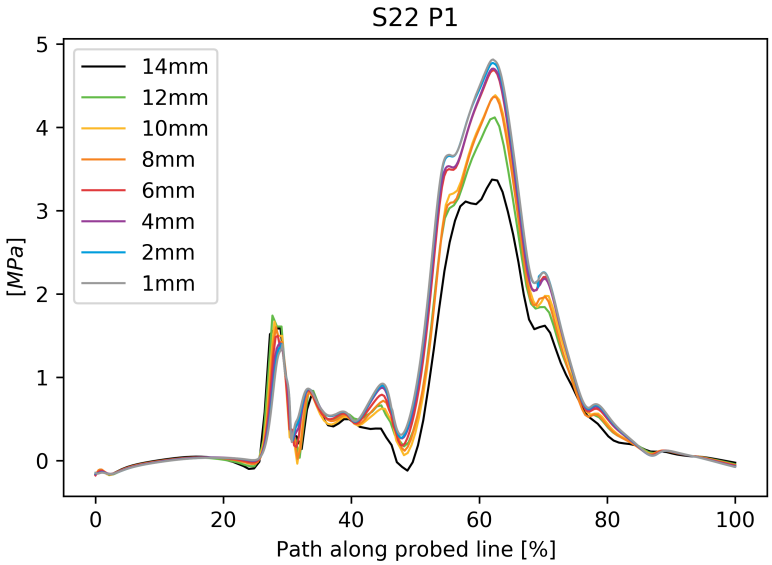

Figure 6.15: Second principal stress in the first ply

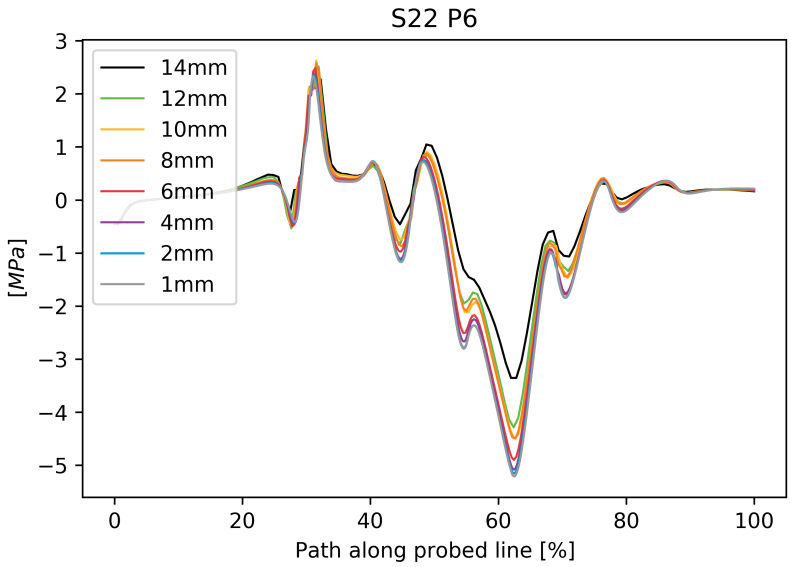

Figure 6.16: Second principal stress in the sixth ply

6.3 Reverse engineering of material

To obtain accurate results, the material properties of the FEA model needs to match reality. Without input from the manufacturer of the material used and the designed layup of the composite, the only option would be to cut the foil into pieces to reverse engineer the layup and obtain test pieces to use in material testing. However, given the price of the hydrofoil and a desire from Chalmers University of Technology to keep the hydrofoil intact for future use, no destructive testing could be carried out. Therefore, another method has to be used. The selected method evaluates the deflection of the hydrofoil when a known load is applied and then matches the load case in ABAQUS. Then the material properties and layup can be iterated until satisfactory results are obtained.

The approach chosen was first to define an isotropic model that gives reasonable results. Then a composite layup is iterated until a satisfactory result is obtained. Due to the unknown internal structure of the hydrofoil and the approximation using a plate stiffener, a perfect match with the real hydrofoil is most likely never not possible. The drawbacks of this approach are many. Unless a large portion of luck is involved, it can be very time-consuming, especially when a composite is iterated. However, if a composite is not established, the twist-bend coupling is lost. The twist-bend coupling is also not manifested if a symmetrical composite layup is used.

6.3.1 Static load testing of the hydrofoil

A wooden beam is secured with two C-clamps and a pair of closed-cell foam blocks at half the length of the diagonal part of the hydrofoil. The wooden beam also serves as a cantilever, allowing a bending moment to be applied by placing weights in front of the leading edge and behind the trailing edge. See figure 6.17. The weights are also applied centered along the chord length. The test matrix for the static test is presented in table 6.3. When the higher loads were applied on the cantilever, the foam blocks used to protect the hydrofoil started slipping, and the test had to be aborted.

Table 6.3: Test matrix for static test load test

Posistion	Loads $[kg]$					
165mm behind trailing edge	5	10	15	20	N/A	N/A
Centred	5	10	15	20	25	30
195 mm in front of leading edge	5	10	15	20	N/A	N/A

(a) Placement of test load at leading edge

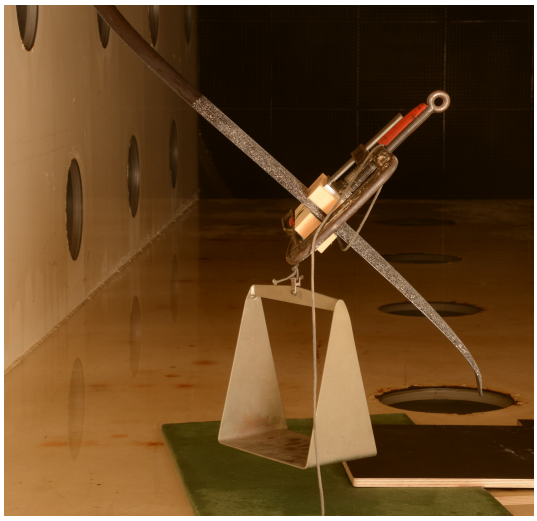

(b) Placement of test load at the center

Figure 6.17: Placement of weights during static load test

6.3.2 Post-processing of captured data

The displacement is recorded with Digital Image Correlation (DIC). This yields a large set of data, as the DIC maps a coordinate system onto the foil surface and records the displacement of the nodes.

The position of the un-deformed nodes from the DIC and from the FEA can be imported into, for example, MATLAB and compared. To do this, the coordinated systems need to be transformed to match one and other. An easy way of doing this is to utilize the capability in CloudCompare, since it offers powerful tools to align surfaces and point clouds that are arbitrarily oriented in space. From CloudCompare a transformation matrix is produced that can be imported into another software to mimic the transformation. In theory, they should line up almost perfectly, since it is known from the 3D-scan that the CAD model of the hydrofoil is rather accurate (see section 4.2.2. However, once the nodes' positions are compared. Given the accuracy of the DIC it is expected that the two geometry would line up perfectly, since the CAD model is verified to be accurate. It is however found that this is not the case, Especially around the tip of the hydrofoil. See figure 6.18.

The difference between the two surfaces can be quantified in CloudCompare, which generates the distribution and a heat map of the deviation of the two point clouds, see figure 6.19. C2C stands for Cloud to cloud.

This discrepancy between the captured geometry and the FEA nodes is most likely either due to the placement of the DIC calibration plane, see figure 6.20. Potentially some lens distortion could be caused by the windows in the cavitation tunnel. The

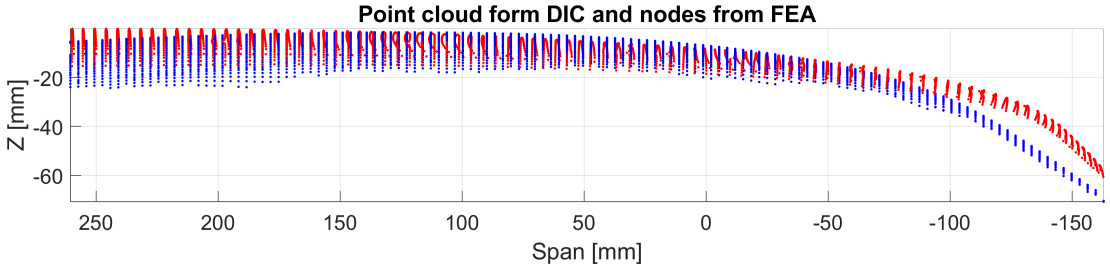

(a) Side view

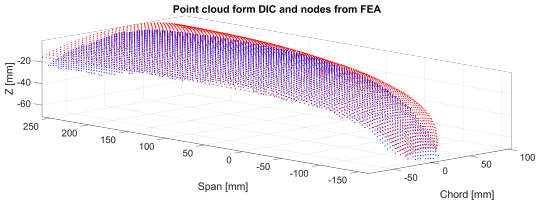

(b) ISO view

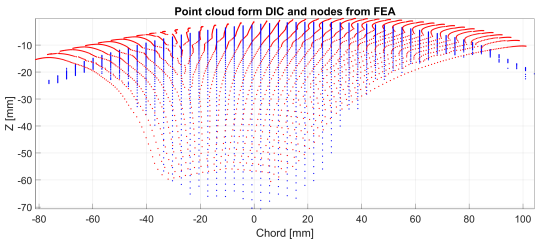

(c) Front view

Figure 6.18: Point cloud of DIC and nodes from FEA, notice the rather large difference between the tip in from the FEA and the DIC. •-FEA, •-DIC

curvature of the hydrofoil around the tip also may affect the accuracy of the DIC since the tip region is further away from the calibration plane. If this error for the position carries over to the captured displacement of the hydrofoil when subjected to a load can not be verified without measuring the deflection with another method during the load test. The error in position is however only discovered after the testing phase is finished, and subsequently there was no possibility of repeating the load test. It is assumed that the displacement is captured accurately even if the original position is not.

A way to reduce the error is to choose a smaller area that is used to compare the test data from the DIC and the FEA. A small region around the origin of the calibration point is selected, stretching from from 50 mm to -22 mm in the span-vise direction , presented in figure 6.21. The selected area is then defined in the FEA model to export the coordinates of the nodes and the displacement, see figure 6.22. The position of the nodes from the FEA model is then compared with the position of the nodes from the DIC measurements in CloudCompare, both to obtain the discrepancy and the transformation matrix used to minimize the distance between the two data sets. See figure 6.23.

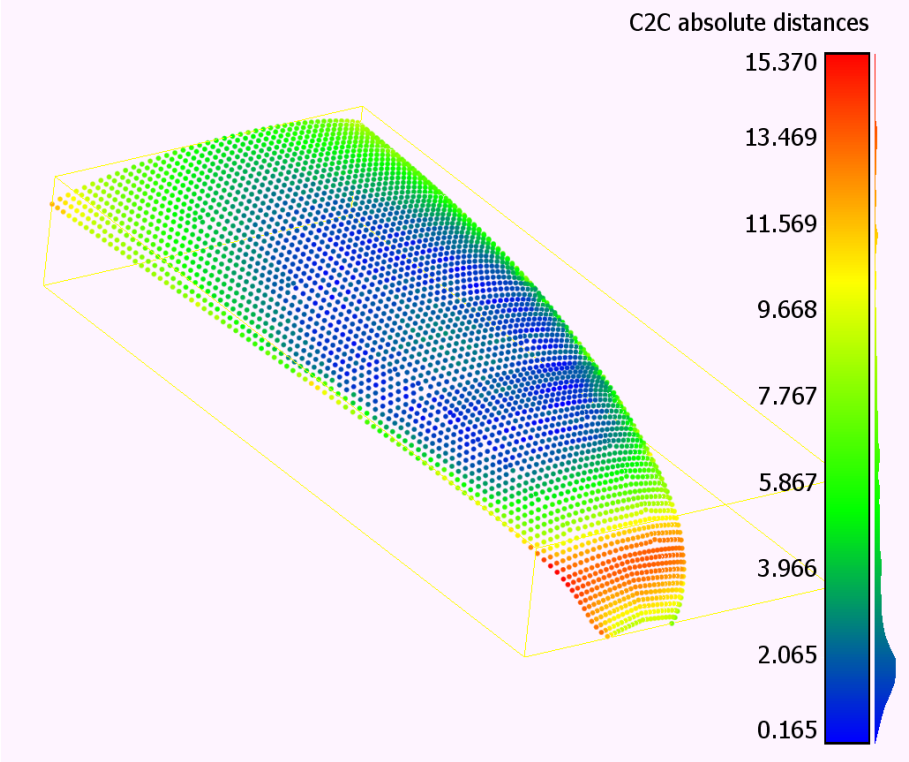

(a) Heat map of the deviation

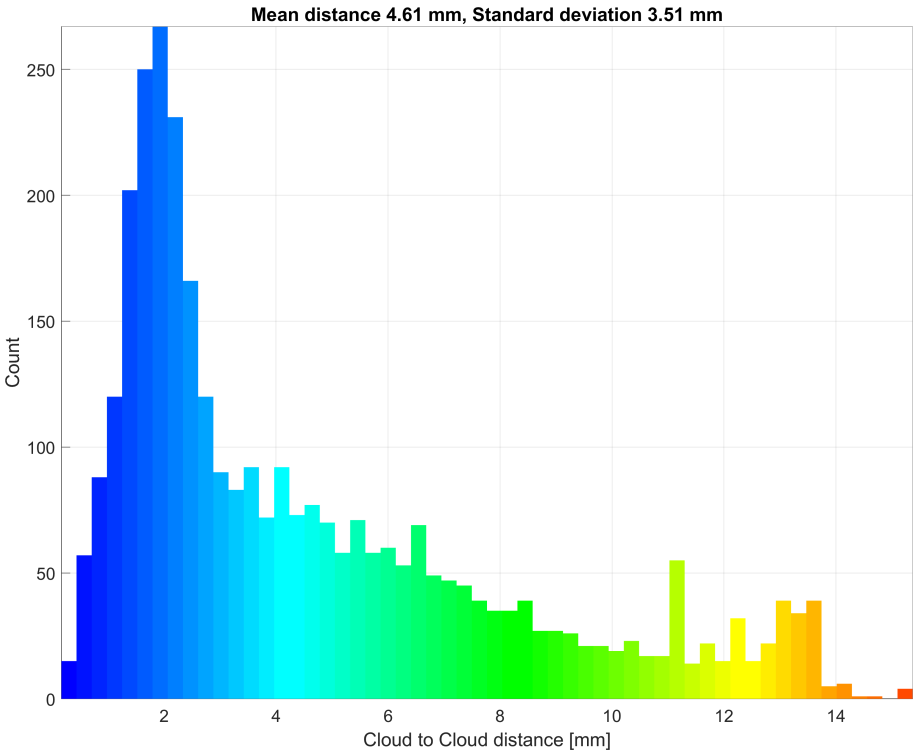

(b) Distribution of the deviation

Figure 6.19: Discrepancy between the FEA model and the captured data

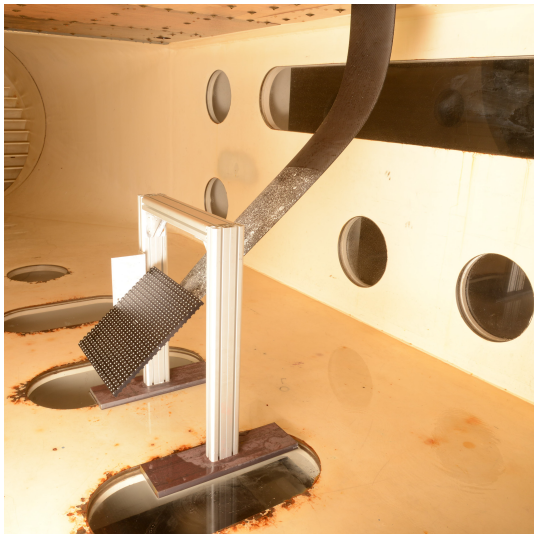

(a) The hydrofoil with the calibration plane

(b) The hydrofoil without the calibration plane

Figure 6.20: Placement of the calibration plane for the DIC

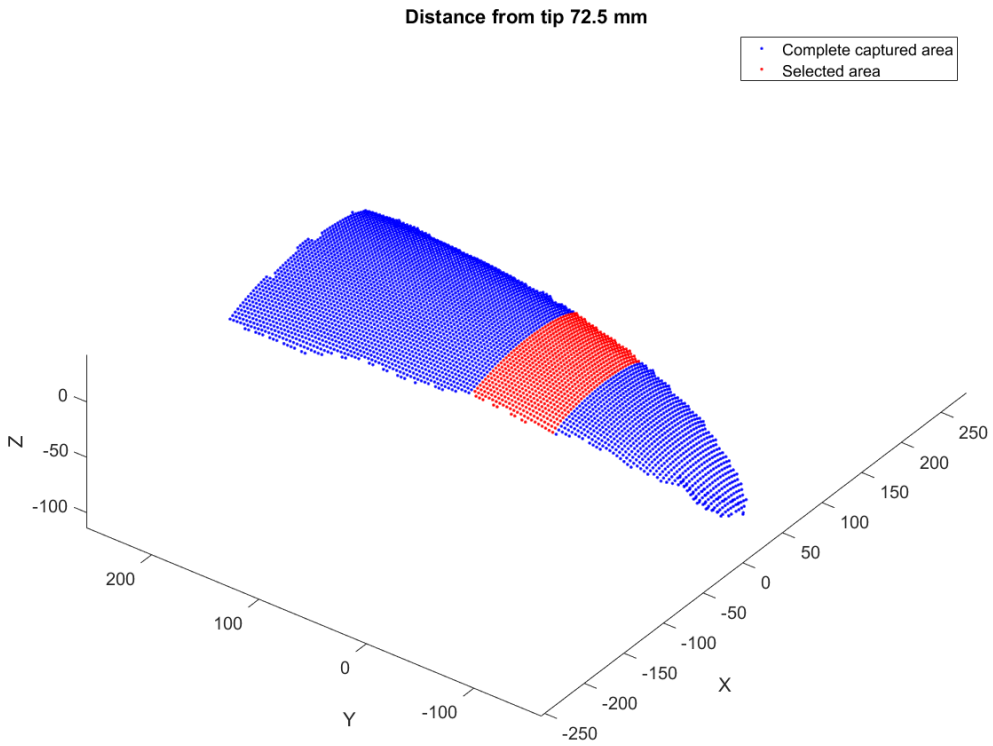

Figure 6.21: Chosen are from where to extract displacement and coordinates used to compare the data from the DIC with the FEA model

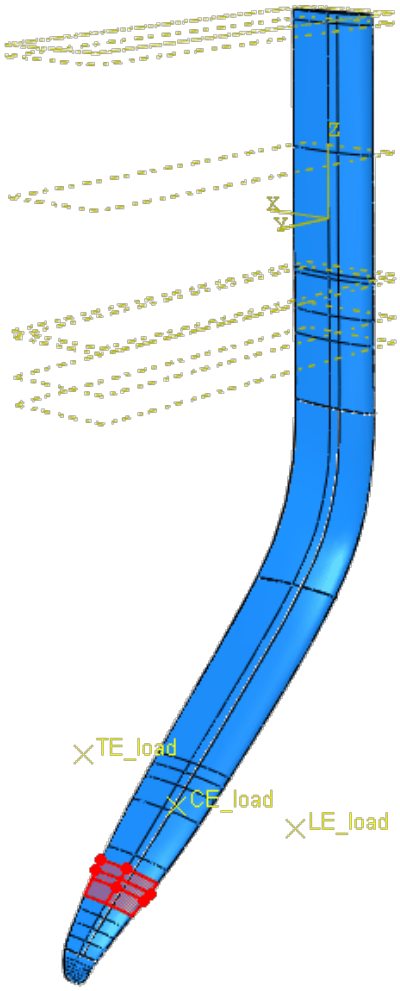

Figure 6.22: Corresponding surface region in the FEA model

The two point clouds are then imported into MATLAB, and a surface can be generated and compared, see figure 6.24. The height of the two surfaces is then subtracted to obtain the difference. This is then plotted in a filled contour plot. See figure 6.25. Comparing the results in figure 6.25 with the deviation from figure 6.23b, it is clear that there is a difference between the two. This has to do with how the surface is in figure 6.24 is interpolated using a cubic triangulation-based interpolation in MATLAB, while the data in 6.24 represents the distance between a node from one data set to its closest neighbor.

Once the orientation and position of the two data sets are confirmed to be good, the tested load cases are reproduced in the FEA model. For simplicity, only three load cases are considered. The assumption is that the load and deflection relation have a linear coupling. The selected load case to simulate is the 20 kg load case for all three positions, found in table 6.3. The node's position and displacement can then be imported into MATLAB to be compared with data from the static testing.

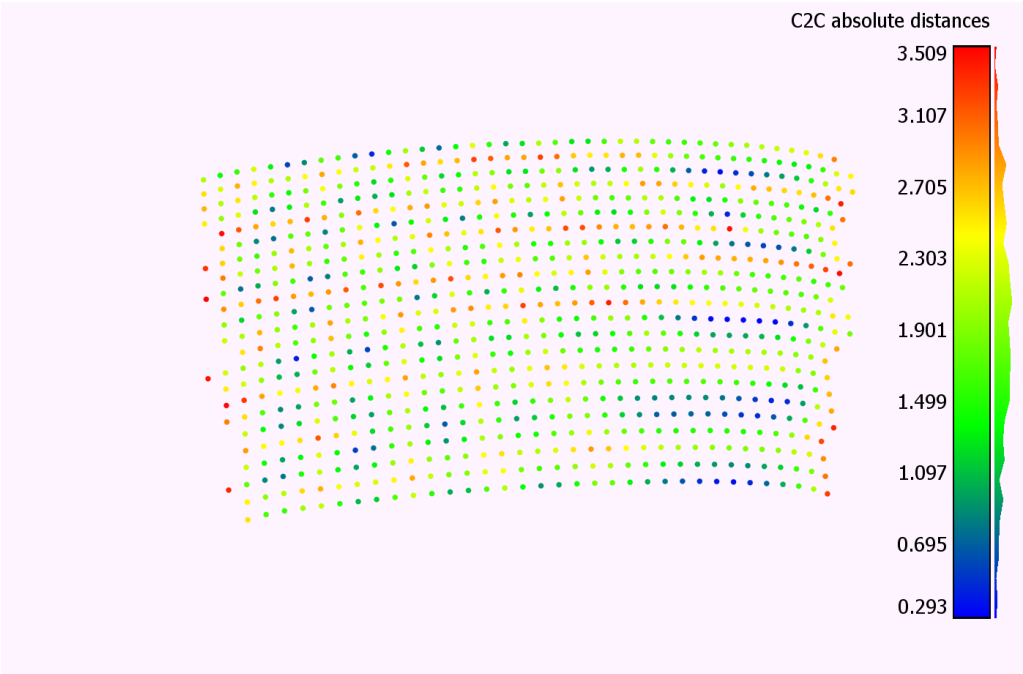

(a) Distance between the reduced surface

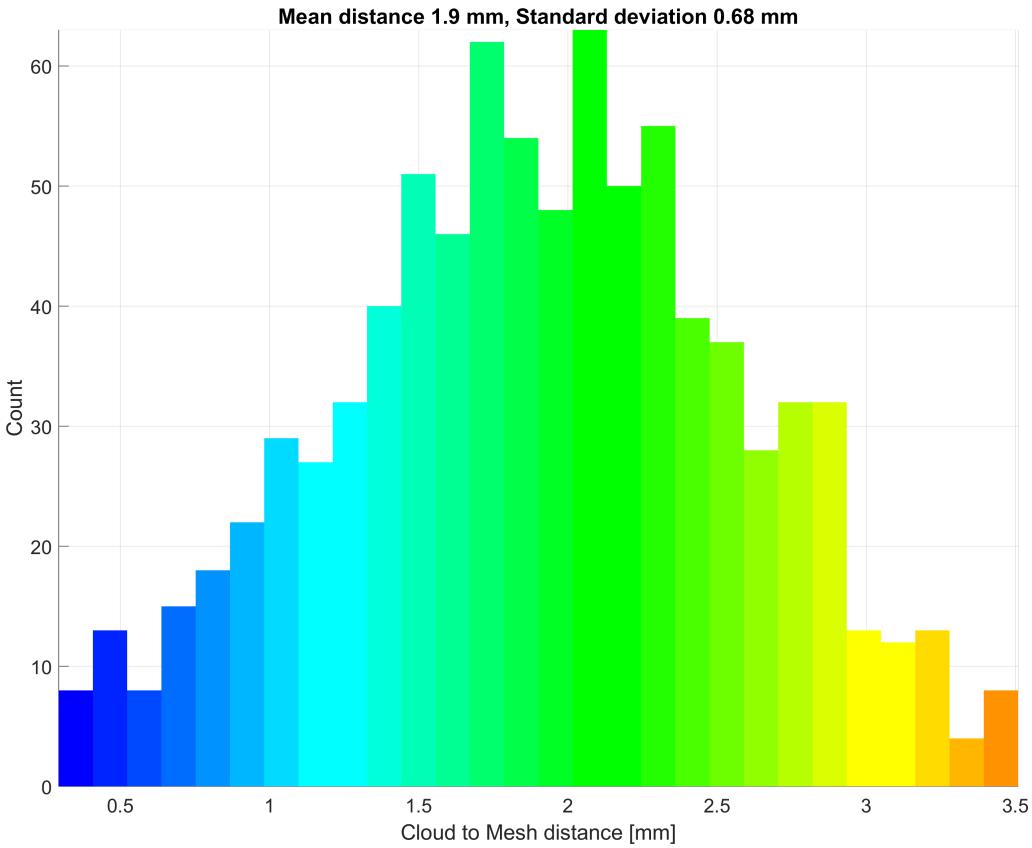

(b) Distribution of the distance between the surfaces

Figure 6.23: CloudCompare of the reduced surface

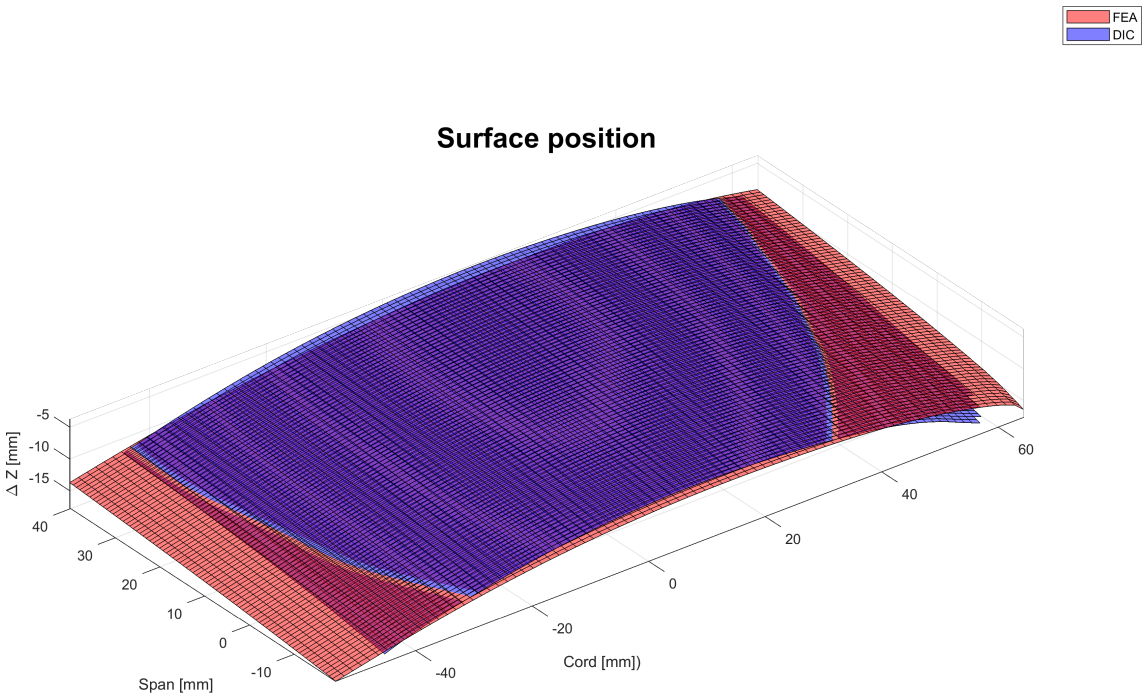

Figure 6.24: Surfaces generated from the point clouds

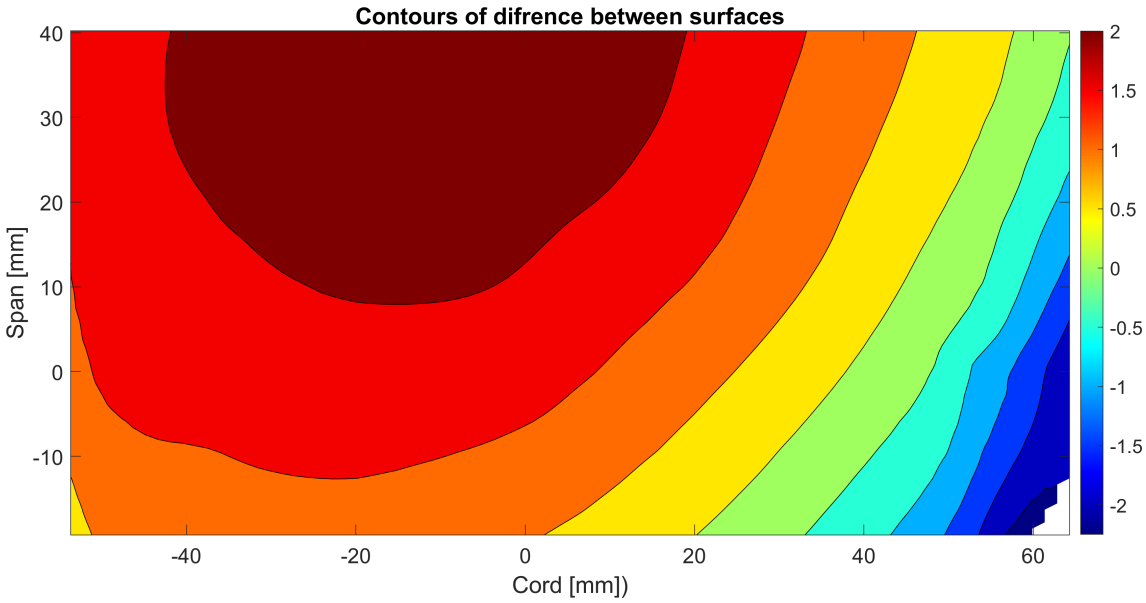

Figure 6.25: Contour plot of the differences in the investigated area

6.3.3 Material selection

As reasoned in section 6.3, first, an isotropic material is selected with a shell thickness of 2.5 mm. After a few iterations, an Young's modules of 55 GPa and a Poisson's ratio of 0.3 are found to give a displacement that is close to the experimental data. The difference in deflection between the isotropic model and the test result is presented in figure 6.26 to 6.28.

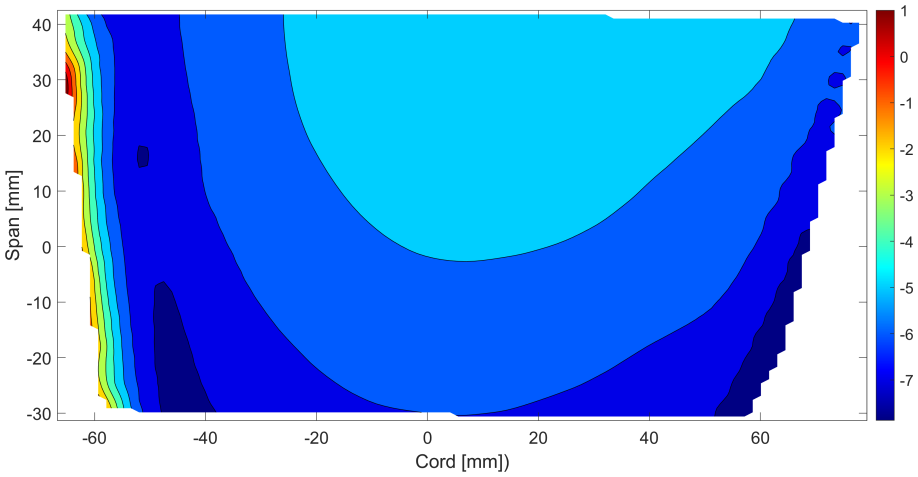

(a) Contour plot

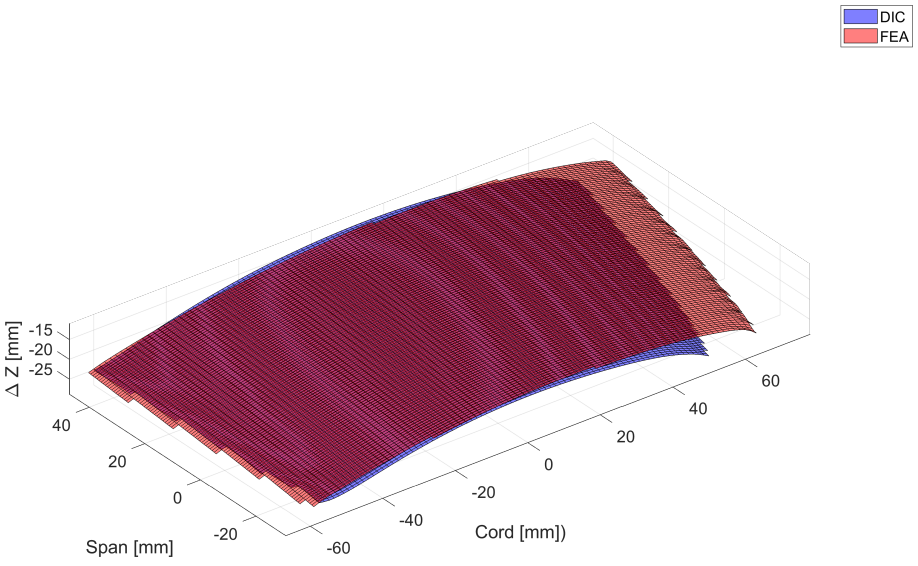

(b) Surface plot

Figure 6.26: Difference in deflection for the trailing edge load case using isotopic material

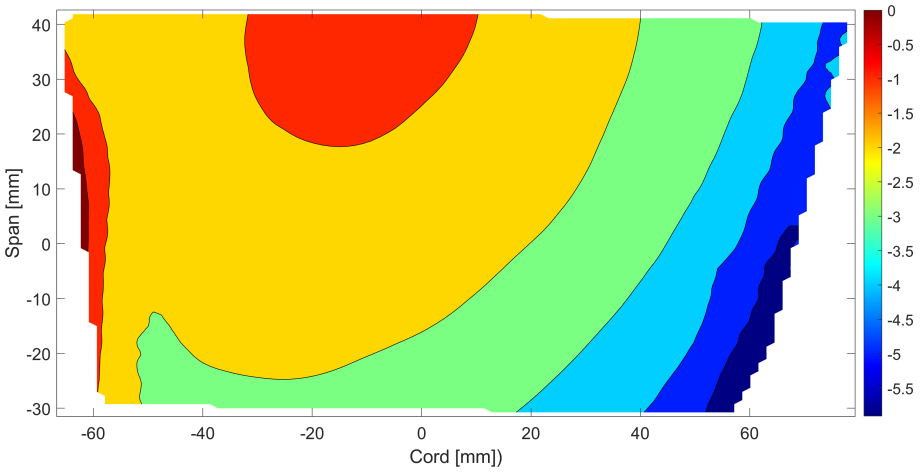

(a) Contour plot

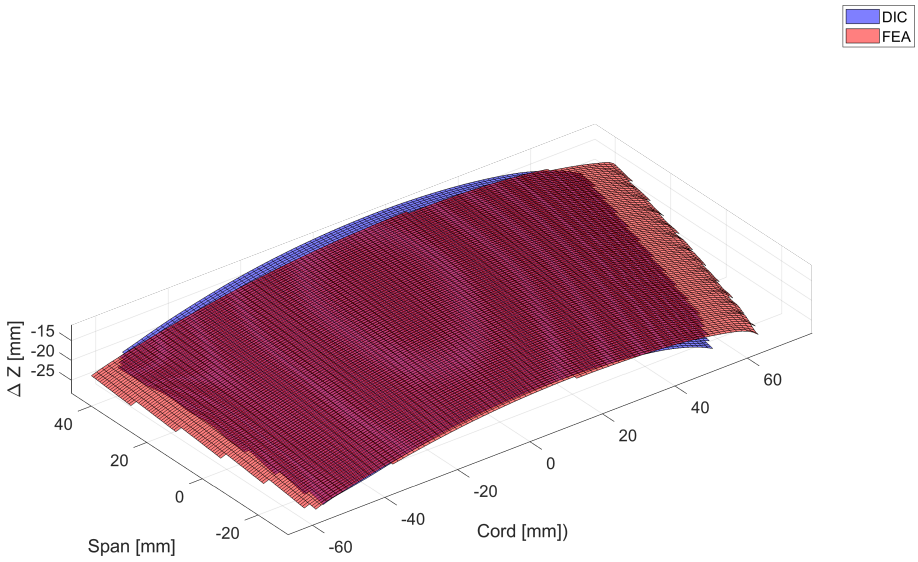

(b) Surface plot

Figure 6.27: Difference in deflection for the center load case using isotopic material

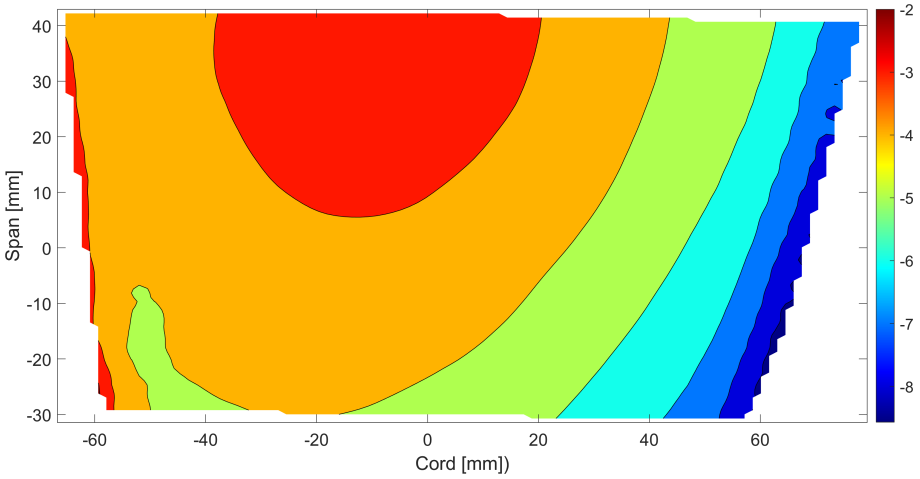

(a) Contour plot

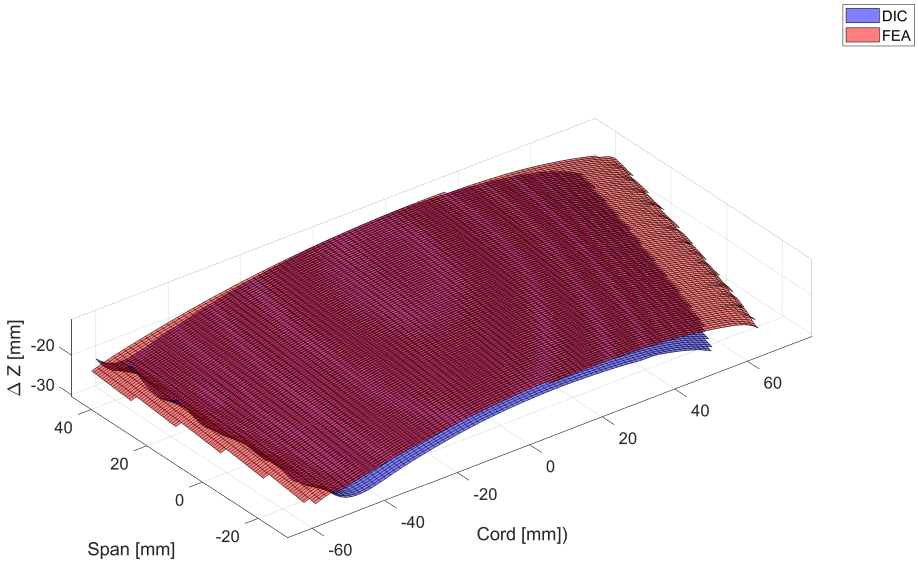

(b) Surface plot

Figure 6.28: Difference in deflection for the leading edge load case using isotopic material

As can be seen in figure 6.27, the difference in displacement between the FEA model and the captured data from the DIC for the 20 kg load in the center load case is rather large compared with the other two load cases. It is assumed that the difference is because of the estimated internal stiffener and the use of isotropic material. The real hydrofoil most likely contains a considerable amount of 0° degree ply's, giving the hydrofoil a high stiffness for bending in one direction but a weaker resistance to twisting, unlike the isotropic model that has the same properties in all directions.

A composite model is also set up, using the material properties from (Giovannetti, 2017) for a pre-preg carbon fiber, presented in table 6.4, with the help of a short Python script that allows the user to specify the desired layup of the composite. The Python script generates an ABAQUS macro that changes the composite layup in the FEA model. This approach was chosen so many composite layups can be tested in a comparably short time. After a few iterations, a layup that gives a comparable error as the isotropic model is found, presented in figure 6.29

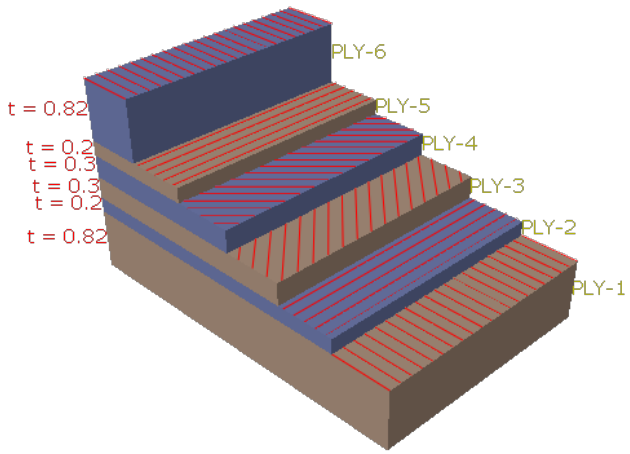

Figure 6.29: The composite layup used in the FEA model

The main difference between the isotropic model and the composite model is the deflection of the investigated surface, the composite model is also slightly better at capturing the twist when a moment is applied from the cantilever. This is best seen in the trailing edge load case in figure 6.30. The difference in deflection is also captured more accurately in the composite model, See figure 6.30 to 6.32. This however is not inherent of the composite model, but rather because of the the lamina and ply thickness, there respective orientation and what material properties are

Table 6.4: Material properties used in the FEA model

E_1 [MPa]	E_2 [MPa]	ν_{12} [-]	G_{12} [MPa]	G_{13} [MPa]	G_{23} [MPa]	ρ [ton/mm^3]
117940	7840	0.25	4400	3600	4400	3E-9

assigned to them. Since no material testing could be conducted and there is no input from the manufacturer, known material properties are obtained from Giovannetti, 2017 where material tests where carried out on a specimen of prepreg carbon fiber[1]. The material properties from Giovannetti, 2017 are presented in table 6.4.

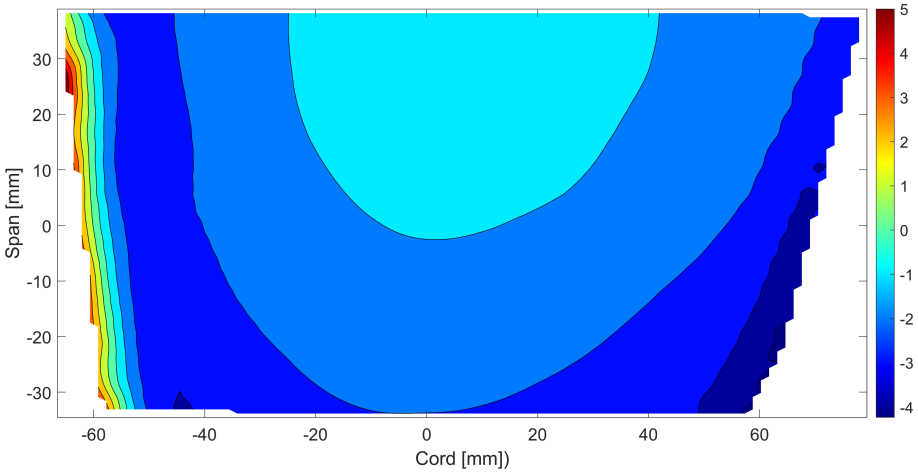

(a) Contour plot

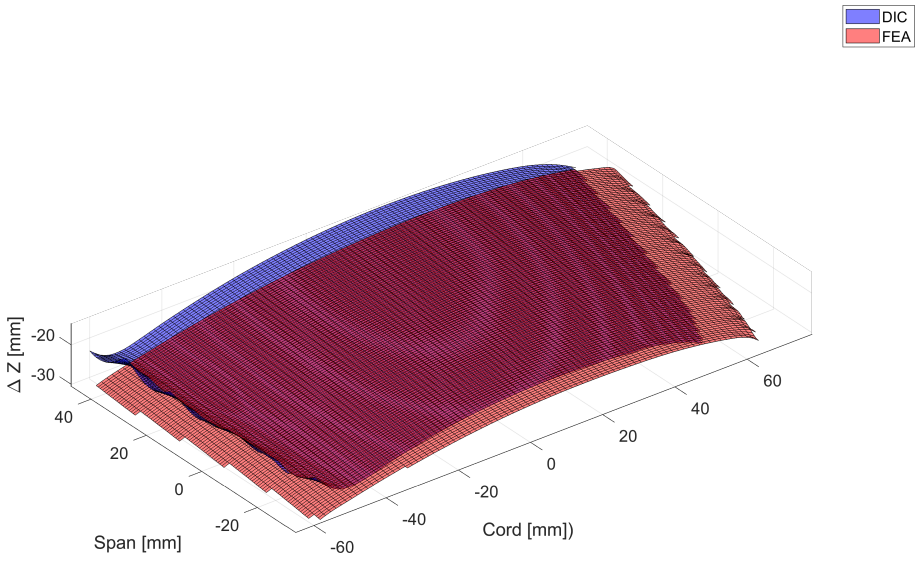

(b) Surface plot

Figure 6.30: Difference in deflection for the trailing edge load case using a composite material

It is worth mentioning that the twist can substantially impact the angle of attack of the hydrofoil, vastly affecting the lift and drag generated by the hydrofoil. However, if the bending is not captured as accurately, it will have a negligible impact on the lift and side force generated by the hydrofoil. Therefore, it is more desirable to capture the twist of the hydrofoil more than any other aspect.

[1]prepreg is when the carbon fiber material is already mixed with the matrix from the manufacturer, eliminating the manufacturing step of infusing the fibers with the matrix

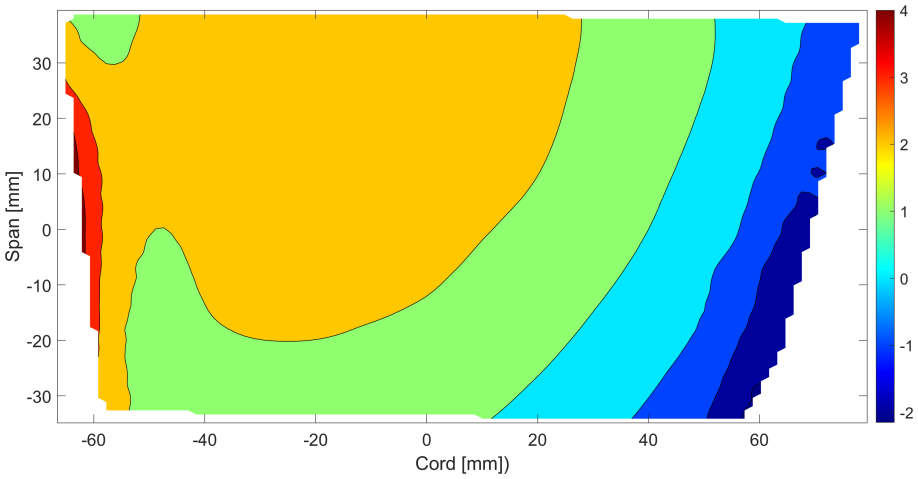

(a) Contour plot

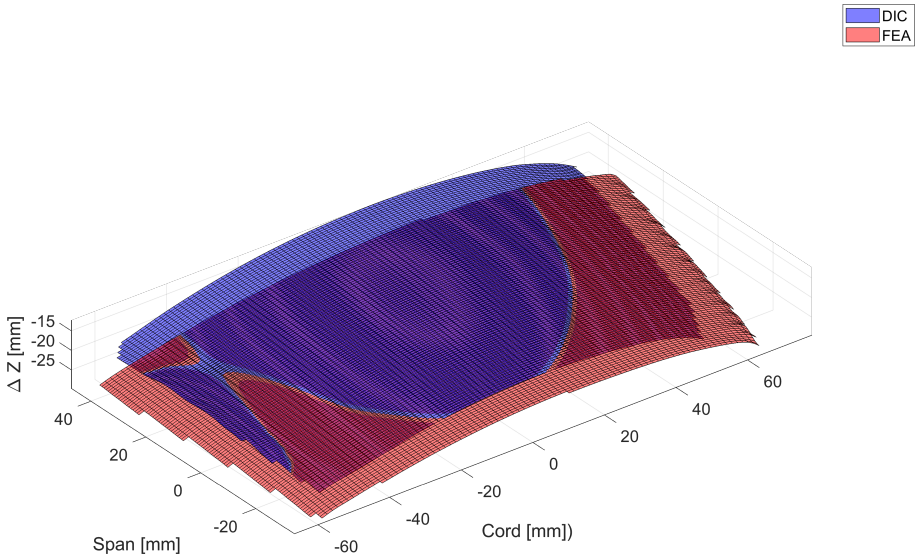

(b) Surface plot

Figure 6.31: Difference in deflection for the center load case using a composite material

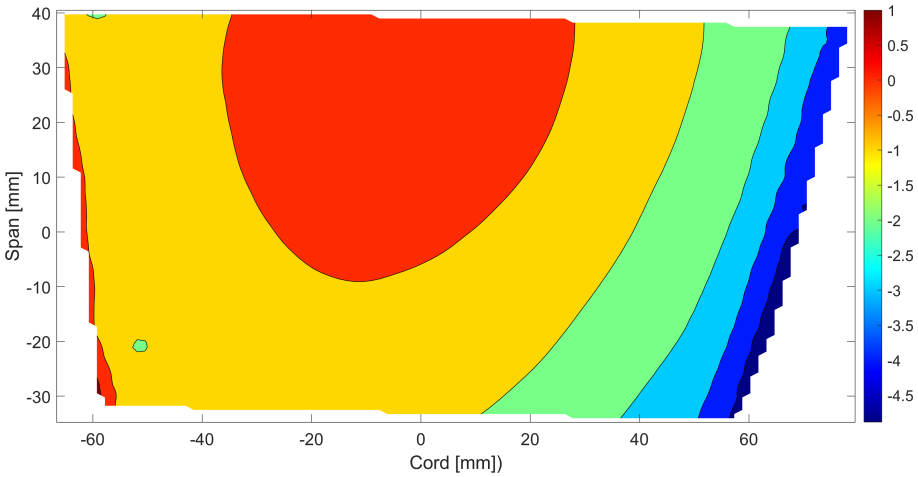

(a) Contour plot

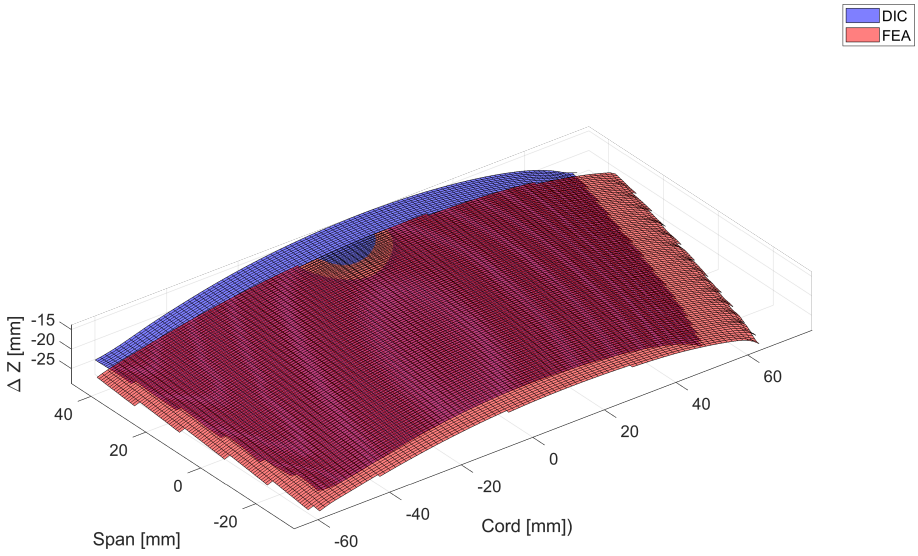

(b) Surface plot

Figure 6.32: Difference in deflection for the leading edge load case using a composite material

7

Validation and results

Good results should be defined and quantified; therefore, the results from the FSI simulations need to be validated. Knowing the model's accuracy enables the possibility of simulating untested conditions, such as different rake and leeway angels, flow velocity, or using a different composite layup. These suggested variables are of great interest because testing components under different conditions is a very costly endeavor, especially if, i.e., a new foil needs to be manufactured to carry out the tests.

Two main parameters are investigated to validate the results. Resulting forces and the displacement of the hydrofoil.

The tests were carried out in the cavitation tunnel at SSPA, following the test matrix in table 7.1. Due to a limitation of Central processing unit hours (CPUh) per month and the difficulties getting the CFD and FEA software to work together on the computing cluster[1] at the beginning of the project. The whole test matrix could not be simulated. The combinations highlighted in table 7.1 with red were excluded from the simulation test matrix. Furthermore, the defined simulation test matrix is utilized only for the validation of the Cavitation Tunnel model in subsection 7.1.2, where it was further reduced (for the same reasons stated above) by also excluding the combination highlighted in blue when carrying out the subsections 7.1.1, 7.1.3, and 7.1.4

Table 7.1: Test matrix used in the project

Leeway angle [T[2]]	**Rake angle [R][3]**
0°	0°, 1°, 1.5°, -1°, -2°
0.5°	0°, 1°, 2°, -1°, -2°
1°	0°, 1°, 2°, 2.5°, -1°, -2°
-0.5°	0°, 1°, -1°, -2°
-1°	0°, 0.3°, -1°, -2°
2.5°	0°, 1°, 2°, 3°, 3.75°, -1°, -2°
3.5°	0°, 1°, 2°, 3°, 4°, 4.75°, -1°, -2°

[1] A cluster is a collection of computers assigned to perform heavy computational tasks

7.1 Lift drag and side force

Initially, the CFD model is defined for both the cavitation tunnel and the towing tank. The two models are verified as shown in sections 5.5 5.5.2.

The results of the two models are expected to be different, which is caused mainly due to the difference in the physical models used. In the cavitation tunnel, the fluid is only water, although the effects from the tunnel's walls are to be present hence have a non-negligible influence on the flow. On the other hand, in the towing tank, wall effects are not present, but instead, the free surface influence exists, which will affect the flow and thus the results. A comparison between the results acquired from running stand-alone simulations (only STAR-CCM+ simulation without coupling with ABAQUS) is performed to define which effect would be the dominant and having the most significant influence on the results,

Validation for the cavitation tunnel CFD numerical model is performed later. A numerical model is validated when comparing its results to the test results carried out in the testing facilities .i.e SSPA cavitation tunnel, to measure the difference and thus define the accuracy of the results.

The same validation procedure should be applied for the virtual Towing Tank model too. However, a comparison with the cavitation tunnel experiment results is only performed due to lack of time.

7.1.1 Comparison between the Cavitation tunnel and Towing Tank results for stand-alone simulations

The resulting forces in the two models are exported from STAR-CCM+ and later imported to a MATLAB script to carry out the comparison. In figures 7.1, 7.2, and 7.3. the resulting drag, lift, and side forces of the decided Leeway and Rake combinations are plotted for both Towing Tank and Cavitation tunnel together with the difference (CFD Cavitation Tunnel - CFD Towing Tank).

- The difference in the drag force in most cases is small.
- In the lift forces, the difference is somewhat high, especially at the positive combination of the Leeway and Rake angels. These effects can be assumed to be caused more likely due to higher lift forces generated at this combination. A bigger foil area will be outside the water in the towing tank model, adding more resistance and thus reducing the lift force.
- It was observed that the difference in the side force is high, especially at the positive combination of the Leeway and Rake angels; this can be connected to the effects from the walls in the Cavitation Tunnel, which is increasing when the lift force increases.

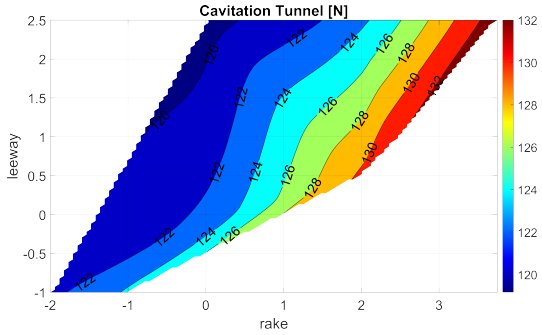

(a) Resulting Drag force from the virtual cavitaion tunnel

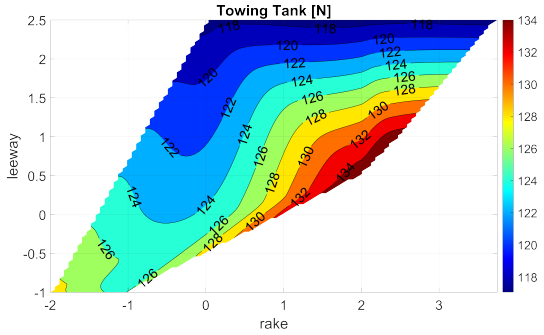

(b) Resulting Drag force from the virtual Towing tank

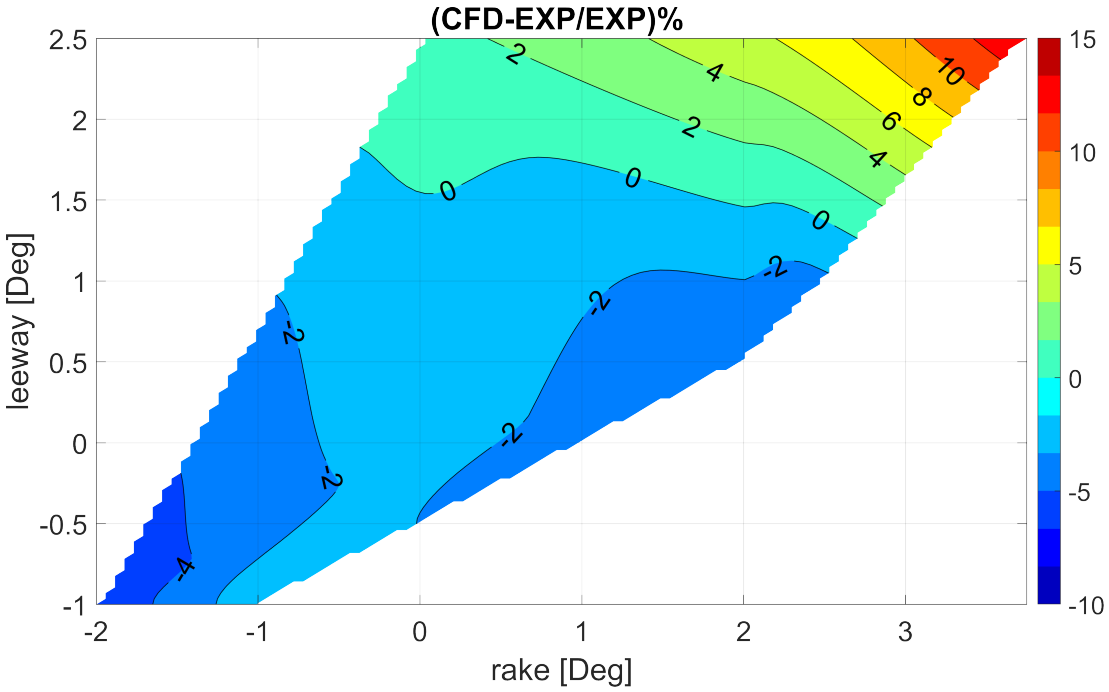

(c) The difference between the Towing tank and the Cavitation Tunnel inCFD

Figure 7.1: The difference in the drag force

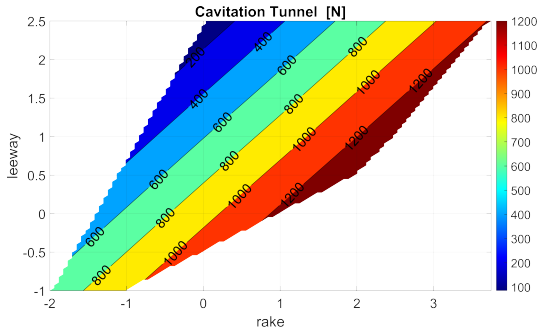

(a) Resulting Lift force from the virtual cavitaion tunnel

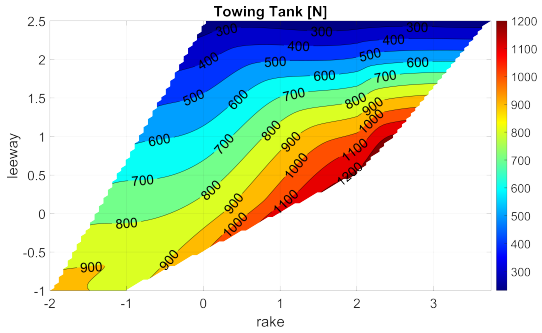

(b) Resulting Lift force from the virtual Towing tank

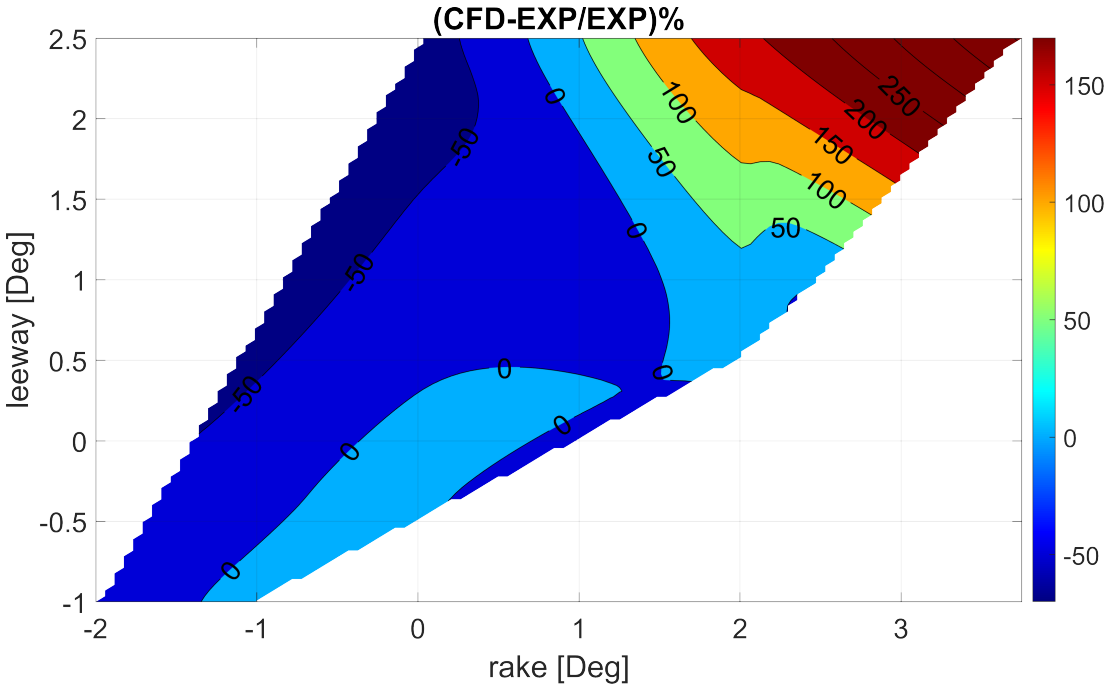

(c) The difference between the Towing tank and the Cavitation Tunnel inCFD

Figure 7.2: The difference in the lift force

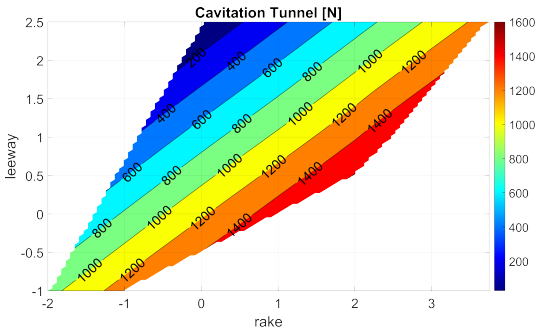

(a) Resulting Side force from the virtual cavitaion tunnel

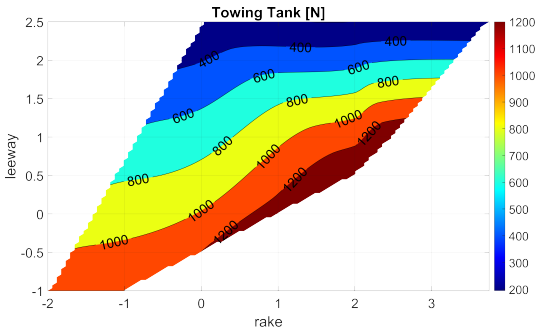

(b) Resulting Side force from the virtual Towing tank

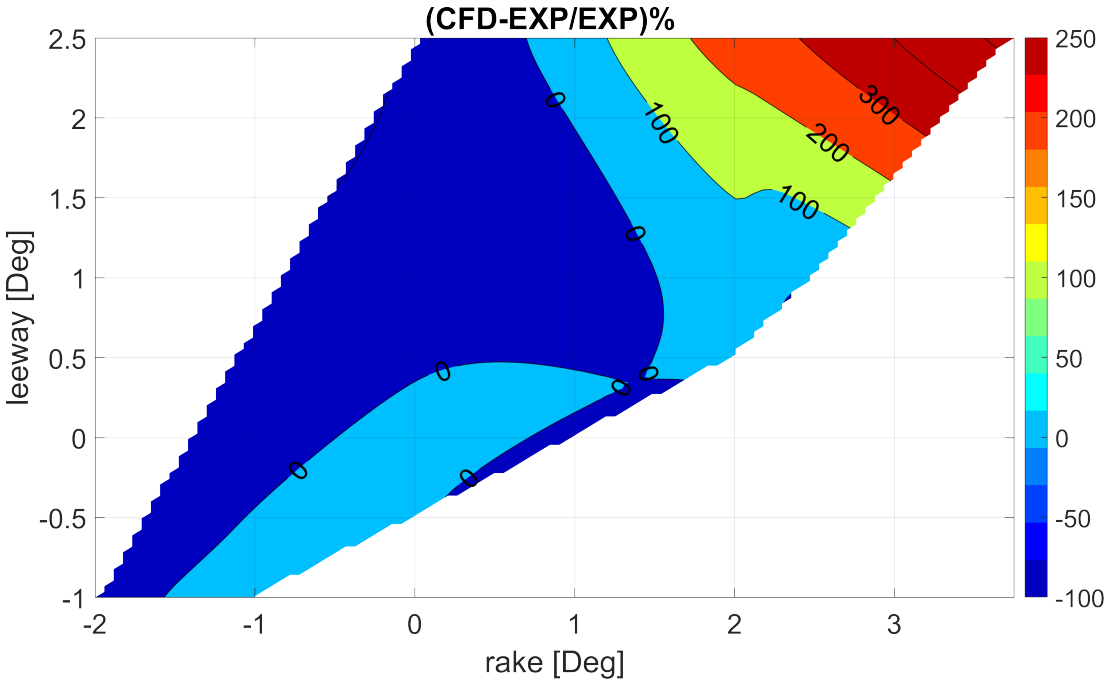

(c) The difference between the Towing tank and the Cavitation Tunnel inCFD

Figure 7.3: The difference in the side force

7.1.2 Validation of the Cavitation tunnel numerical module results

During the tests carried out at SSPA, the forces were recorded using a six-component balance (Kempf Remmers type R41)[4]. The forces in the simulations are saved for each time step and then compared with measured forces from the testing.
Due to the limitation as mentioned earlier in the CPUh, and that the co-simulations are heavy computationally and need to simulate on a considerably high number of CPUh. Hence, it was decided to run all simulations until reaching between 5-6 seconds of physical time, which was observed to be enough to reach convergence. It was decided to take the range between the 3^d and the 5^{th} second of the physical time, where the solution is considered to be converged, and then take the mean value of the extracted data to account for any slight variation in the data thus to be more accurate. The resulting mean values of the drag, lift, and side forces from the STAR-CCM+ were imported to a MATLAB script together with the time-average of the measured drag, lift. Side forces during the experiment and plotted in contour plots see figures 7.4, 7.5, and 7.6.

The validation was performed on the isotropic model only due to a limitation in the time since the obtained composite model showed inaccurate results (see section 7.3). It can be observed from figures 7.4, 7.5, and 7.6, the currently obtained results for the isotropic material model is promising, where the forces of the CFD are somewhat within the same range as the one of the experimental data. A difference in the results was expected and can be related to several reasons:

- During the tests setting up the leeway angel can be tricky and might cause errors when collaborating with the angel.
- The velocity of the flow in the two models could be considered another reason. The velocity is calculated in the cavitation tunnel thanks to a difference of mean pressure between two surfaces, while the velocity for the flow in the CFD model is calculated at the inlet of the virtual cavitation tunnel through the mass conservation (see section 5.2.1.1)
- The properties of the foil used to preformed the simulations in CFD (guessed properties for the isotropic material) is not the same as in the foil used in the tests (composite materials).

[4]A tool designed for force measurements with foils was mounted in the cavitation tunnel

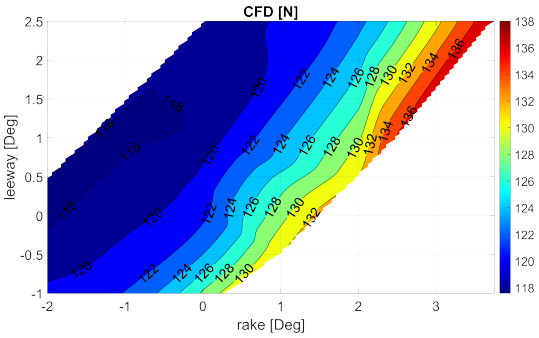

(a) Resulting Drag force from the virtual cavitaion tunnel in CFD

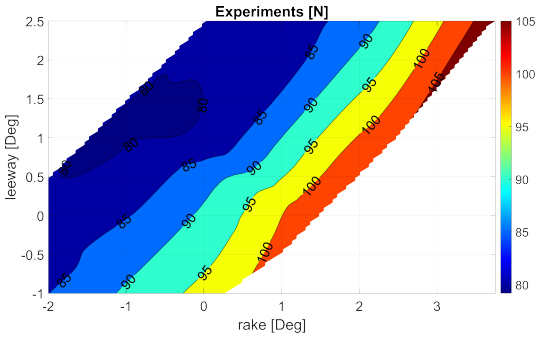

(b) Resulting Drag force from the cavitaion tunnel in the experiments

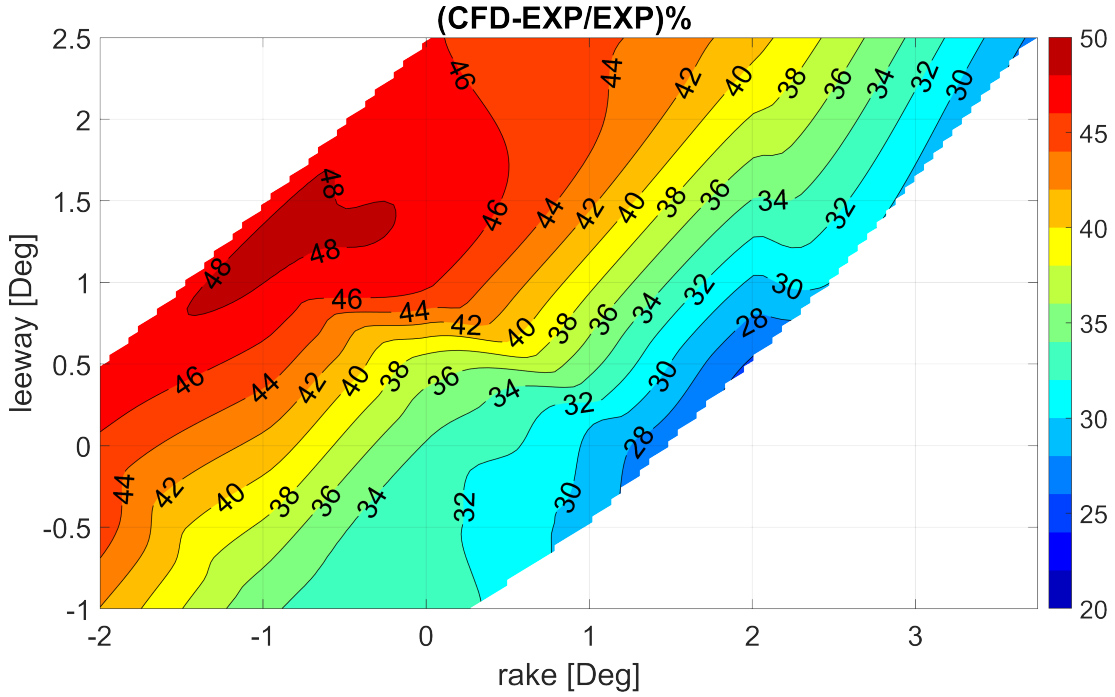

(c) The difference in drag between the CFD and the experiments

Figure 7.4: Validation for the drag force

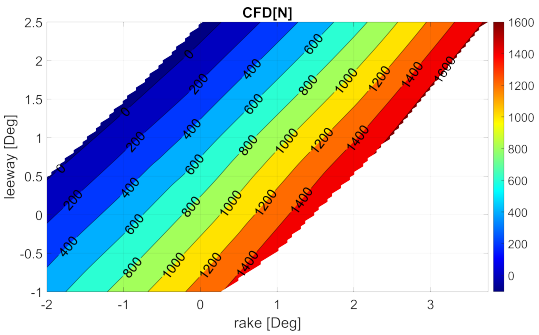

(a) Resulting Lift force from the virtual cavitaion tunnel in CFD

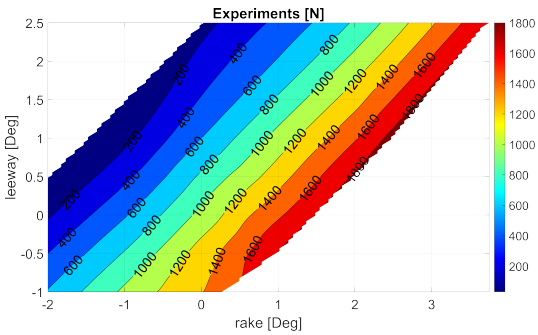

(b) Resulting lift force from the cavitaion tunnel in the experiments

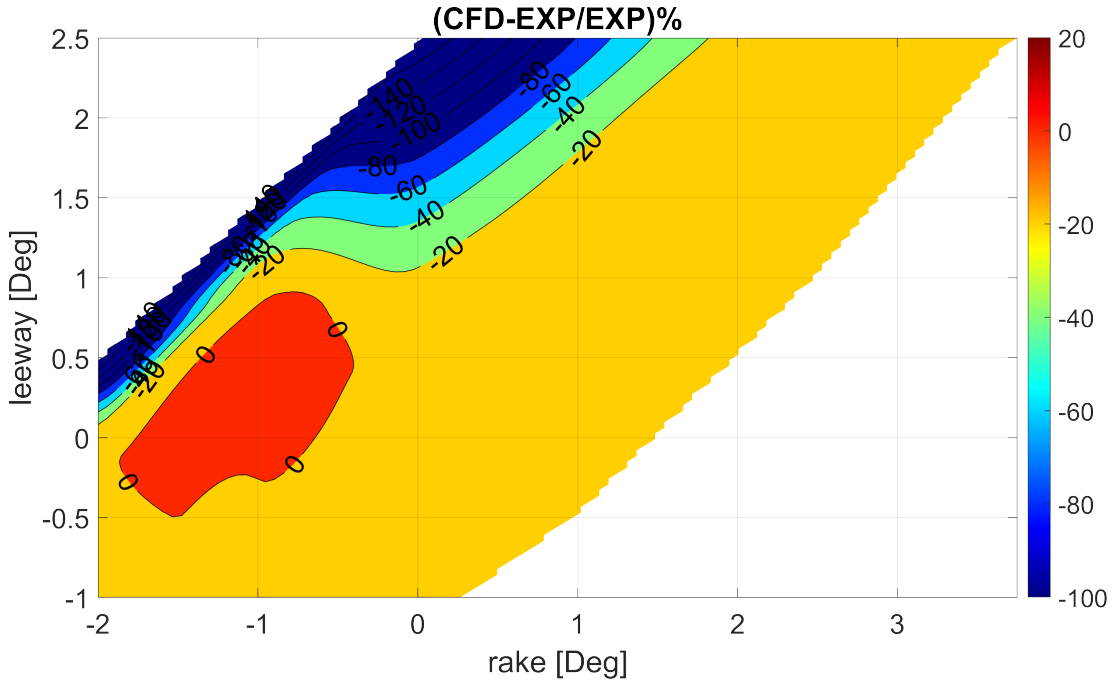

(c) The difference in lift between the CFD and the experiments

Figure 7.5: Validation for the drag force

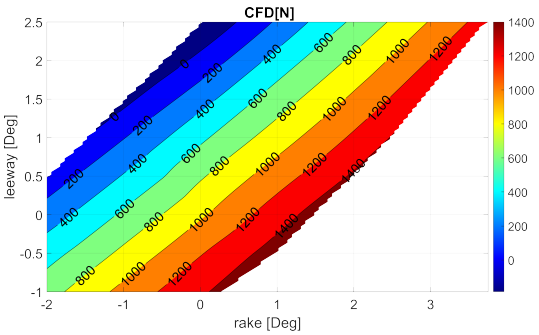

(a) Resulting Side force from the virtual cavitaion tunnel in CFD

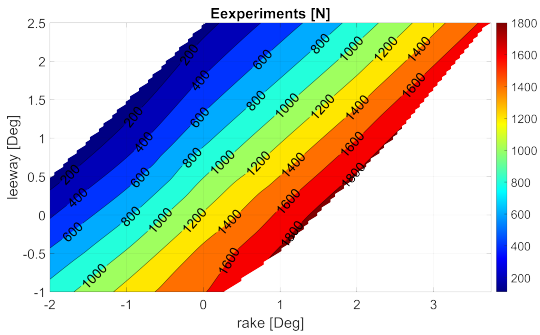

(b) Resulting side force from the cavitaion tunnel in the experiments

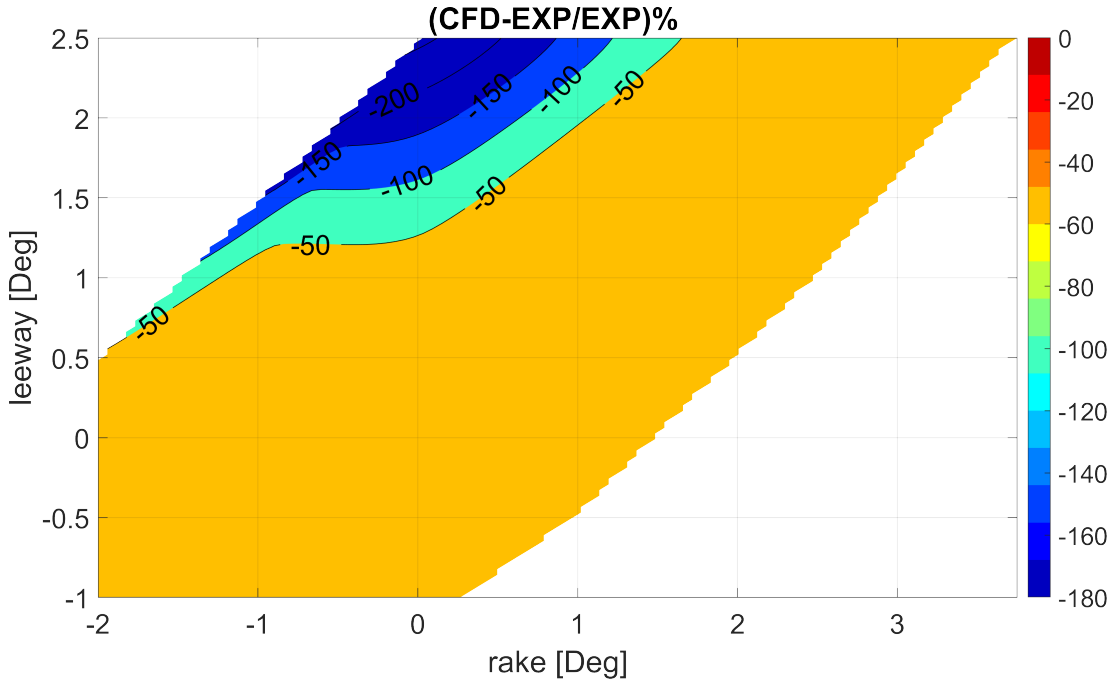

(c) The difference in side force between the CFD and the experiments

Figure 7.6: The difference between the CFD and the experiments

7.1.3 Comparison between the towing tank numerical model and the experimental results in the cavitation tunnel (Isotropic material)

The results from the CFD towing tank model are plotted the same way achieved in subsection 7.1.2, see figures 7.7, 7.8, and 7.9. Moreover, the same comparison is achieved for the isotropic model in this subsection and for the composite model in 7.1.4.

Based on the obtained results, one would observe that the results from the numerical model somewhat follow the same pattern of the testing results with some acceptable differences. The differences between the results were expected since the two models differ from each other .i.e in the cavitation tunnel, the effects from the walls will influence the flow field, which will not be present in the towing tank model. However, the free surface influence will be present instead, thus impacting the flow field differently. In general, such a comparison would give an idea about how accurate the results obtained from the numerical model in the towing tank are.

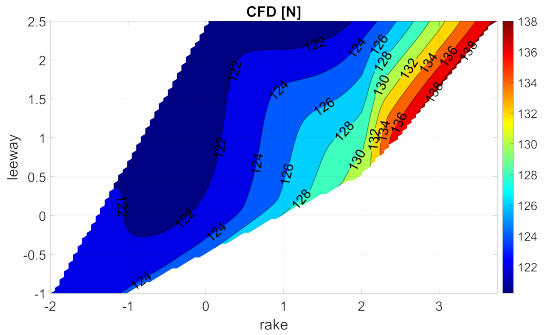

(a) Resulting Drag force from the virtual Towing Tank in CFD

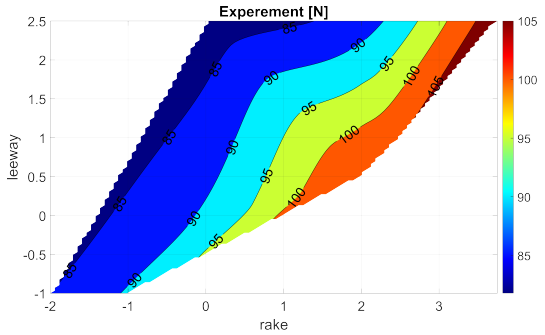

(b) Resulting Drag force from the cavitaion tunnel in the experiments

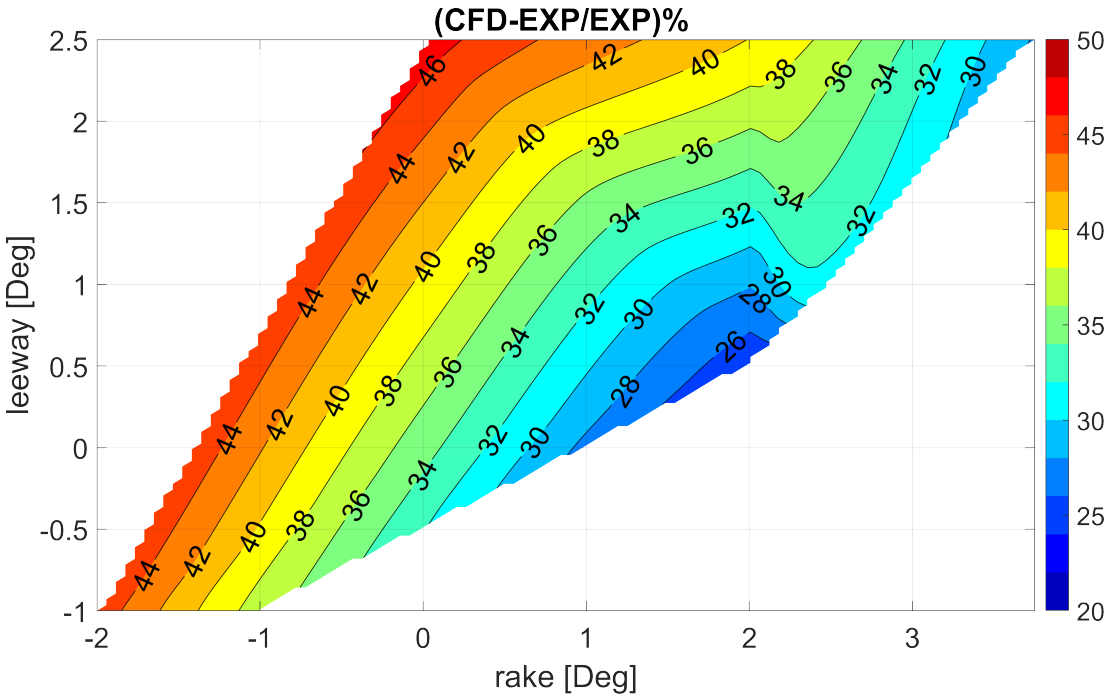

(c) The difference in drag force between the CFD and the experiments

Figure 7.7: Comparison for drag force between the Towing tank, for the isotropic material and the experimental results

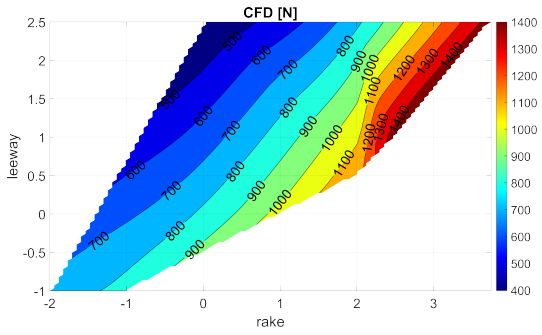

(a) Resulting Lift force from the virtual Towing Tank in CFD

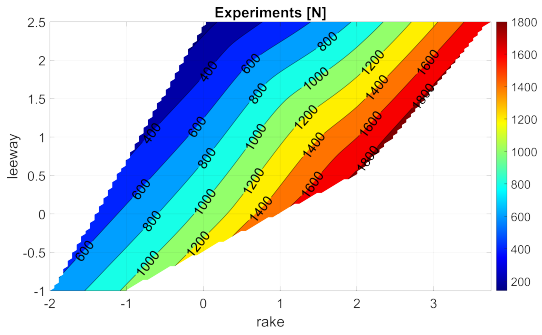

(b) Resulting lift force from the cavitaion tunnel in the experiments

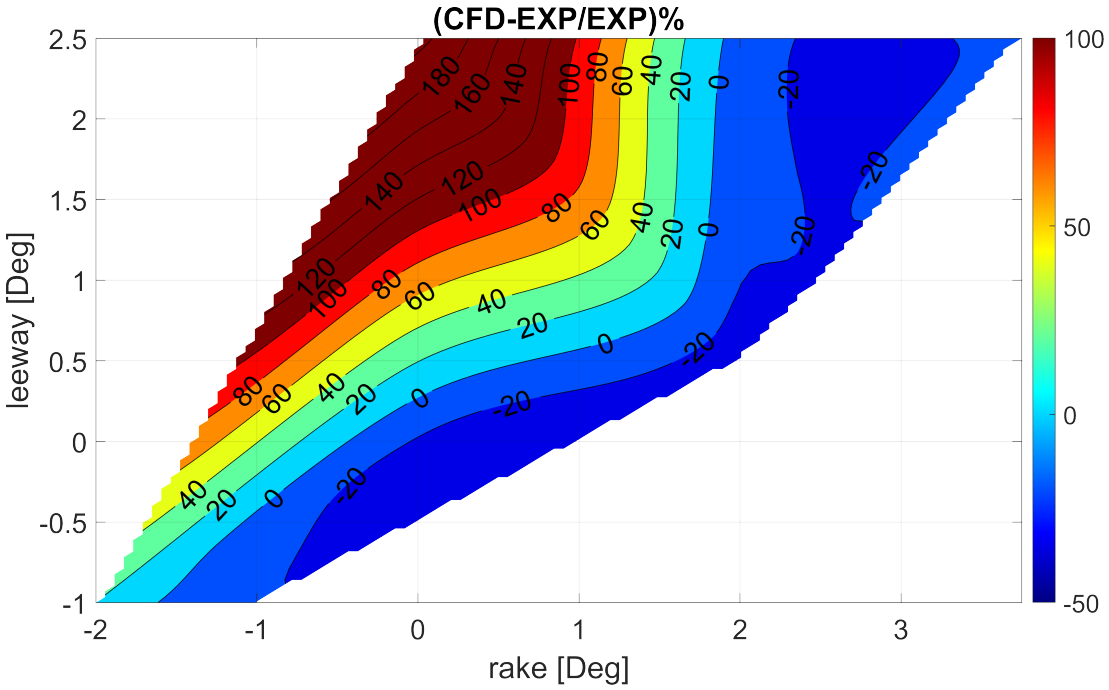

(c) The difference in lift force between the CFD and the experiments

Figure 7.8: Comparison for the lift force between Towing tank, for the isotropic material and the experimental results

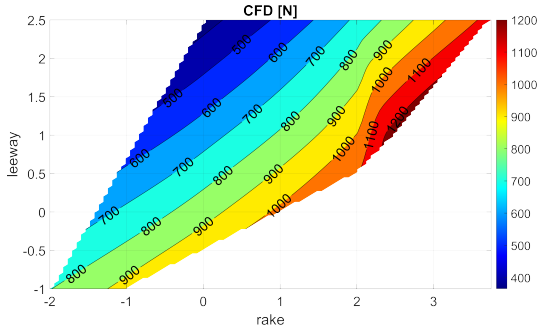

(a) Resulting Side force from the virtual Towing Tank in CFD

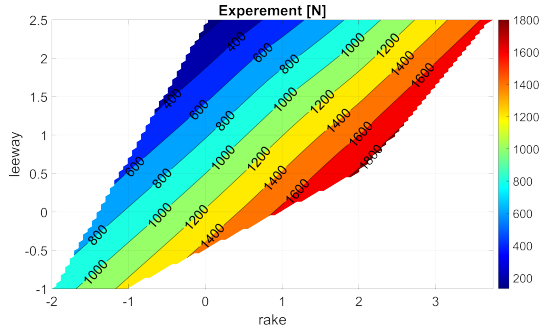

(b) Resulting side force from the cavitaion tunnel in the experiments

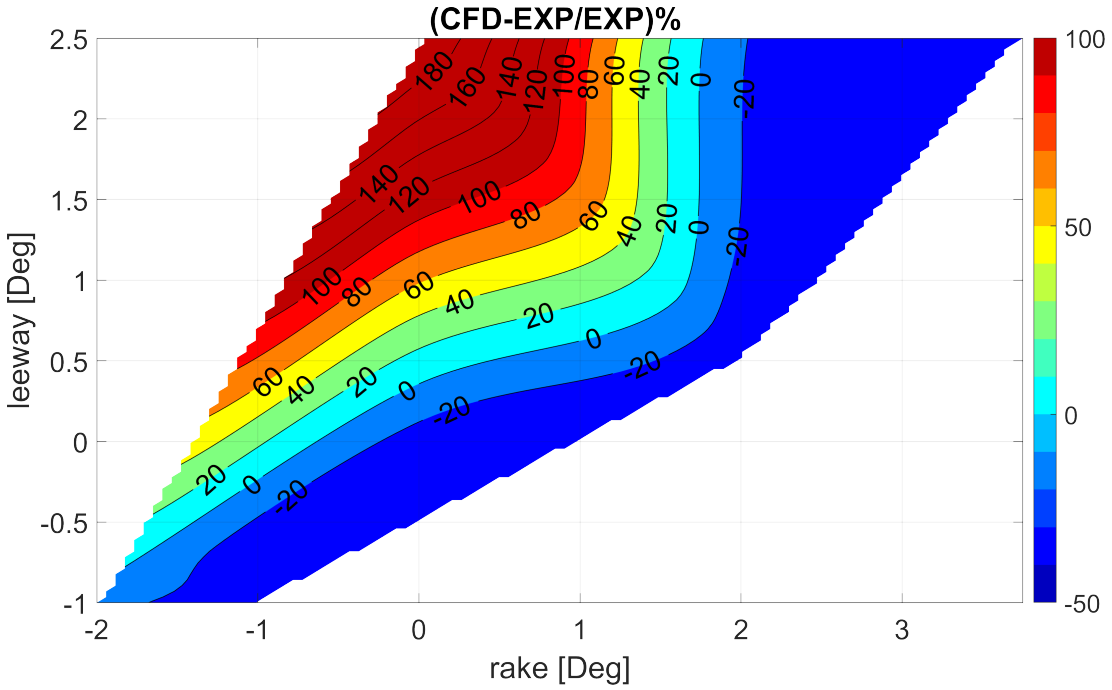

(c) The difference in side force between the CFD and the experiments

Figure 7.9: Comparison for the side force between the Towing tank, for the isotropic material and the experimental results

7.1.4 Comparison between the towing tank numerical model and the experimental results in the cavitation tunnel (Composite material)

Similarly as in the subsection 7.1.3 the plots were obtained for the composite material see figures 7.10, 7.12, and 7.11. The results show a high reduction in the forces, especially for the lift force. Further, analyze the data and find an explanation for the lift reduction. An investigation for the surface pressure at the pressure side of the foil is to be carried out since this side of the foil contributes directly to generating the lift force. Then a comparison with the surface pressure resulting from the isotropic model for the same surface side is to be preform. Moreover, the investigation is to be carried out for the case (T0R0) of the Leeway/Rake combination.

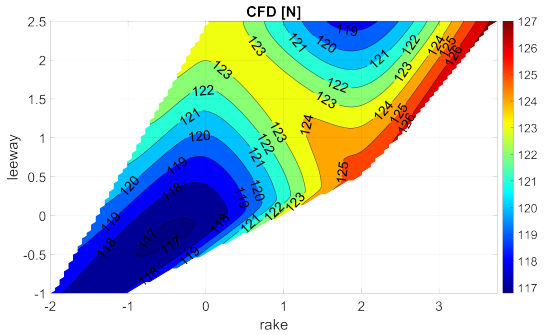

(a) Resulting Drag force from the virtual towing tank in CFD

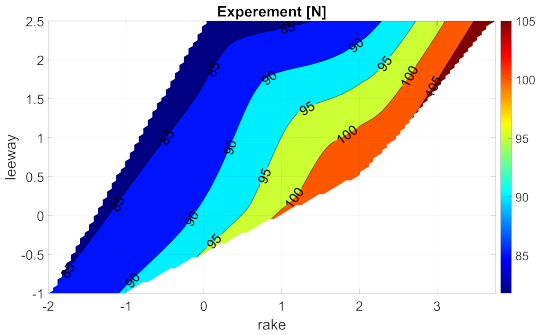

(b) Resulting Drag force from the cavitaion tunnel in the experiments

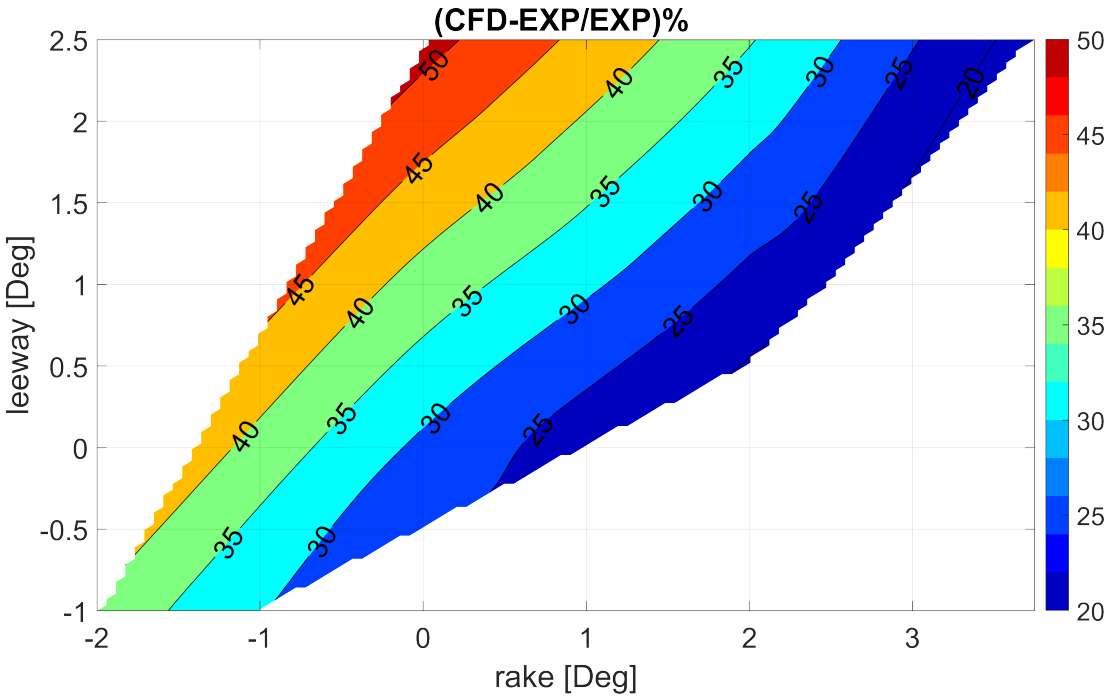

(c) The difference between the CFD and the experiments

Figure 7.10: Comparison for the lift force between the Towing tank, for the composite material and the experimental results

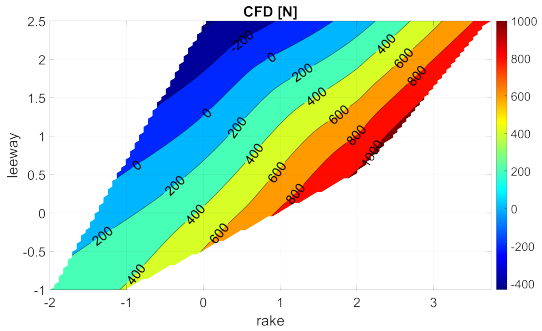

(a) Resulting Lift force from the virtual towing tank in CFD

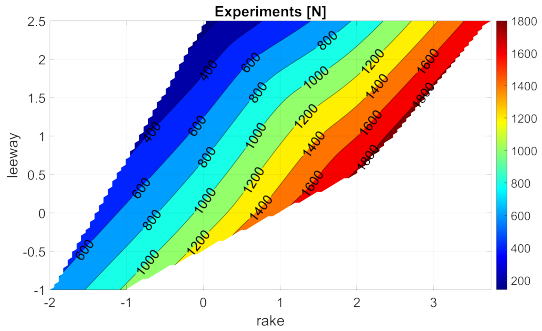

(b) Resulting lift force from the cavitaion tunnel in the experiments

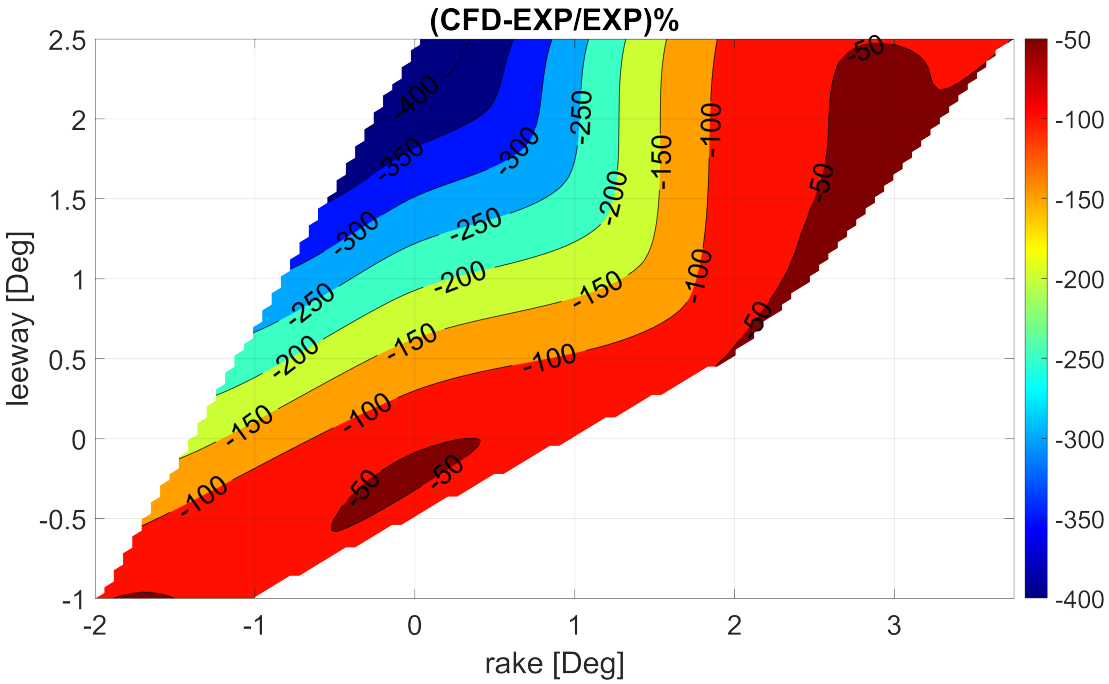

(c) The difference between the CFD and the experiments

Figure 7.11: Comparison for the lift force between the Towing tank, for the composite material and the experimental results

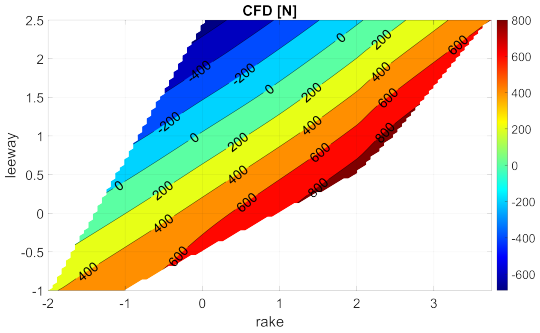

(a) Resulting Side force from the virtual towing tank in CFD

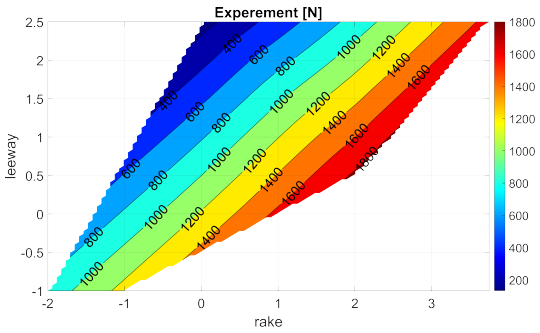

(b) Resulting side force from the cavitaion tunnel in the experiments

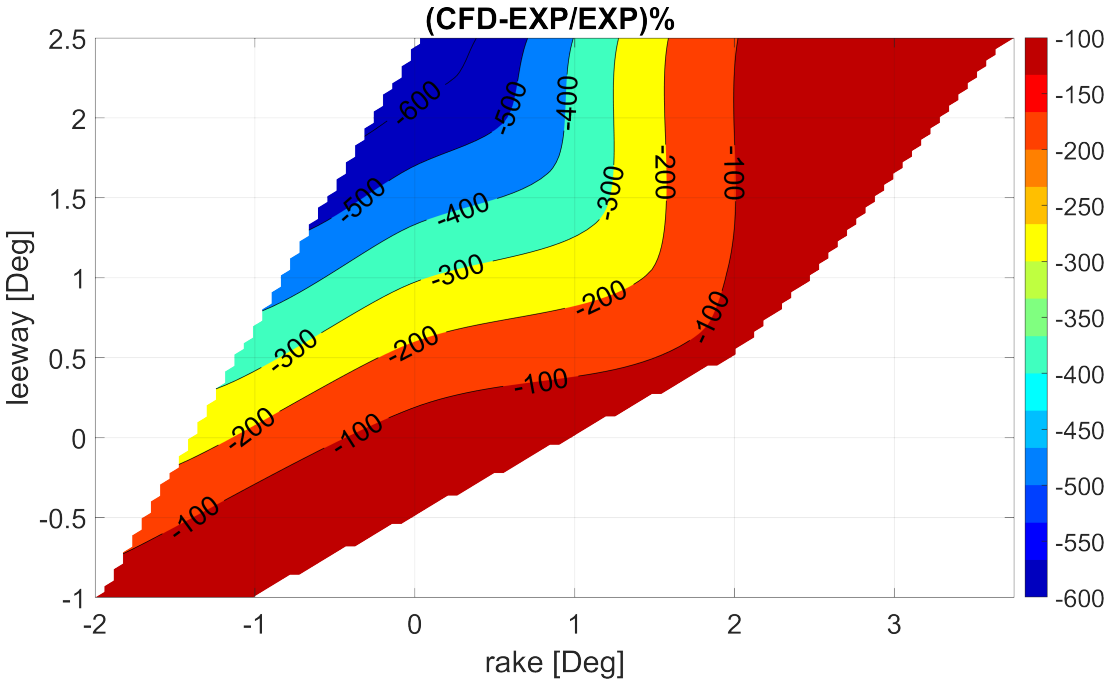

(c) The difference between the CFD in the towing tank and the experiments

Figure 7.12: Validation for the drag force

In figures 7.13a and 7.13b, contour plots of the surface pressure at the pressure side of the foil exported from STAR-CCM+ can be seen. It is noticed that a reduction in the high-pressure area on the surface of the foil can be observed in the composite model compared to the isotropic one. Also, the low-pressure area on the composite model's surface is larger than the isotropic one. Based on the mentioned observations and the fact that the pressure surface of the foil contributes directly to generating the lift force, a reduction in the lift force would be expected.

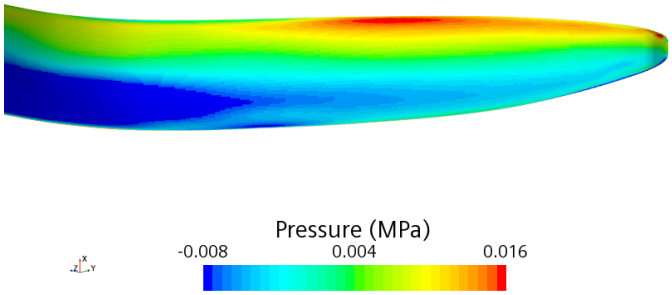

(a) Pressure surface plot for the pressure side of the foil and for the isotropic material model

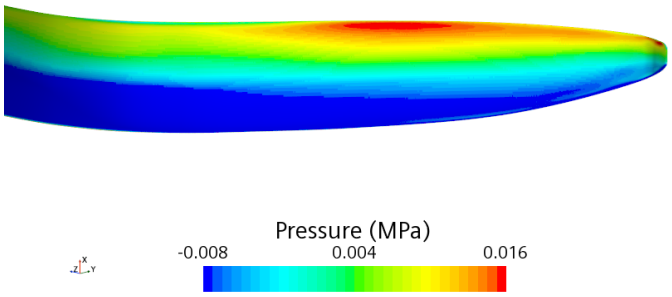

(b) Pressure surface plot for the pressure side of the foil and for the composite material model

Figure 7.13: Comparison for the surface pressure at the pressure side of the foil between the isotropic and the composite models

Furthermore, the cross-section of the hydrofoil in the composite and the isotropic material is investigated in section 7.3 by comparing the deformations of each model in the cross-section at the same position.

7.2 Displacement and position

The displacement was captured using DIC equipment, rented from Lavision, see figure 7.14a. The DIC captured an area close to the tip of the hydrofoil, using a speckle pattern, see figure 7.14b, to allow the cameras to track the surface. The frequency of the high-speed camera is 0.2 kHz.

(a) DIC setup

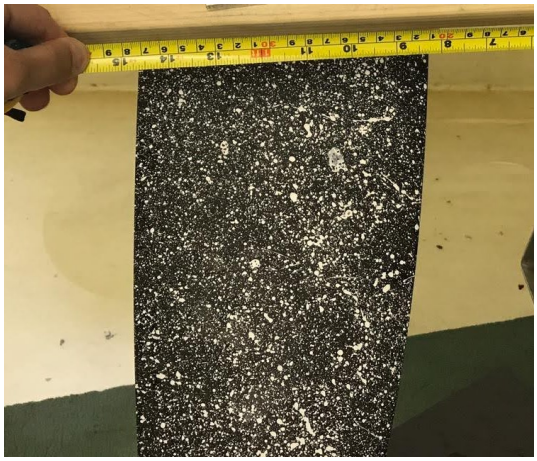

(b) Applied speckle pattern

Figure 7.14: Scens from testing at SSPA

Capturing the out-of-plane displacement with respect to the calibration plane (see figure 7.15) can reveal if the angle of attack is changed. If the displacement is not constant on an arbitrary line across the cord length, the hydrofoil is twisting. If the hydrofoil bends, it will change the magnitude of the force components generated by the pressure difference of the pressure and suction side of the hydrofoil.

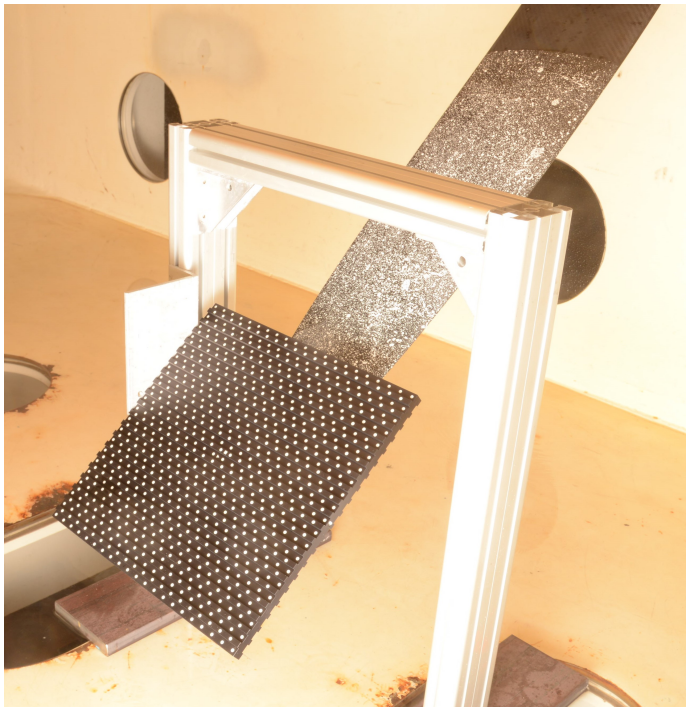

Figure 7.15: Placement of calibration plane

The displacement recorded in each frame is saved and provided by L.Giovannetti. First, the mean displacement for each captured frame was plotted over time, see figure 7.16. As can be seen from the figure, the mean value has a slight variation of about 2mm. If this is because of poor accuracy of the DIC equipment or if the hydrofoil is moving in the assumed steady flow is not known, but according to L.Giovannetti, the accuracy of the DIC equipment should be very high. So the assumption is made that the foil does move a bit in the flow during the testing. The cause of this could either be that the flow has some properties, for example, vortex shedding, or that the flow in the cavitation tunnel is not as steady as it is assumed. In figure 7.16, the test case for 0° leeway and 0° rake is presented. In appendix C.2, the same plot for all the test cases simulated is presented.

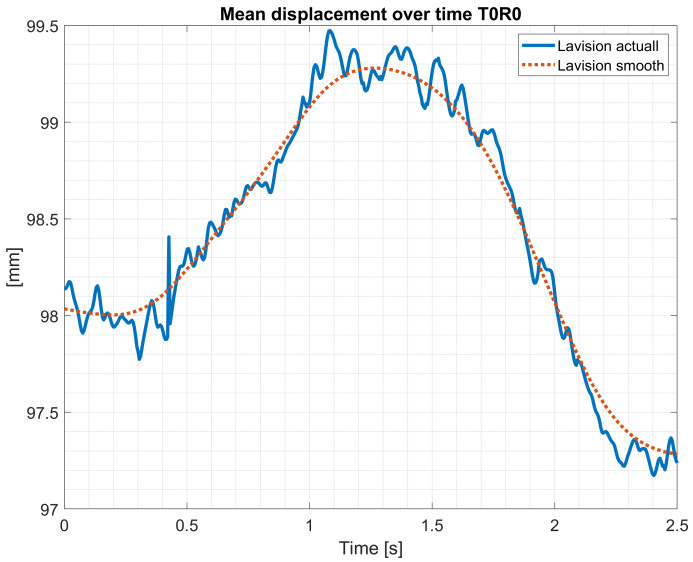

Figure 7.16: Mean displacement over time for T0R0 case

The mean displacement in the FEA model for the last 2.5 s. of simulation time is also calculated to see if the same behavior could be observed in the simulation. This is done for both the isotropic model and the composite model. In figure 7.17, the mean displacement is shown, together with the normalized displacement from the FSI simulation, and the normalized displacement scaled with the range of the displacement. As seen from the figure, similar behavior can be observed when the mean value is normalized. However, once the range of the mean value is taken into consideration, the similarity is lost. The difference in mean displacement over time can be partly some numerical error caused by the criteria of convergence in displacement for taking a time step or that the simulation needs to run for a longer time to settle in. The same plots for all the cases can be found in appendix C.3

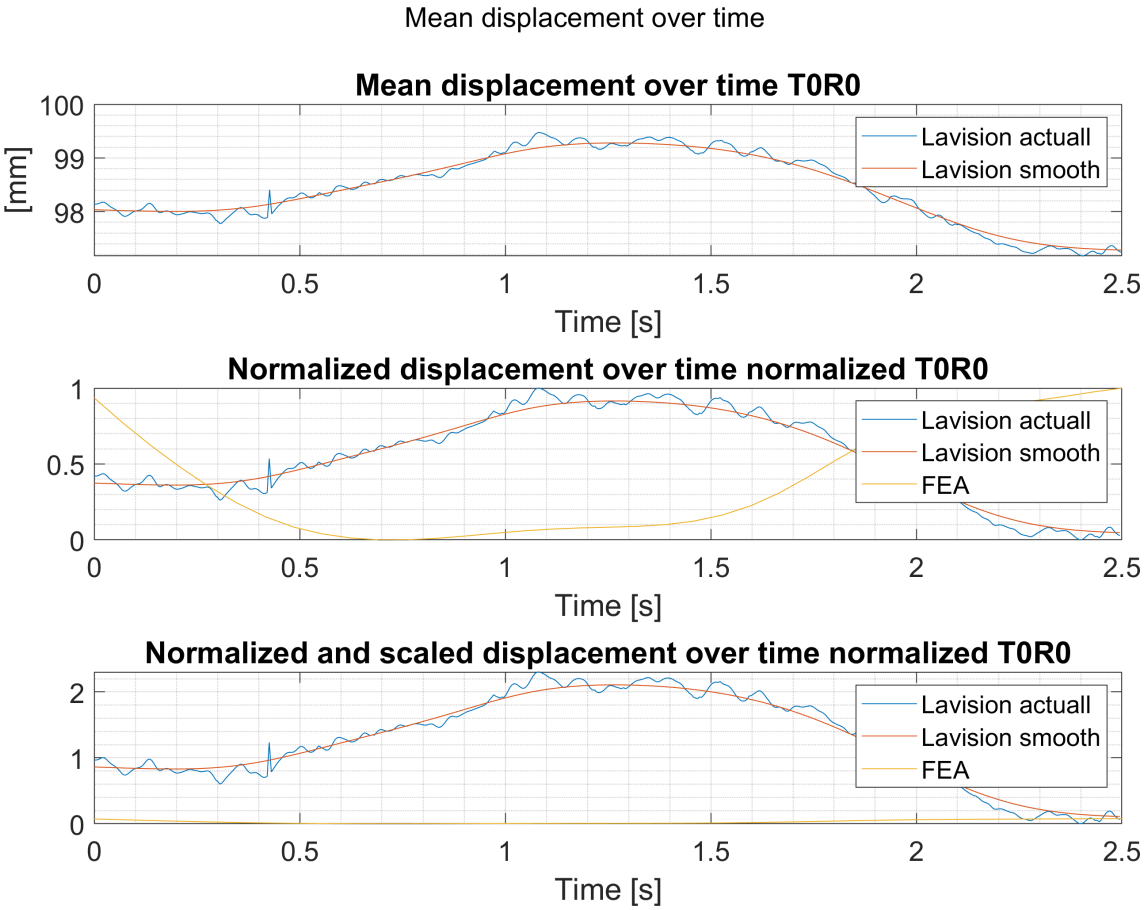

Figure 7.17: Mean displacement, normalized and scaled T0R0 isotropic model

The mean value in displacement from the testing is calculated using MATLAB to compare the displacement over the surface. The data is imported as a point cloud for all the frames for a specific test case, and all the frames are combined into one point cloud. A de-noise function from the package Computer Vision Toolbox (Mathworks, 2021) is applied to the data set to remove any noise that might be present, an example of this is included in figure 7.18 and 7.19. A surface is then fitted to the point cloud.

In figure 7.20, the *Chord* and *Span* values represent the position in the plane of the investigated are presented in section 6.3.2, figure 6.21 and 6.22, and the Z value is the displacement. In figure C.11a, the difference between the test and the simulation is presented, and from the gradient of the contour plot its possible to see that in the test of the hydrofoil, it twisted, increasing the angle of attack in a way that is not reproduced for the isotropic model during the simulations. The difference in angle of attack can be estimated using trigonometry, and it is estimated to be about 1.6° deg for the T0R0 case. In figure 7.20b the new displacement of the surface is presented. From these two figures, it is possible to conclude that the isotropic model is too stiff, and it fails to capture the twist of the hydrofoil. If the model had captured the twist better, the angle of attack would increase, and subsequently, the force excerpted on the foil would increase in the simulation and thus increase the deflection of the hydrofoil.

In figure 7.21, the displacement has been added to the Z position of the hydrofoil. It is worth mentioning that the difference in position is larger than the difference in displacement. Disregarding extreme values close to the leading edge of the hydrofoil (most likely caused by the fitted surface), the difference between the displacement and the position is approximately 2mm. Some of this can be explained by the difference presented in figure 6.25 in section 6.3.2. The rest is assumed to be because of the fitted surface and the error introduced in the DIC equipment when the measured area is not co planar with the calibration plane. (As discovered when comparing the geometry captured by the DIC with the geometry from the CAD and FEA model in section 6.3.2, figure 6.18.)

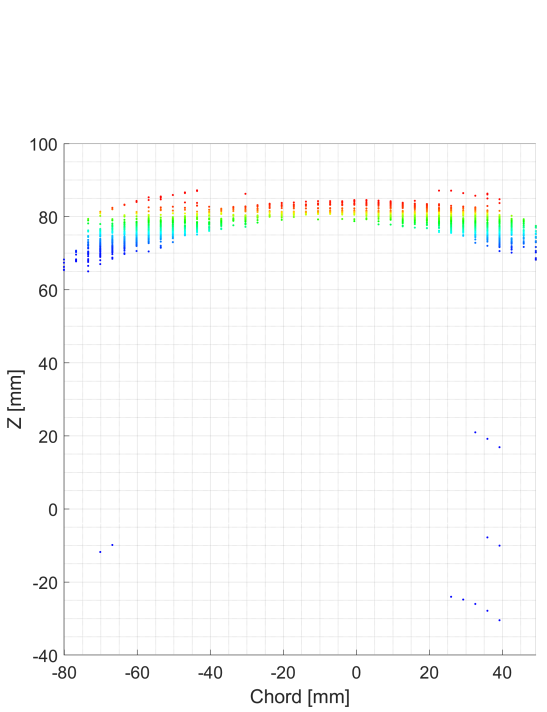

(a) Chord view

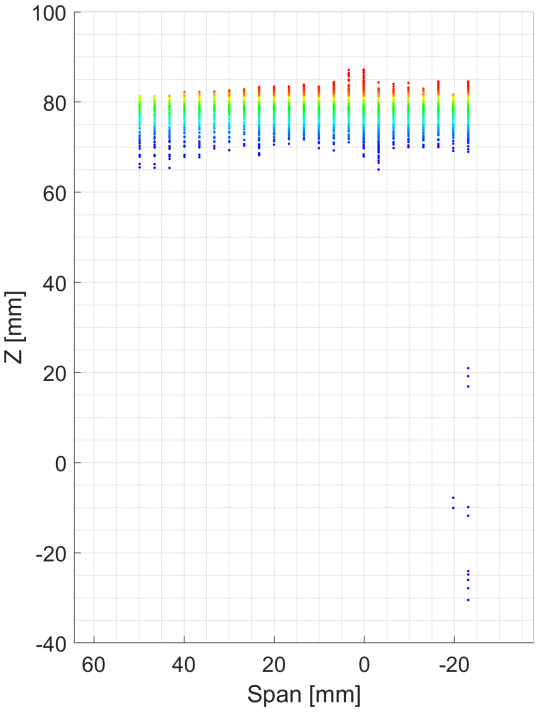

(b) Span view

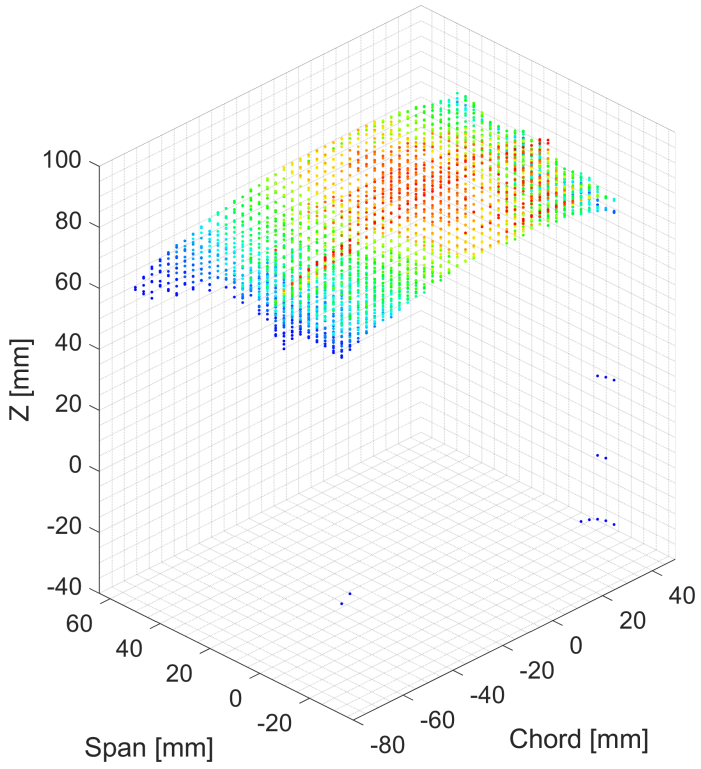

(c) ISO view

Figure 7.18: Example of unfiltered data, test case T2.5R2

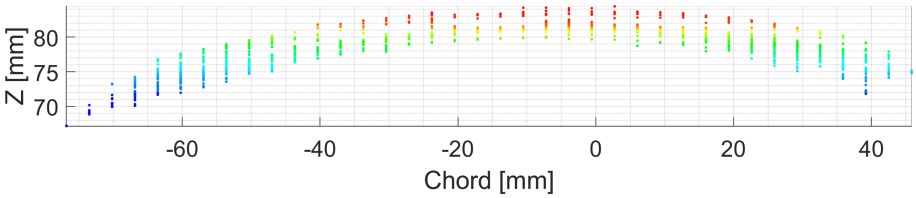

(a) Chord view

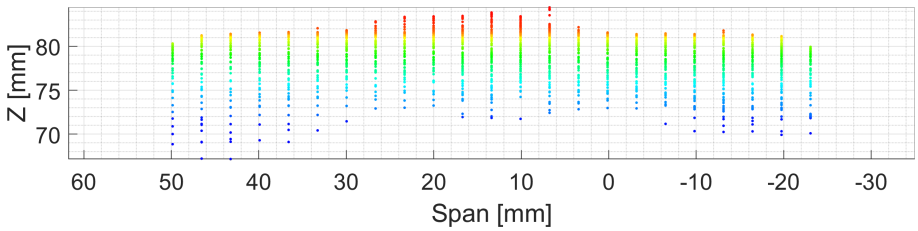

(b) Span view

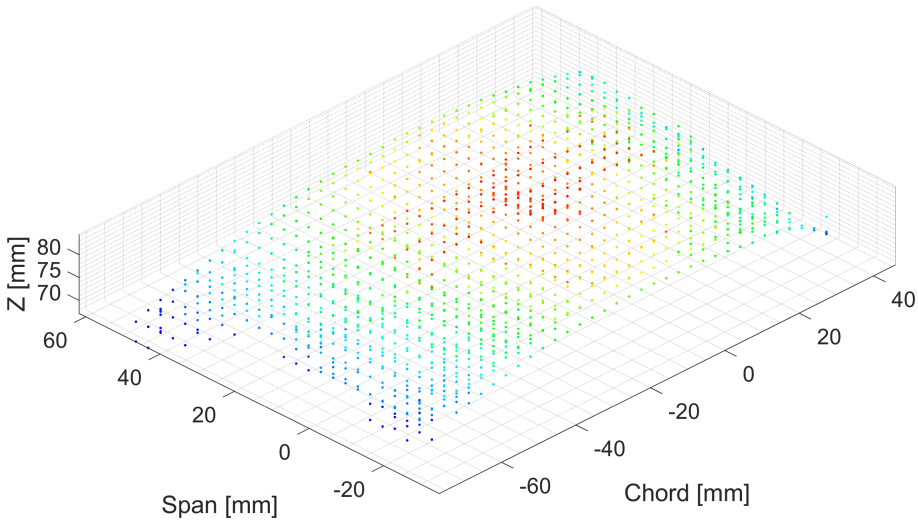

(c) ISO view

Figure 7.19: Example of filtered data, test case T2.5R2

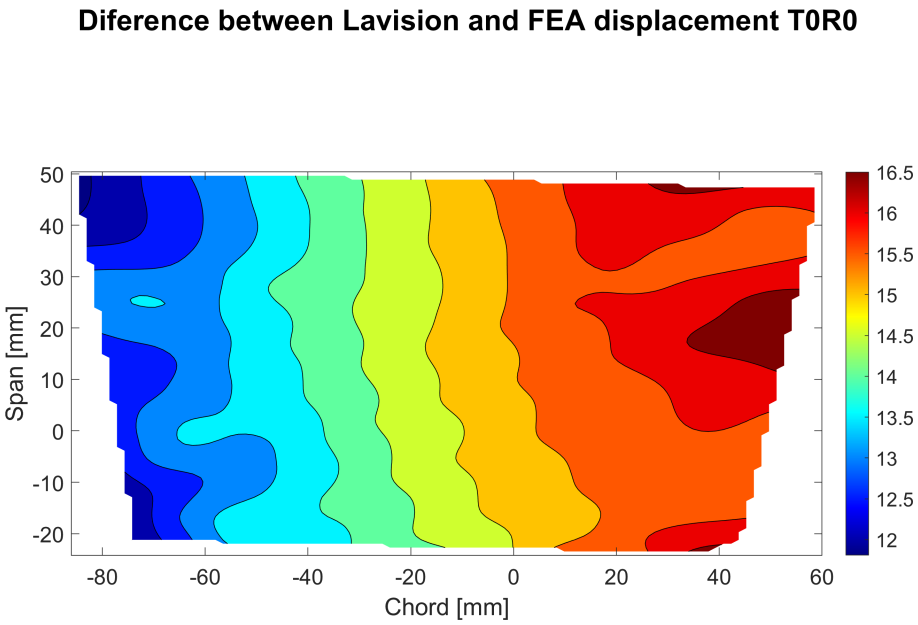

(a) Lavision - FEA displacement T0R0

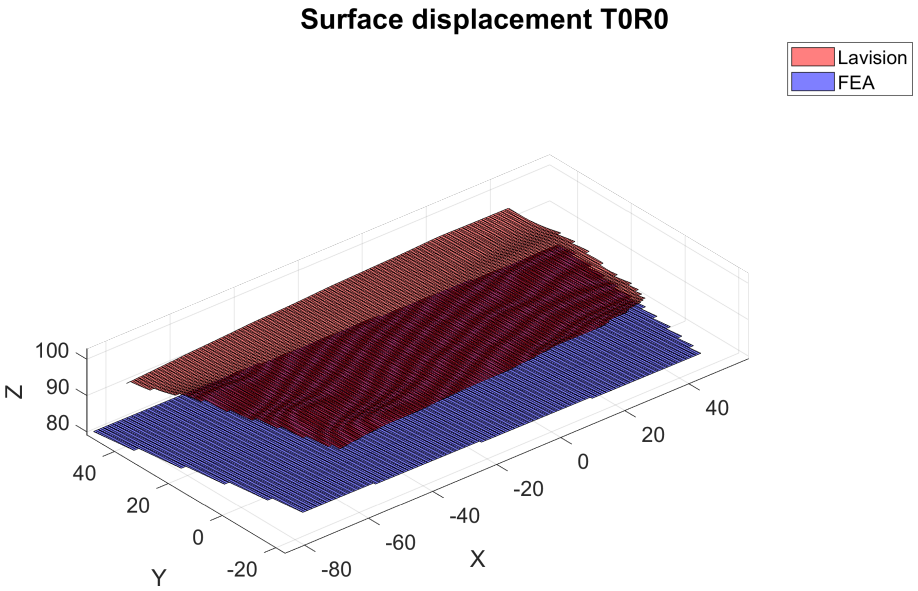

(b) Surface displacement T0R0

Figure 7.20: Simulation case T0R0, isotropic model

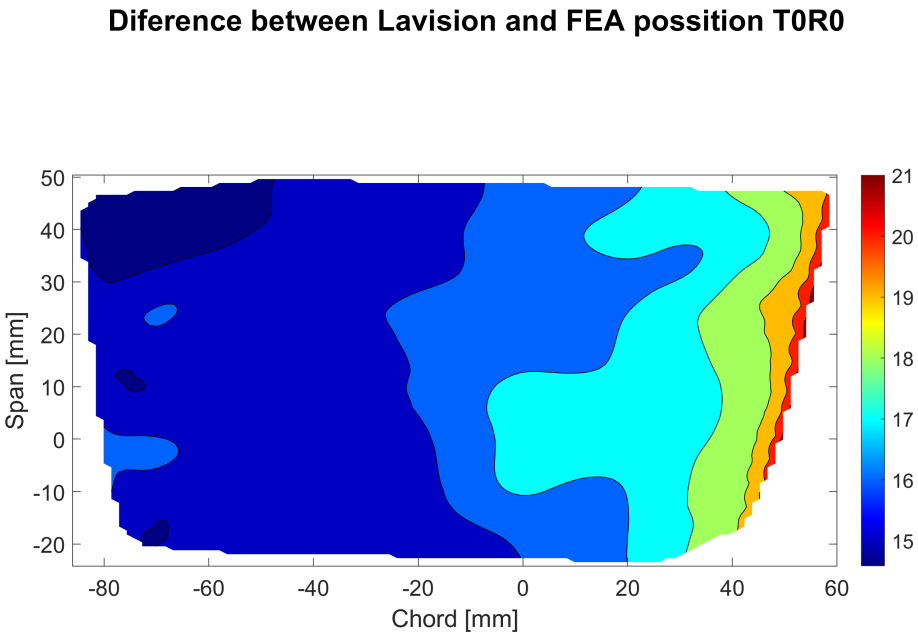

(a) Lavision - FEA possition T0R0

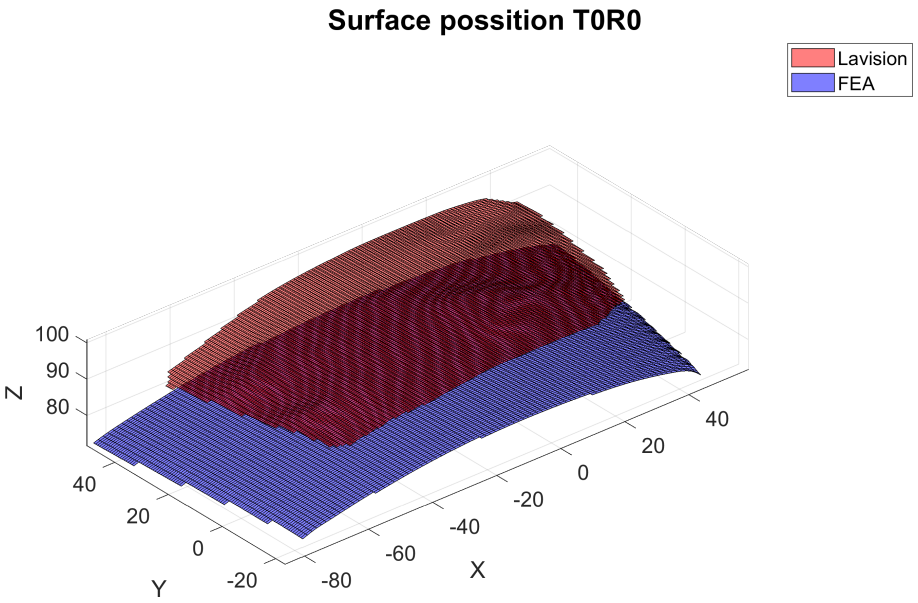

(b) Surface possition T0R0

Figure 7.21: Simulation case T0R0, isotropic model

7.3 Cross section deformation of composite model

To find an explanation for the reduced lift in the composite model compared with the isotopic model, the cross-section of the hydrofoil is investigated. The FEA composite model is loaded into ABAQUS, with the deformation scale set to 10. Then a cut is made in the wing section of the hydrofoil to understand the deformation of the cross-section, as shown in figure 7.22

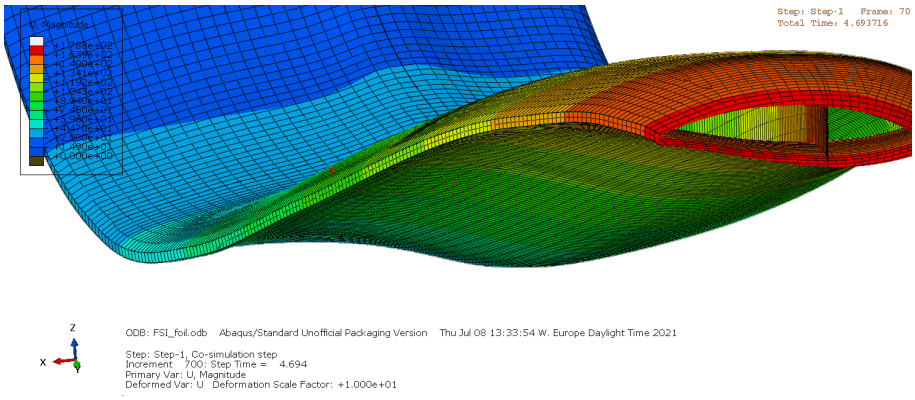

Figure 7.22: Scaled deformation in ABAQUS

As can be seen in figure 7.22, the cross-section of the hydrofoil is heavily deformed. The nodes along a cross-section at 572 mm from the tip are selected. Their position and displacement in the first and last time step of the simulations are exported from ABAQUS to MATLAB for further analysis. In MATLAB the coordinates are transformed from the $[X, Y, Z]$ coordinate system to a new $[X_T, Y_T, Z_T]$ coordinate system, defined together with the position of the cross-section in figure 7.23. The deformed cross-section is plotted together with the undeformed cross-section. In figure 7.24 it is possible to see that the deformed cross-section has a slightly reduced angle of attack while maintaining the overall cross-section to a reasonable degree.

Comparing with the composite model, it is clear that the trailing edge is not stiff enough to cope with the pressure forces acting on it. It deforms by a non-negligible amount and is most likely the culprit of the flow separation on the pressure side along the trailing edge. The deformation in the composite model also causes the hydrofoil to assume a smaller angle of attack, further reducing the lift generated by the hydrofoil.

The reason why the composite model deforms so much more than the isotropic model could be because of the poor out-of-plane properties that are very characteristic of a long fiber composite structure. It could also be that the actual hydrofoil has an internal stiffener that is not included in the numerical model. To reduce the deformation of the cross-section, a more accurate composite model needs to be established with the actual geometry of the internal stiffeners. The deformation for the simulated test cases with both the composite and isotropic model is included in

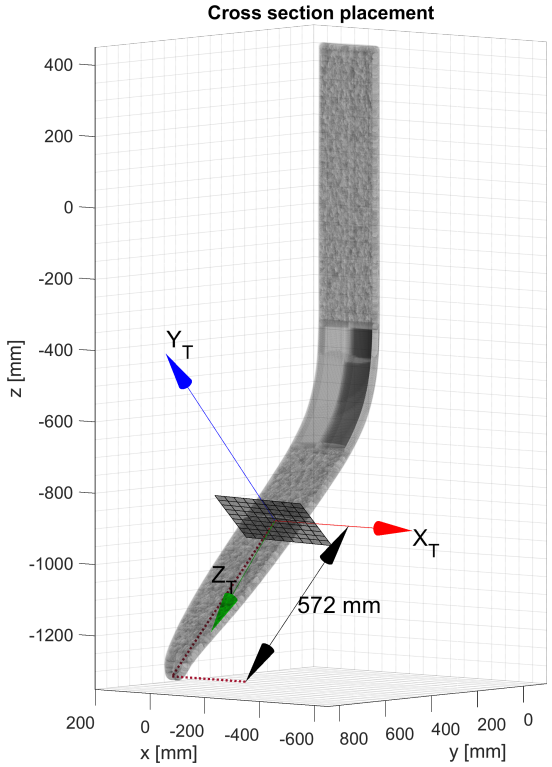

Figure 7.23: Selected cross-section for deeper analysis

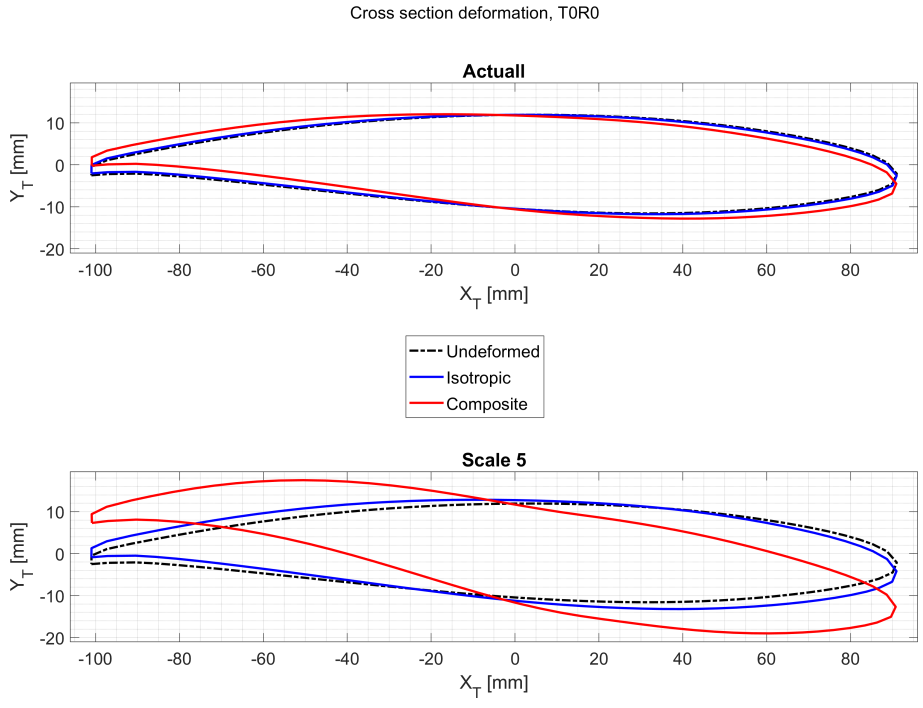

Figure 7.24: Deformed cross section at test case T0R0

appendix C.4.

7.4 Eigenmodes of the structure

Thanks to the contribution of ReVibe Energy, the Eigenmodes of the hydrofoil could also be measured with a commercial device developed by ReVibe Energy. The device, ReLog (ReVibe Energy, 2021), captures the vibrations that it is attached to, and the eigenmodes of a structure can then be calculated in the specialized software Vibinspect, developed by ReVibe.

The foil is held in place using the same milled clamping device that was used in the cavitation tunnel. The aluminum fixture is clamped to a table with a heavy steel tabletop measuring around 2.5cm in thickness using C-clamps. The setup is isolated between the table and the C-clamps using a thick rubber mat to minimize the influence of the table. see figure 7.25d.

The vibrations are recorded from two positions, one close to the clamping device, and on close to the tip, see figure 7.25a to 7.25c. The hydrofoil is then taped lightly with a dead blow hammer to induce a vibration in the hydrofoil, see figure 7.25d.

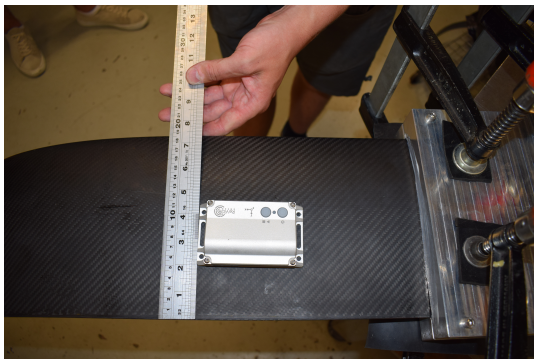

(a) Position of ReLog close to the clamp

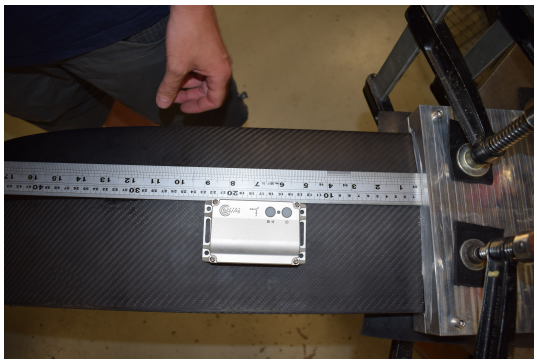

(b) Position of ReLog close to the clamp

(c) Position of ReLog close to the tip

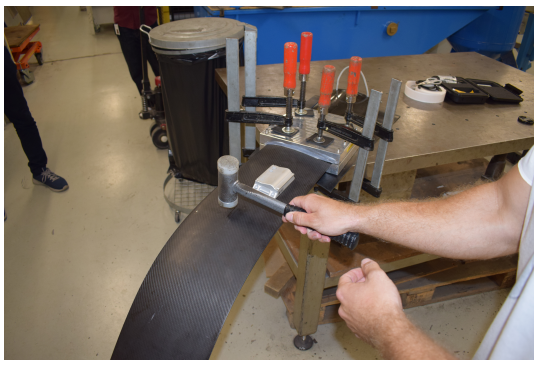

(d) Foil being taped with dead low hammer

Figure 7.25: Process of capturing the eigenmodes of the hydrofoil

Once the measured acceleration is processed in Vibinspect, figure 7.26 is obtained. The figure shows three distinct peaks around 17.6, 71.7, and 164.3 Hz. which indicate the frequencies of the 1st, 2nd and 3rd vibration modes.

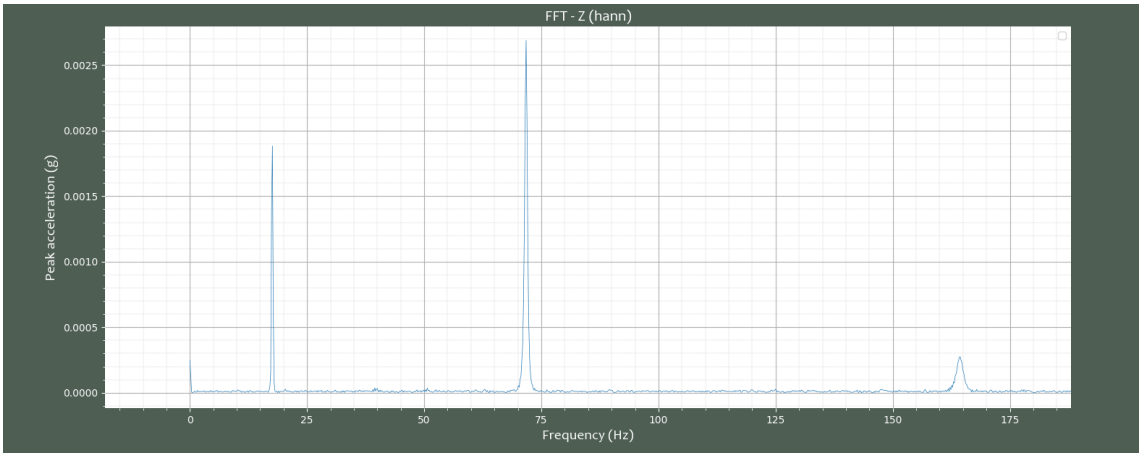

Figure 7.26: Vibration peaks recorded with the ReLog placed close to the fixture shown in figure 7.25d

The eigenmodes of the isotropic and composite model are also analyzed in ABAQUS between 0 to 200 Hz. The result is presented in table 7.2. As can be seen, the results from the composite FEA model for the first three modes are different from the results obtained from the test. The reason for this is believed to be caused by the discrepancy between the internal stiffener in the FEA model and in the actual hydrofoil, a dissimilarity of the composite layup between the FEA model and the actual foil, since the layup will also influence the eigenmodes. The isotropic model is a closer match to the experimental data compared with the composite model. Despite the closer match, it is still a significant difference between the two.

Table 7.2: Eigenmodes from FEA model

Mode	1	2	3	4	5	6	
Isotropic	12.96	31.23	59.95	141.11	OOR	OOR	$[Hz]$
Composite	12.13	19.32	57.75	121.20	142.47	179.19	$[Hz]$
Experimental	17.6	71.7	164.3	N/A	N/A	N/A	$[Hz]$

It should also be stated that the vibration tests were carried out at the end of the project, and no adaptations were made based on the findings from the impact test. The full report from ReVibe Energy can be found in appendix C.5.

8

Suggested improvements

8.1 Geometry

The geometry obtained after the refinement carried out based on the 3D scan is very accurate to the real hydrofoil. There is, however, still room for improvement. Especially for the internal structure of the hydrofoil that is currently only estimated with a plate member. To obtain the geometry of the internal stiffener either input from the the manufacturer is needed, or alternatively, the hydrofoil could be cut open to inspect the internal structure.

8.2 Structural model

The structural model is using shell elements. It would be interesting to quantify the difference, if any, between a shell model and a model using a different type of element.

The composite layup used in the simulations is estimated based on static load tests of the hydrofoil. To obtain accurate results from the simulation, the material properties, and the exact layup need to be mimicked. The composite layup could either be provided by the manufacturer or be obtained by extensive destructive testing.

Assuming a better model of the composite layup and the internal stiffener is established, the stress in the material should be analyzed together with the failure criteria. Without a better-defined model of the aspects mentioned earlier, such an analysis can merely be considered an academic exercise and would not give any meaningful result.

It would also be of great interest to investigate different materials, such as bio-based composites, different composite layups, and even internal structures. Alternatively, how the foil would perform using a foam or wood core rather than a internal composite structure.

8.3 Co-simulation

Running the full test matrix for the both CFD models would be interesting to obtain to cover all different combinations of the Leeway and Rake angels and thus be more accurate in the validation.

Throughout the study, coupling between STAR-CCM+ and ABAQUS was preformed to obtain the FSI of the NACRA17, although it should be mentioned that carrying out a FSI simulations in one of the softwares only is possible. However, running FSI simulations within the the same code might have some limitations. It would be interesting to further investigate the possibility to run within the same code, which could be beneficial to reduce the complexity of connecting the two codes.

8.4 Validation and results

From the tests, a variation in the force and deflection was detected. The same variation is not reproduced in the simulations. Why the same behavior was not captured in the simulations is not known currently. One theory is that the convergence criteria for the displacement of the hydrofoil masked this behavior or that that the CFD model fails to capture some aspect of the flow. Another theory is that the CFD model assumes a smooth inflow to the domain. In reality, the flow in the cavitation tunnel could have some turbulence or motions that are not included in the CFD model.

s why
known?

Given the budget, it would be beneficial to test in the towing tank to obtain test data with the free water surface, allowing for the validation of the free surface model.

It would also be interesting to test with two hydrofoils, to establish if they have any significant interaction between the pair of hydrofoils. The interaction of the hydrofoil and the rudder is also an aspect that could be investigated if the budget allows it.

9
Conclusions

When carrying out FSI simulations, both the accuracy of the CFD and FEA model is essential. The fact that there are three significant unknown aspects of the hydrofoil from a structural perspective. The material used, the composite layup, and the internal structure all contribute to poor accuracy for the structural computed response of the hydrofoil, primarily the heavily deformed cross-section of the composite model. These problems with the structural models are unfortunately not isolated to the FEA model. Since the deformed hydrofoil updates the geometry in the FSI simulation, it also changes the flow around the hydrofoil and thus affects the overall performance.

With the given prerequisites for the project, an unknown geometry, composite layup, material, and internal structure, caused by not having input from the manufacturer and limitations of not doing any destructive testing, the isotropic model is still considered to be reasonably accurate and can be used to capture the most important aspects in a FSI simulation. It is possible that with more time, a method of trial and error could be used to achieve a more accurate FEA model without resorting to destructive testing. The accurate reconstruction of the hydrofoil's geometry is possible thanks to the 3D scanning of the actual hydrofoil. However, it would still be preferable to obtain the geometry from the manufacturer since it is both costly and time-consuming to re-create a complex free-surface model of the hydrofoil.

Since the simulations required for FSI problems are very computationally heavy, it is of out most importance to ensure that enough resources are available for the simulations. One unforeseen problem that occurred during the project was that the computing cluster performs the computation across multiple nodes[1] if more than 32 CPU cores are requested for a simulation. (It is desired to use at least 128 CPU cores for the simulations.) At first the cross node communication between ABAQUS and STAR-CCM+ did not work, but with help from the technical support at Tetralith a solution was found and implemented. However, after a firmware update to the cluster the solution stopped working. The result of this is that one simulation took about 14 to 16 days to complete. It is advised that any continuation of the project ensures that the computing resource used for the simulations does not encounter the same problem.

The testing carried out at SSPA makes it possible to validate the numerical models

[1] A node refers to one computer in the computer cluster, that is the collection of computers that make up the super computer

and offered valuable experience in post-processing test data. However, the facilities at SSPA are primarily intended to do scale model experiments of ships and their appendices. Because of this, the size of the cavitation tunnel is large enough to conduct full-scale experiments, a luxury seldom seen in the marine industry.[2] The information about the hydrofoil obtained during the testing at SSPA, should be used to validate any refinement made of the numerical models, assuming a continuation of the project.

If a continuation of the project is to be carried out, a better understanding of the hydrofoil structure would be the most important and obvious step. Either by destructive testing to obtain the material properties and layup, x-ray to determine the internal structure. However, the preferred option would be a collaboration with the manufacturer of the *NACRA 17*. This would alleviate our successors from some of the mysteries regarding the structure of the hydrofoil.

[2]The benefit of carrying out full-scale experiments is that no scaling for Froude number, Raynold's number, cavitation number, or Weber numbers have to be taken into consideration.

Bibliography

ABAQUS documentation. (2021). *Solid (continuum) elements*. https://abaqus-docs.mit.edu/2017/English/SIMACAEELMRefMap/simaelm-c-solidcont.htm

ANSYS. (2021). *Granta EduPack*. https://www.ansys.com/products/materials/granta-edupack

Artec 3D. (2021). *Artec Eva*. https://www.artec3d.com/portable-3d-scanners/artec-eva

Bazilevs, Y., Takizawa, K., & Tezduyar, T. E. (2013). *Computational fluid-structure interaction: methods and applications*. John Wiley; Sons.

Bhaqwan, D. A., Lawrence, J. B., & Chandrashekhara, K. (2018). *Analysis and performance of fiber composites*. John Wiley; Sons, Inc.

Caminha, G. (2019). *The CFL Condition and How to Choose Your Timestep Size*. https://www.simscale.com/blog/2017/08/cfl-condition/

Chapman, D. R. (1979). Computational aerodynamics development and outlook. *AIAA*, *17*(12), 1293–1313.

CloudCompare. (2021). *3D point cloud and mesh processing software Open Source Project*. https://www.danielgm.net/cc/

Donea, J., Giuliani, S., & Halleux, J. P. (1982). An arbitrary Lagrangian-Eulerian finite element method for transient dynamic fluid-structure interactions. Computer methods in applied mechanics and engineering. *Elsevier Ltd*, *33*, 689–723.

Eça, L., & Hoekstra, M. (2014). A procedure for the estimation of the numerical uncertainty of CFD calculations based on grid refinement studies. *Journal of computational physics*, *262*, 104–130.

Fédération Internationale de l'Automobile (FIA). (2020). *2021 Formula 1 Technical Regulations1 16 December 2020*. https://www.fia.com/sites/default/files/2021_formula_1_technical_regulations_-_iss_7_-_2020-12-16.pdf

Giovannetti, L. M. (2017). Fluid structure interaction testing, modelling and development of Passive Adaptive Composite foils.

Laney, C. B. (1998). *Computational gasdynamics*. Cambridge university press.

Lawrence Barretto. (2021). *Flexi wings What are they and why is everyone talking about them?* https://www.autosport.com/f1/news/banned-flexible-wings-in-formula-1-4982063/4982063/

Mathworks. (2021). *Computer vision*. https://se.mathworks.com/products/computer-vision.html

Nacra17.org. (2021). *Nacra 17 daggerboard templates*. https://nacra17.org/daggerboard-templates/

photomodeler.com. (2021). *Factors Affecting Accuracy in Photogrammetry*. https://www.photomodeler.com/kb/factors_affecting_accuracy_in_photogramm/

ReVibe Energy. (2021). *ReLog specifications*. https://revibeenergy.com/product-overview-relog/#detailed

Siemens. (2020). *STAR-CCM+ Documentation. Siemens PLM Software*.

Sigrist, J. F. (2015). *Fluid-structure interaction: An introduction to finite element coupling*. John Wiley; Sons.

Wendt, J. F. ((2008). *Computational fluid dynamics: An introduction*. Springer Science; Business Media.

Wikipedia. (2021). *Nacra 17*. https://en.wikipedia.org/wiki/Nacra_17

Xiaodong (Sheldon) Wang. (2008). *Fundamentals of fluid-solid interaction*. Elsevier B.V.

Zienkiewicz, O. C., Taylor, R. L., & Nithiarasu, P. (2014). *The finite element method for fluid dynamics - 7th edition*. Elsevier Ltd.

A

Geometry

A.1 Geometry

A.1.1 3D-scanning

TECHNICAL SPECIFICATIONS

3D point accuracy, *up to*	0.1 mm
3D resolution, *up to*	0.2 mm
3D accuracy over distance, *up to*	0.1 mm + 0.3 mm/m
HD Mode	Yes
Working distance	0.4 – 1 m
Linear field of view, *H×W @ closest range*	214 × 148 mm
Linear field of view, *H×W @ furthest range*	536 × 371 mm
Angular field of view, *H×W*	30 × 21°
Ability to capture texture	Yes
Texture resolution	1.3 mp
Colors	24 bpp
3D reconstruction rate, *up to*	16 fps
Data acquisition speed, *up to*	18 mln points/s
3D exposure time	0.0002 s
2D exposure time	0.00035 s
3D light source	Flash bulb
2D light source	White 12 LED array
Interface	1 × USB 2.0, USB 3.0 compatible
Calibration	No special equipment required

Computer requirements

Supported OS	Windows 7, 8 or 10 x64
Recommended computer requirements	Intel Core i7 or i9, 64+ GB RAM, NVIDIA GPU with CUDA 6.0+ and 8+ GB VRAM
Minimum computer requirements	**HD:** Intel Core i7 or i9, 32 GB RAM, NVIDIA GPU with CUDA 6.0+ and 2 GB VRAM **SD:** Intel Core i5, i7 or i9, 12 GB RAM, GPU with 2 GB VRAM

Output formats

3D mesh formats	OBJ, PLY, WRL, STL, AOP, ASC, PTX, E57, XYZRGB
CAD formats	STEP, IGES, X_T
Formats for measurements	CSV, DXF, XML

Power source and dimensions

Power source	AC power or external battery pack
Dimensions, *H × D × W*	262 × 158 × 63 mm
Weight	0.9 kg / 2 lb

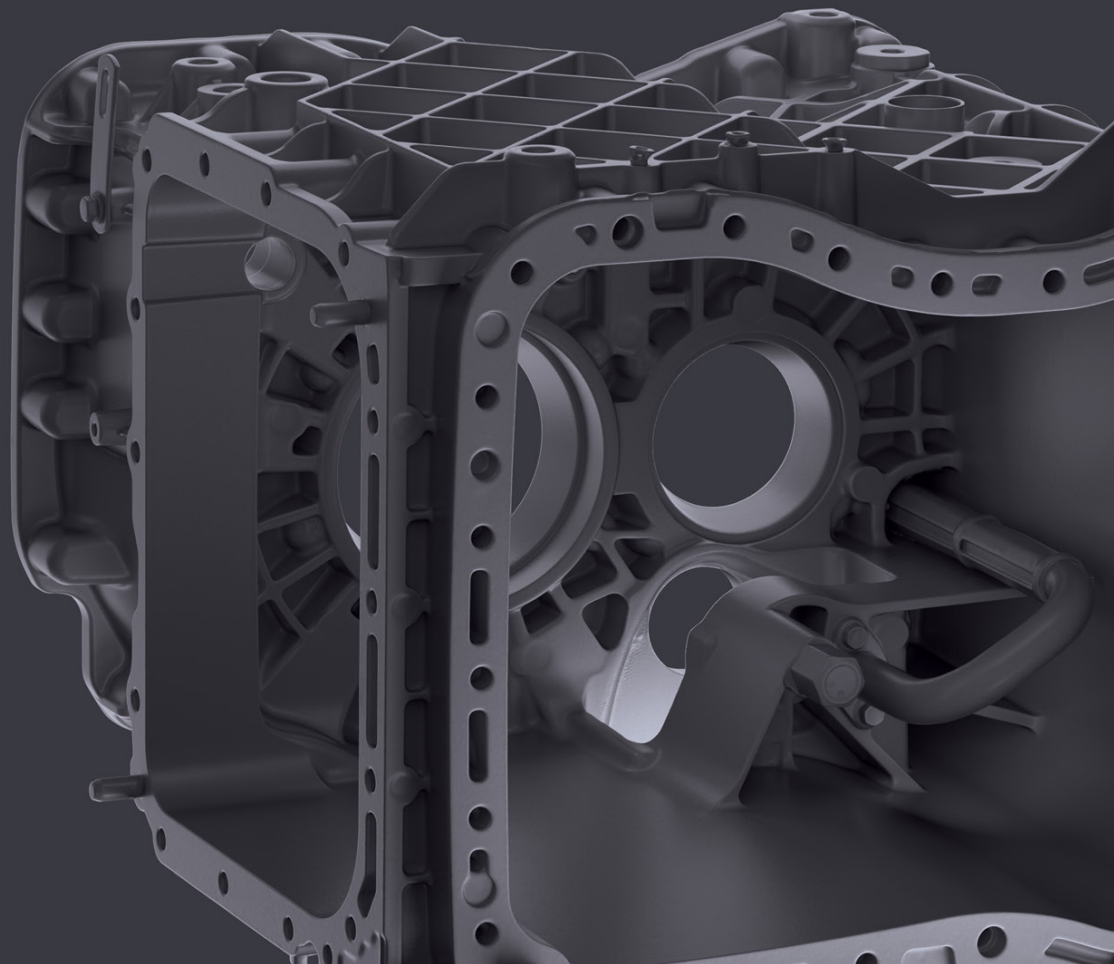

1. General Information

Even with state-of-the-art scanners, it is necessary to apply matting spray in several application cases:

a) *Transparent parts*

As we are dealing with optical technologies, light needs to be reflected off the surface back into the detector of the scanner. In case of a transparent surface, however, the light will go through the surface instead of being reflected by the same. In consequence, the scanner is not able to capture the surface structure.

b) Reflective parts

In case of reflective parts, such as a mirror, the light beams will be reflected in a focused way instead of in a diffused way. This means that the chance of a beam hitting the reflector of the scanner is greatly reduced and the scanner will only capture a fraction of the reflected light beams.

c) Deep Pocket

When the object to be scanned has deep pockets, the scanner receives a reflection from the walls of the pocket onto the bottom. This causes disturbance in the pattern of the light manifesting in the scan as “artefacts” or bad data.

Scanningspray Vertriebs UG
Gersdorffstr. 20a
44225 Dortmund

www.aesub.com
info@aesub.com

d) High quality and accuracy

When quality and accuracy are important, you might want to apply spray to remove as much as possible all the causes like colour differences, differences in reflection, texture, etc.

The use of spray creates a matt, white coat reducing reflection and other inhomogeneities and thus provides perfect scanning condition.

Spaying parts for reverse engineering and prototype parts using traditional permanent pigment spray has become a generally accepted practice. Spraying large volume of parts in production application, however, is problematic due to the pigment-contamination.

In general, matting sprays used in 3D metrology for antireflective coating can be classified into the following two product groups:

Permanent pigment sprays

- surface remains white from pigments after scan
- intensive cleaning required or disposal of scanned object
- pigment-contamination of laboratories, sensors, environments, scanners and users

Vanishing sprays

- coating evaporates automatically after scanning
- no cleaning after scanning required
- no pigment-contamination of laboratories, sensors, environments, scanners and users

2. Value proposition

AESUB® blue is a self-vanishing scanning spray developed by scanning experts. The spray evaporates within a few hours without leaving any residues, meaning that there is no need for cleaning after scanning. Unlike traditional sprays, AESUB® blue does not contain pigments and thus avoids pigment-contamination of sensitive areas, such as laboratories and production sites, equipment and users. You can therefore apply AESUB® blue directly on spot of scanning without any costly transport to avoid said pigment-contamination in sensitive areas. Overall, AESUB® blue greatly increases efficiency and productivity within the measuring processes.

AESUB® blue characteristics are:

- residue-free sublimation
- layer thickness of ~8-15 µm
- consistent and homogenous coating
- optimized material compatibility

AESUB® blue forms a thin layer of white, homogeneous coating resulting in ideal conditions for optical scanning. AESUB® blue contains active substances, propellant and solvent and has

Scanningspray Vertriebs UG
Gersdorffstr. 20a
44225 Dortmund

www.aesub.com
info@aesub.com

been optimized with regards to material compatibility. Independent analyses certify that AESUB® blue sublimates without leaving any residues on the surface of the scanned object. See the safety data sheet (https://aesub.com/download) for further information.

3. Areas of application

AESUB® blue facilitates and enables optical digitization in a wide variety of industrial sectors and range of applications:

- automotive
- engineering
- aerospace
- energy sector
- medical sector
- architecture
- plastic design / art
- digital archiving
- reverse engineering
- optical metrology
- research and development
- process monitoring
- inlinescanning
- measurement services
- surface inspection

4. Material compatibility

Material compatibility for specific applications cannot guaranteed. Users should check specific material compatibility before use. AESUB® blue contains solvents. See the safety data sheet (https://aesub.com/download) for further information.

5. Layer thickness

The layer thickness of AESUB® blue ranges between 5 µm and 15 µm depending on the user-specific application.

Scanningspray Vertriebs UG
Gersdorffstr. 20a
44225 Dortmund

www.aesub.com
info@aesub.com

6. Surface coating

AESUB® blue forms a consistent and very homogeneous coating on the surface of the object to be scanned. The figure below provides a surface comparison between AESUB® blue (left) and a vanishing spray previously used in measurement technology (right). The measurement shows a 3D scan of a glass sphere with a diameter of approx. 130 mm.

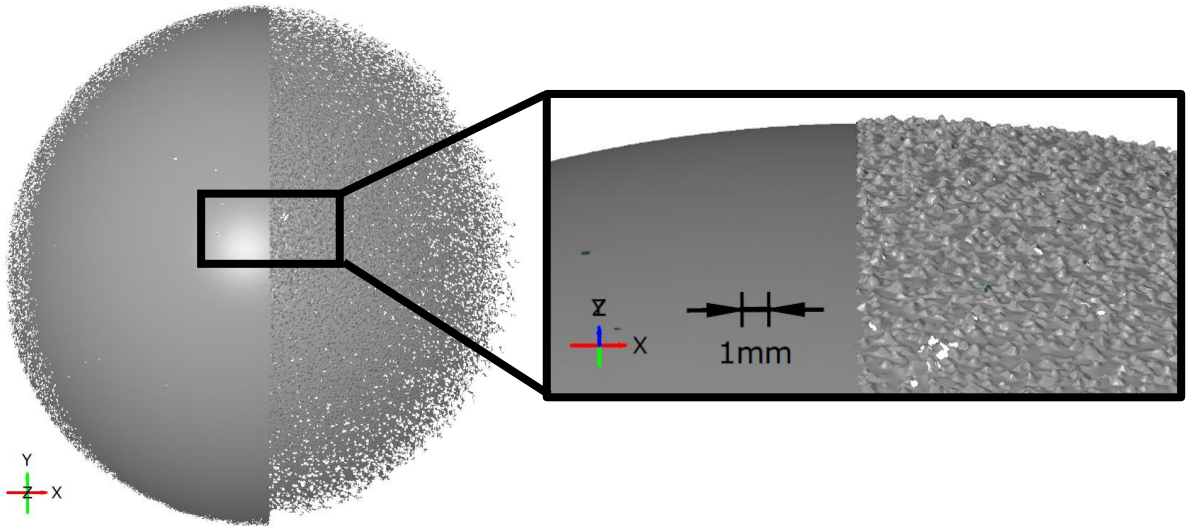

Figure 1: Surface comparison AESUB® blue vs. CCD

7. Application

Apply AESUB® blue from 15-20 cm away. Spray over the entire surface that you will be scanning. Gently push down the spray button and move the can across the area using even, back and forth strokes. Move at a consistent pace without pausing at one point to achieve an even coat. Once the coat is applied, you can scan the object in usual manner. Unlike traditional pigment spray, the applied coat of AESUB blue sublimes after scanning and thus eliminates the need for complex cleaning after use.

AESUB® blue is applied "wet". The solvent vanishes within a few seconds while the active substance remains as coat on the surface. The degree of whiteness of the coat still increases during the evaporation process of the solvent, which, however, does not affect scanning directly after application of AESUB® blue.

Increase spraying distance or pace in case of drop formation or when coat remains "wet" for too long. Note that multiple spraying increases layer thickness. The ideal ambient temperature is 21°C/66.2°F.

Do not spray on an open flame or other ignition. Use only outdoors or in well-ventilated areas. Protect from sunlight. Do not use on products intended for contact with food - exclude food

Scanningspray Vertriebs UG
Gersdorffstr. 20a
44225 Dortmund

www.aesub.com
info@aesub.com

contact. Also read carefully the safety instructions in the associated safety data sheet (https://aesub.com/download).

8. Sublimation of AESUB® blue

The sublimation time of AESUB® blue is less than 4 hours and depends largely on the following five factors:

a) Temperature

- high ambient temperatures shortens sublimation time
- low ambient temperatures extends sublimation time

b) Airflow

- ventilation shortens sublimation time

c) Surface structure

- uneven surface structures extend sublimation time
- even surface structures shorten sublimation time
- sublimation starts at exposed areas, such as outer corners or edges

d) Material

- sublimation time also depends on the material to which AESUB® blue is applied: Sublimation starts earlier on plastics and later an metals

e) Layer thickness

- Higher layer thickness extends sublimation time

Empirical tests show that objects treated with AESUB® blue remain scannable for approximately 1 hour. Scan-time can be easily extended by re-applying AESUB® blue at individual contours when sublimation commences and by spraying several layers. Increase temperature and / or air ventilation in case you want to accelerate the sublimation process.

9. Residue analysis

Independent experts examined AESUB® blue for potential residues and came to the following conclusion:

AESUB® blue provides neither recognizable nor measurable residues and can thus be regarded as residue-fee

Please find the entire report at https://aesub.com/download and note that we do not guarantee the complete sublimation of AESUB® blue.

Scanningspray Vertriebs UG
Gersdorffstr. 20a
44225 Dortmund

www.aesub.com
info@aesub.com

10. Further Information

a) Storage

- optimal storage temperature ranges between 18°C and 21°C
- shelf life of three years
- store at dry conditions with no direct sunlight

b) Risk information center

- If you feel unwell after use please call the 24-hours emergency number +49 (0) 761/192 40 for assistance.

You will find further information our website (https://aesub.com) and in particular in the safety data sheet (https://aesub.com/download).

Disclaimer

The above information was prepared carefully. We, however, cannot be held liable for any incorrect or incomplete information.

Scanningspray Vertriebs UG
Gersdorffstr. 20a
44225 Dortmund

www.aesub.com
info@aesub.com

A.1.2 CloudCompare

A.1.2.1 Initial geometry

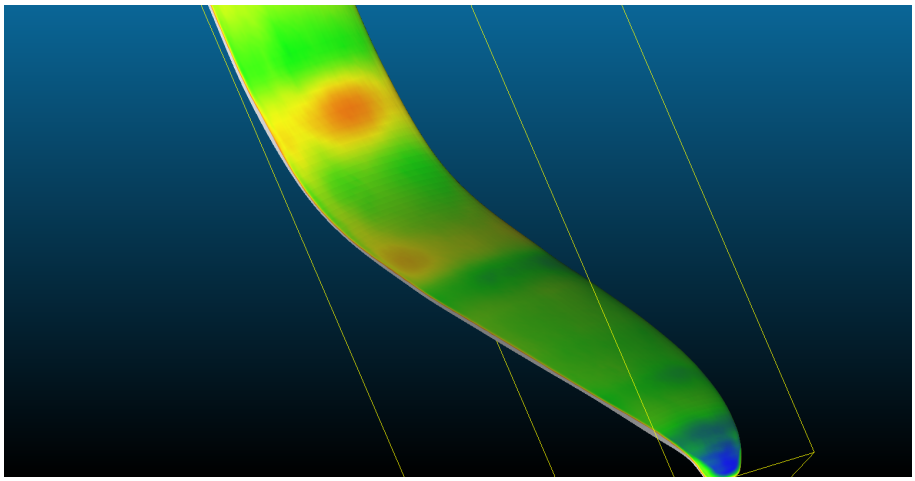

Figure A.1: Comparison of the scanned geometry and the initial geometry around the knee

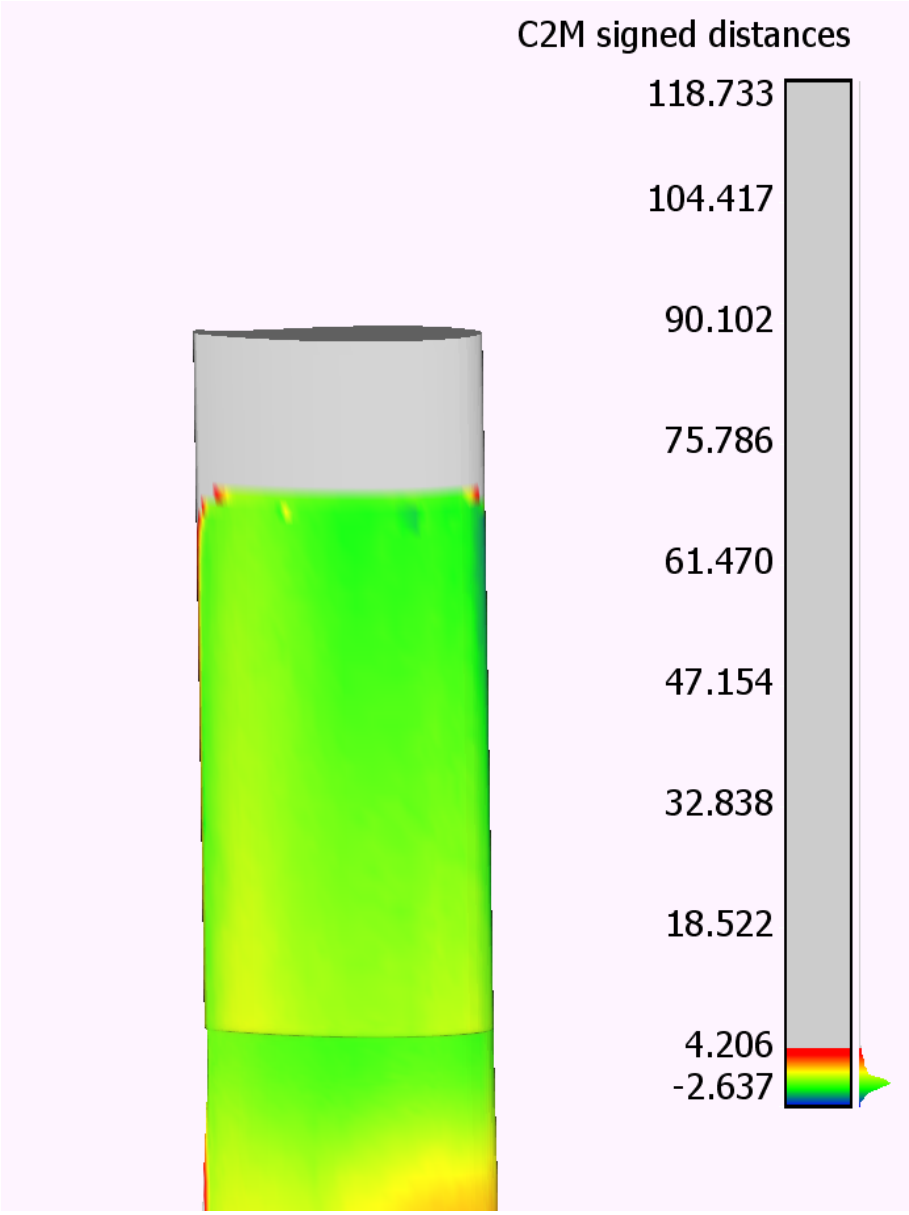

Figure A.2: Comparison of the scanned geometry and the reverse engineered geometry around the top

A.1.2.2 First draft based on 3D-scan

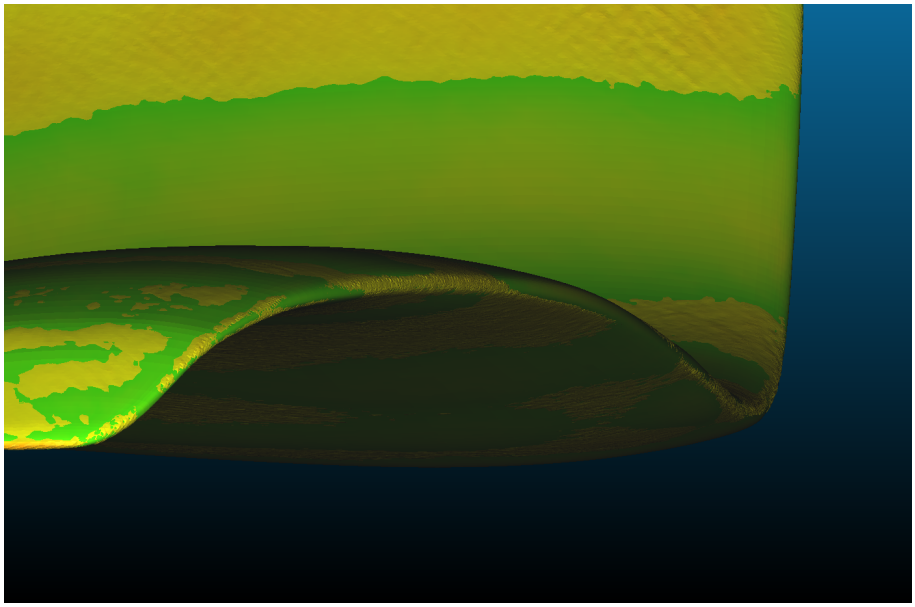

Figure A.3: Comparison of the scanned geometry and the initial reverse engineered geometry around the leading edge

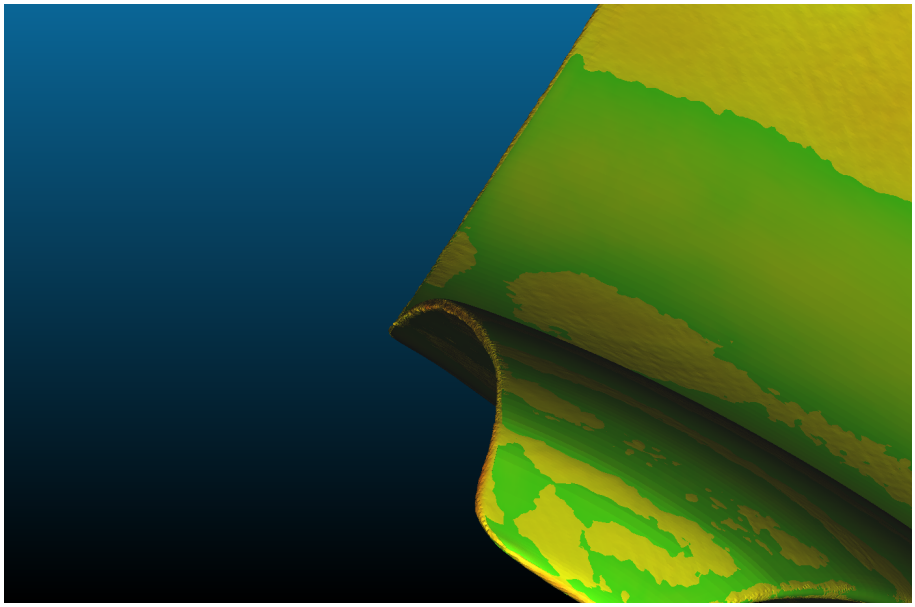

Figure A.4: Comparison of the scanned geometry and the initial reverse engineered geometry around the trailing edge

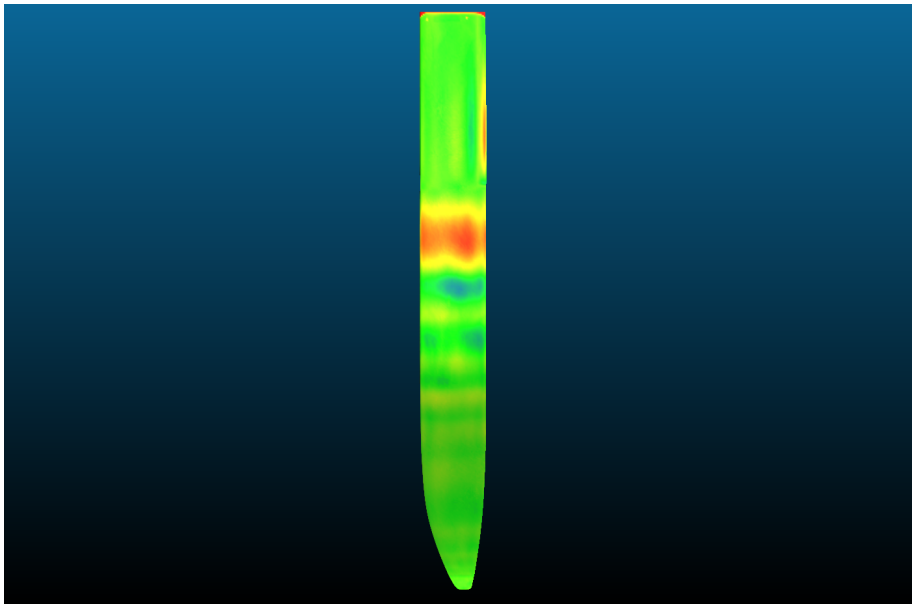

Figure A.5: Comparison of the scanned geometry and the initial reverse engineered geometry around the pressure side

A.1.2.3 Final geometry

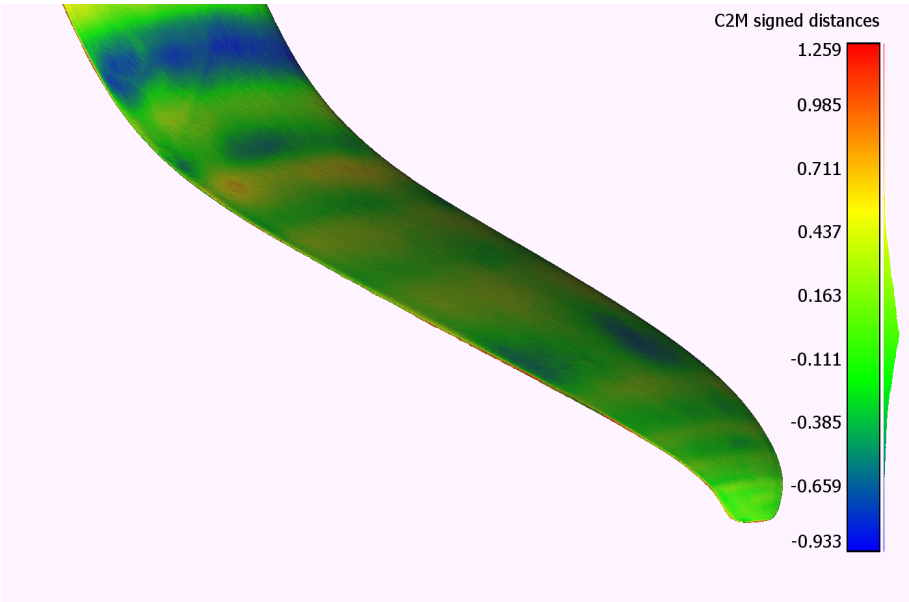

Figure A.6: Comparison of the scanned geometry and the reverse engineered geometry around the tip and the trailing edge

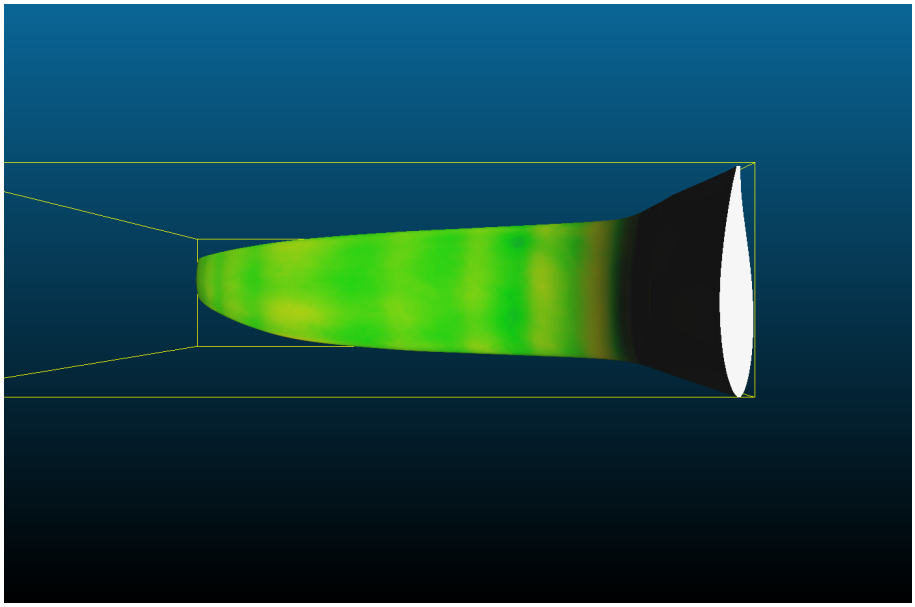

Figure A.7: Comparison of the scanned geometry and the reverse engineered geometry, top view

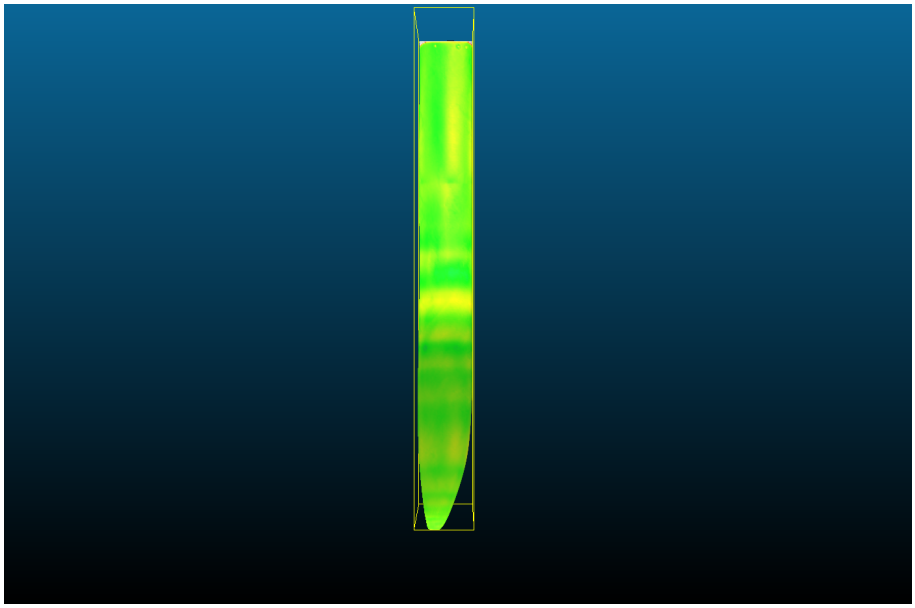

Figure A.8: Comparison of the scanned geometry and the reverse engineered geometry, suction side

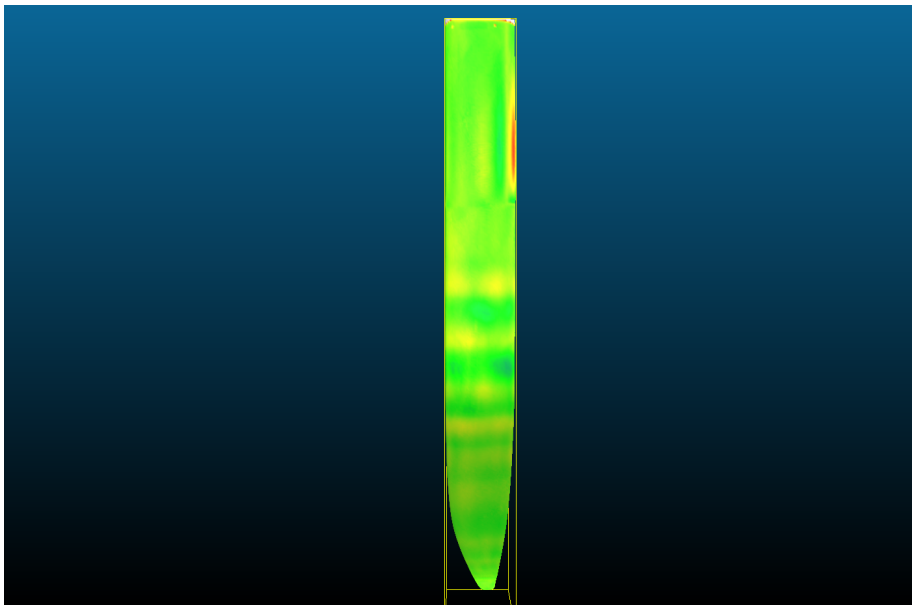

Figure A.9: Comparison of the scanned geometry and the reverse engineered geometry, pressure side

B

Structural model

FloatBarrier

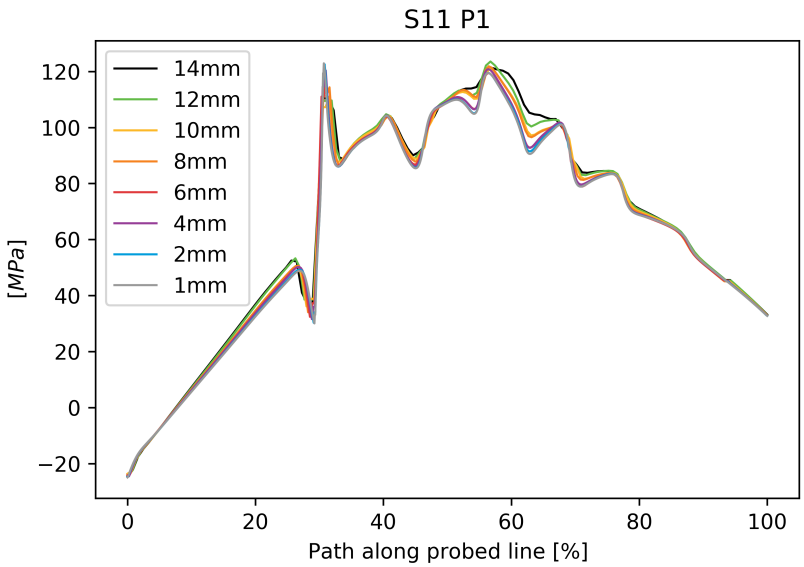

Figure B.1: σ_{11} Ply 1

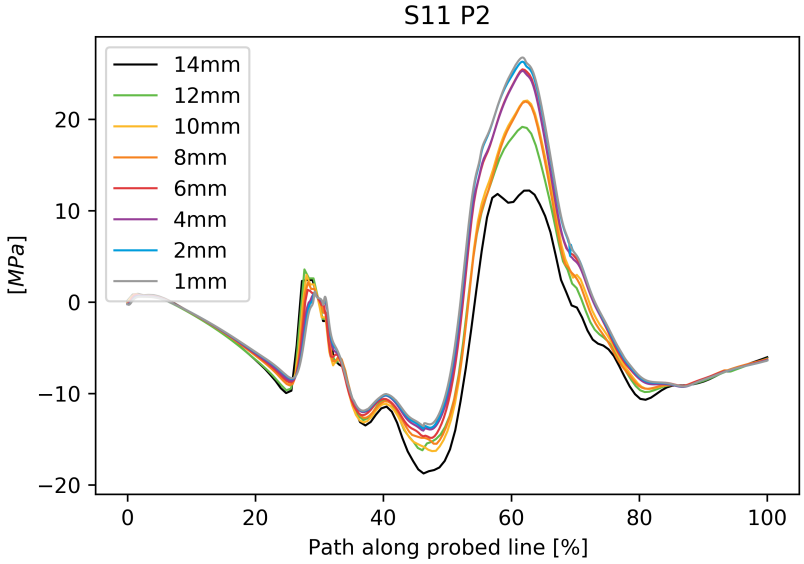

Figure B.2: σ_{11} Ply 2

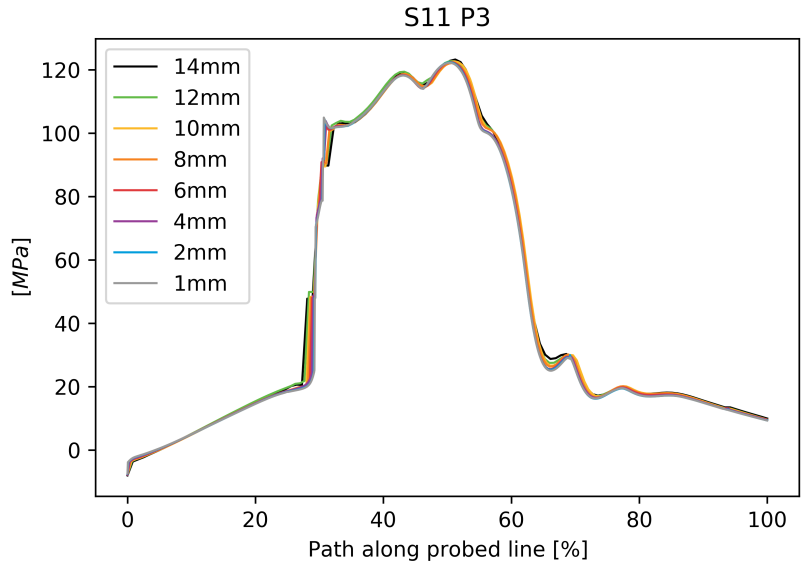

Figure B.3: σ_{11} Ply 3

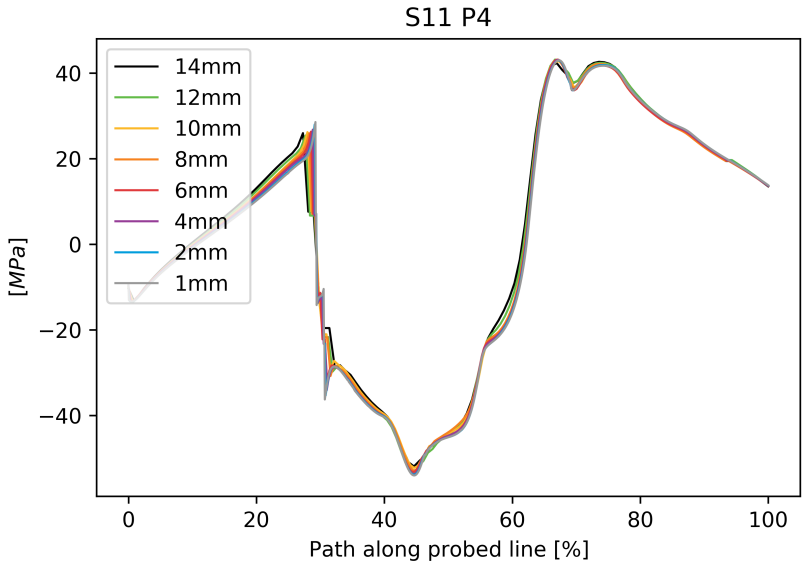

Figure B.4: σ_{11} Ply 4

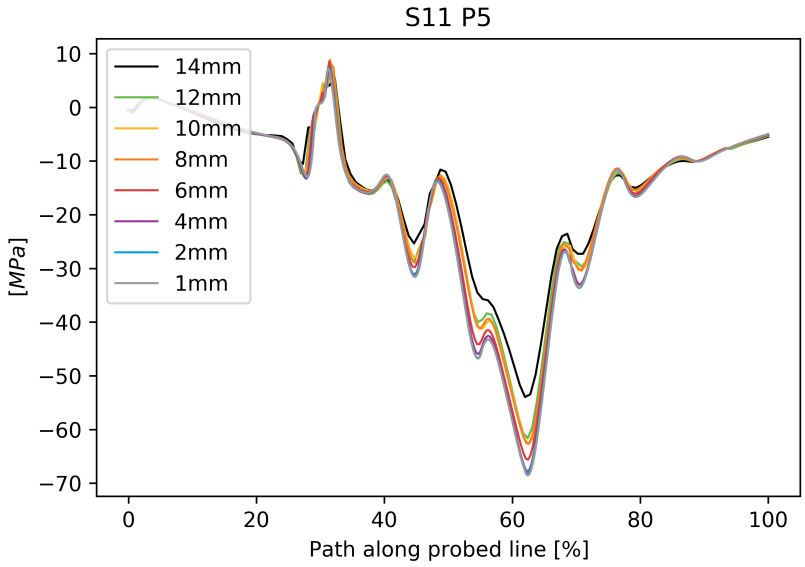

Figure B.5: σ_{11} Ply 5

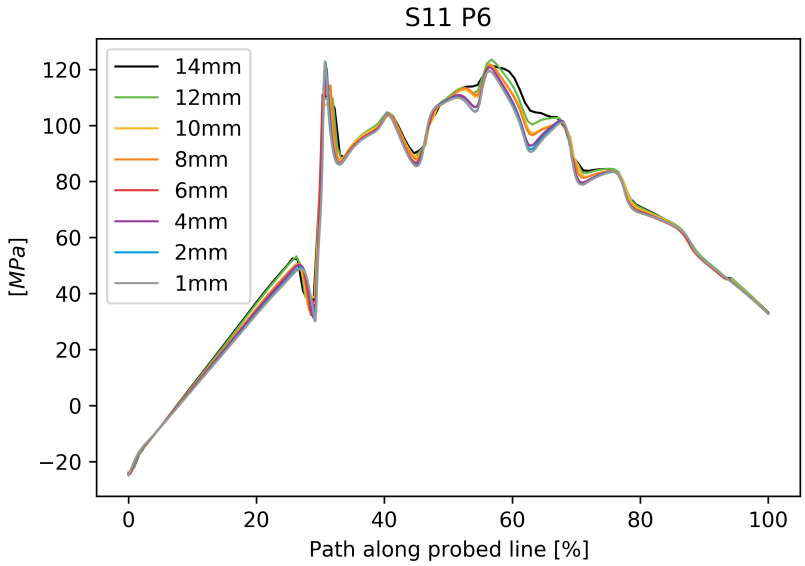

Figure B.6: σ_{11} Ply 6

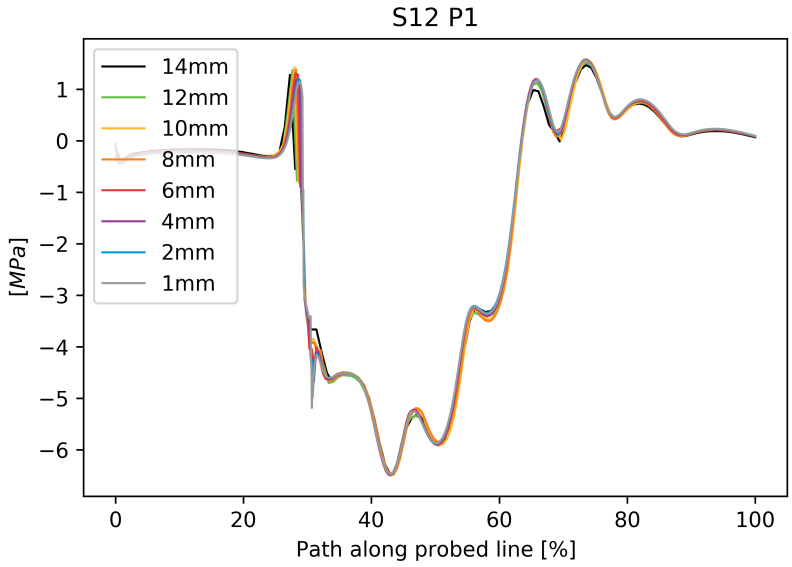

Figure B.7: σ_{12} Ply 1

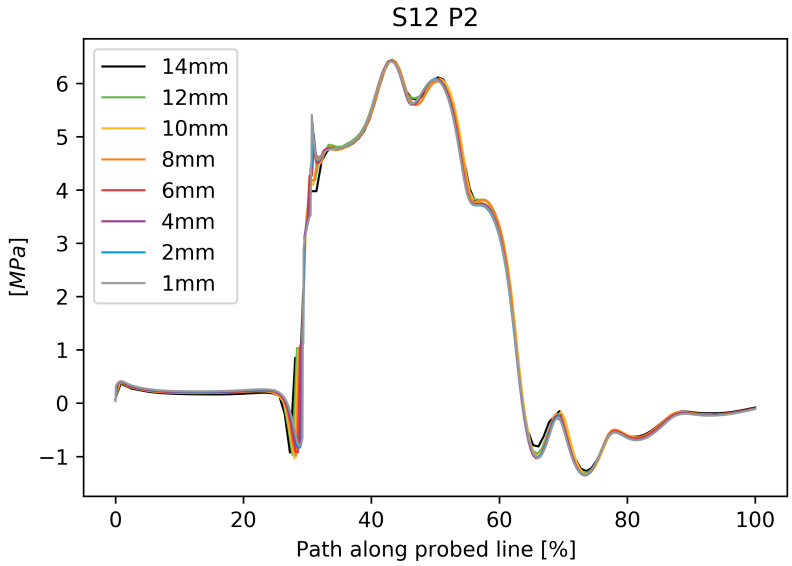

Figure B.8: σ_{12} Ply 2

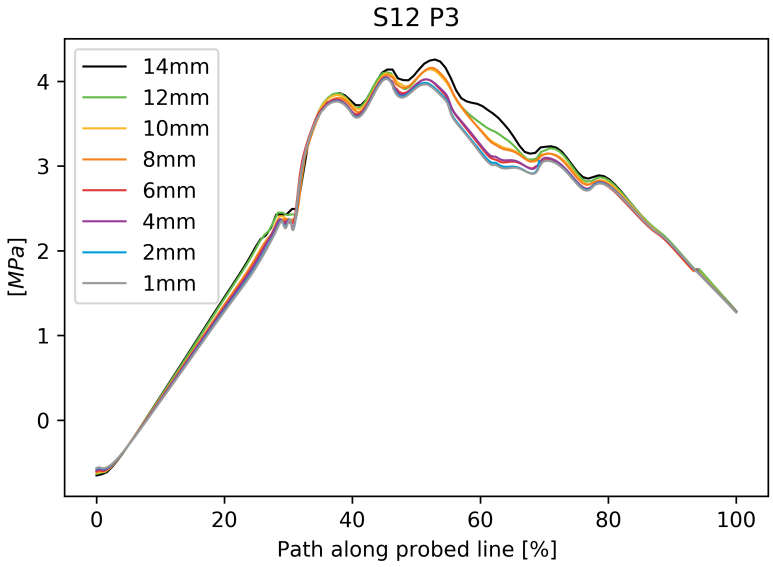

Figure B.9: σ_{12} Ply 3

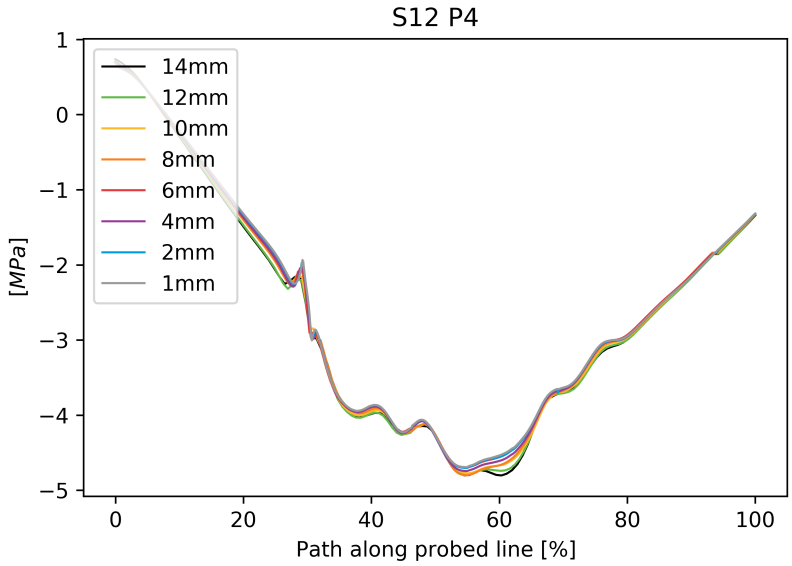

Figure B.10: σ_{12} Ply 4

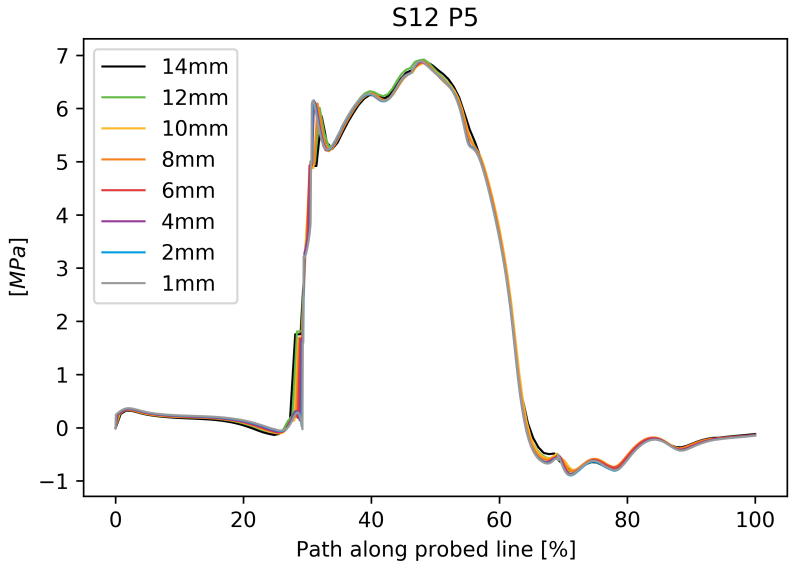

Figure B.11: σ_{12} Ply 5

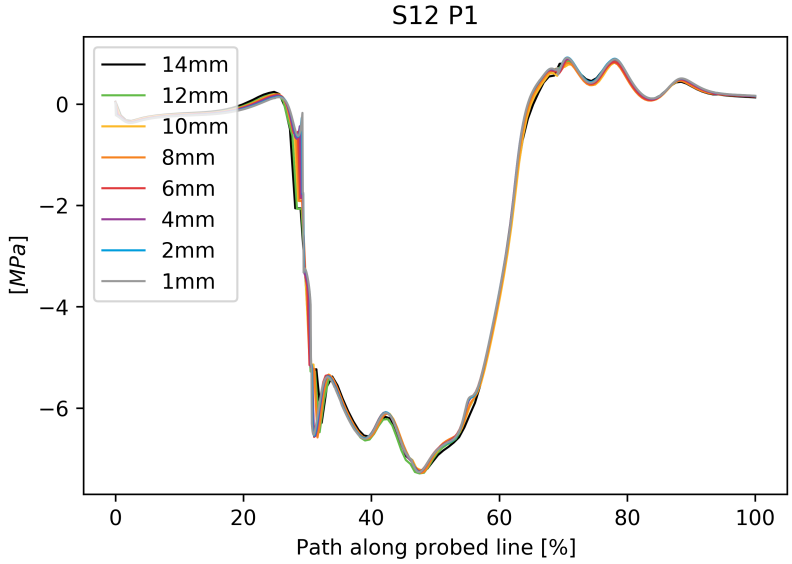

Figure B.12: σ_{12} Ply 6

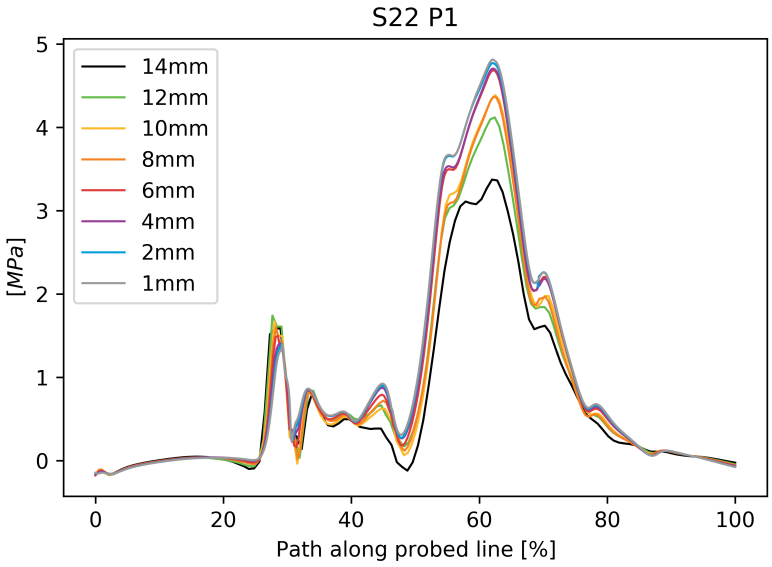

Figure B.13: σ_{22} Ply 1

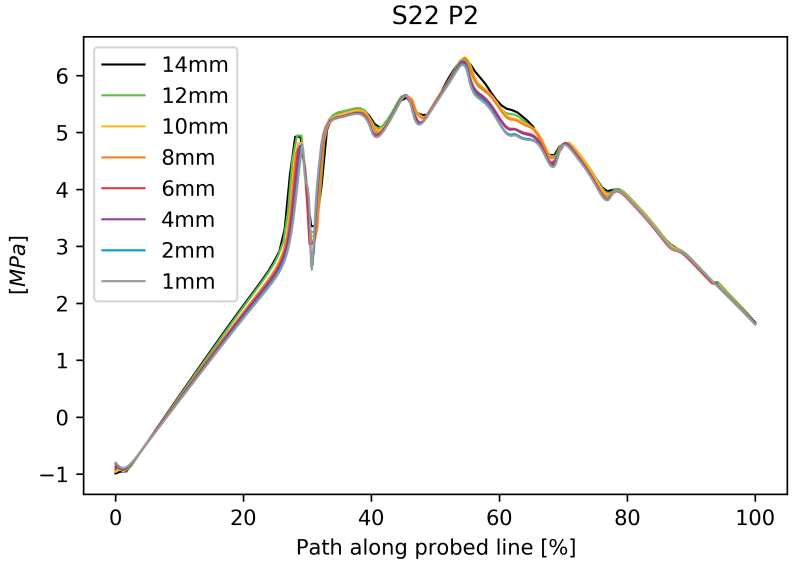

Figure B.14: σ_{22} Ply 2

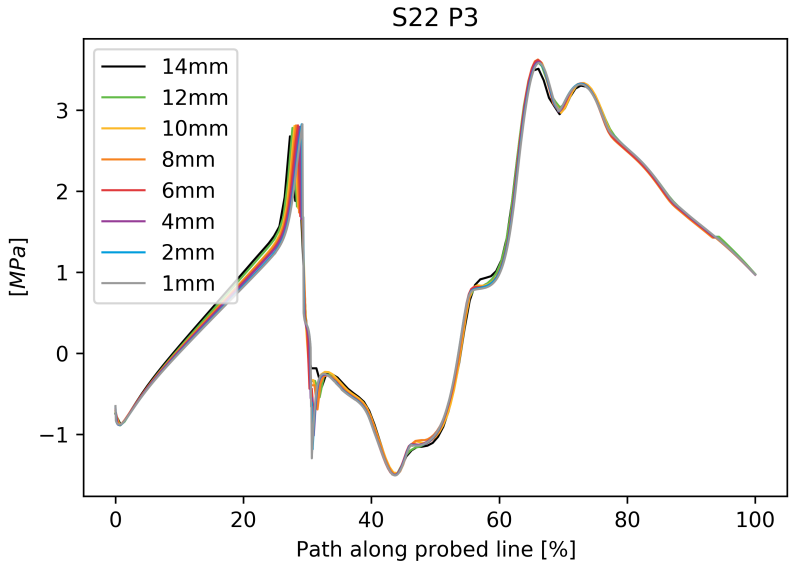

Figure B.15: σ_{22} Ply 3

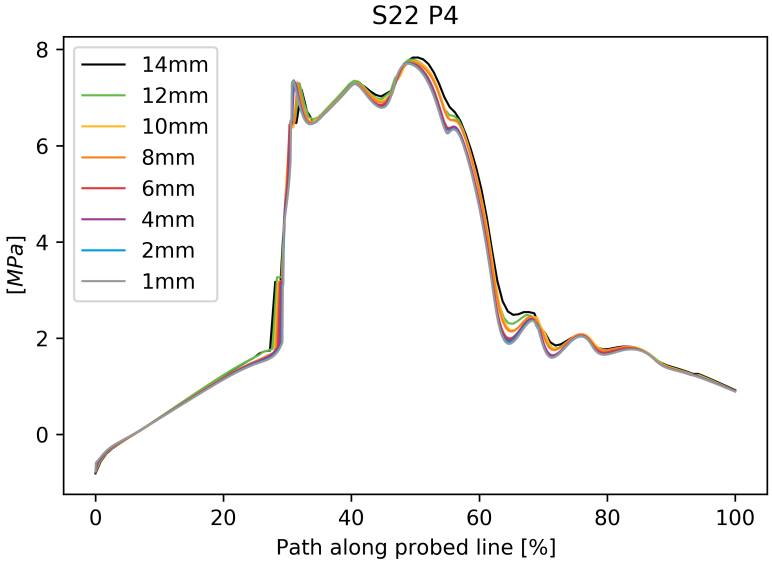

Figure B.16: σ_{22} Ply 4

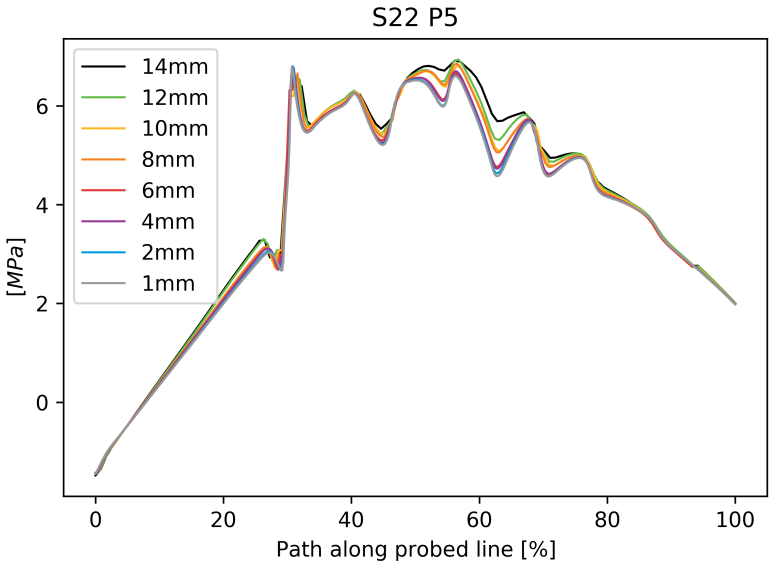

Figure B.17: σ_{22} Ply 5

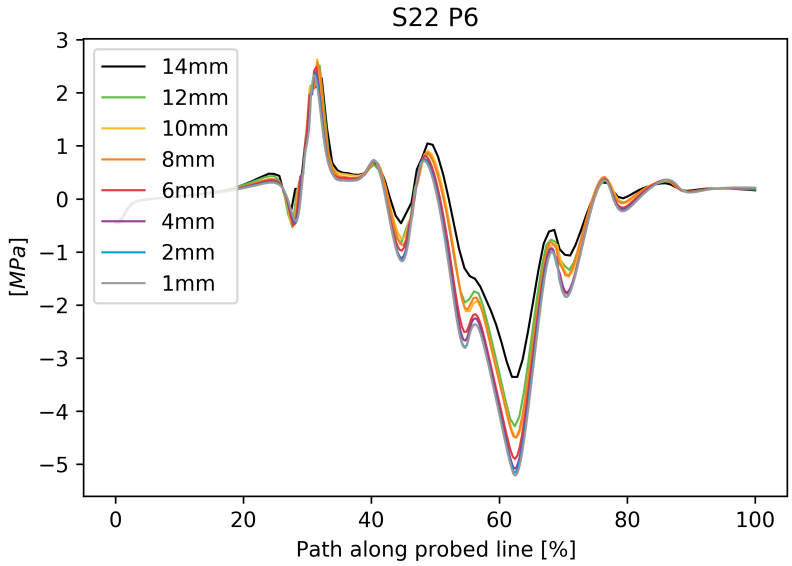

Figure B.18: σ_{22} Ply 6

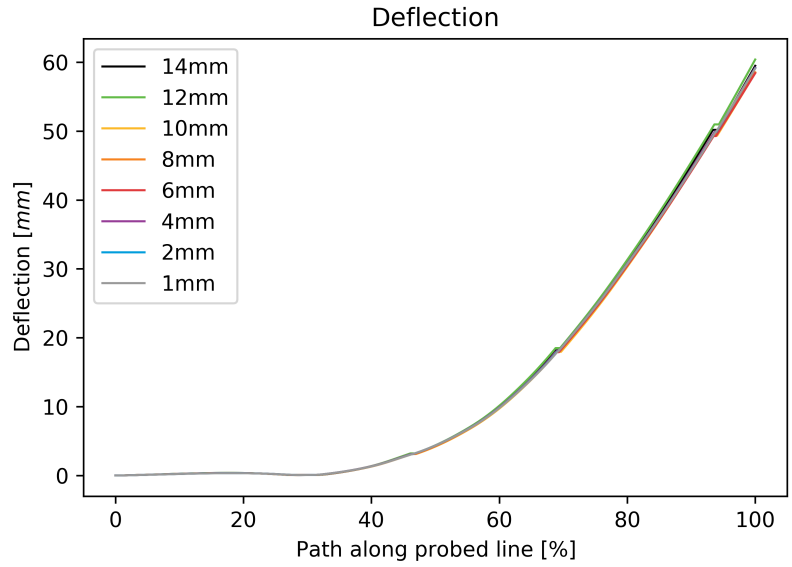

Figure B.19: Deflection magnitude

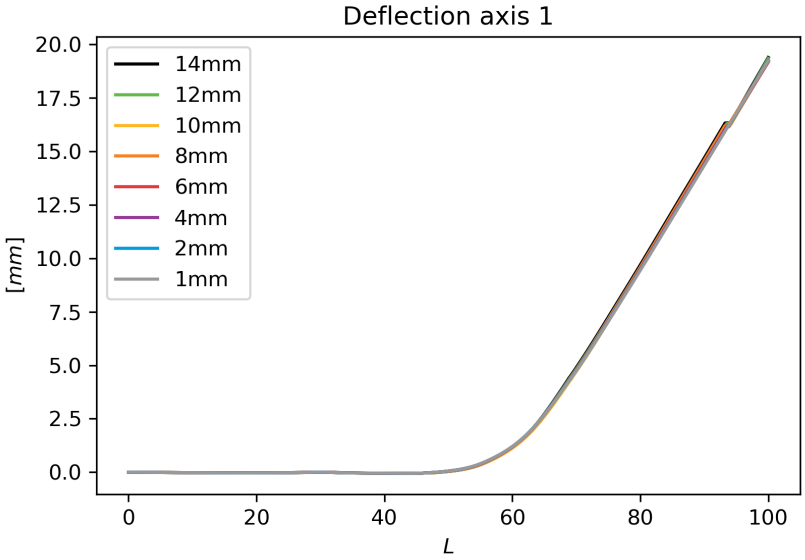

Figure B.20: Deflection axis 1

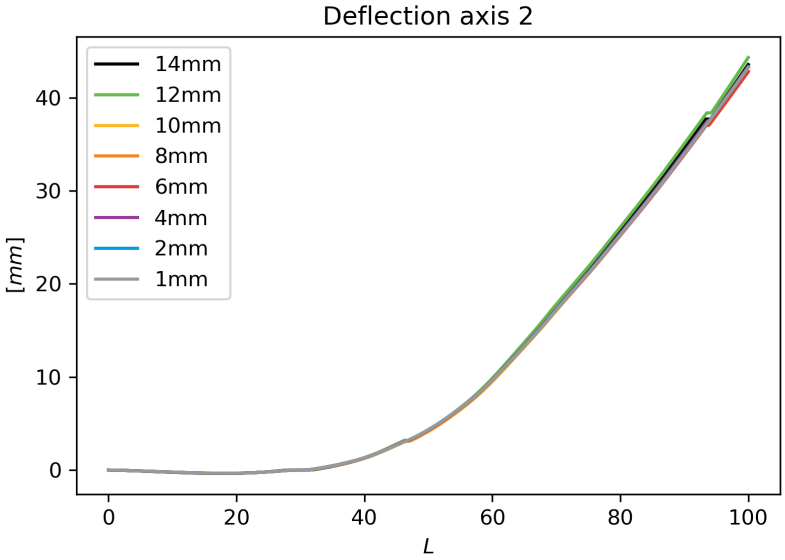

Figure B.21: Deflection axis 2

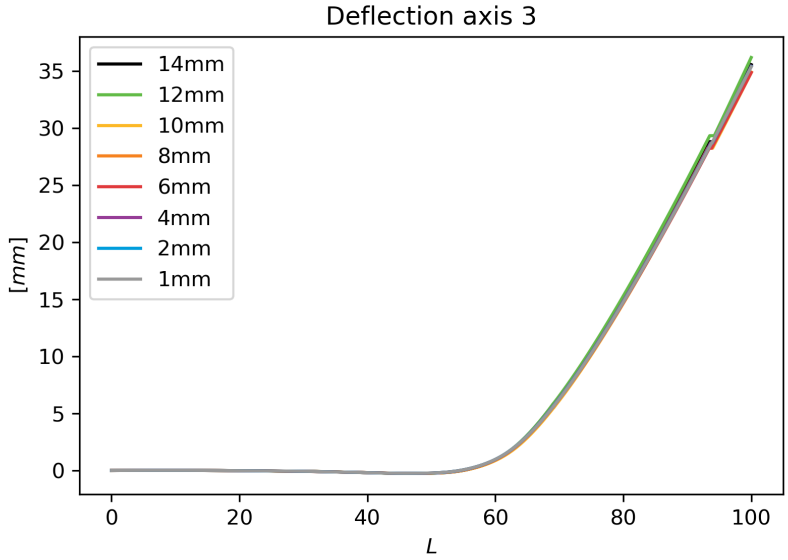

Figure B.22: Deflection axis 3

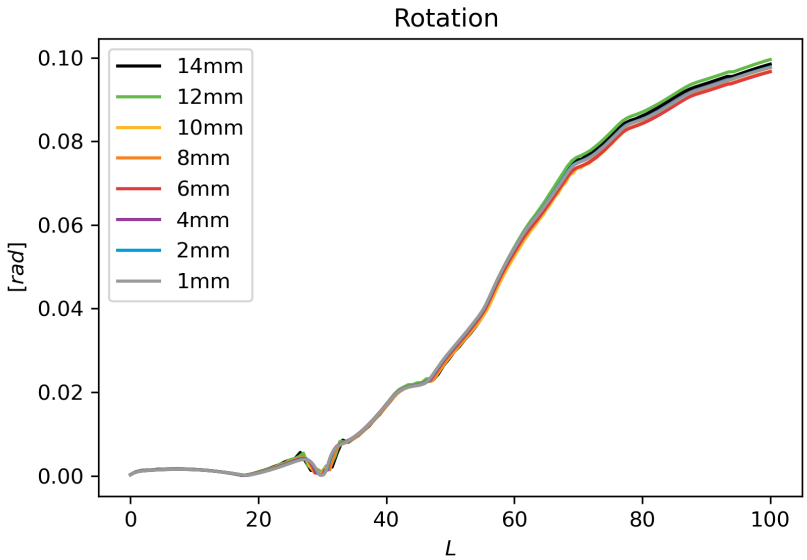

Figure B.23: Rotation magnitude

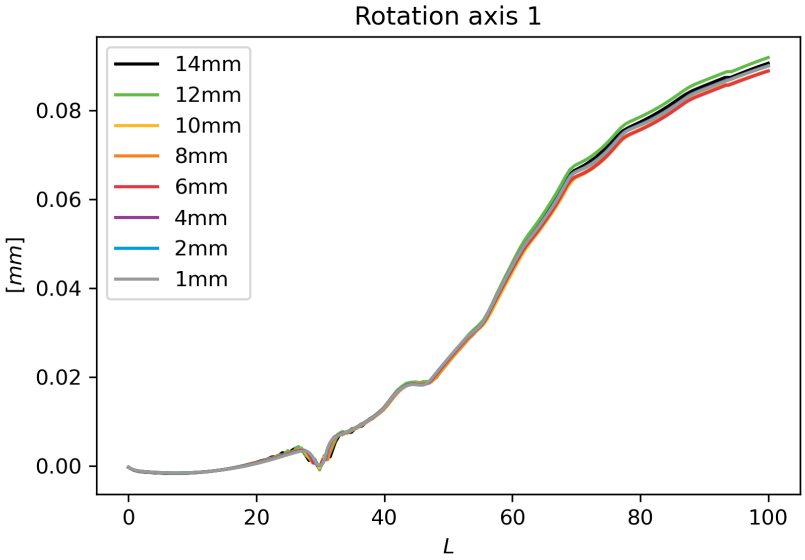

Figure B.24: Rotation axis 1

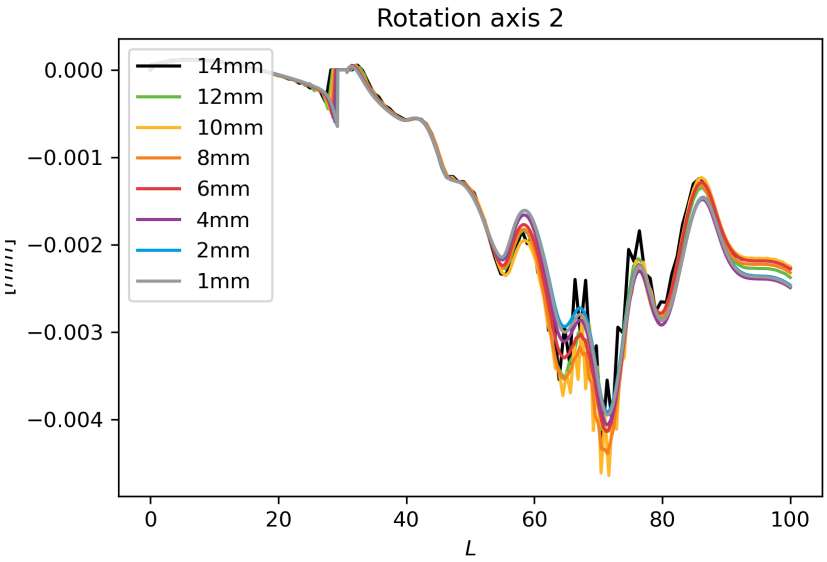

Figure B.25: Rotation axis 2

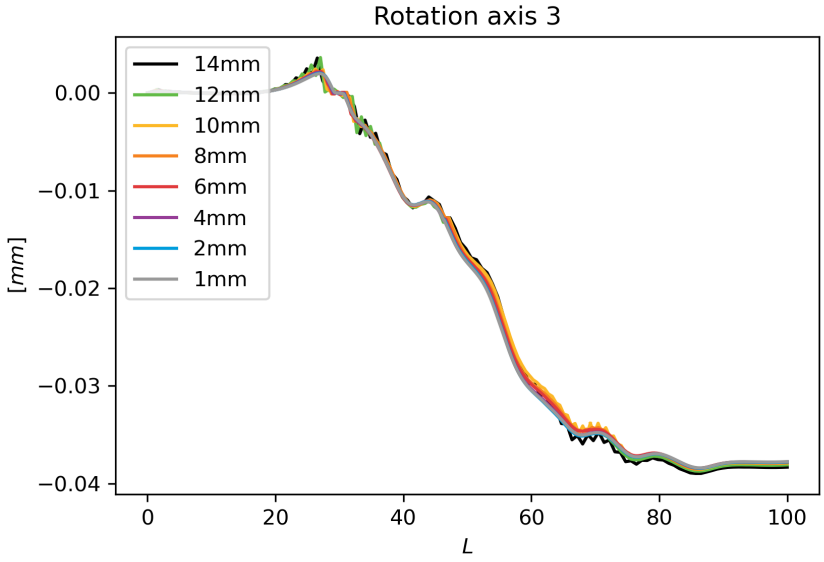

Figure B.26: Rotation axis 3

B.1 Impact test

Eigenfrequency investigation

Measurements and analysis performed on hydrofoil

Report date: 2021-07-14

Issue: 1
Revision: 1

ReVibe Energy responsible:
Erik Godtman Kling
Niklas Illipe

Test setup and execution

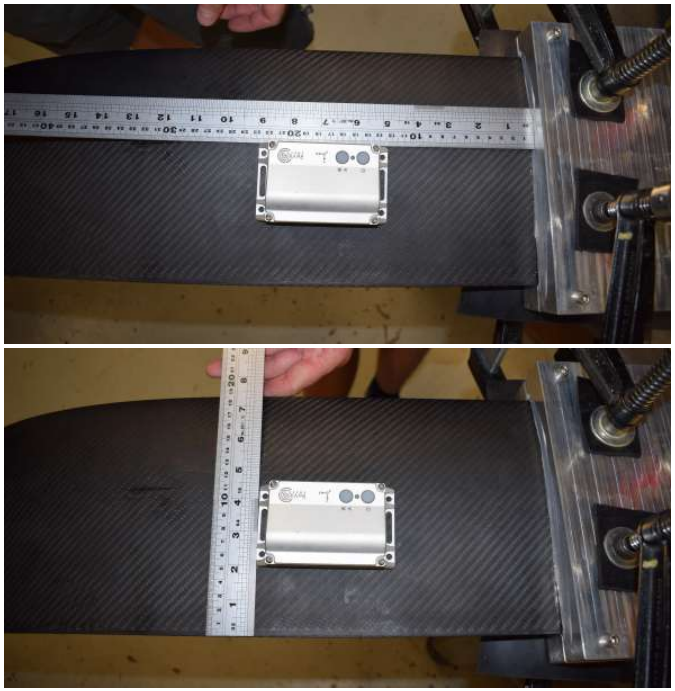

- Hydrofoil clamped at the base
- Hydrofoil excited with rubber hammer at different points
- Frequency response measured with ReLog datalogger unit mounted on tip and base of hydrofoil, respectively

Results

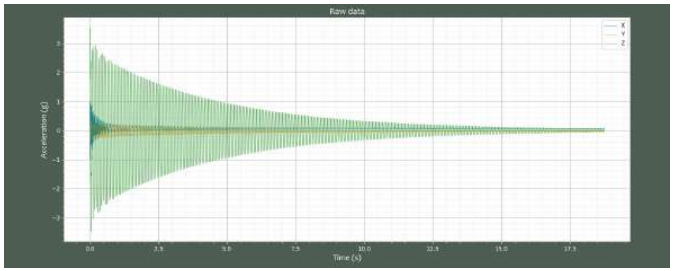

Raw acceleration signal of impulse

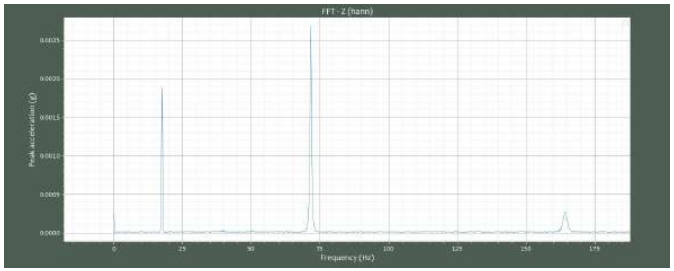

Peaks, base mounting & base excitation point

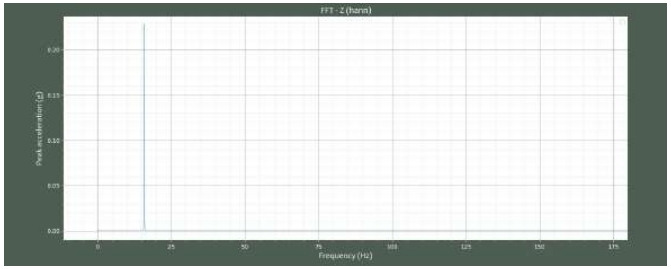

Peaks, tip mounting & tips excitation point

Eigenfrequencies				
ReLog position	Base		Tip	
Excitation point	Base	Tip	Base	Tip
1st	17.6	17.6	15.9	15.9
2nd	71.7	71.6	67.3	67.3
3rd	164.3	-	-	-

Summary/comments:

- No significant difference between base/tip excitation point
- Some shift in resonance peaks for tip mounting vs. base mounting (approx. 10 % lower for first mode), likely due to the added weight of the data logger.

B.2 Post processing

B.2.1 Isotropic model

C

Validation and results

C.1 Displacement

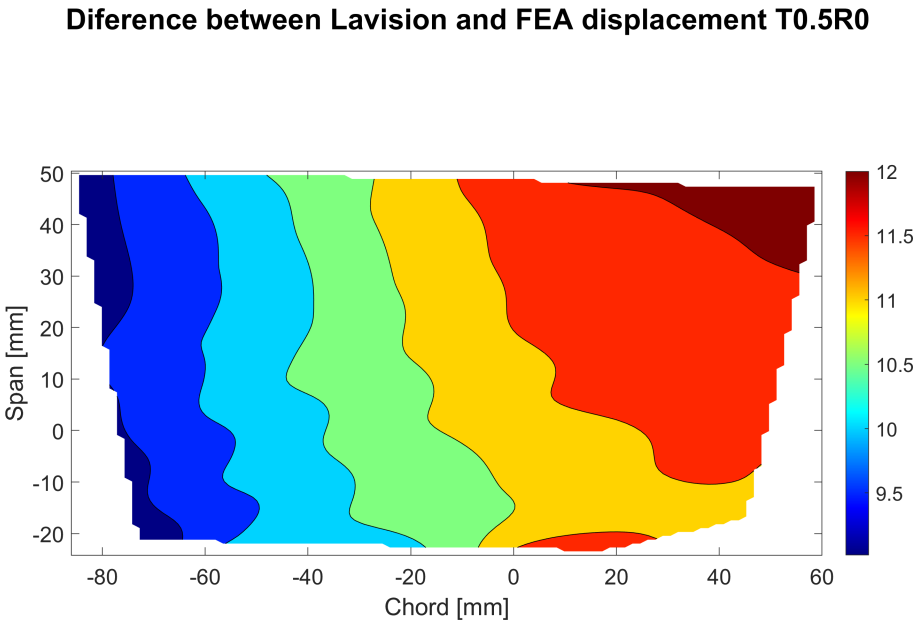

(a) Lavision - FEA displacement T0.5R0

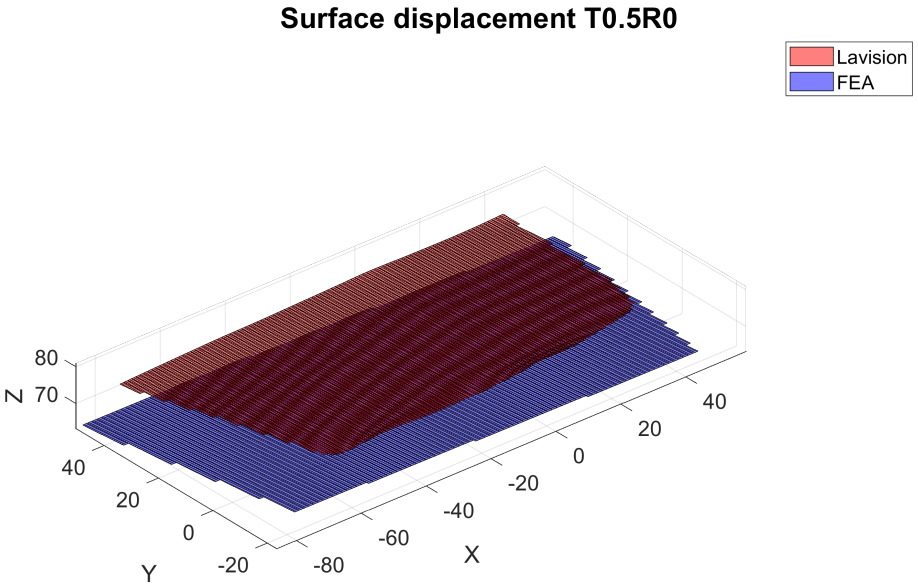

(b) Surface displacement T0.5R0

Figure C.1: Simulation case T0.5R0isotropic model

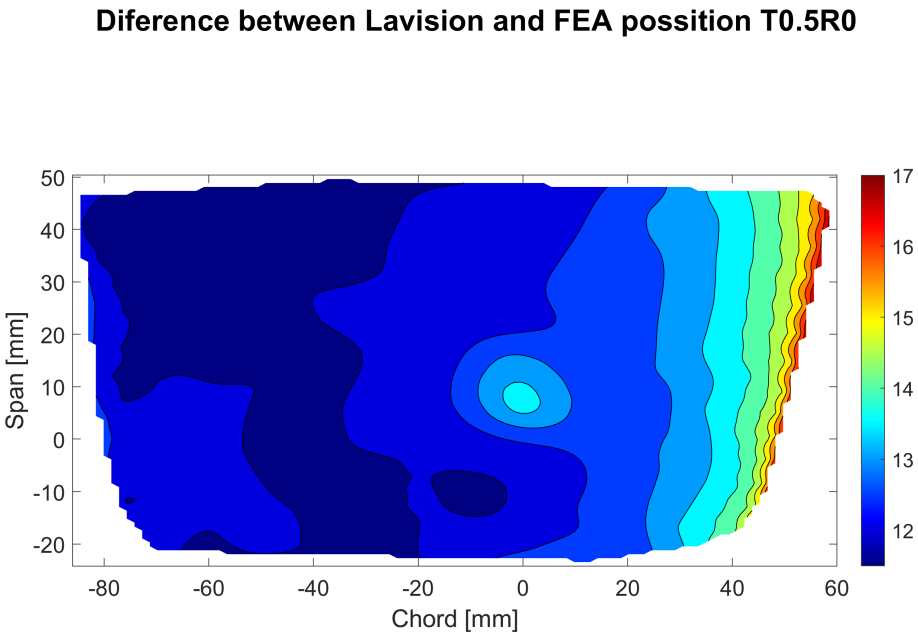

(a) Lavision - FEA possition T0.5R0

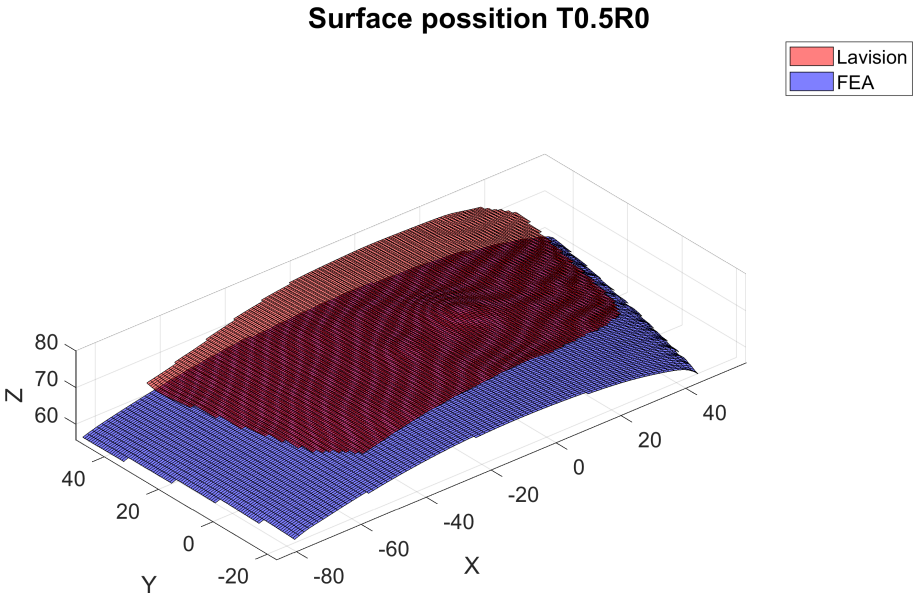

(b) Surface possition T0.5R0

Figure C.2: Simulation case T0.5R0isotropic model

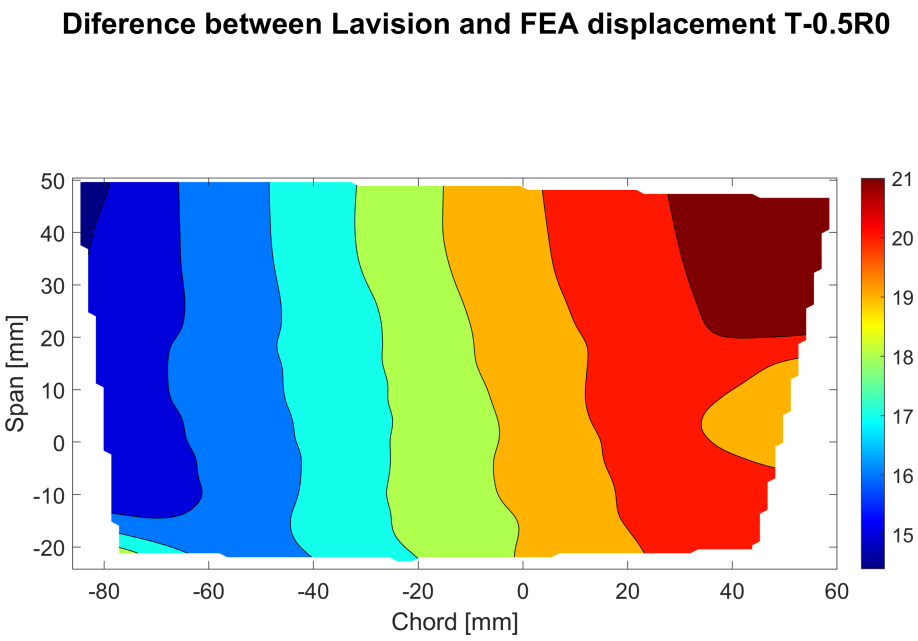

(a) Lavision - FEA displacement T-0.5R0

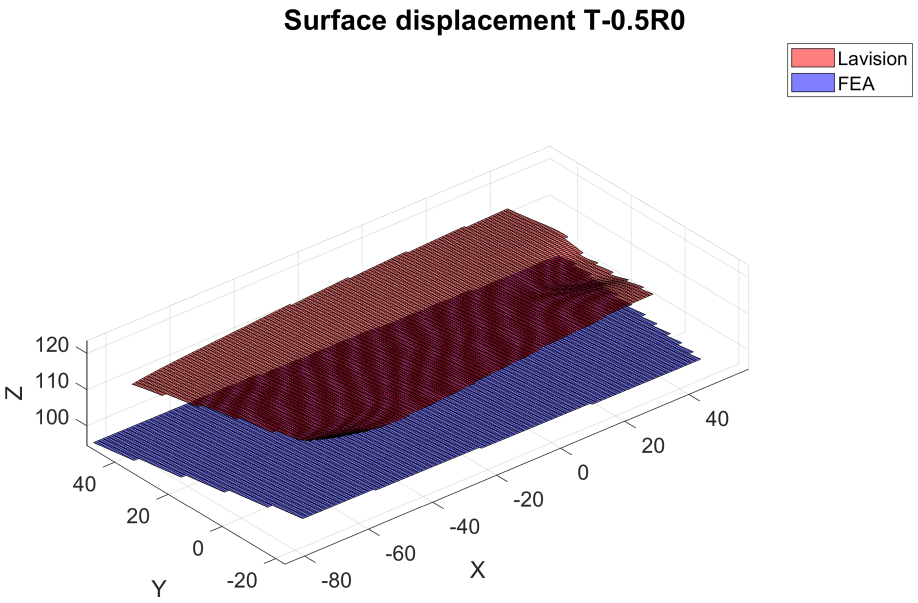

(b) Surface displacement T-0.5R0

Figure C.3: Simulation case T-0.5R0isotropic model

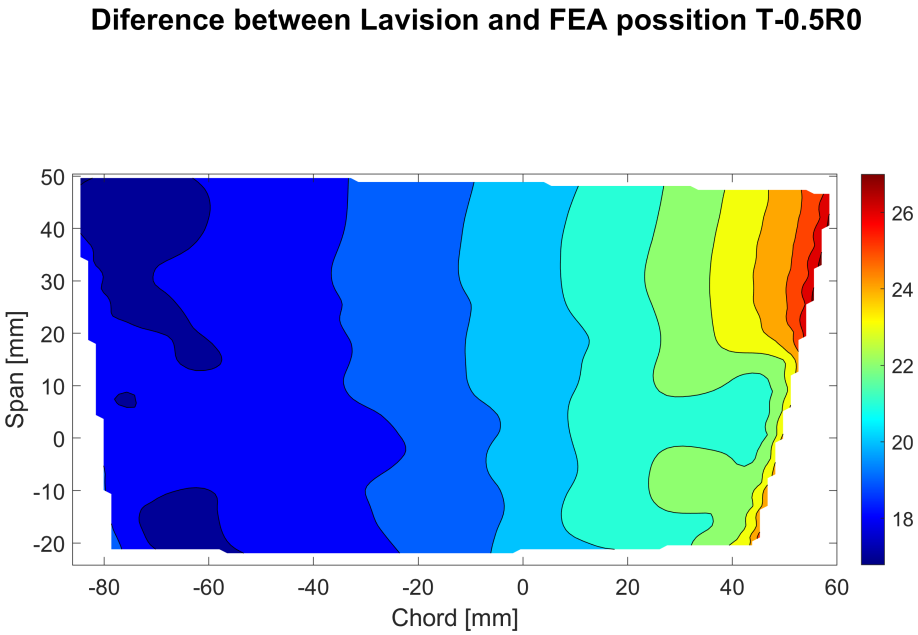

(a) Lavision - FEA possition T-0.5R0

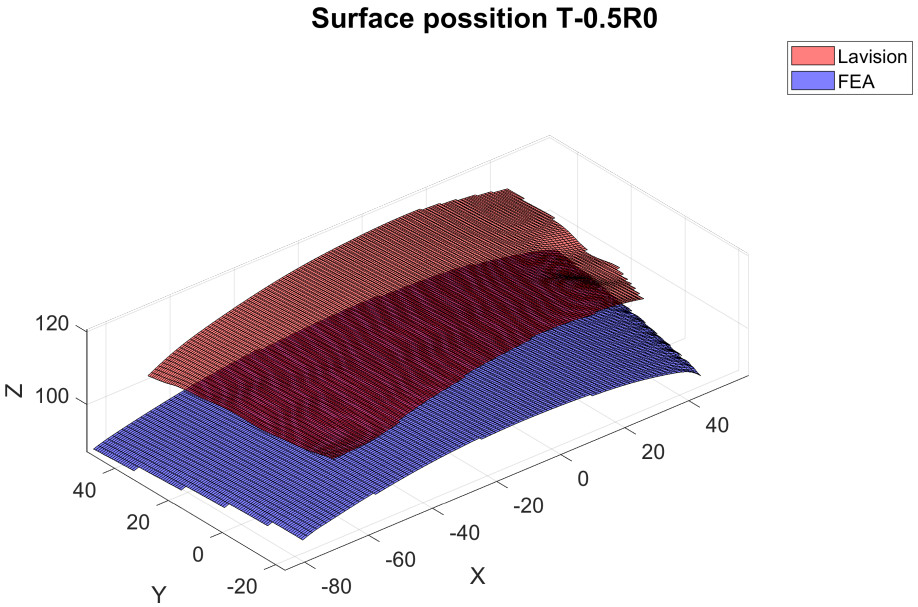

(b) Surface possition T-0.5R0

Figure C.4: Simulation case T-0.5R0isotropic model

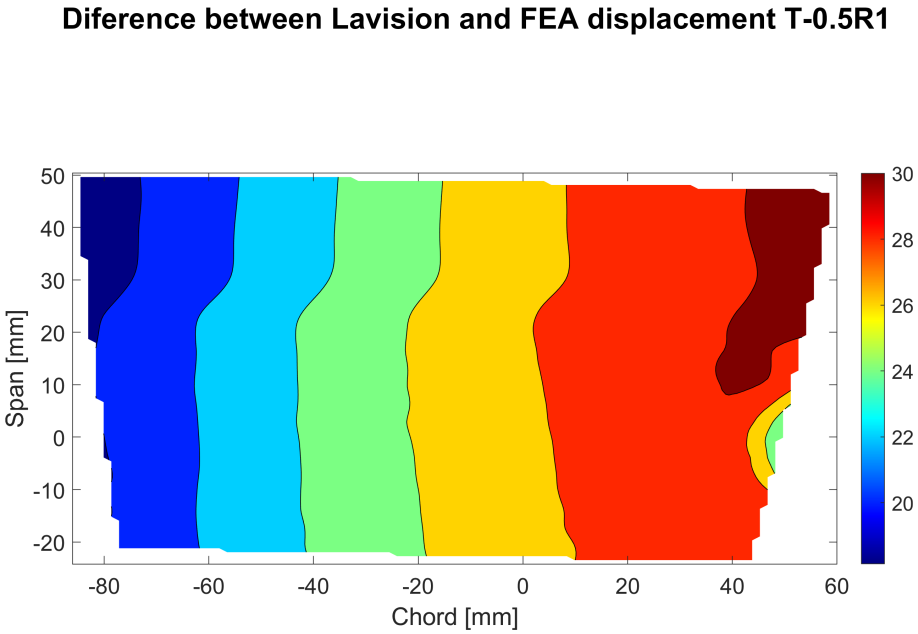

(a) Lavision - FEA displacement T-0.5R1

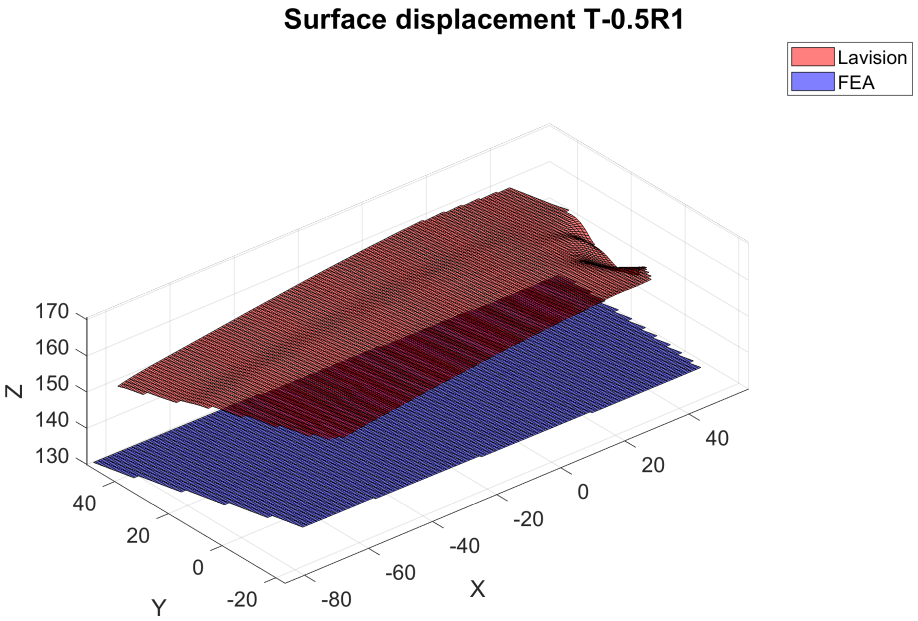

(b) Surface displacement T-0.5R1

Figure C.5: Simulation case T-0.5R1isotropic model

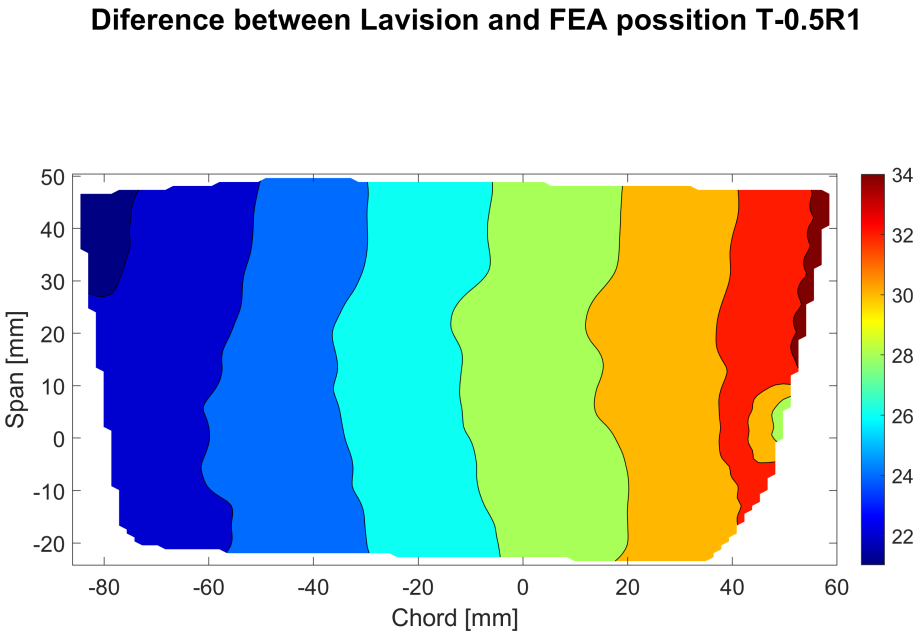

(a) Lavision - FEA possition T-0.5R1

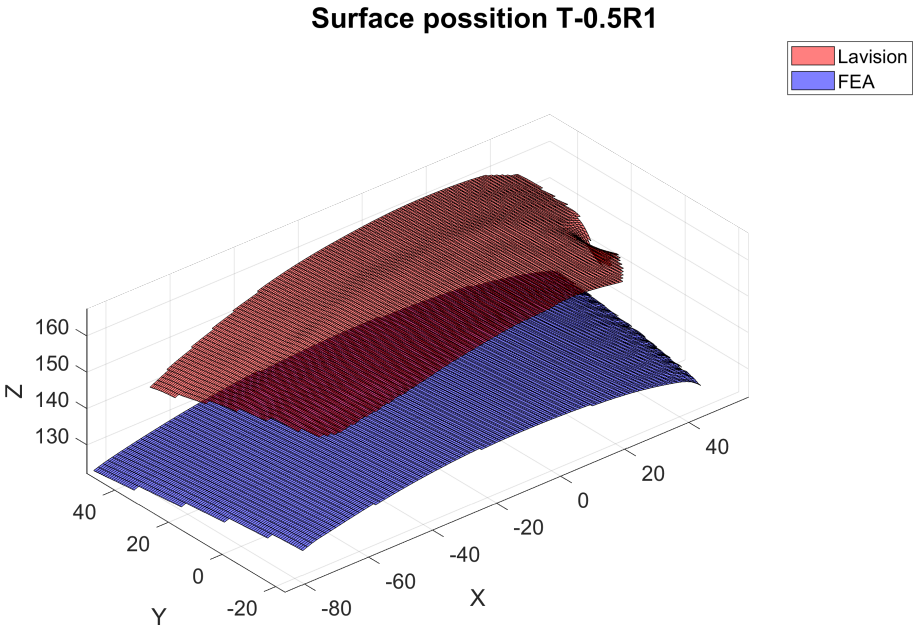

(b) Surface possition T-0.5R1

Figure C.6: Simulation case T-0.5R1isotropic model

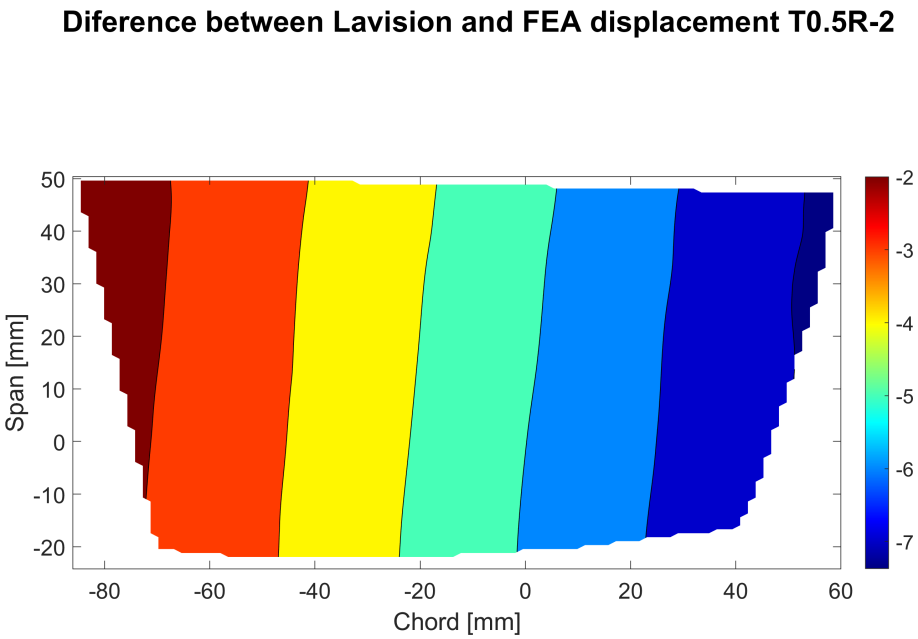

(a) Lavision - FEA displacement T0.5R-2

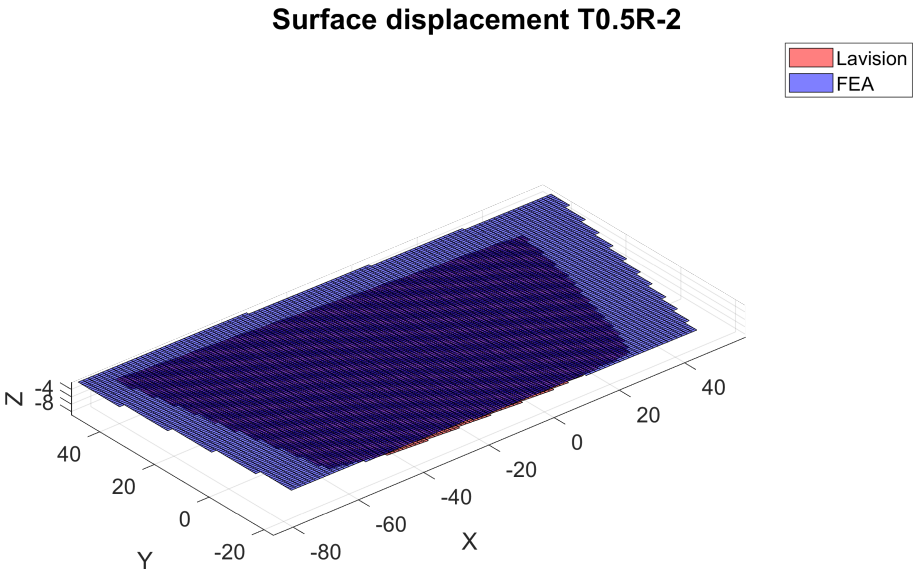

(b) Surface displacement T0.5R-2

Figure C.7: Simulation case T0.5R-2isotropic model

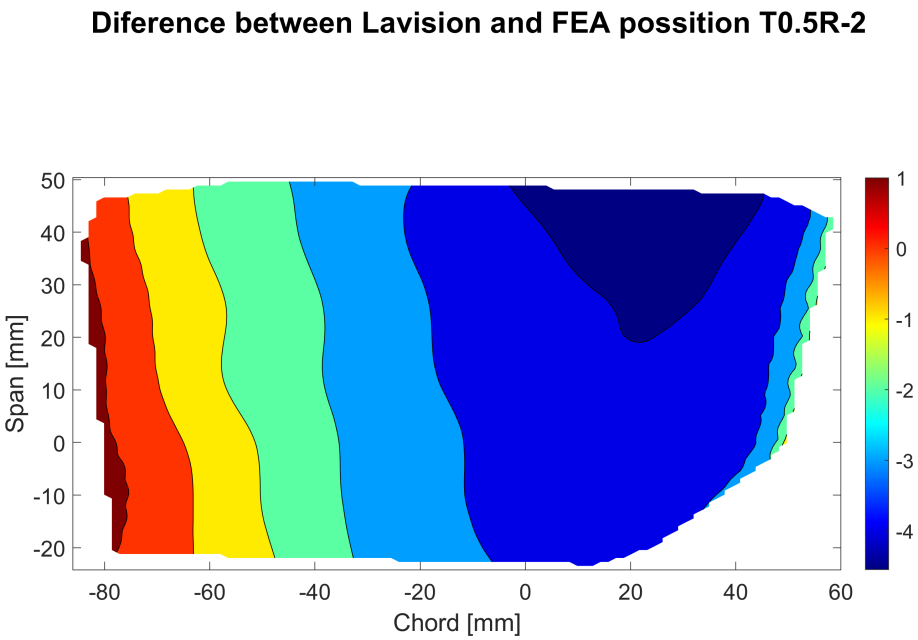

(a) Lavision - FEA possition T0.5R-2

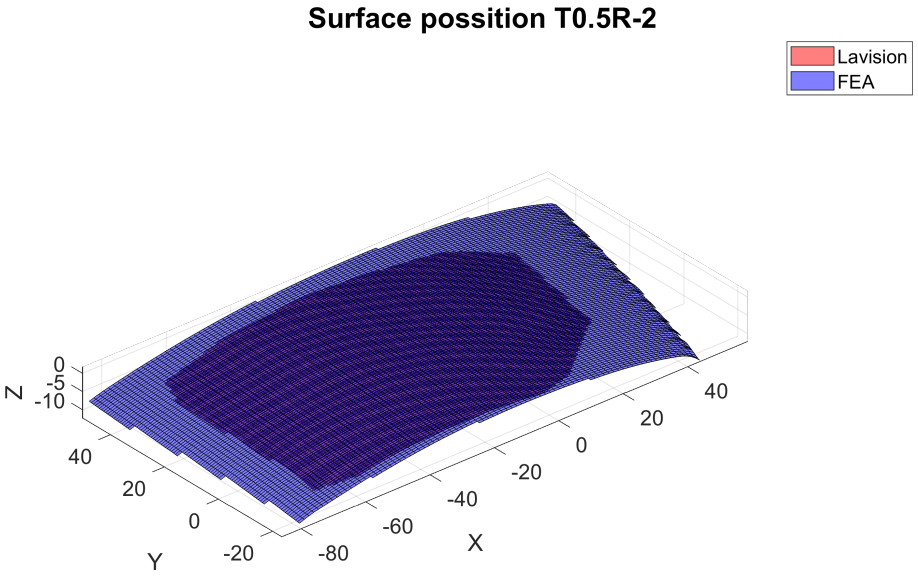

(b) Surface possition T0.5R-2

Figure C.8: Simulation case T0.5R-2isotropic model

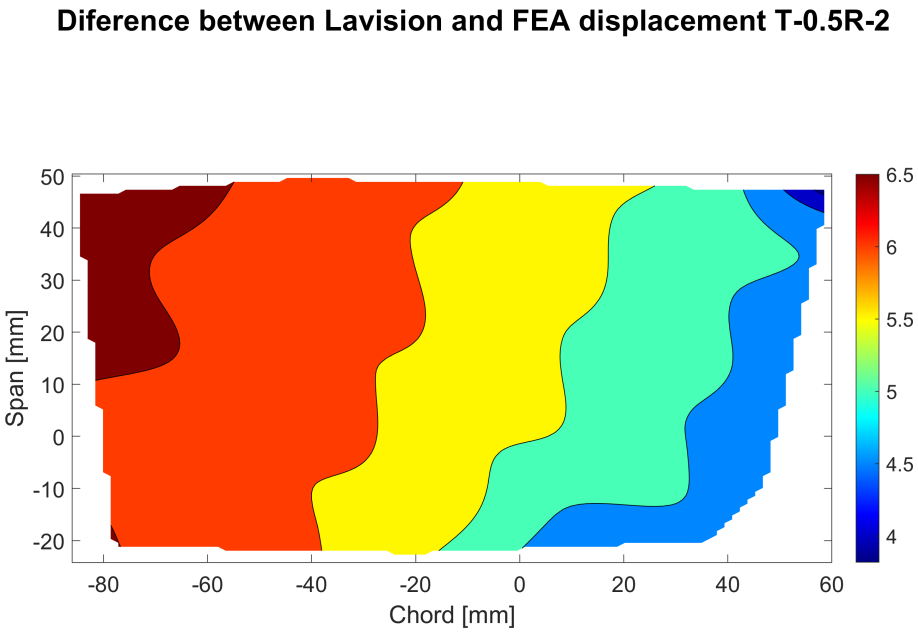

(a) Lavision - FEA displacement T-0.5R-2

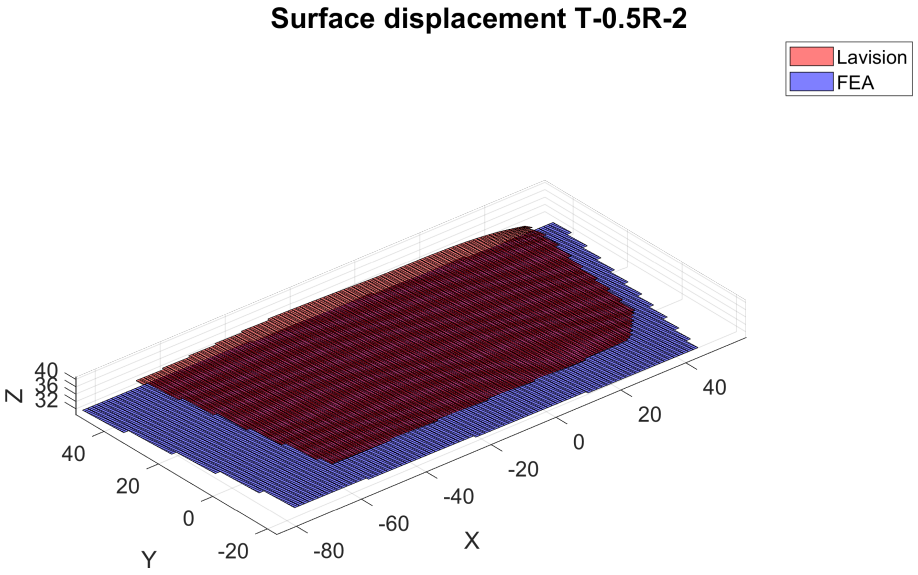

(b) Surface displacement T-0.5R-2

Figure C.9: Simulation case T-0.5R-2isotropic model

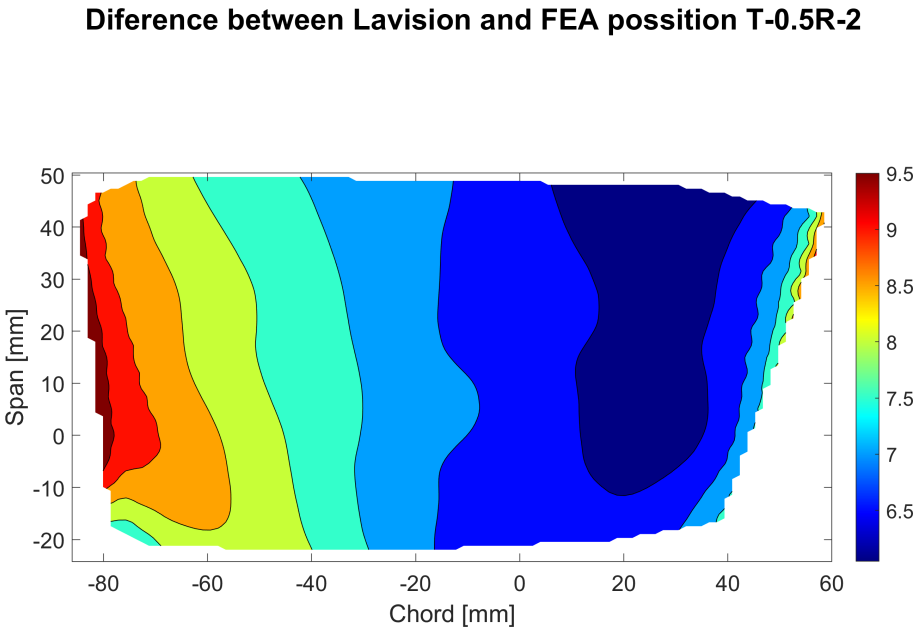

(a) Lavision - FEA possition T-0.5R-2

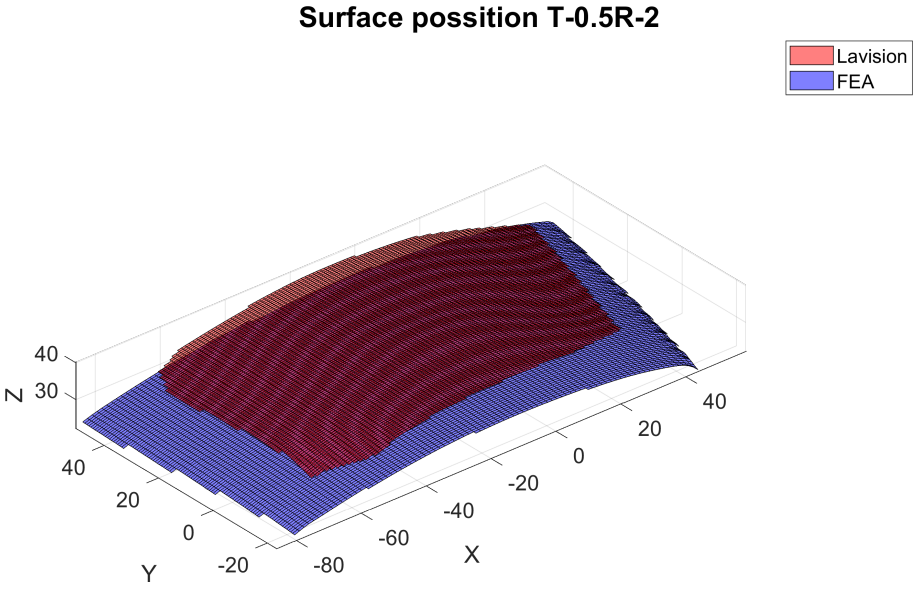

(b) Surface possition T-0.5R-2

Figure C.10: Simulation case T-0.5R-2isotropic model

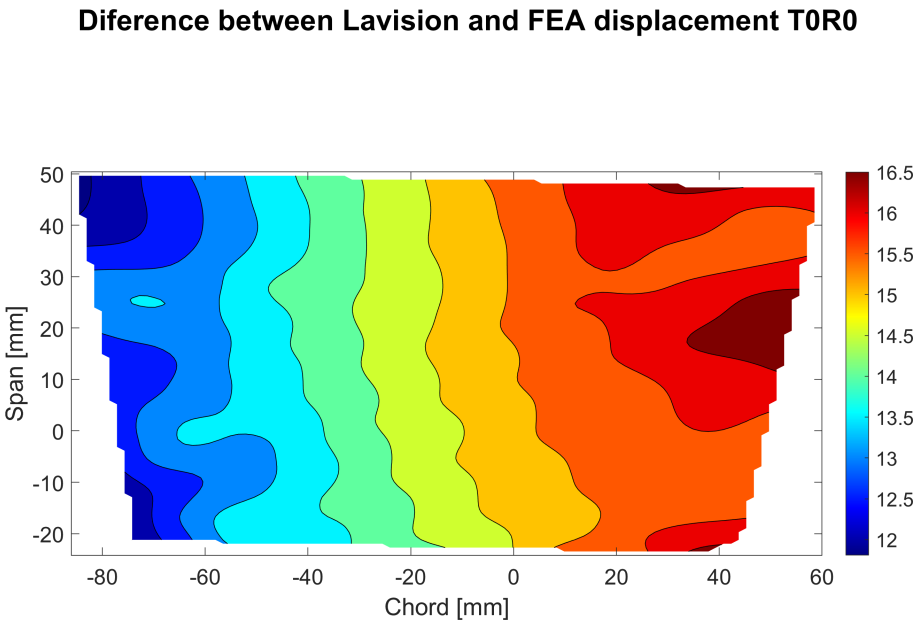

(a) Lavision - FEA displacement T0R0

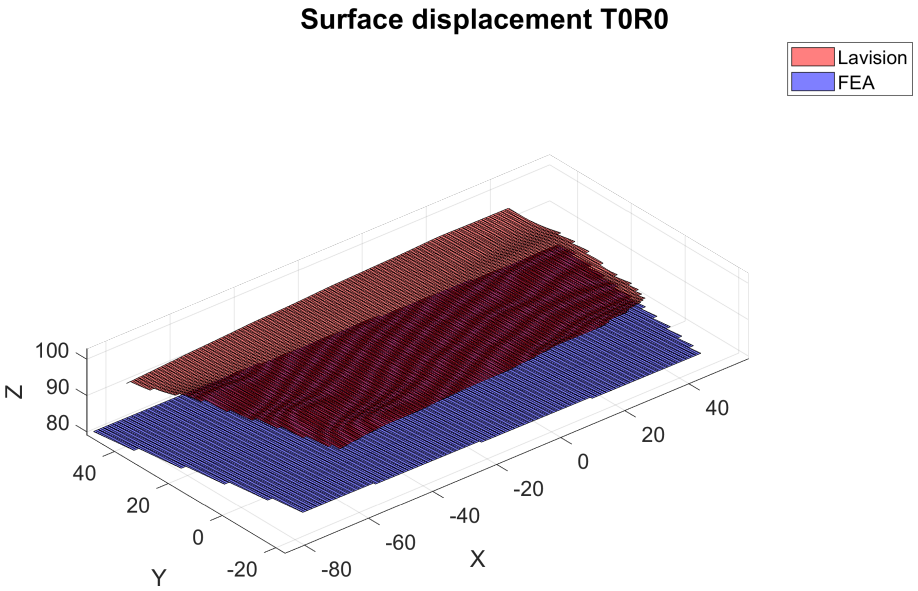

(b) Surface displacement T0R0

Figure C.11: Simulation case T0R0isotropic model

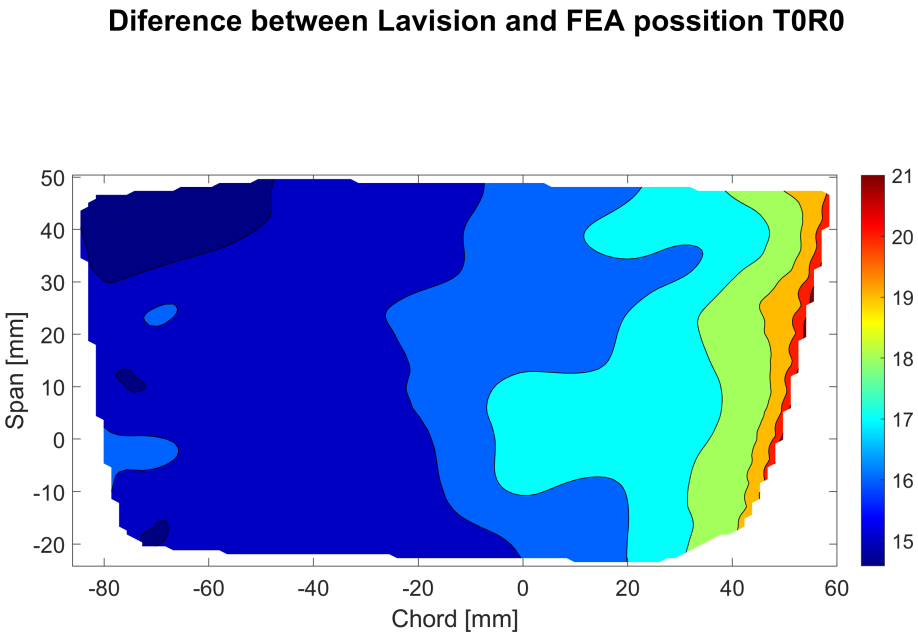

(a) Lavision - FEA possition T0R0

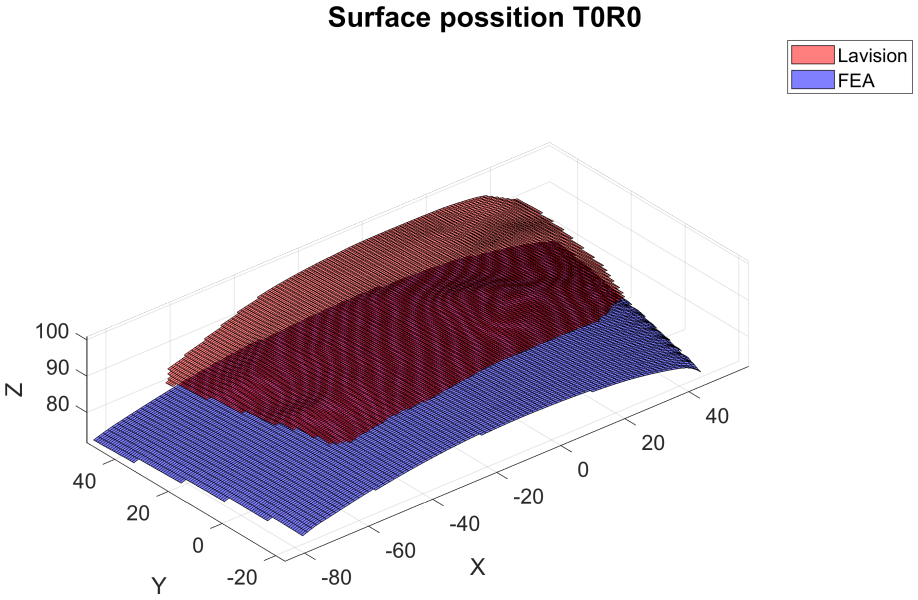

(b) Surface possition T0R0

Figure C.12: Simulation case T0R0isotropic model

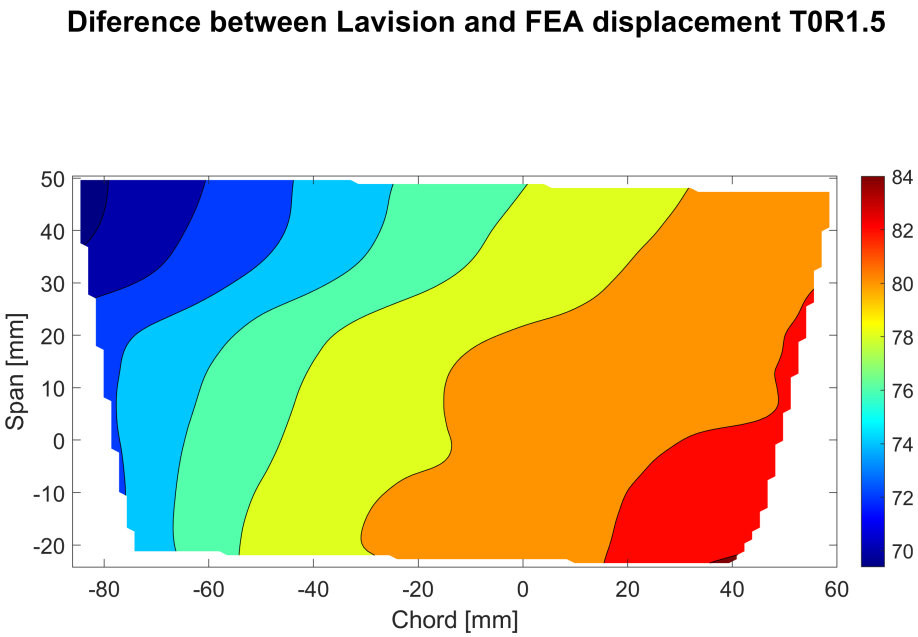

(a) Lavision - FEA displacement T0R1.5

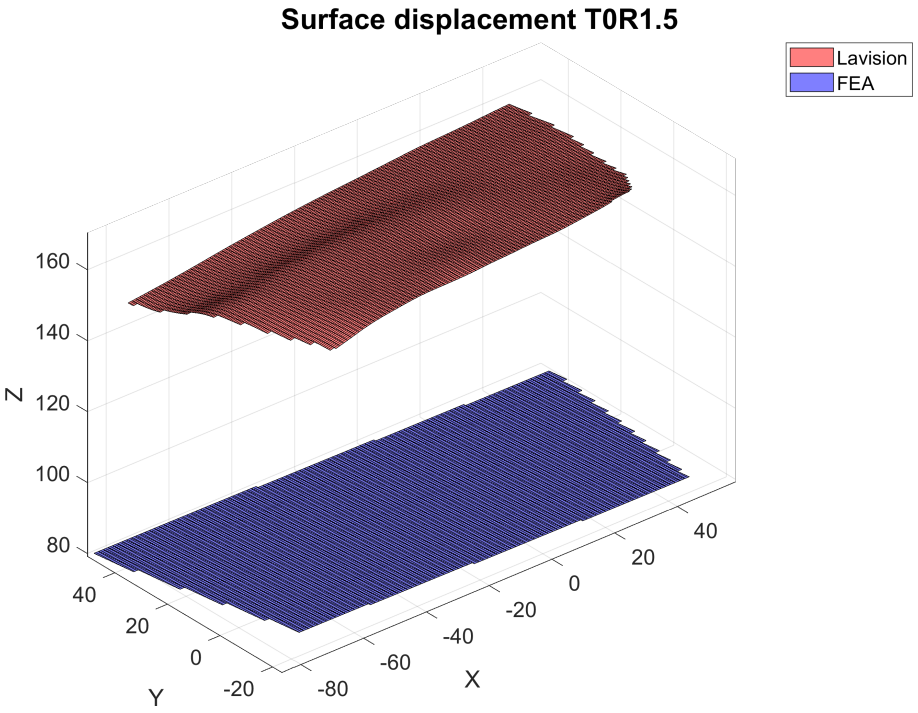

(b) Surface displacement T0R1.5

Figure C.13: Simulation case T0R1.5isotropic model

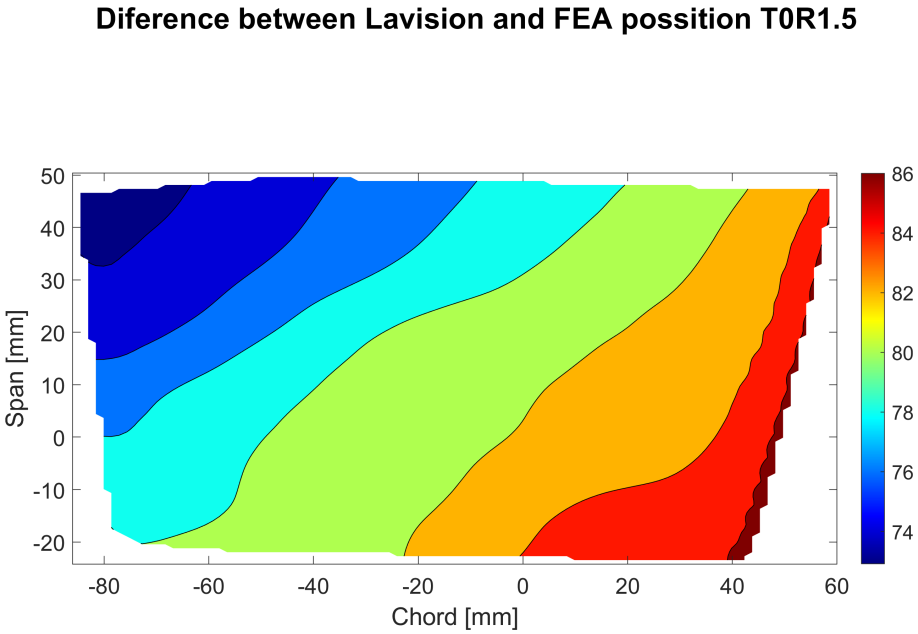

(a) Lavision - FEA possition T0R1.5

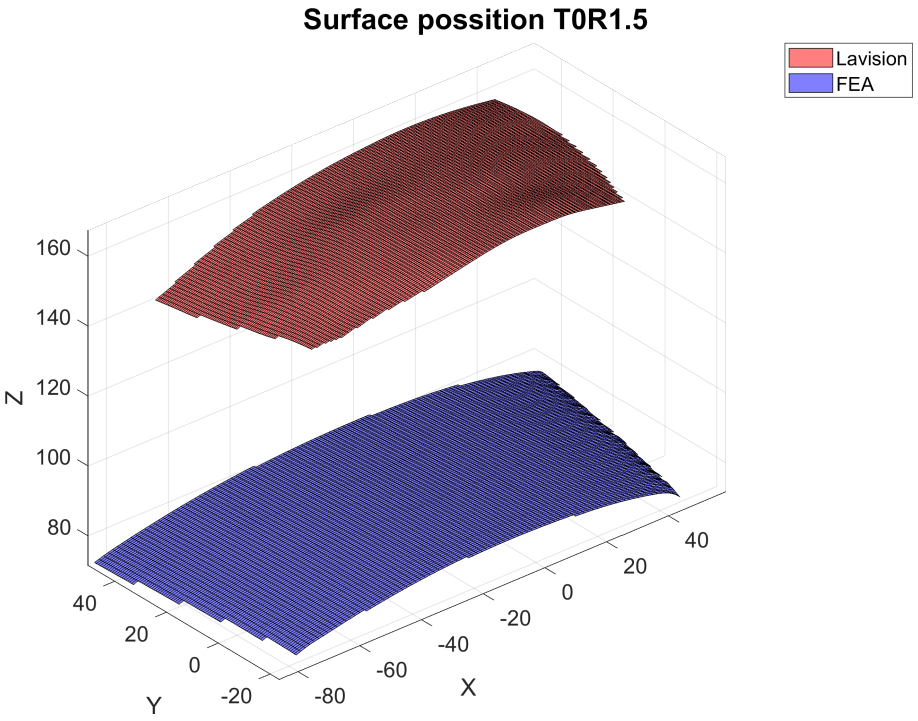

(b) Surface possition T0R1.5

Figure C.14: Simulation case T0R1.5isotropic model

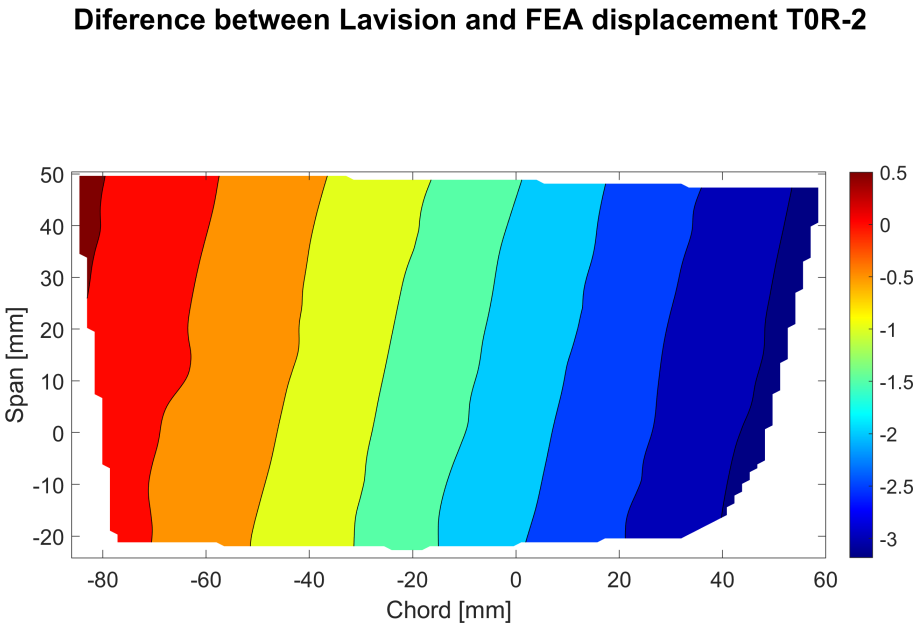

(a) Lavision - FEA displacement T0R-2

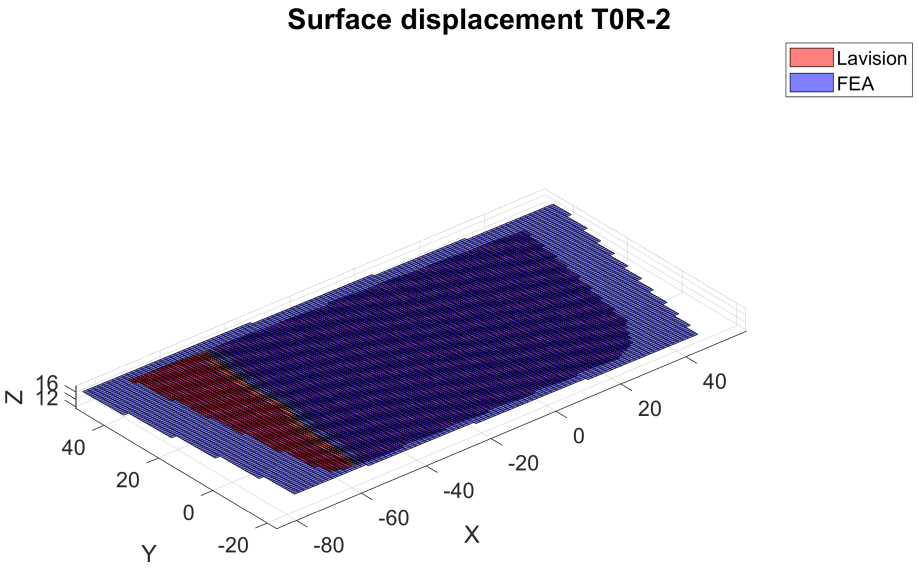

(b) Surface displacement T0R-2

Figure C.15: Simulation case T0R-2isotropic model

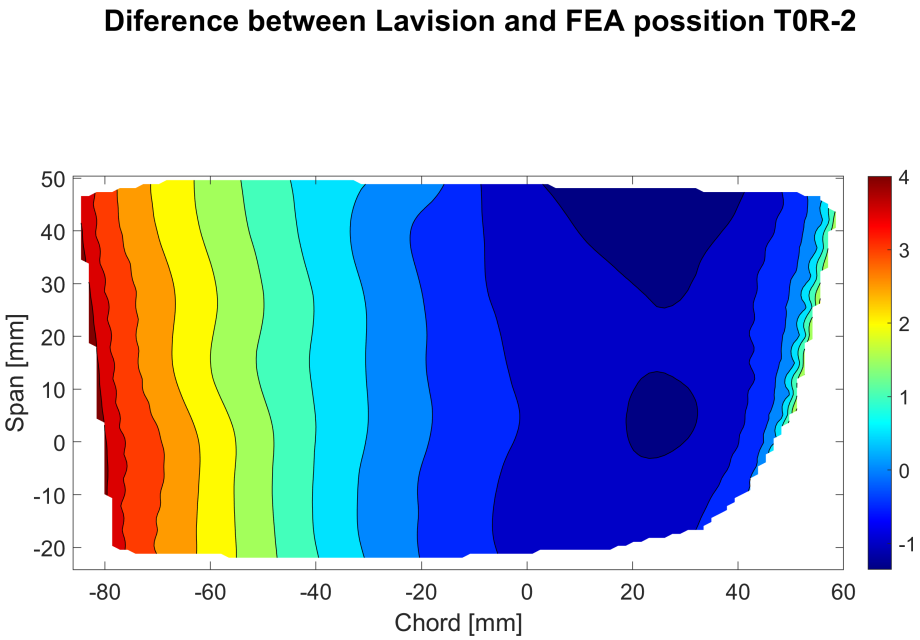

(a) Lavision - FEA possition T0R-2

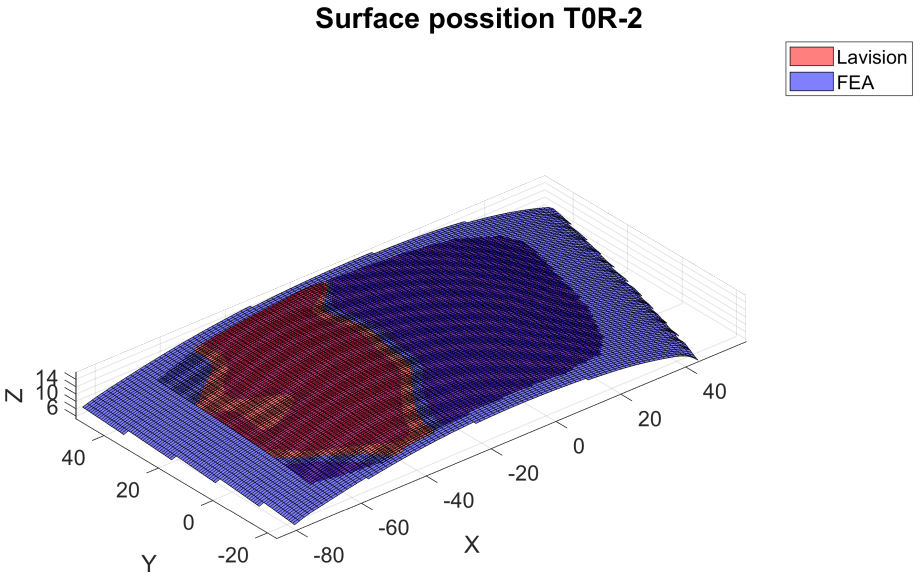

(b) Surface possition T0R-2

Figure C.16: Simulation case T0R-2isotropic model

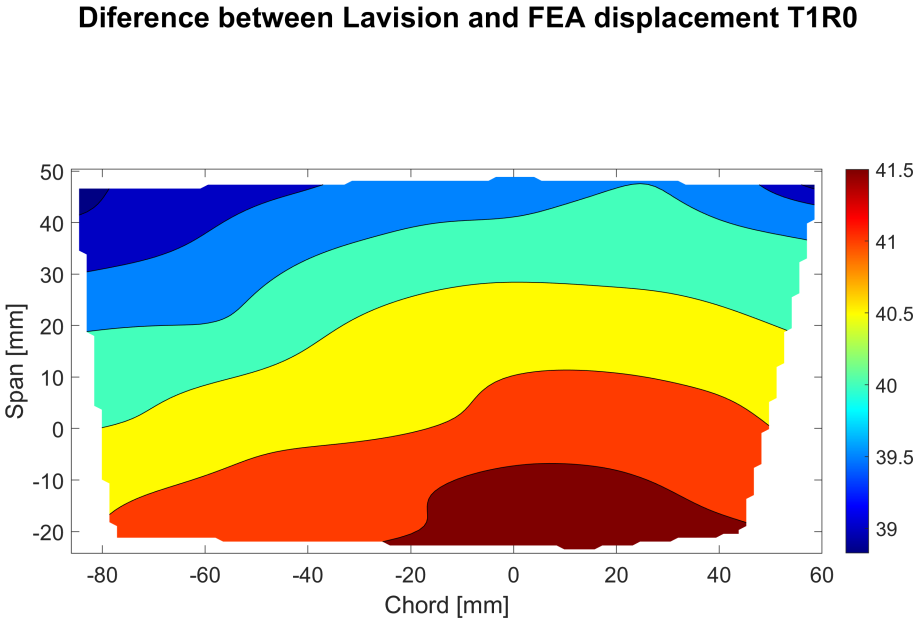

(a) Lavision - FEA displacement T1R0

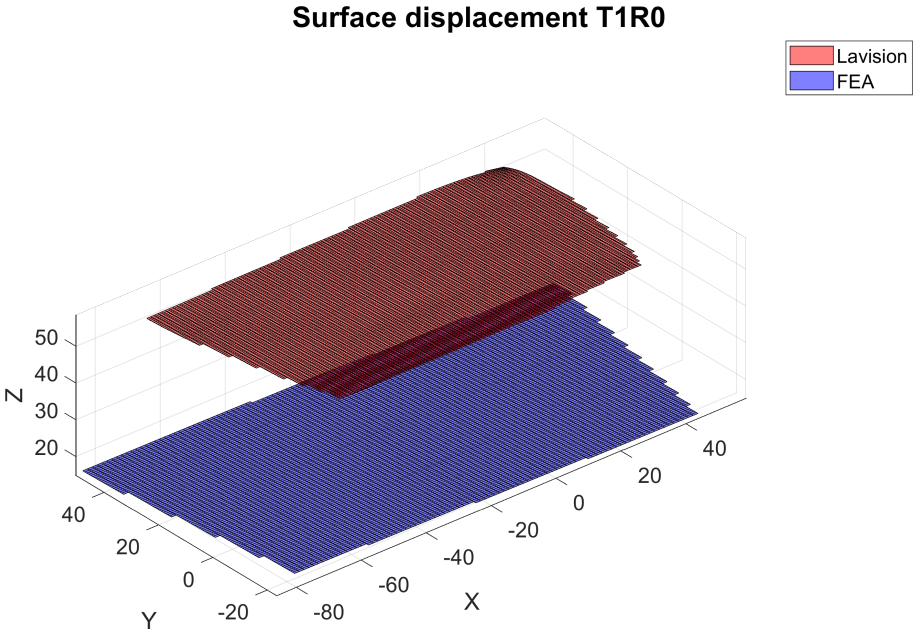

(b) Surface displacement T1R0

Figure C.17: Simulation case T1R0isotropic model

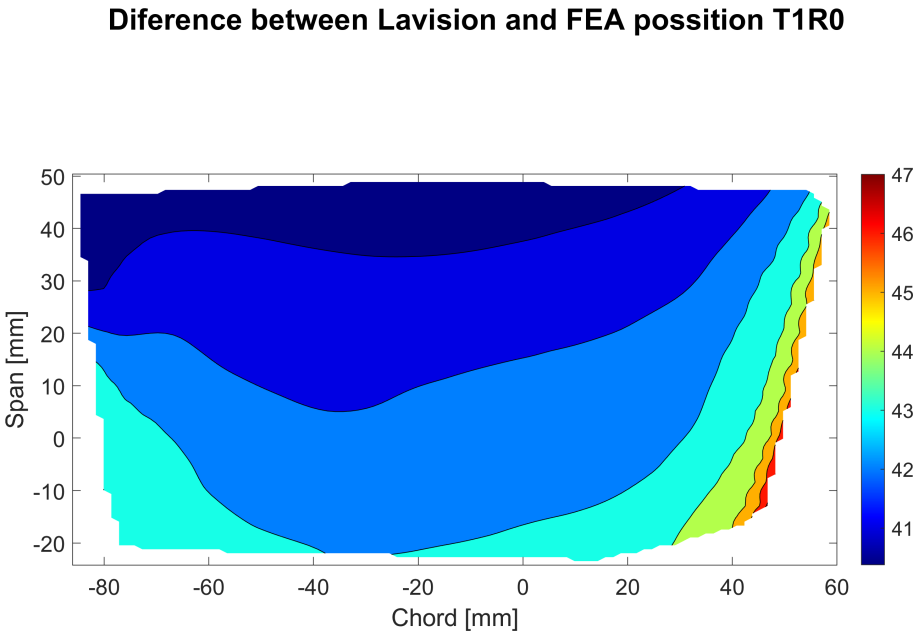

(a) Lavision - FEA possition T1R0

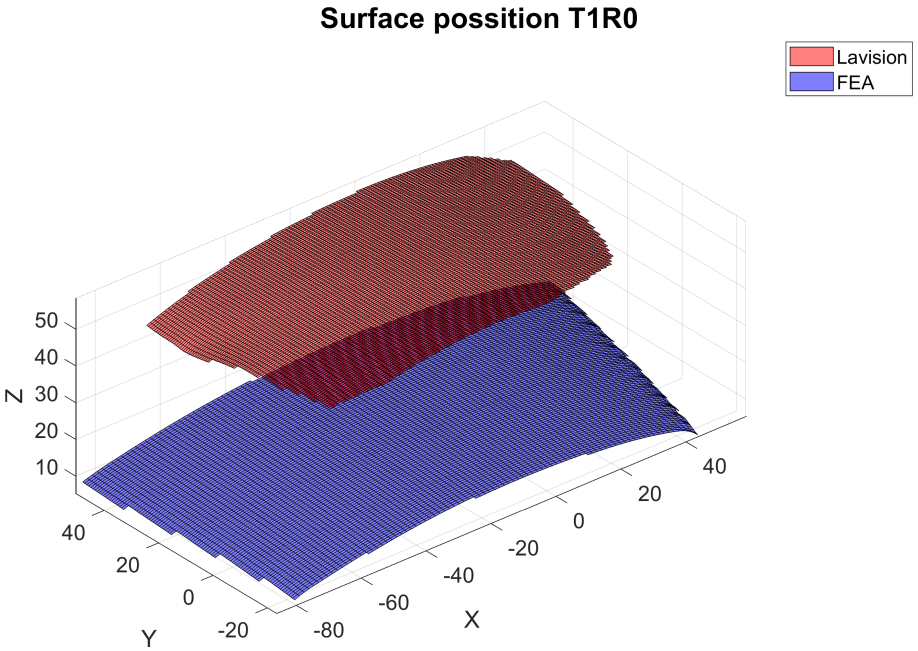

(b) Surface possition T1R0

Figure C.18: Simulation case T1R0isotropic model

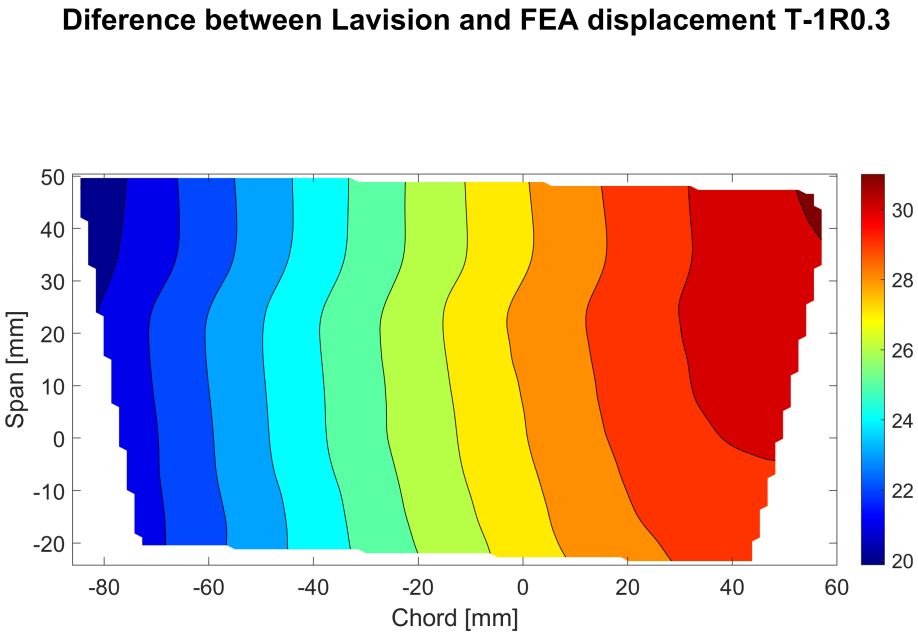

(a) Lavision - FEA displacement T-1R0.3

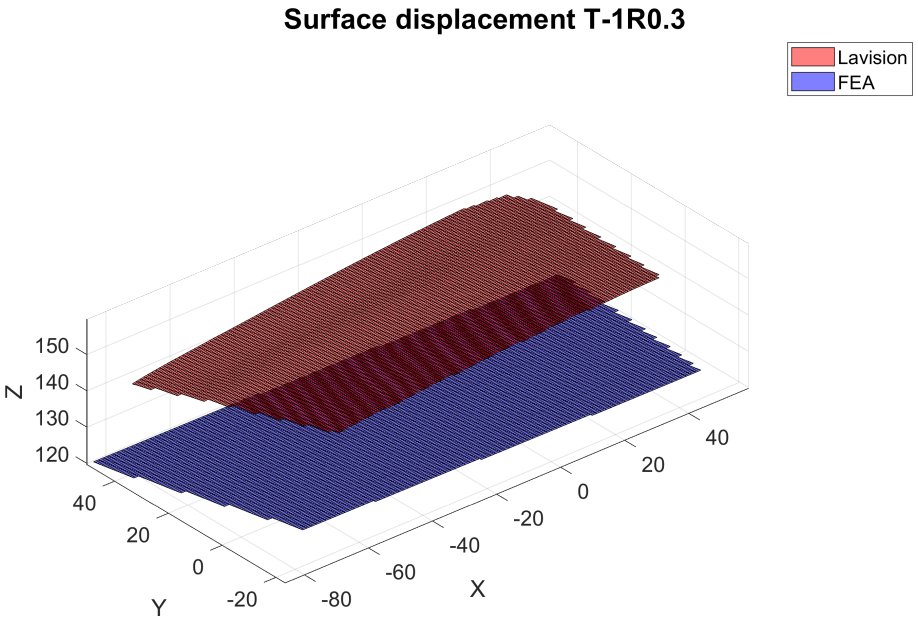

(b) Surface displacement T-1R0.3

Figure C.19: Simulation case T-1R0.3isotropic model

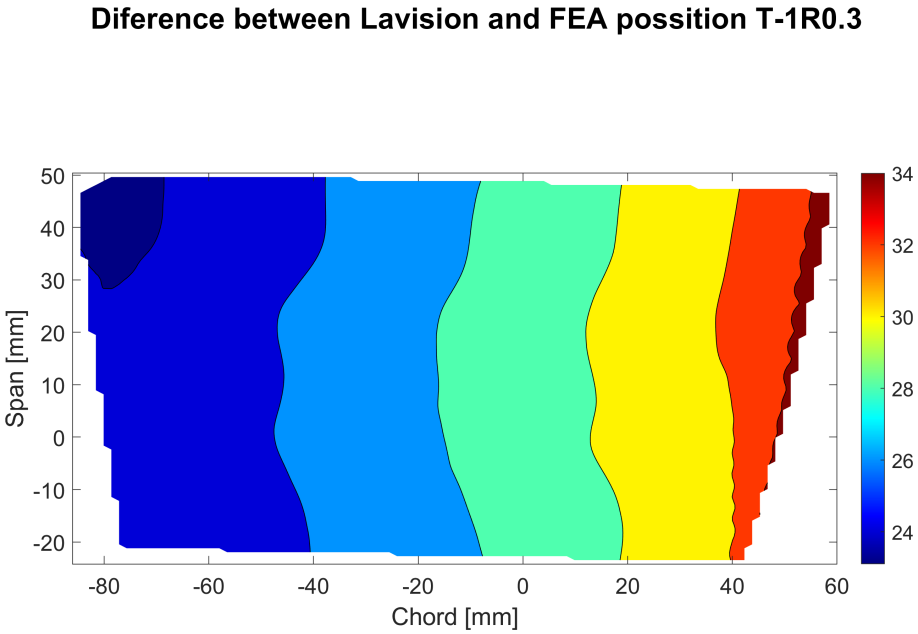

(a) Lavision - FEA possition T-1R0.3

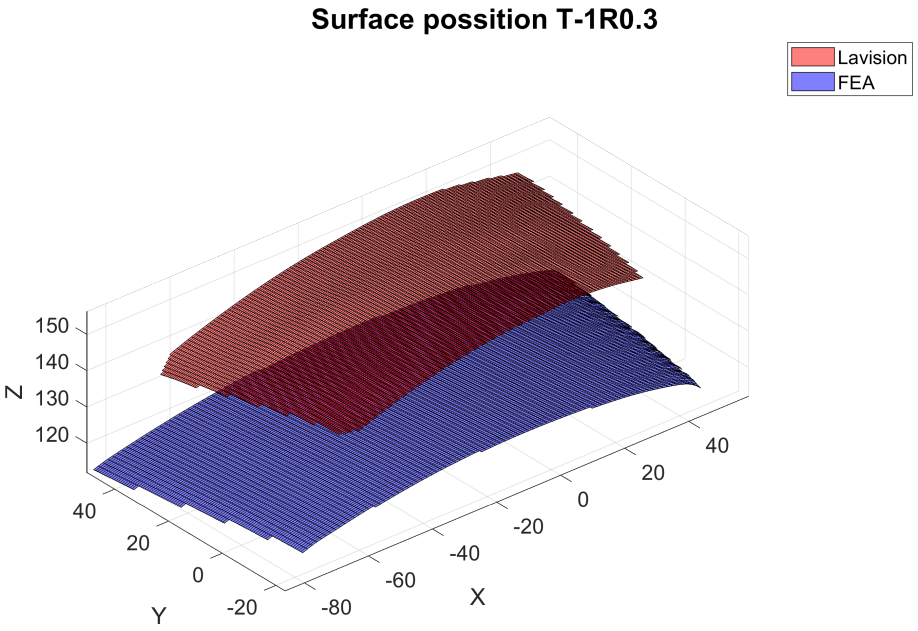

(b) Surface possition T-1R0.3

Figure C.20: Simulation case T-1R0.3isotropic model

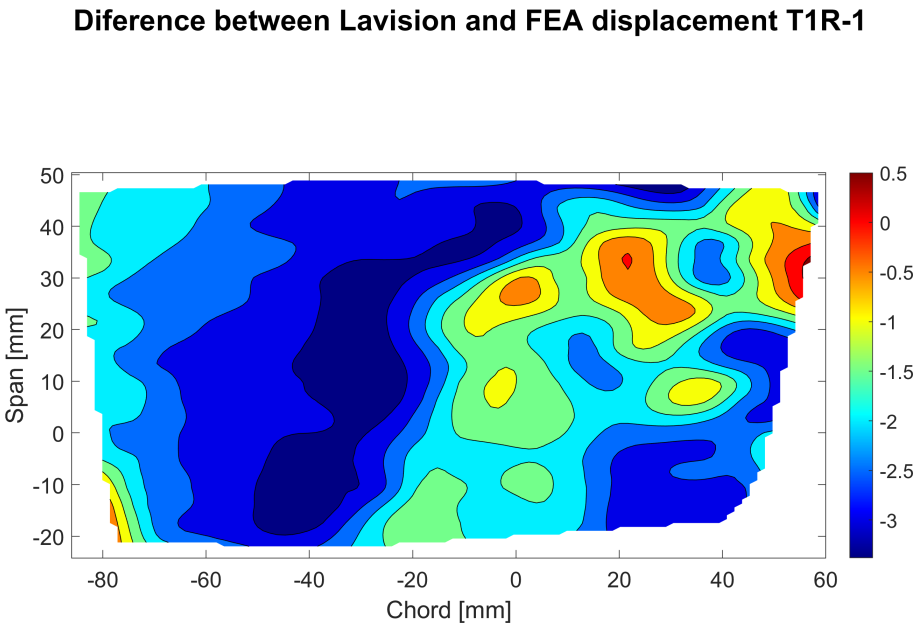

(a) Lavision - FEA displacement T1R-1

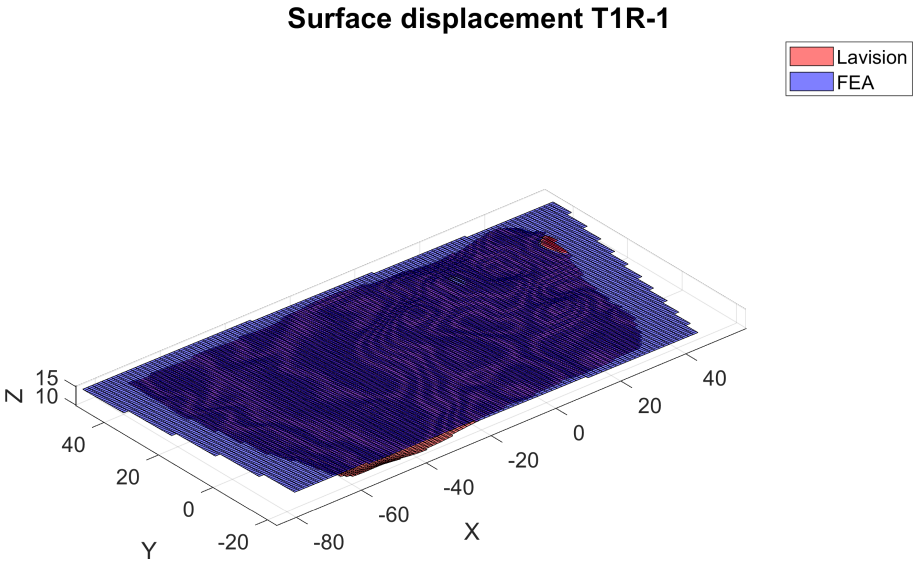

(b) Surface displacement T1R-1

Figure C.21: Simulation case T1R-1isotropic model

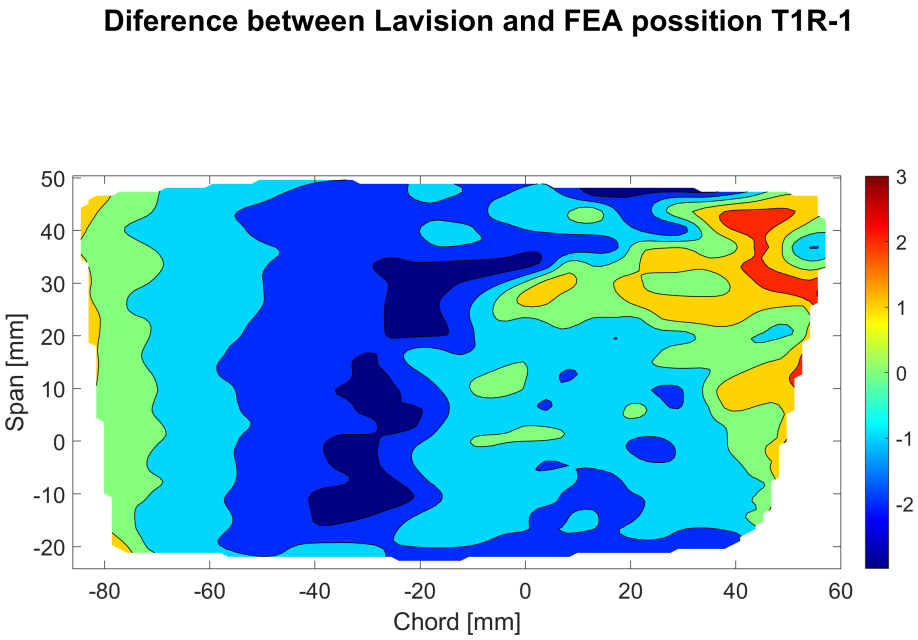

(a) Lavision - FEA possition T1R-1

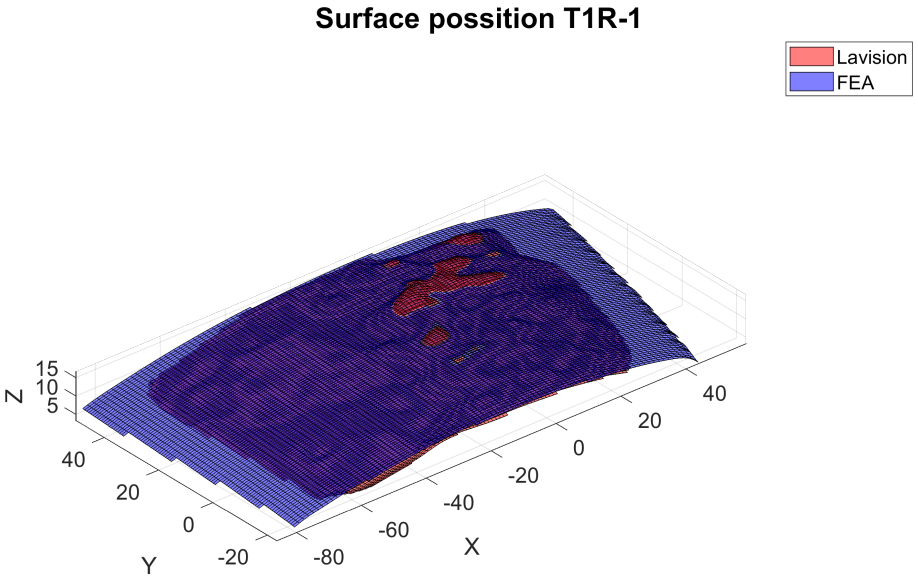

(b) Surface possition T1R-1

Figure C.22: Simulation case T1R-1isotropic model

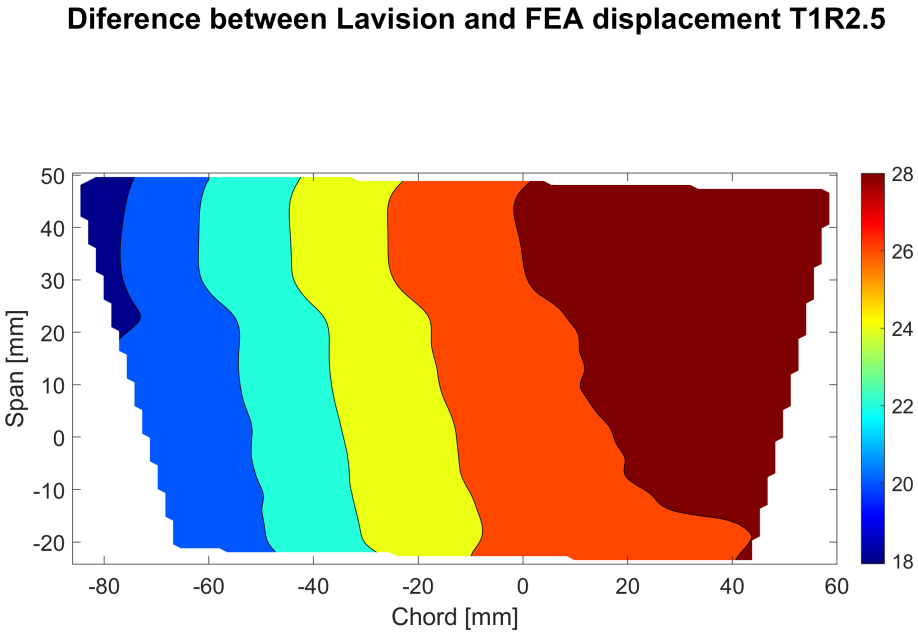

(a) Lavision - FEA displacement T1R2.5

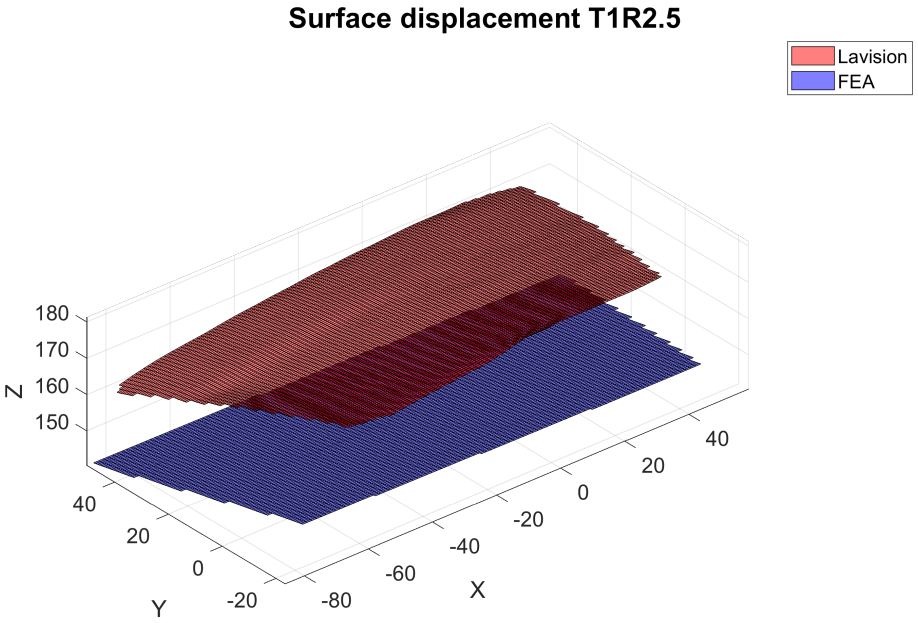

(b) Surface displacement T1R2.5

Figure C.23: Simulation case T1R2.5isotropic model

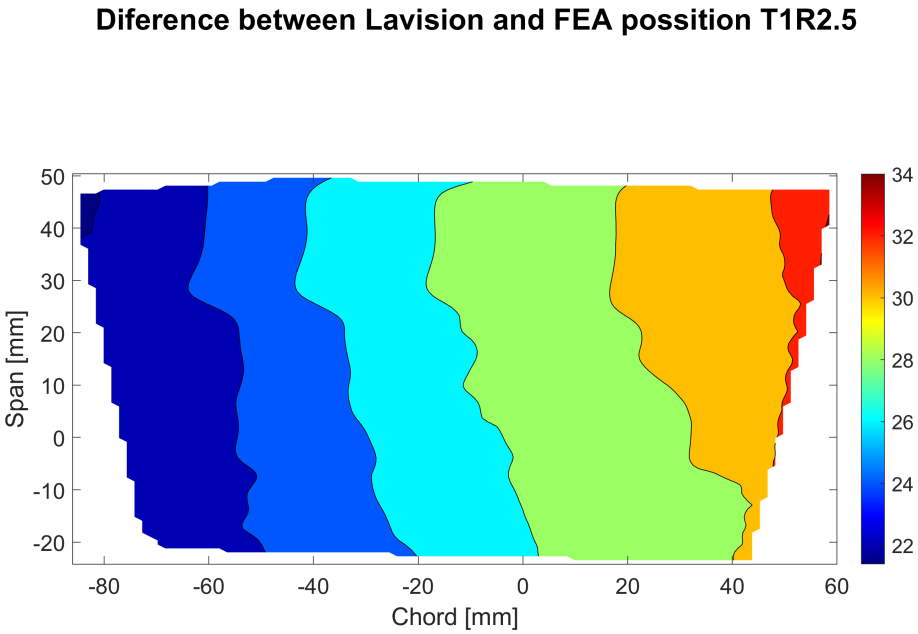

(a) Lavision - FEA possition T1R2.5

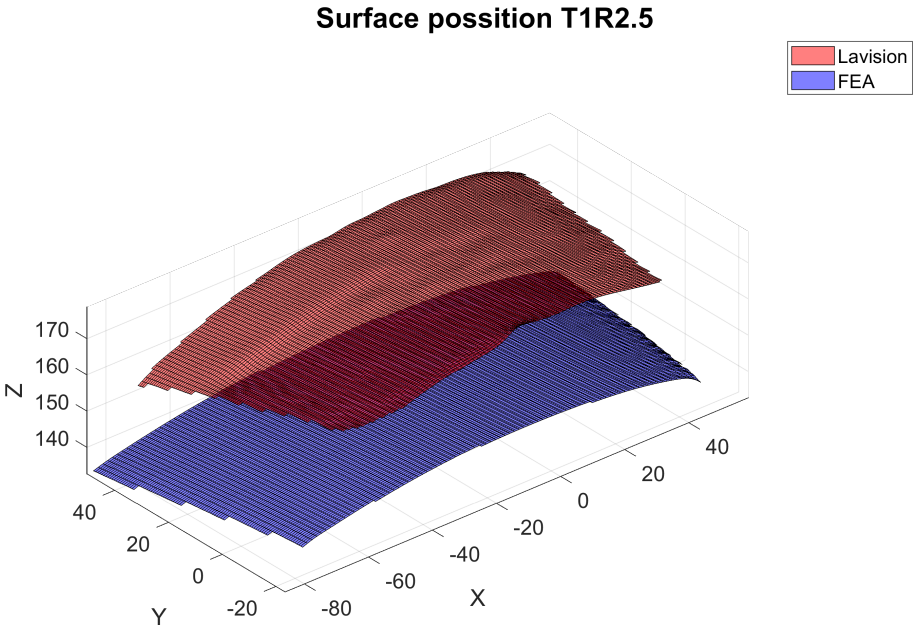

(b) Surface possition T1R2.5

Figure C.24: Simulation case T1R2.5isotropic model

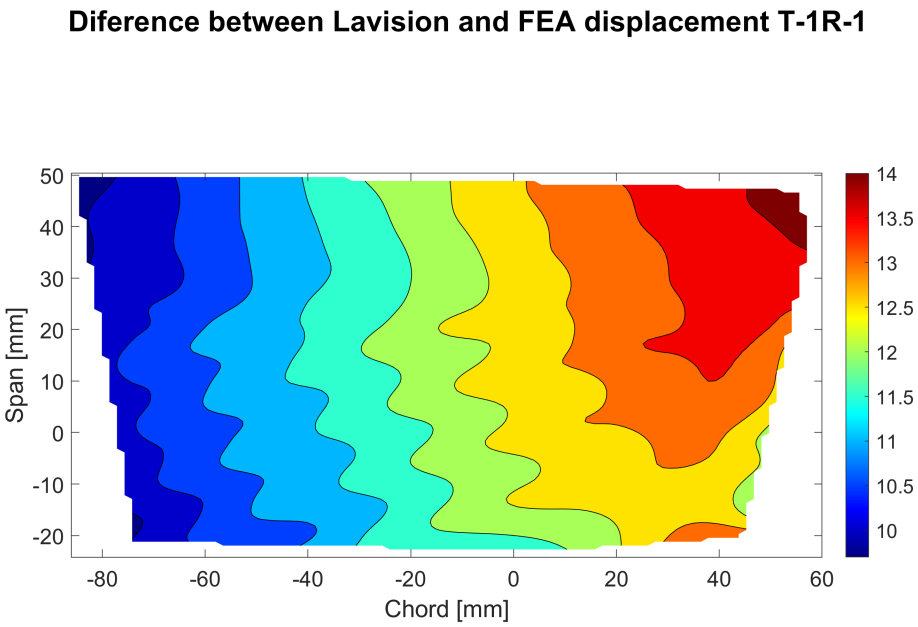

(a) Lavision - FEA displacement T-1R-1

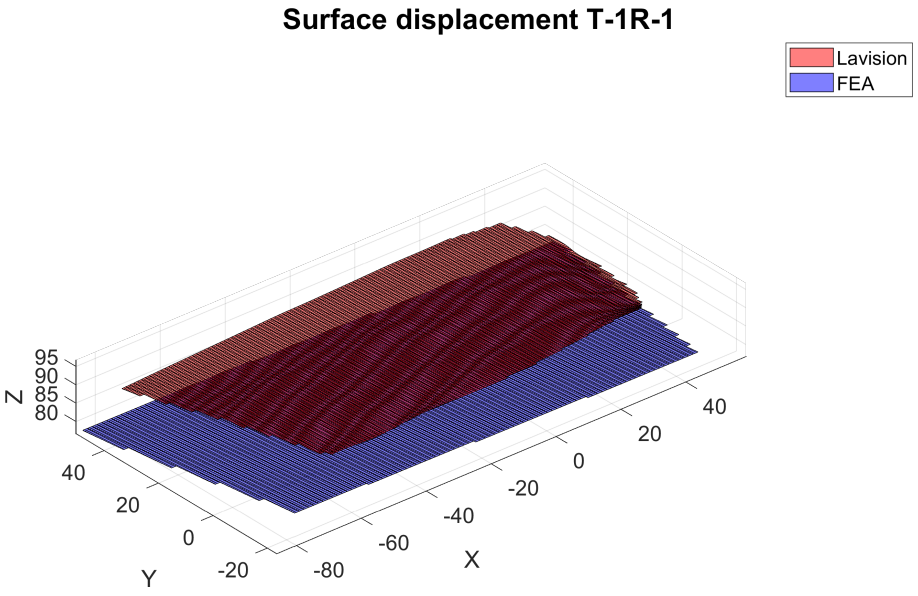

(b) Surface displacement T-1R-1

Figure C.25: Simulation case T-1R-1isotropic model

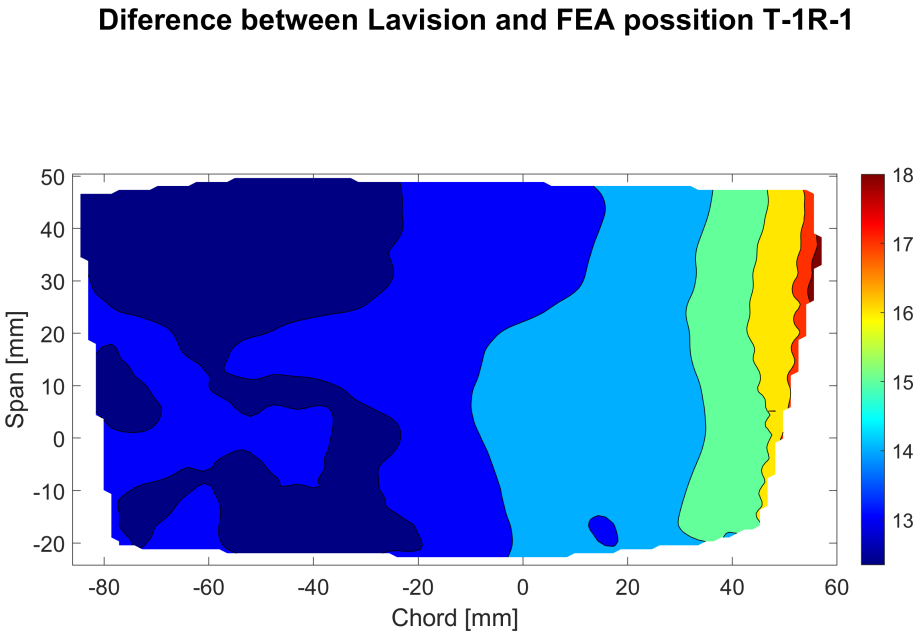

(a) Lavision - FEA possition T-1R-1

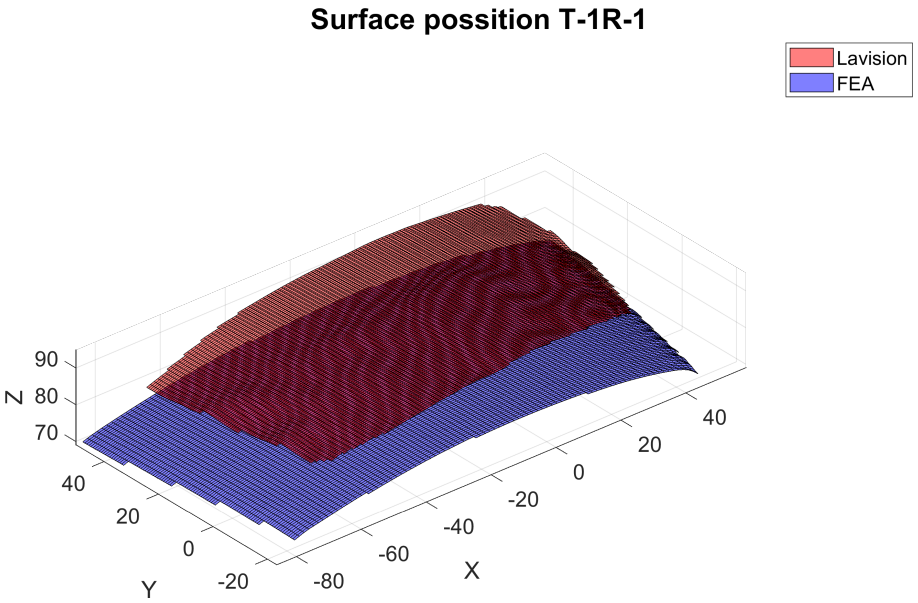

(b) Surface possition T-1R-1

Figure C.26: Simulation case T-1R-1isotropic model

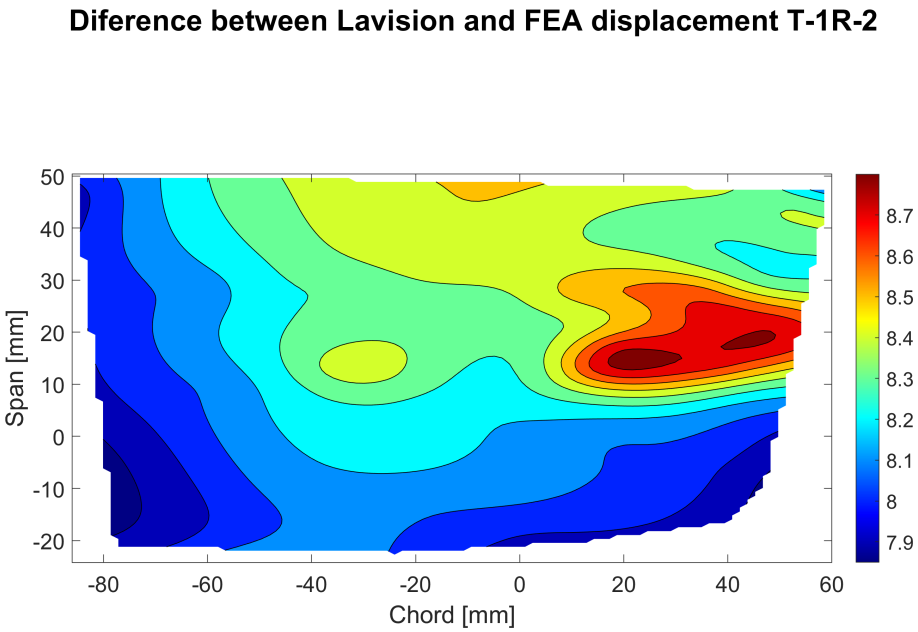

(a) Lavision - FEA displacement T-1R-2

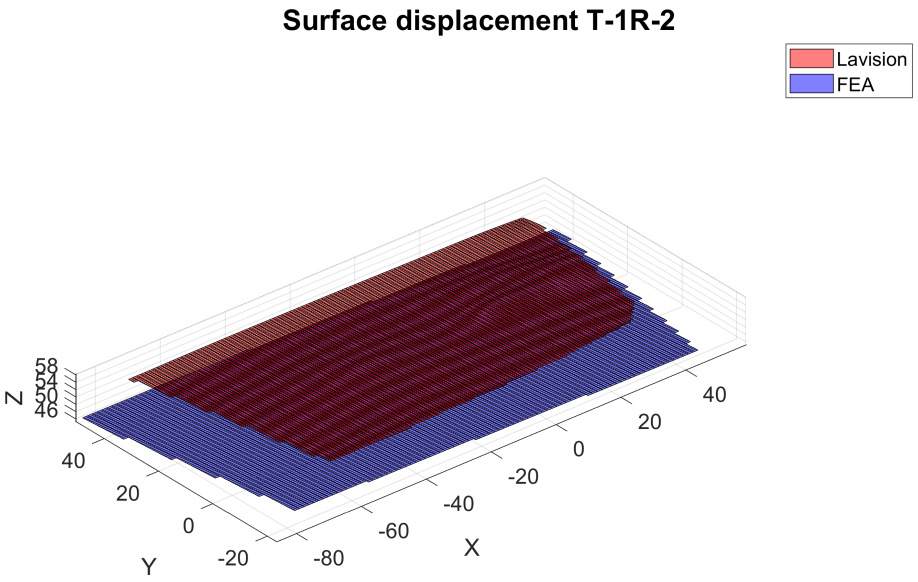

(b) Surface displacement T-1R-2

Figure C.27: Simulation case T-1R-2isotropic model

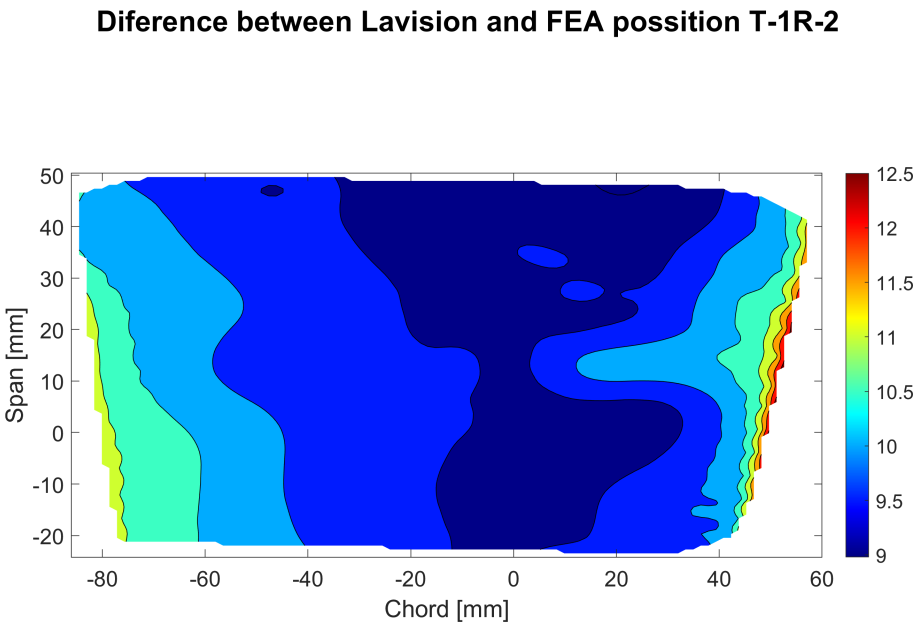

(a) Lavision - FEA possition T-1R-2

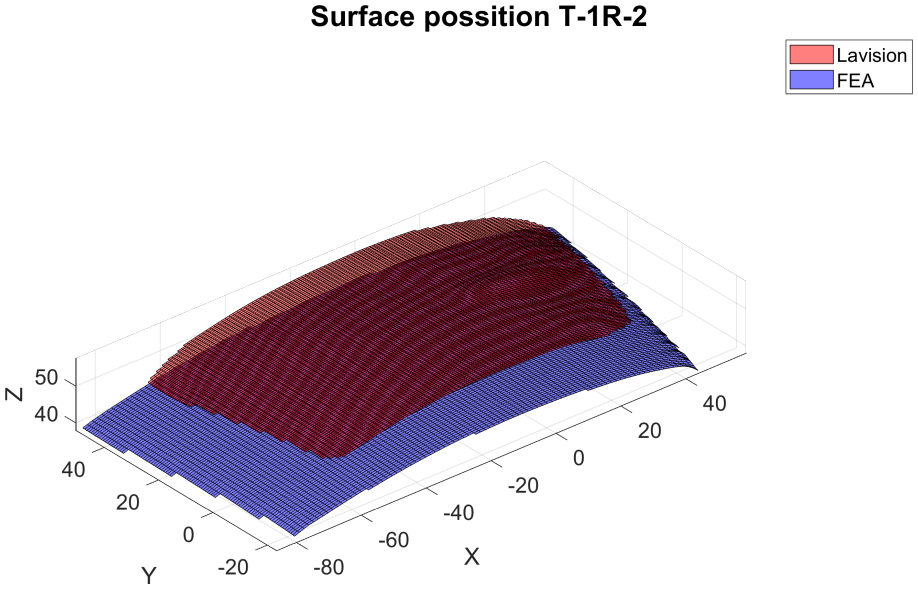

(b) Surface possition T-1R-2

Figure C.28: Simulation case T-1R-2isotropic model

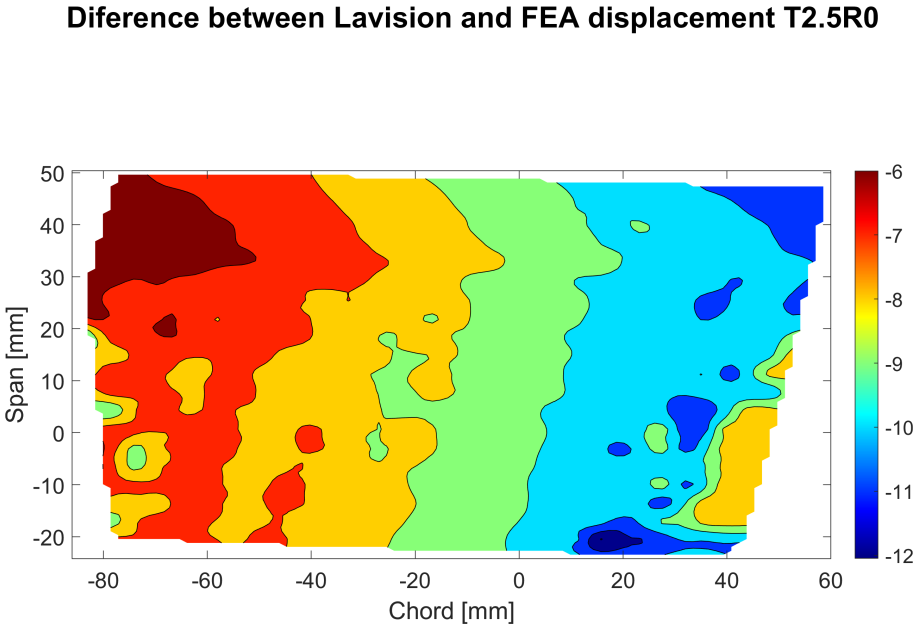

(a) Lavision - FEA displacement T2.5R0

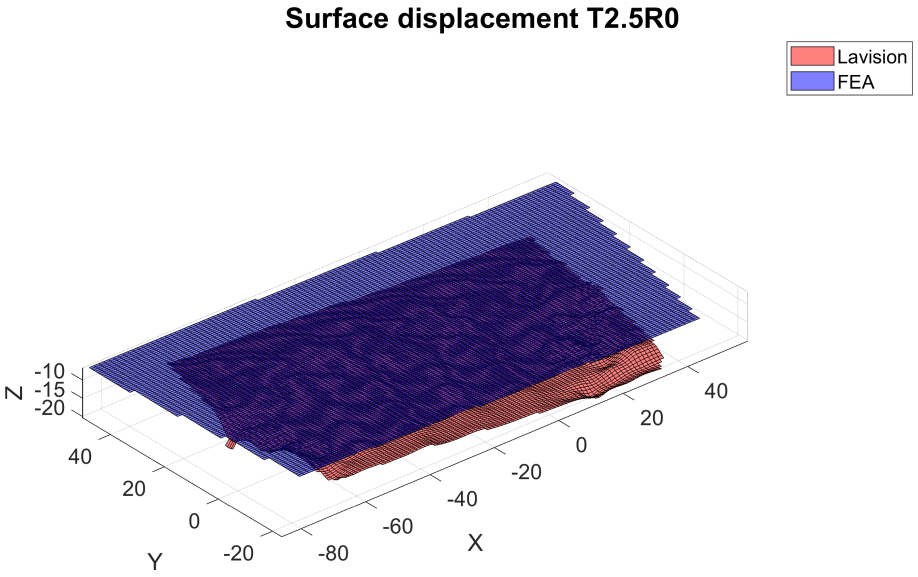

(b) Surface displacement T2.5R0

Figure C.29: Simulation case T2.5R0isotropic model

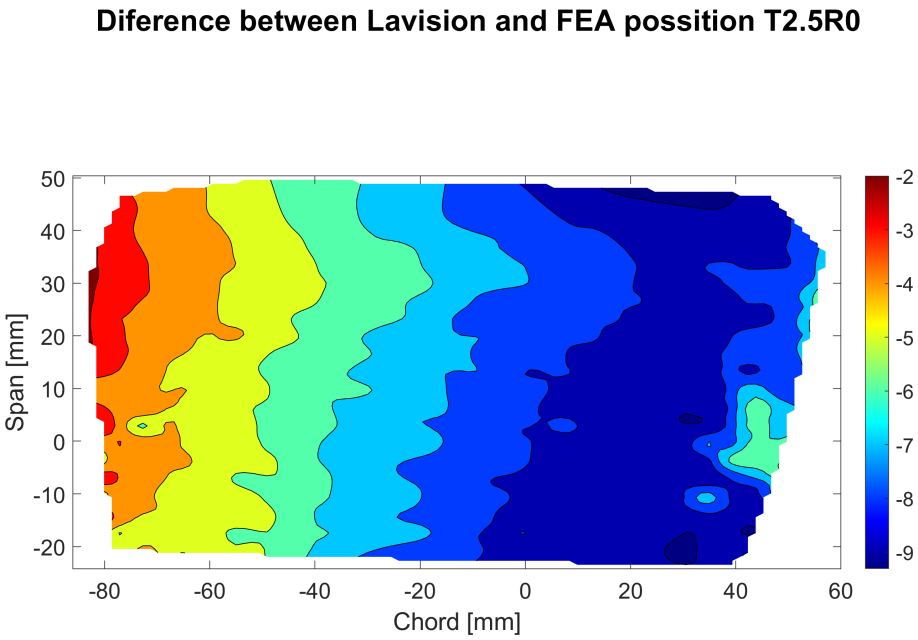

(a) Lavision - FEA possition T2.5R0

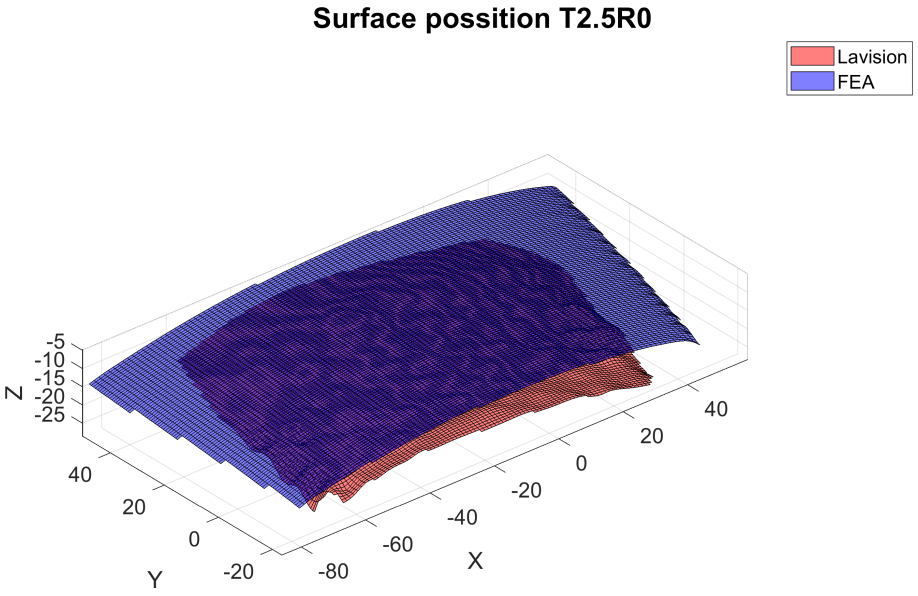

(b) Surface possition T2.5R0

Figure C.30: Simulation case T2.5R0isotropic model

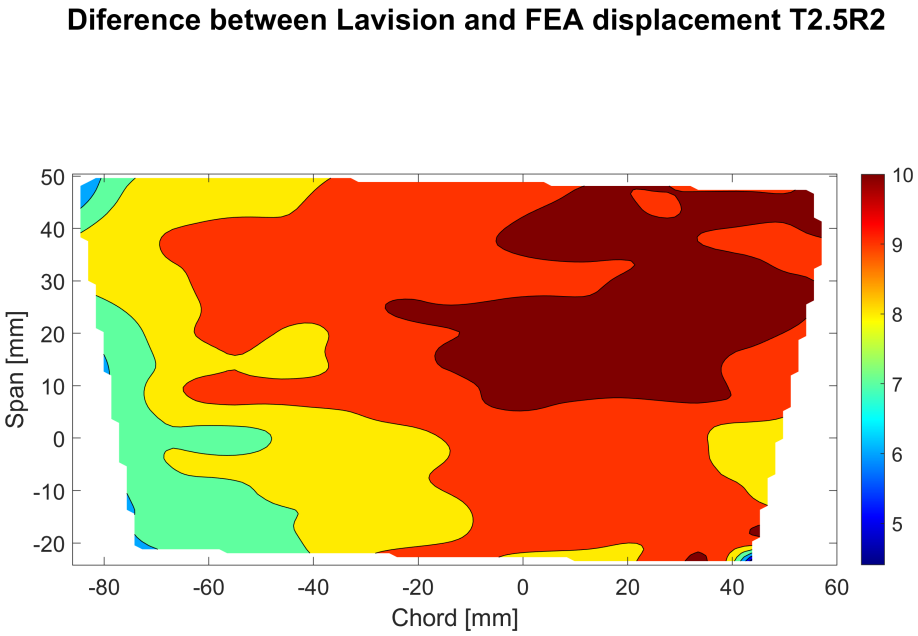

(a) Lavision - FEA displacement T2.5R2

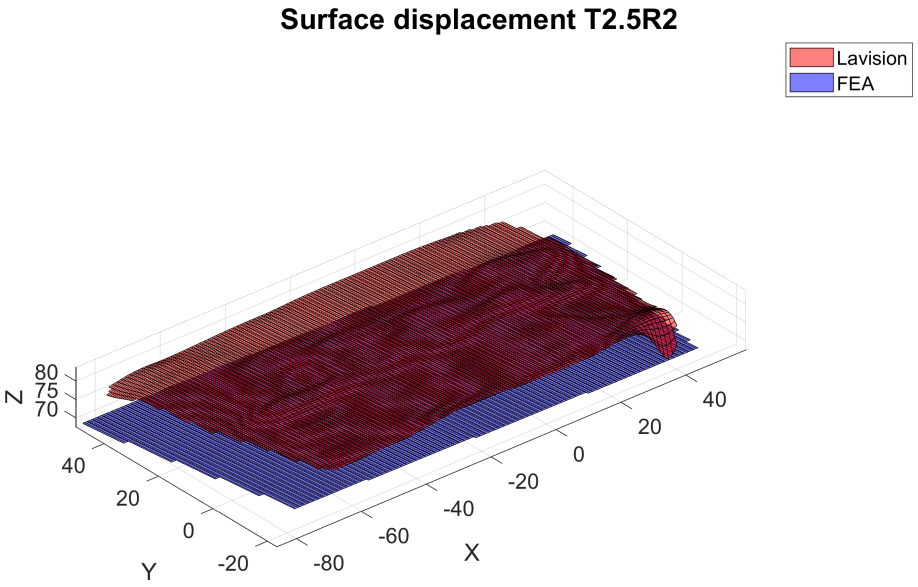

(b) Surface displacement T2.5R2

Figure C.31: Simulation case T2.5R2isotropic model

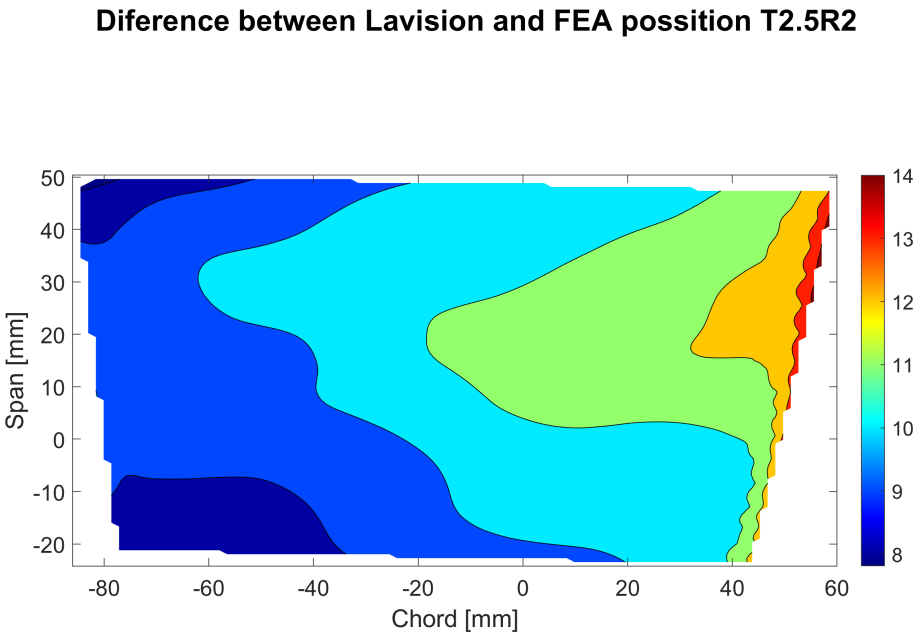

(a) Lavision - FEA possition T2.5R2

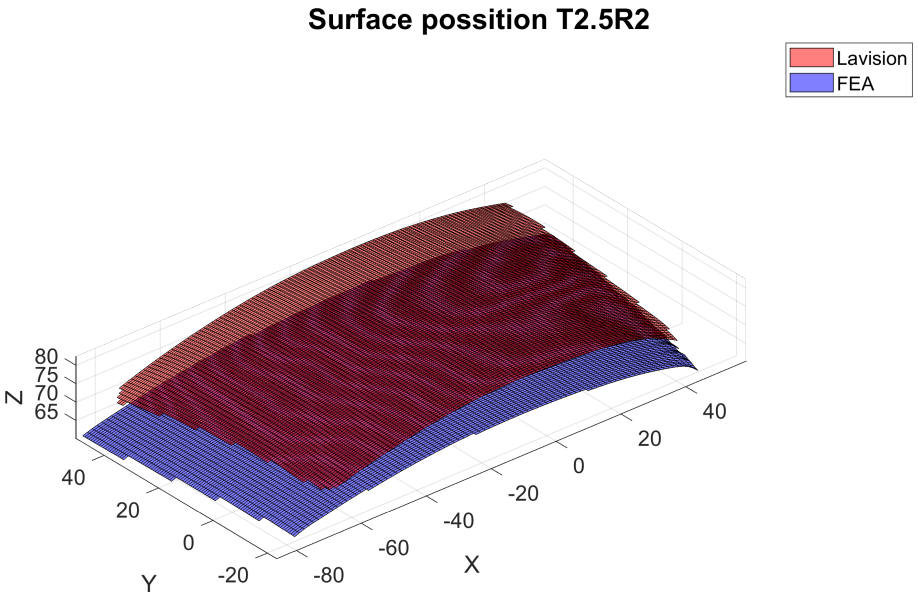

(b) Surface possition T2.5R2

Figure C.32: Simulation case T2.5R2isotropic model

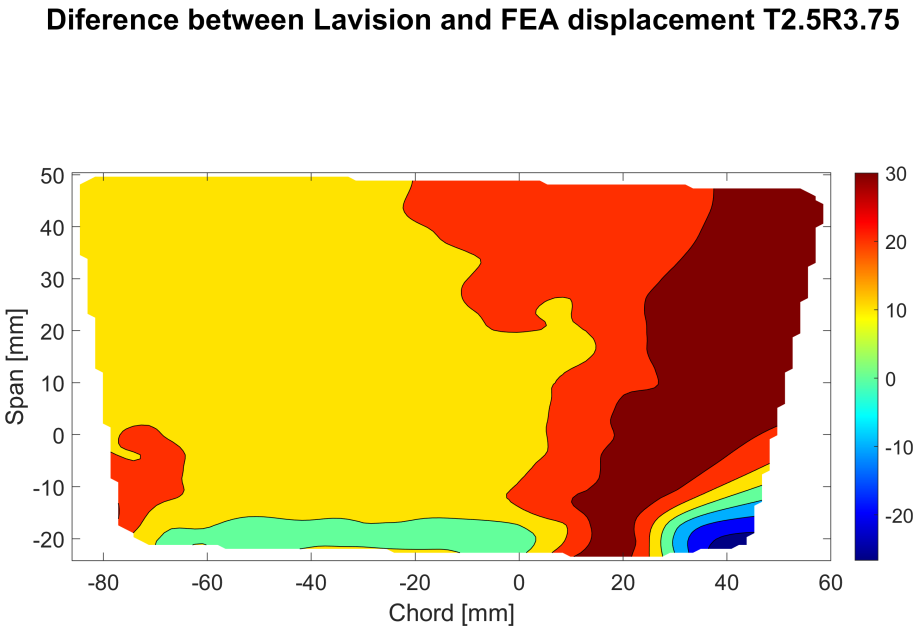

(a) Lavision - FEA displacement T2.5R3.75

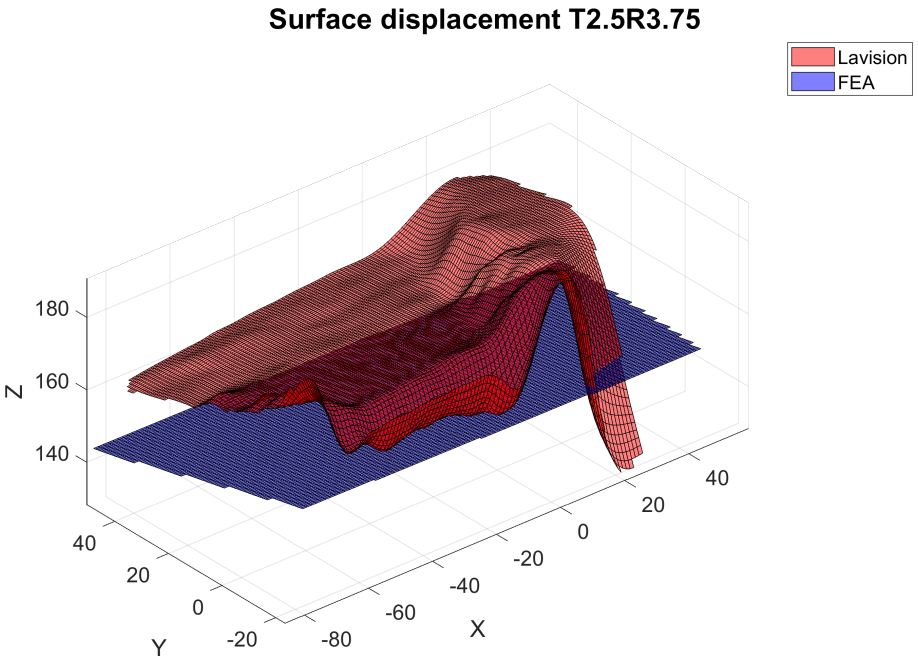

(b) Surface displacement T2.5R3.75

Figure C.33: Simulation case T2.5R3.75isotropic model

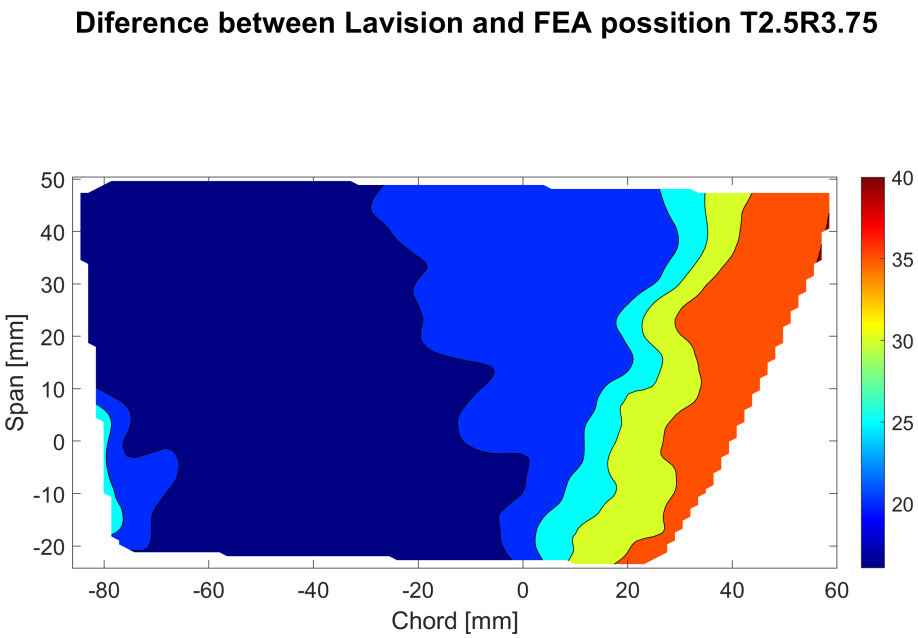

(a) Lavision - FEA possition T2.5R3.75

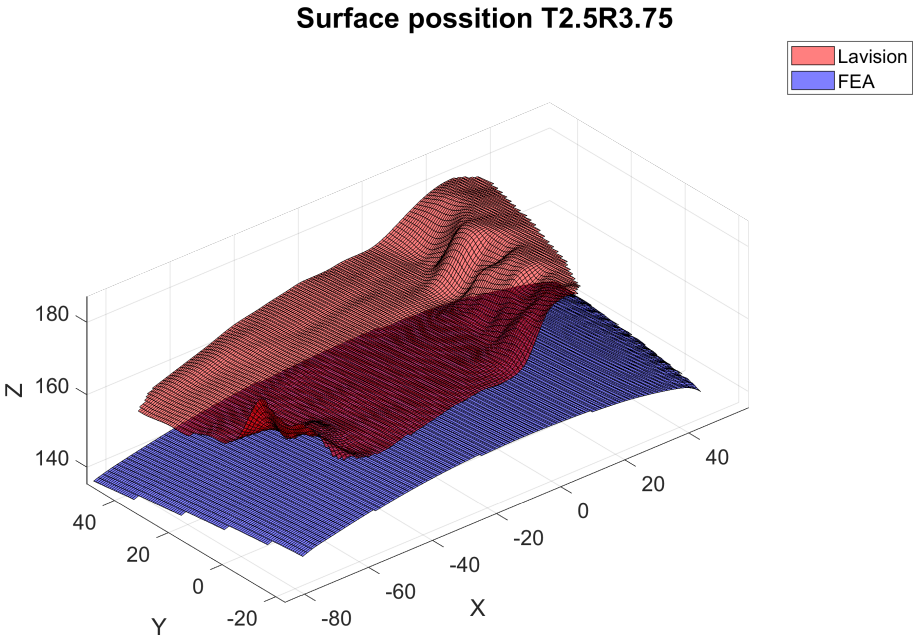

(b) Surface possition T2.5R3.75

Figure C.34: Simulation case T2.5R3.75isotropic model

C.2 Mean displacement during testing

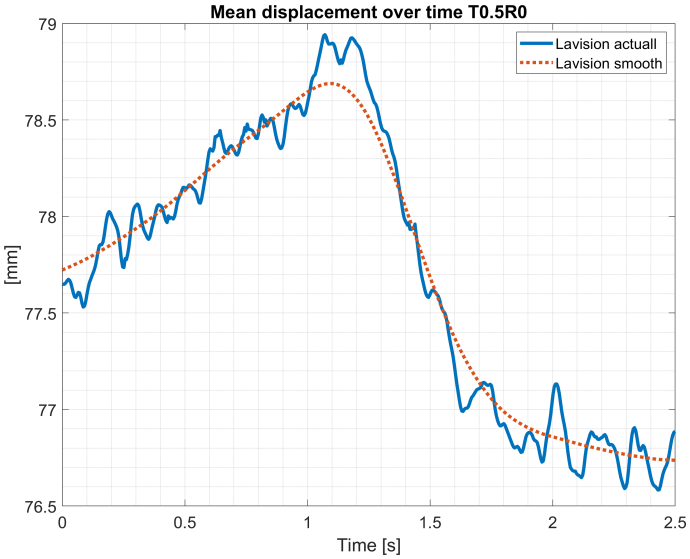

Figure C.35: Mean displacement, normalized and scaled T0.5R0 isotropic model

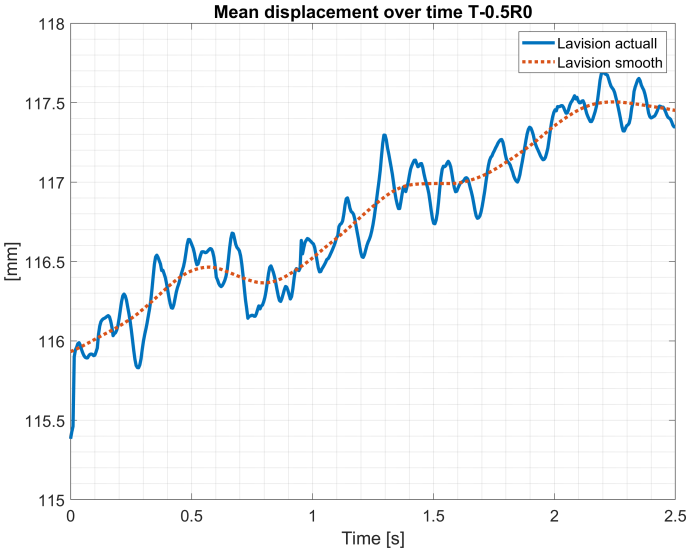

Figure C.36: Mean displacement, normalized and scaled T-0.5R0 isotropic model

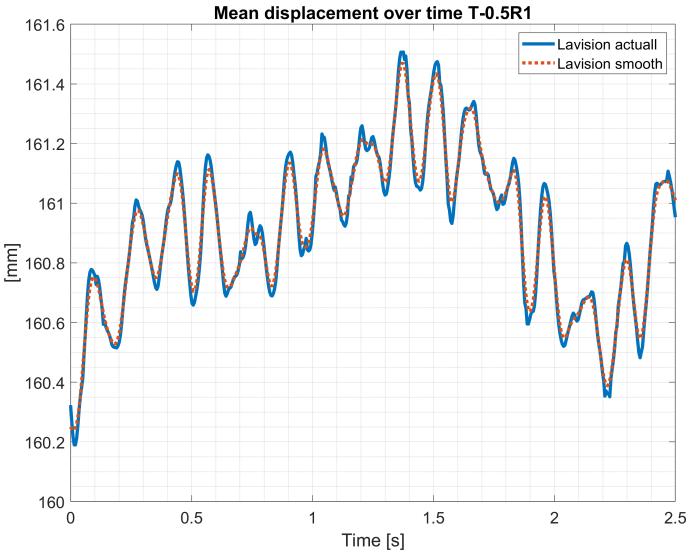

Figure C.37: Mean displacement, normalized and scaled T-0.5R1 isotropic model

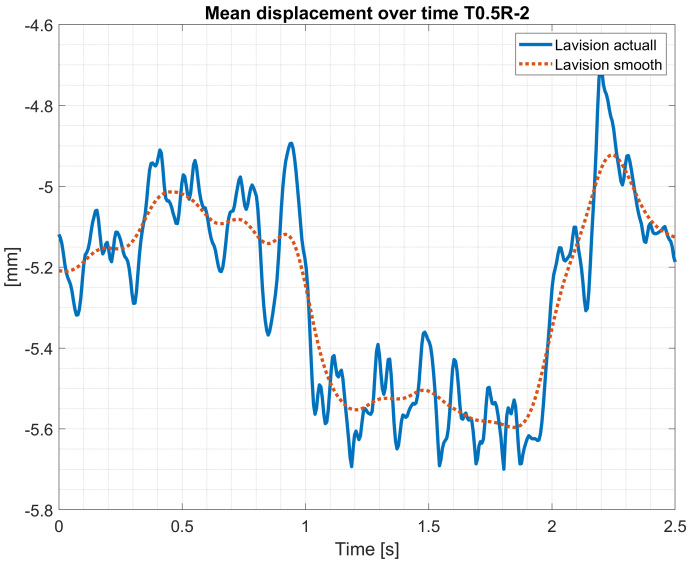

Figure C.38: Mean displacement, normalized and scaled T0.5R-2 isotropic model

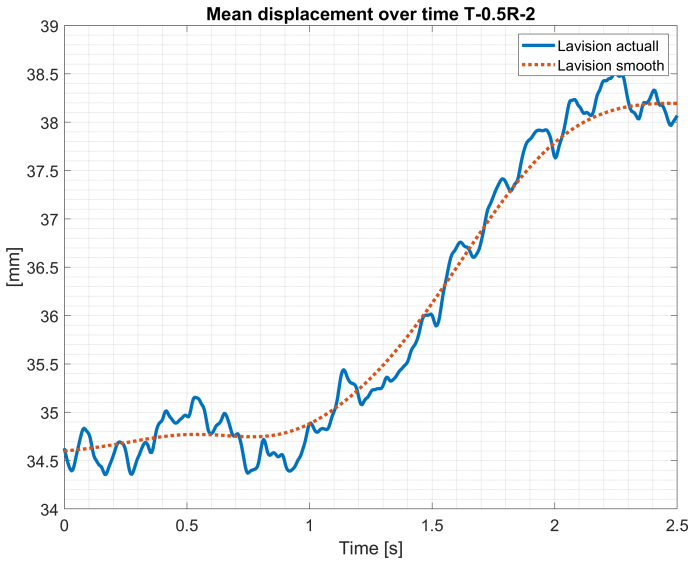

Figure C.39: Mean displacement, normalized and scaled T-0.5R-2 isotropic model

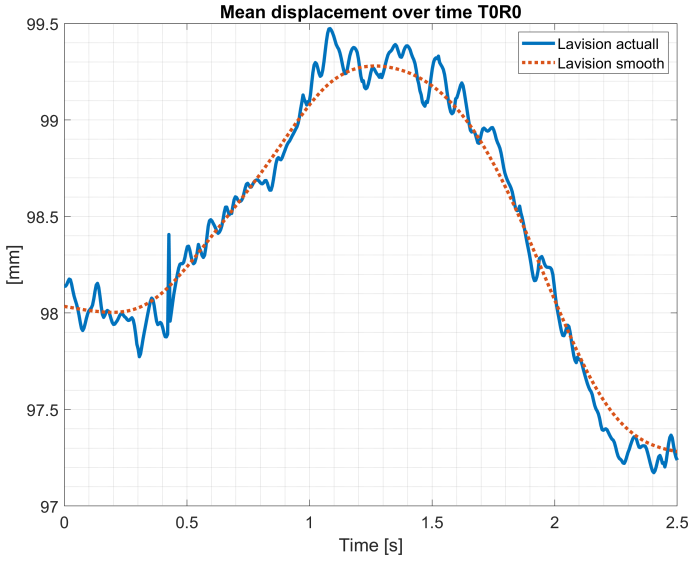

Figure C.40: Mean displacement, normalized and scaled T0R0 isotropic model

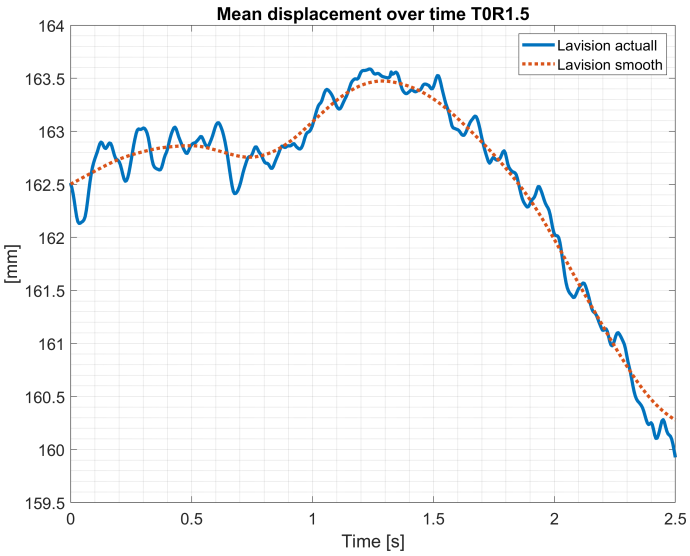

Figure C.41: Mean displacement, normalized and scaled T0R1.5 isotropic model

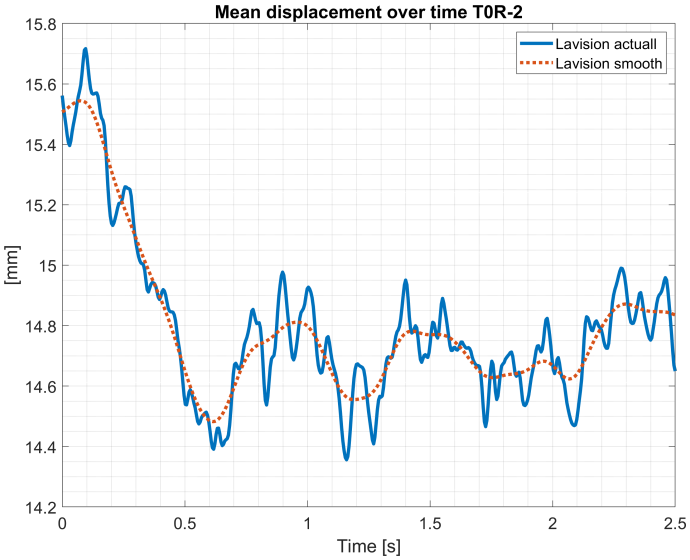

Figure C.42: Mean displacement, normalized and scaled T0R-2 isotropic model

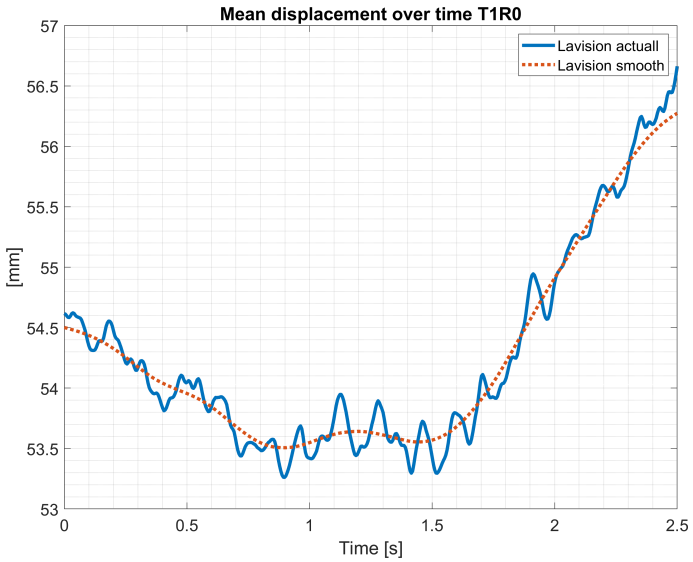

Figure C.43: Mean displacement, normalized and scaled T1R0 isotropic model

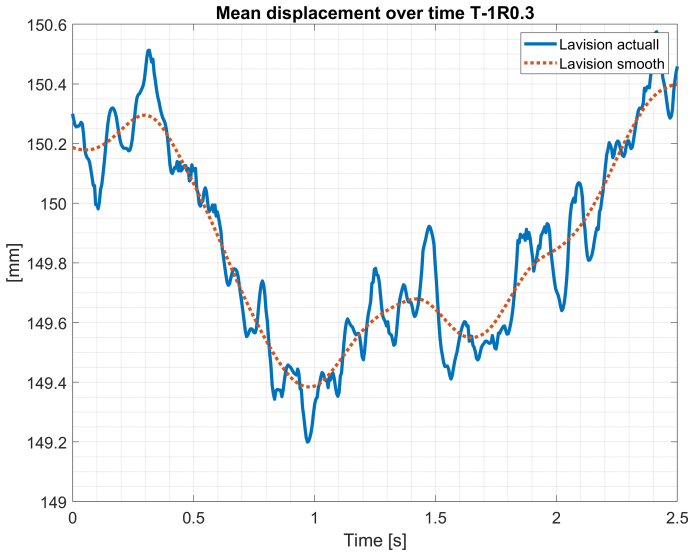

Figure C.44: Mean displacement, normalized and scaled T-1R0.3 isotropic model

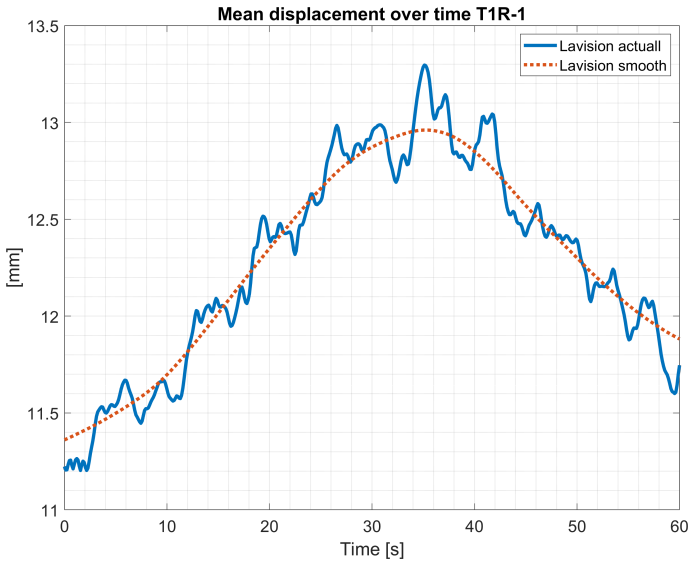

Figure C.45: Mean displacement, normalized and scaled T1R-1 isotropic model

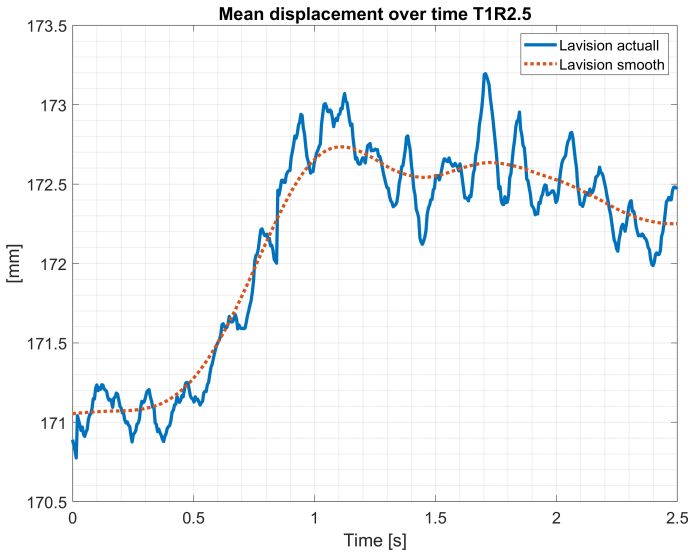

Figure C.46: Mean displacement, normalized and scaled T1R2.5 isotropic model

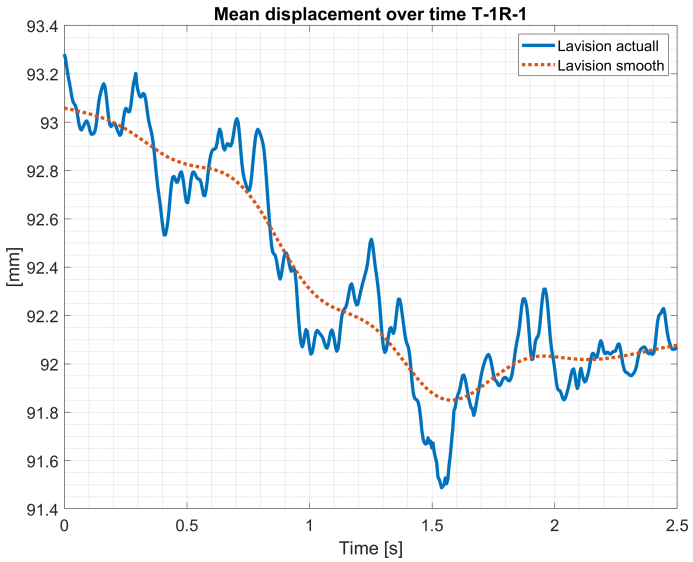

Figure C.47: Mean displacement, normalized and scaled T-1R-1 isotropic model

Figure C.48: Mean displacement, normalized and scaled T-1R-2 isotropic model

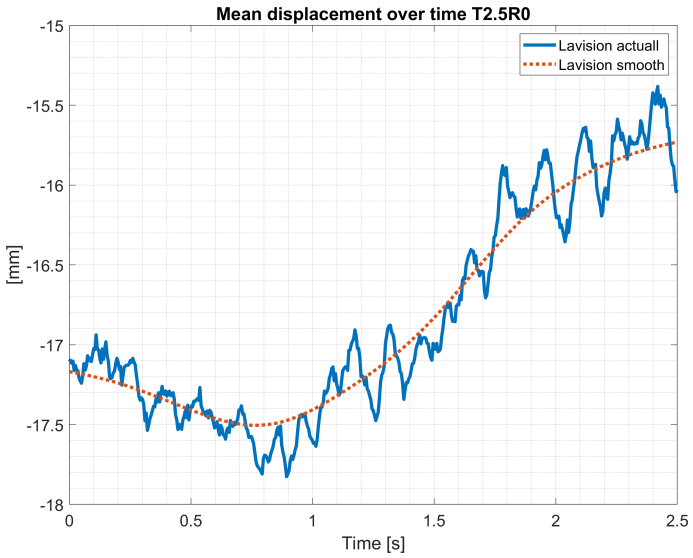

Figure C.49: Mean displacement, normalized and scaled T2.5R0 isotropic model

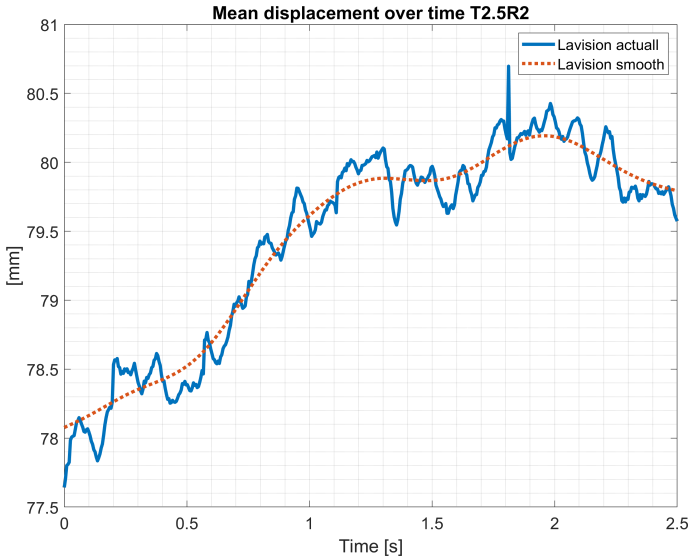

Figure C.50: Mean displacement, normalized and scaled T2.5R2 isotropic model

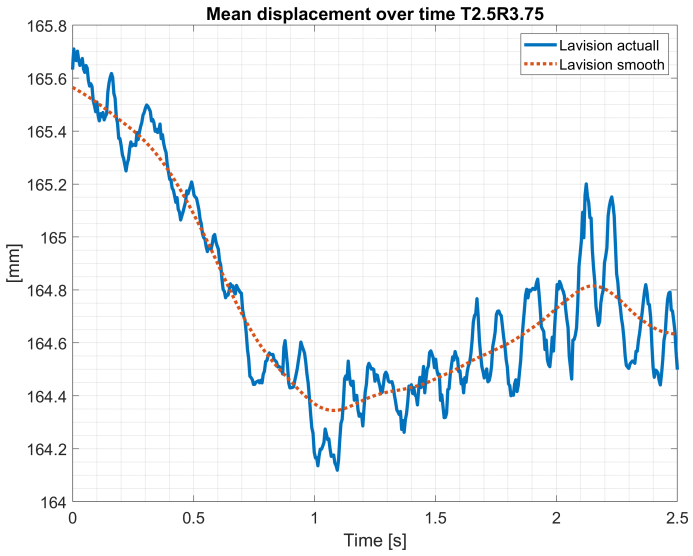

Figure C.51: Mean displacement, normalized and scaled T2.5R3.75 isotropic model

C.3 Mean displacement in test cases with FEA

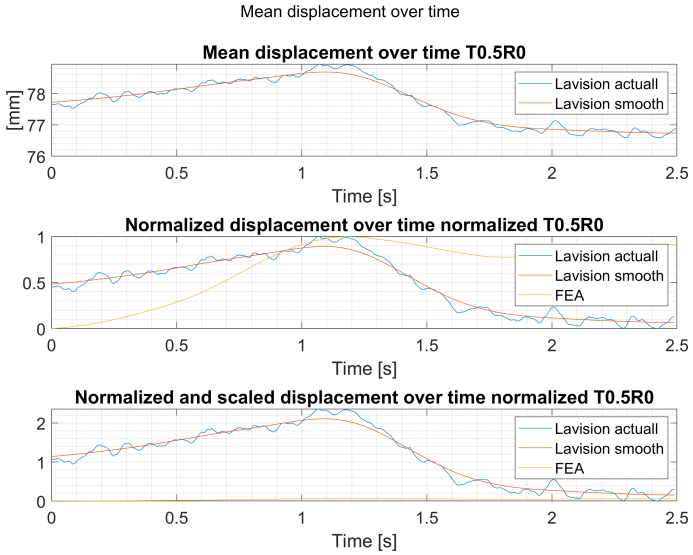

Figure C.52: Mean displacement, normalized and scaled T0.5R0 isotropic model

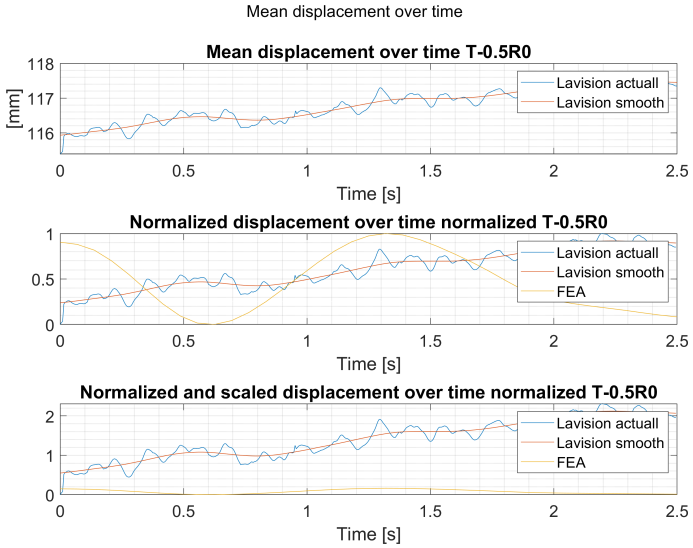

Figure C.53: Mean displacement, normalized and scaled T-0.5R0 isotropic model

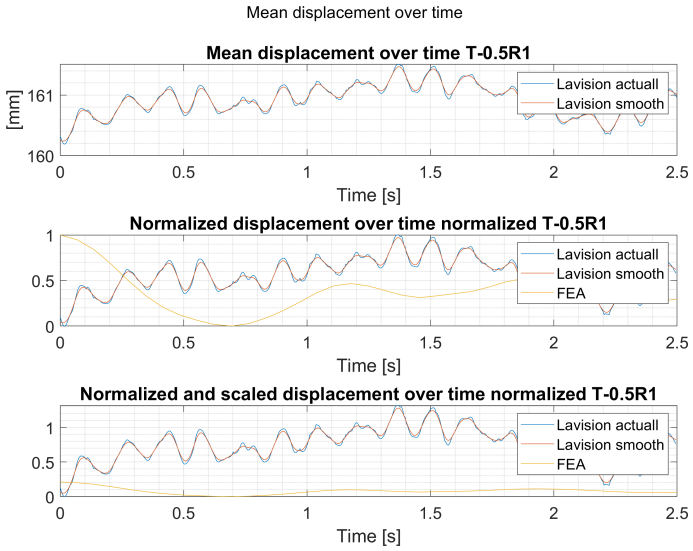

Figure C.54: Mean displacement, normalized and scaled T-0.5R1 isotropic model

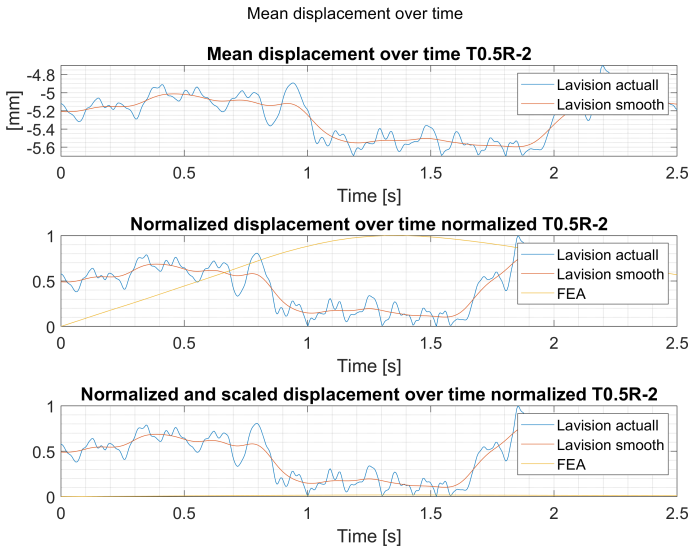

Figure C.55: Mean displacement, normalized and scaled T0.5R-2 isotropic model

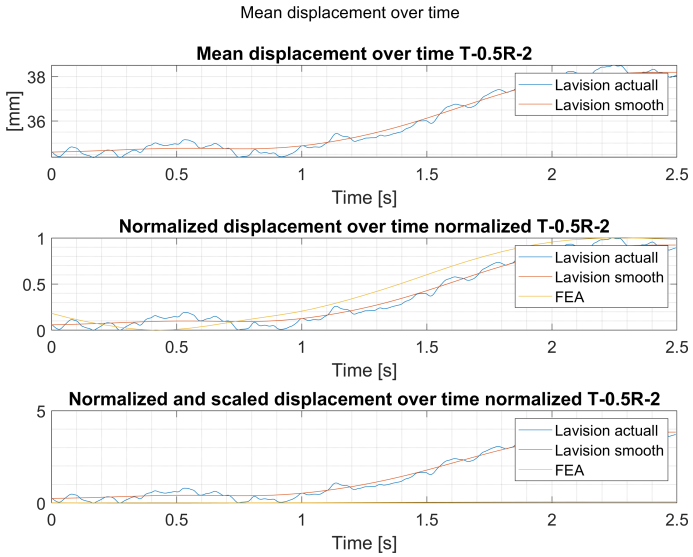

Figure C.56: Mean displacement, normalized and scaled T-0.5R-2 isotropic model

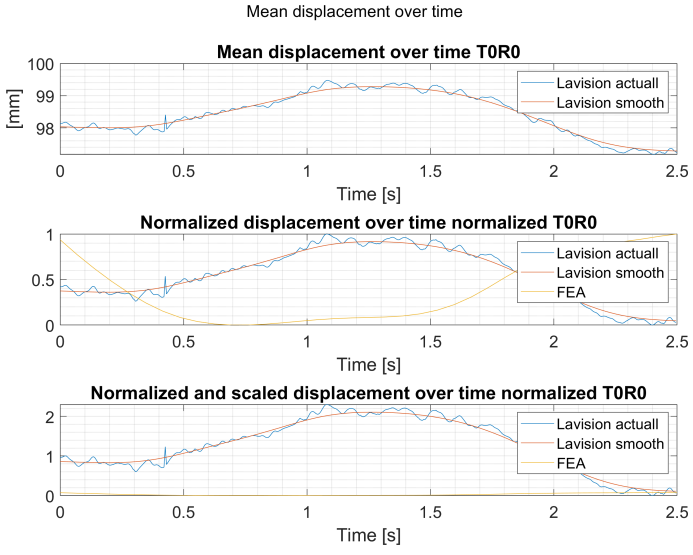

Figure C.57: Mean displacement, normalized and scaled T0R0 isotropic model

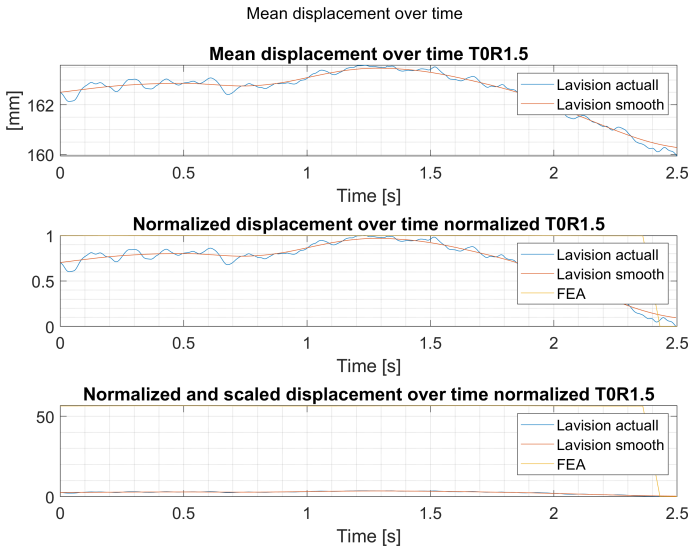

Figure C.58: Mean displacement, normalized and scaled T0R1.5 isotropic model

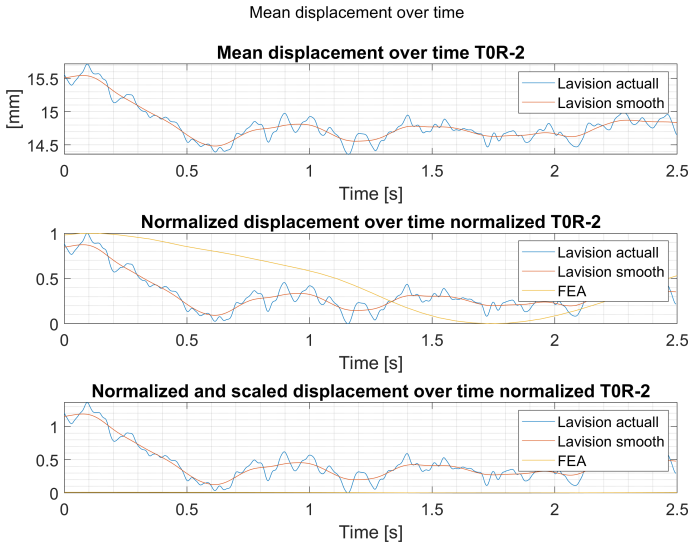

Figure C.59: Mean displacement, normalized and scaled T0R-2 isotropic model

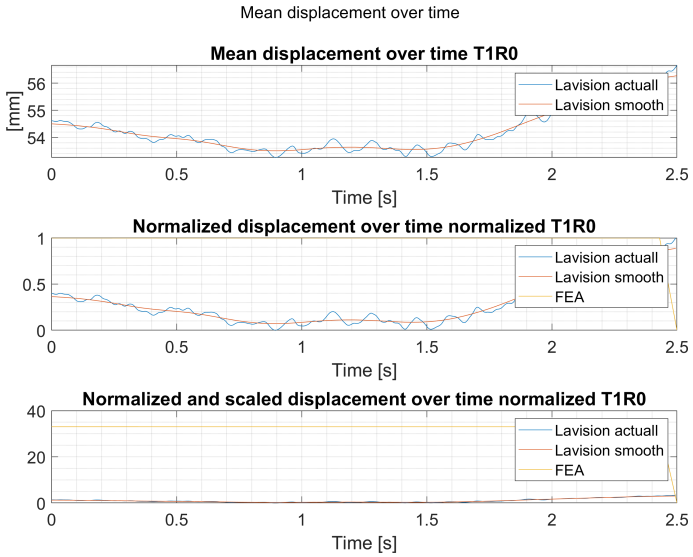

Figure C.60: Mean displacement, normalized and scaled T1R0 isotropic model

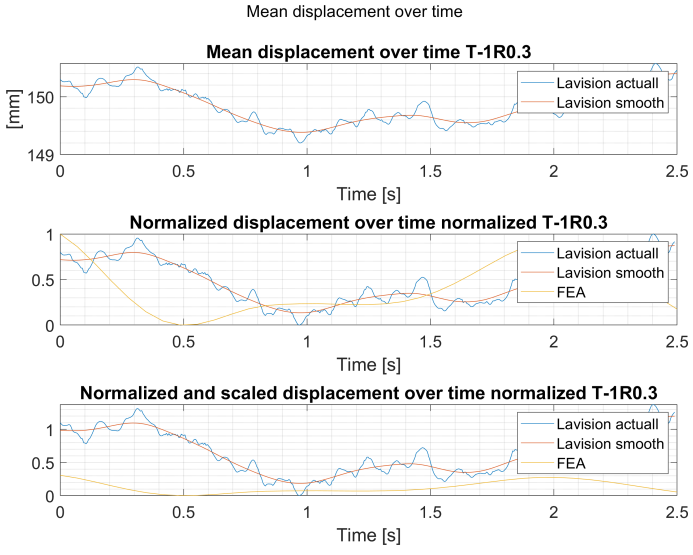

Figure C.61: Mean displacement, normalized and scaled T-1R0.3 isotropic model

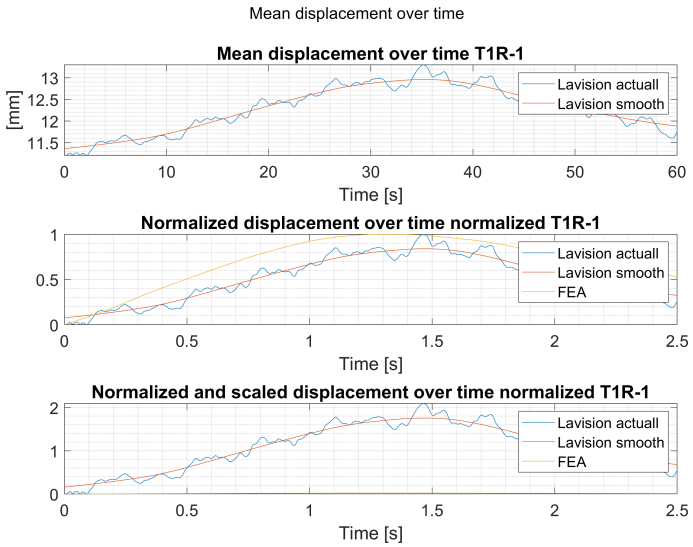

Figure C.62: Mean displacement, normalized and scaled T1R-1 isotropic model

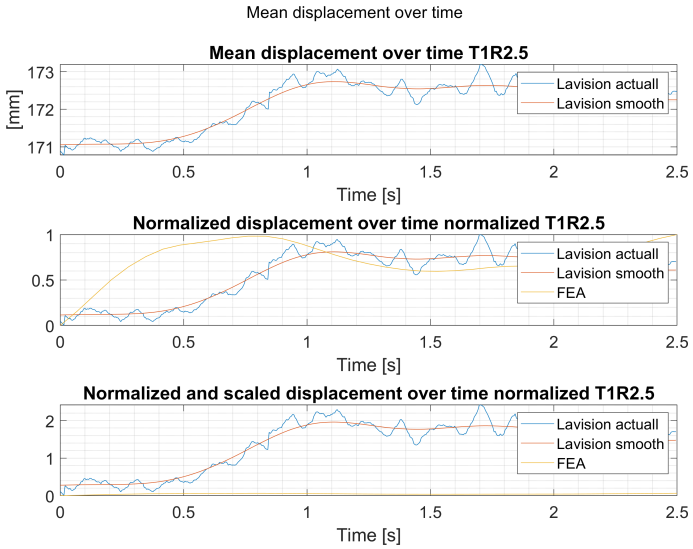

Figure C.63: Mean displacement, normalized and scaled T1R2.5 isotropic model

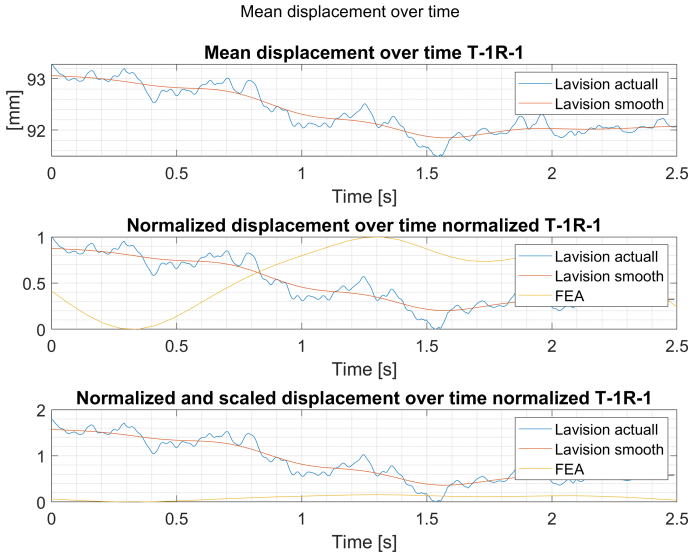

Figure C.64: Mean displacement, normalized and scaled T-1R-1 isotropic model

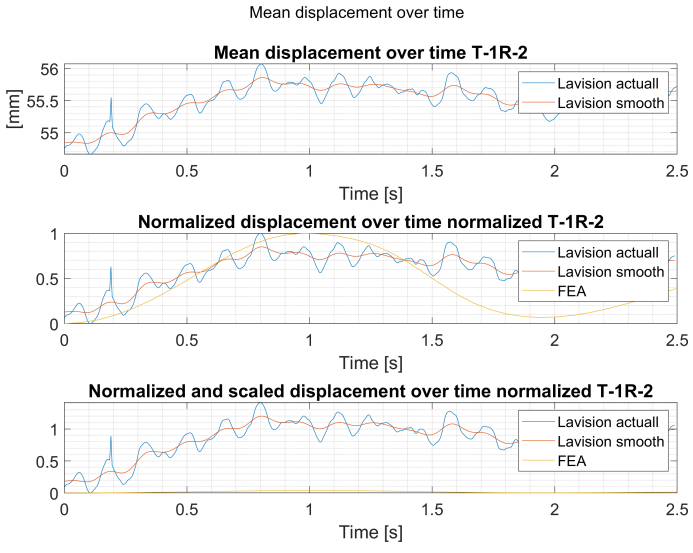

Figure C.65: Mean displacement, normalized and scaled T-1R-2 isotropic model

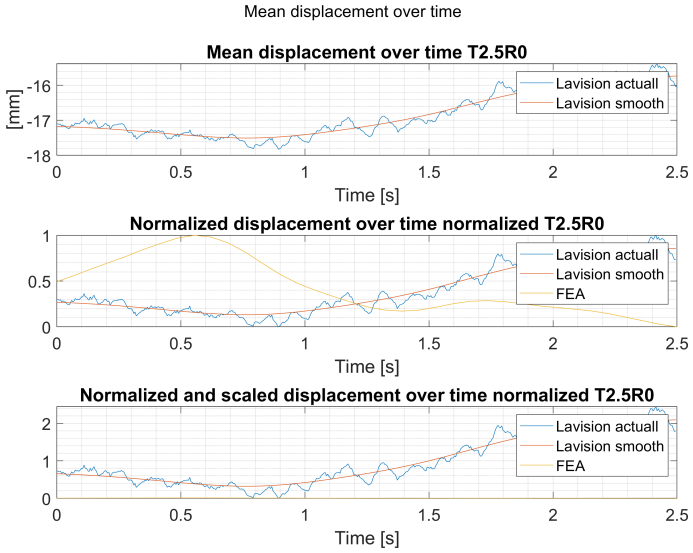

Figure C.66: Mean displacement, normalized and scaled T2.5R0 isotropic model

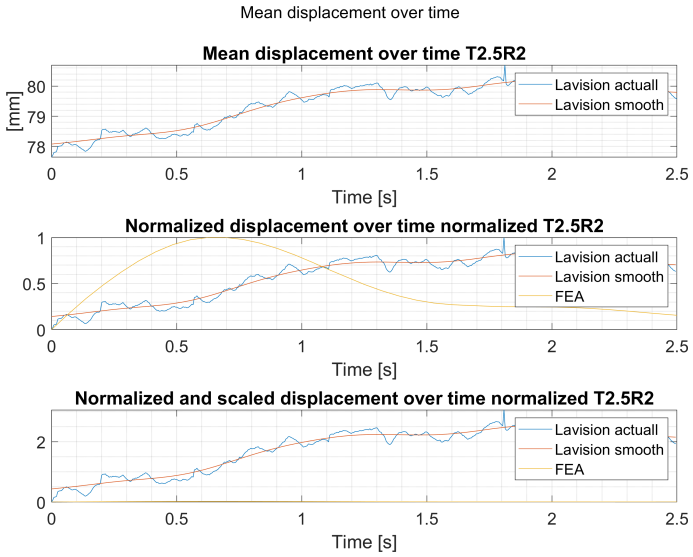

Figure C.67: Mean displacement, normalized and scaled T2.5R2 isotropic model

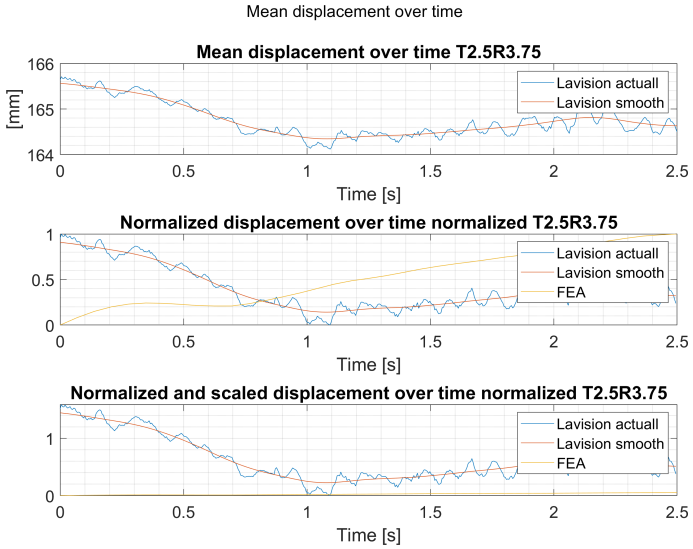

Figure C.68: Mean displacement, normalized and scaled T2.5R3.75 isotropic model

C.4 Cross section deformation

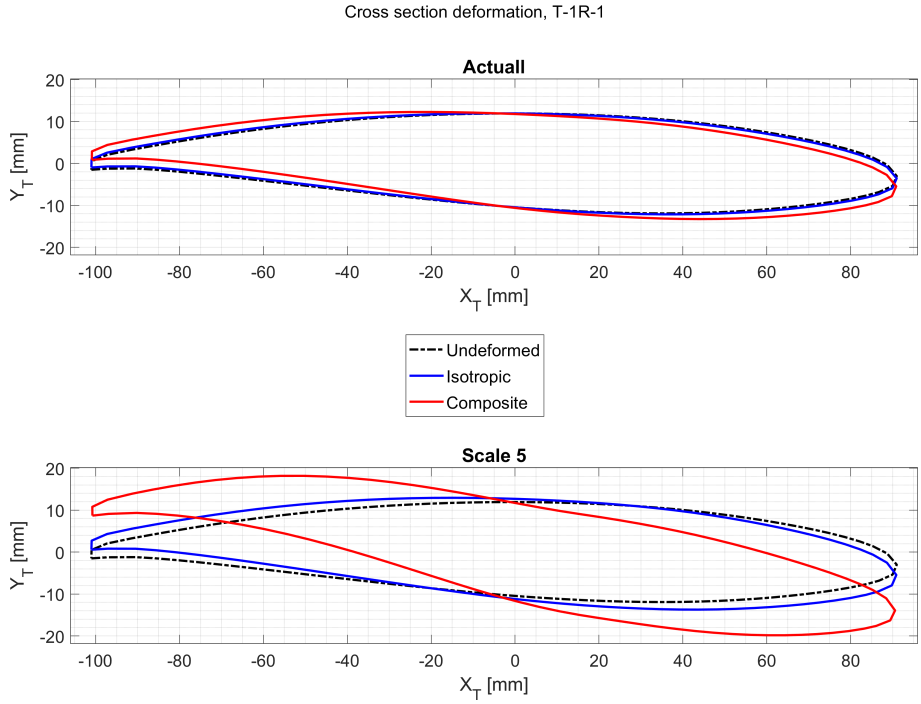

Figure C.69: Isotropic model T-1R-1

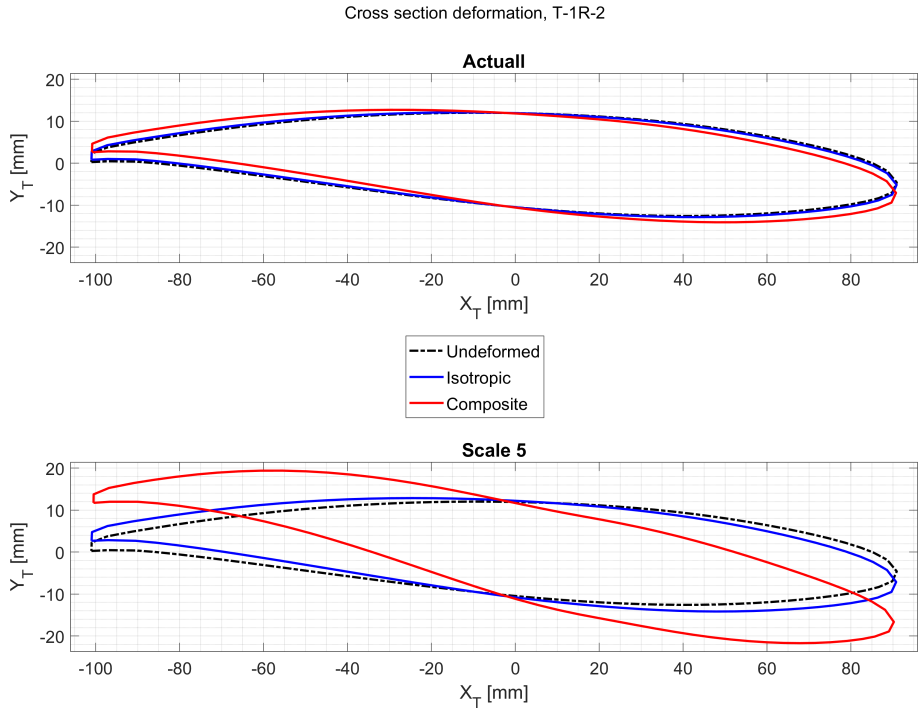

Figure C.70: Isotropic model T-1R-2

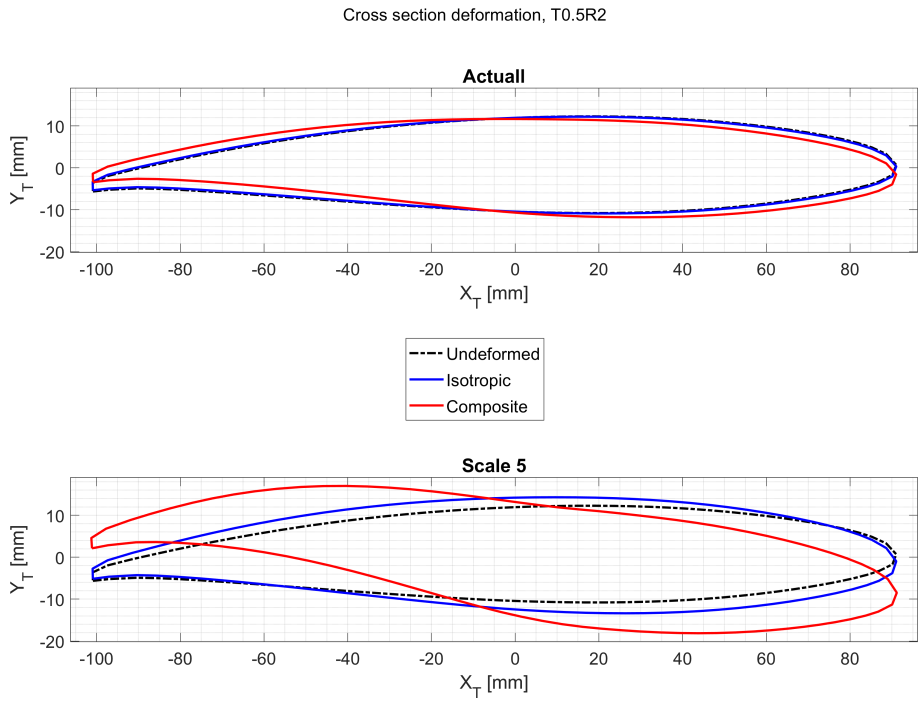

Figure C.71: Isotropic model T0.5R2

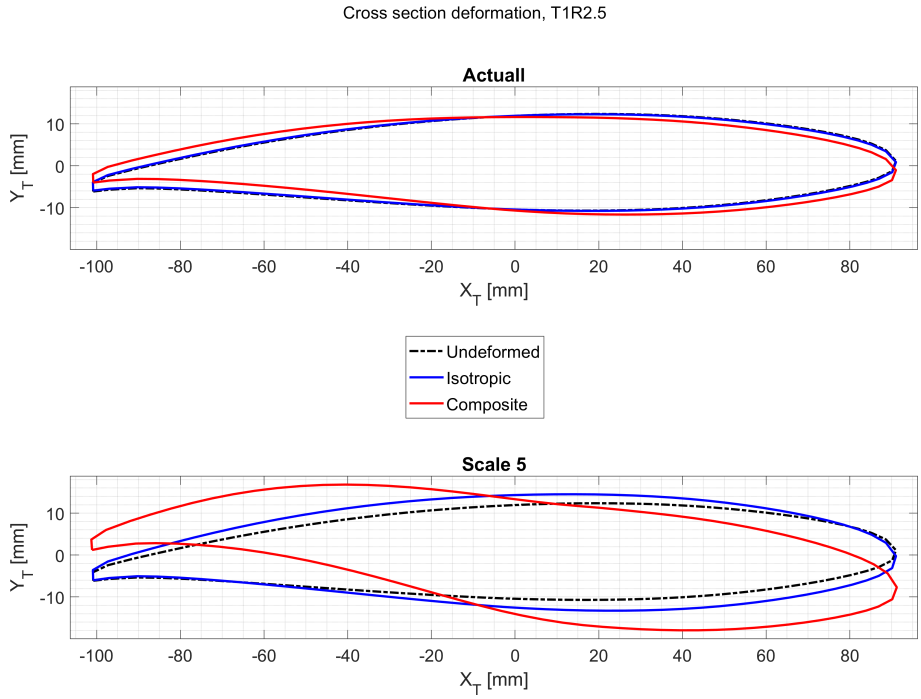

Figure C.72: Isotropic model T1R2.5

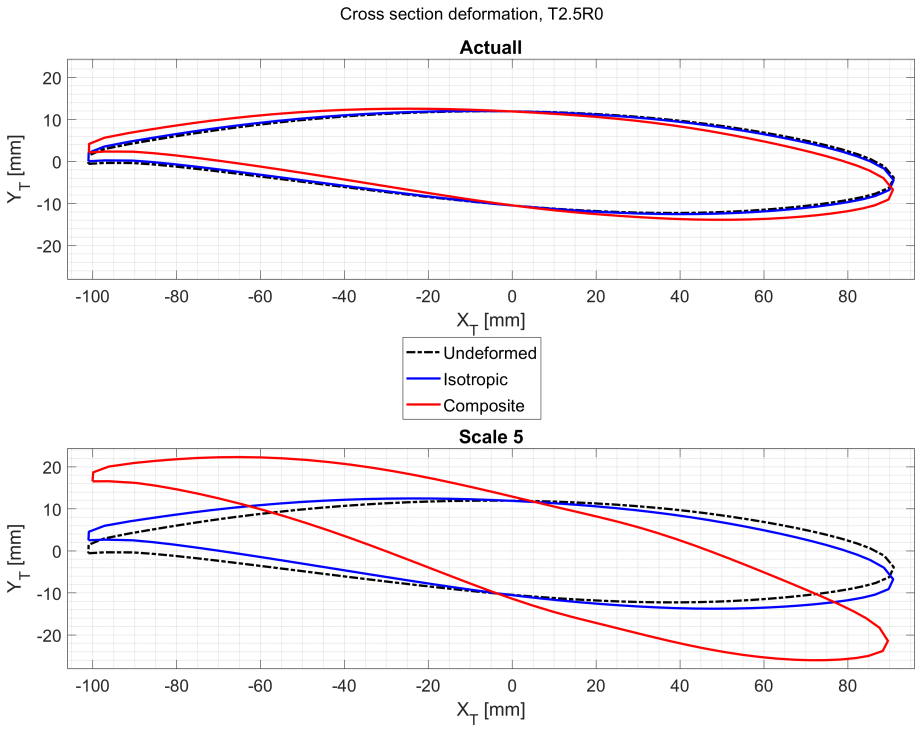

Figure C.73: Isotropic model T2.5R0

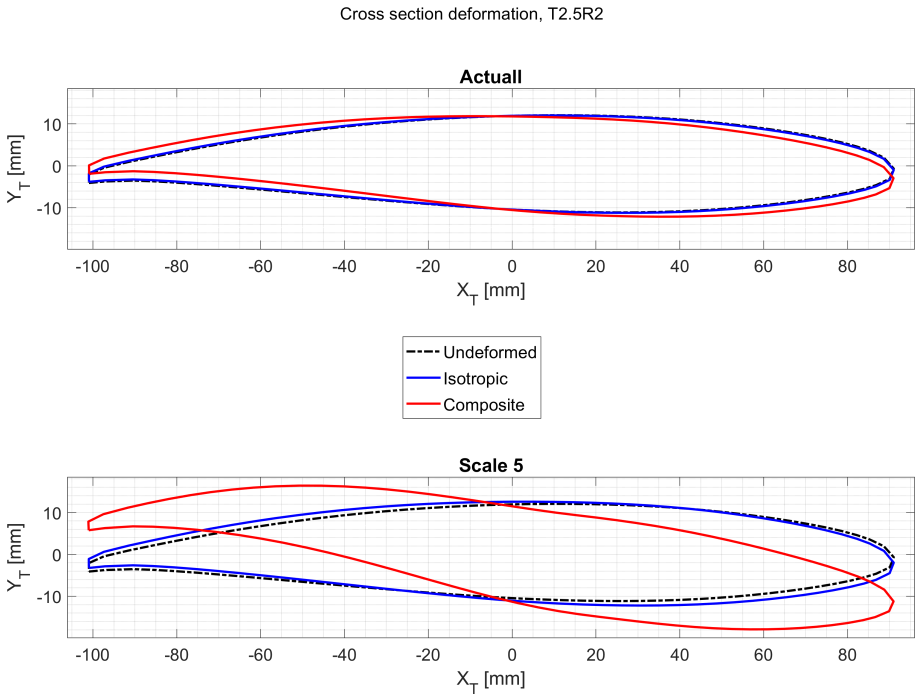

Figure C.74: Isotropic model T2.5R2

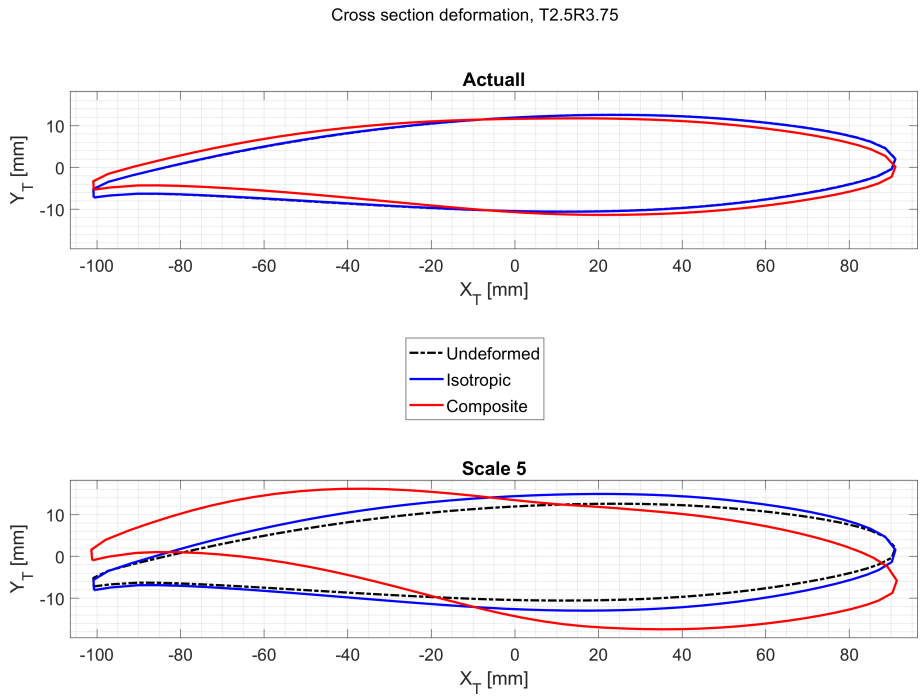

Figure C.75: Isotropic model T2.5R3.75

C.5 Impact test

Eigenfrequency investigation

Measurements and analysis performed on hydrofoil

Report date: 2021-07-14

Issue: 1
Revision: 1

ReVibe Energy responsible:
Erik Godtman Kling
Niklas Illipe

Test setup and execution

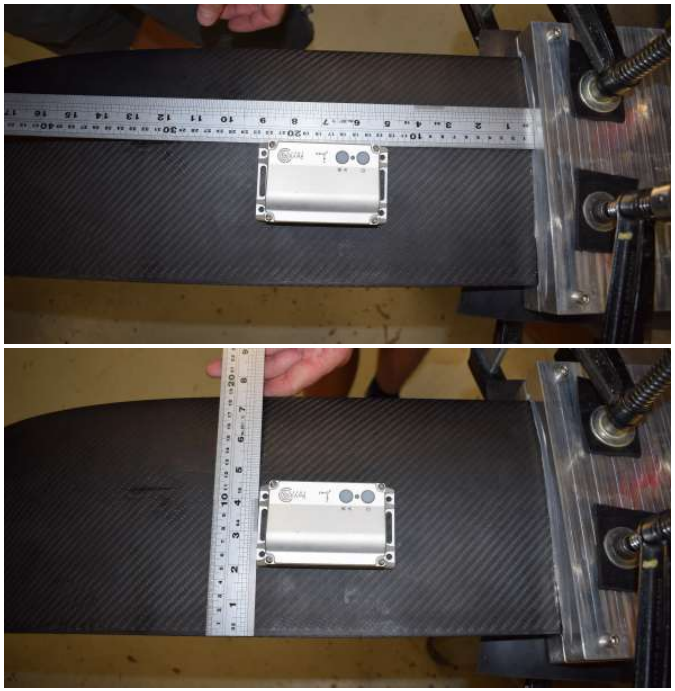

- Hydrofoil clamped at the base
- Hydrofoil excited with rubber hammer at different points
- Frequency response measured with ReLog datalogger unit mounted on tip and base of hydrofoil, respectively

Results

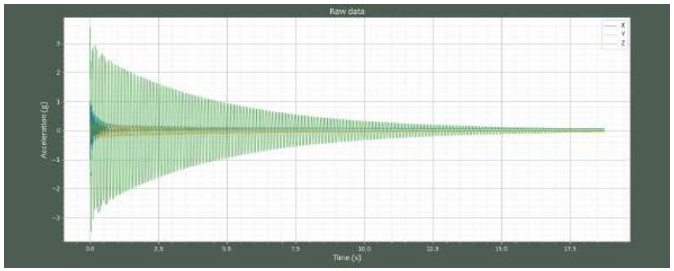

Raw acceleration signal of impulse

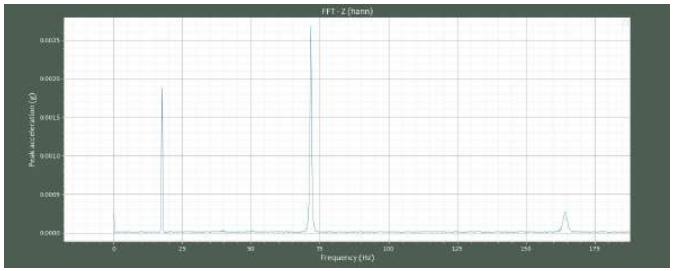

Peaks, base mounting & base excitation point

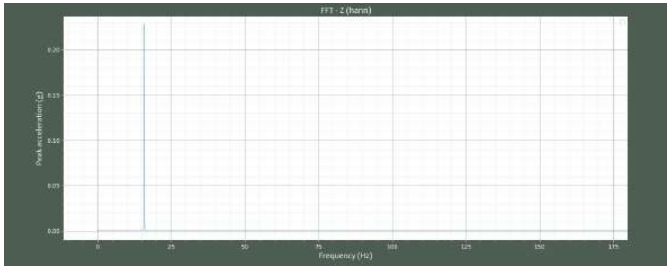

Peaks, tip mounting & tips excitation point

Eigenfrequencies				
ReLog position	Base		Tip	
Excitation point	Base	Tip	Base	Tip
1st	17.6	17.6	15.9	15.9
2nd	71.7	71.6	67.3	67.3
3rd	164.3	-	-	-

Summary/comments:

- No significant difference between base/tip excitation point
- Some shift in resonance peaks for tip mounting vs. base mounting (approx. 10 % lower for first mode), likely due to the added weight of the data logger.

C.6 Post processing

C.6.1 Isotropic model

D

Computational fluid dynamics CFD

D.0.1 Estimation of the Re number:

$$Re = \frac{VL\rho}{\mu} \tag{D.1}$$

where:

- V: Velocity (5-10) [m/s].
- L: the chord-length (0.2) [m].
- μ: Dynamic viscosity 10^{-6} Pa-s.
- ρ: Water density kg/m^3.

The estimated Re values for range of speed [5:10] are [1.1225 1.3470 1.5715 1.7960 2.0205 2.2450]$*10^6$

E

Fluid-Structure Interaction between SATR-CCM+ and ABAQUS practical aspects

E.1 Fluid-Structure Interaction between SATR-CCM+ and ABAQUS practical aspects

E.1.1 Co-simulation Setup

The co-simulation setup contains several modifications on the created modules, specially in STAR-CCM+. In the next to paragraphs a description of the modifications are to be shown and described according to Siemens, 2020.

E.1.2 STAR-CCM+ Setup

As a starter, a solution for a standalone steady-state flow is to be obtained for the CFD model in STAR-CCM+, the purpose is to initiate the flow field which will be used later as an initial conditions for the flow when the co-simulation starts. The next step is to add the relevant extra models to the obtained numerical model, adapting it to solve a FSI problem.

During the co-simulation and as a resultant of the deformation caused by the pressure, shear forces and the motion of the fluid, the fluid will be disturbed back. Although, the mesh needs to move and follow the displacement, at the same time without adding any extra cells. One way is to make use of the morpher. A module available in STAR-CCM+. According to Siemens, 2020 the morpher allows the mesh vertices to be redistributed as a response on the nodal displacement of the specified boundaries from ABAQUS. A group of control points will be used to obtain the initial motion that the morpher asses on the mesh. The control points are created from the mesh vertices on the morpher boundary. The control points are connected with a known displacement vector. To calculate the displacements of all mesh vertices, an interpolation field is to be constructed by using the morpher which uses the displacement vector.
After adding the morpher, one need to activate the morpher for the coupled boundaries specified in the fluid continuum allowing them to morph with respect to the nodal displacement imported from ABAQUS.

As mentioned before extra modules are to be added to the continuum that symbolizes the solved physics in STAR-CCM+ to preform a co-simulation between STAR-CCM+ and ABAQUS. The moudles are:

- Co-simulation
- ABAQUS: to specify what type of co-simulation, since other types of coupled systems are provided in STAR-CCM+.
- ABAQUS implicit coupling: in general, in the strongly coupled systems implicit coupling scheme are implemented. This types of schemes give the chance to exchange data between the coupled softwares more than once per time-step, which allow for larger time-steps compared to the explicit coupling scheme.

In order to represent the solid physics solved in ABAQUS one needs to create and specify the external continuum in STAR-CCM+. The external continuum includes the following physical modules:

- Physics: External continuum
- External software: ABAQUS
- Time: Implicit unsteady

After adding the co-simulation module to STAR-CCM+, an addition module will be added automatically to the simulation tree, External links. In the added module one would be able to connect the created external solid continuum with an external software e.g. ABAQUS. In addition, the co-simulation setup will be modified at the created External links.

The co-simulation setups are essential to make the co-simulation between STAR-CCM+ and ABAQUS to run. The setups works as a translator for both softwares. Where one can define some specifications about the external software e.g. ABAQUS, the input file from that software, the type of imported/exported data, and other settings regarding time steps and the interval between the softwares.
The descriptions of the utilized settings in STAR-CCM+ for the co-simulation are given below:

- External Continua: the solid physics that is created in the continua for the co-simulation.
- ABAQUS release: one need to specify the version of the software that is used in the coupled system.
- ABAQUS library file and path: in order to let the two softwares communicate with each other, in STAR-CCM+ one need to specify the location of the li-

brary file and the absolute path as well.

- Time marching Sequence: one need to specify for the trend that the two softwares are proceeding with. Two alternatives are provided in STAR-CCM+, simultaneously and sequentially. Although, run sequentially is the only one applicable for implicit coupling and thus to be used in the module. In sequential run either softwares can start first and lead where the other one follows. The two options have the same stability and the computational costs. However, the software that leads should be the one which is less critical to the initial prediction. Since, the results form the initial prediction is to be utilized in the first time step in a co-simulation. It is recommended to let the solid solver to lead according to STAR-CCM+ manual.

- Coupling negotiation method: defines the time interval for the exchanged data between the two softwares. According to Siemens, 2020, one way to improve convergence in an implicit co-simulation with ABAQUS is to set this option to minimum. This option allow the co-simulation to choose and run on the smallest time-step possible defined in either softwares (0.007 s for the Cavitation Tunnel model and 0.0067 for the Towing Tank model).

- External code units manger: this option specify the units of the data which are imported and exported between the two softwares. Hence, it tells STAR-CCM+ in which unit the imported data are, and it assure that the data is to be exported to ABAQUS in the correct unit as well.

- Inner iteration per exchange: define the number of fluid inner iterations among two exchanges with the solid solver ABAQUS within one time step. According to Siemens, 2020, 3 inner iterations per exchange is efficient for convergence proposes for fluid with high density such as water.

- Minimum number of exchange: Controls the minimum number for the co-simulation to exchange data with the solid solver within one time step. According to Siemens, 2020, 15 would be sufficient enough for convergence proposes as well.

- Exported traction Field Control:
  In mechanical coupling simulations, numerical instabilities could be present. This could be caused by misalliance in the initial condition, high inertia resultant from the added mass, or other reasons. Utilizing the option provided in STAR-CCM+ Exported Traction Fields would be beneficial to avoid theses instabilities. Set the option pressure ramping time scale to STAR-CCM+ indicates that the pressure ramping is to be established on the STAR-CCM+ time. Another parameter is the Pressure Ramping, it helps to gradually raise the pressure component of the transmitted load to ABAQUS see figure E.1. The pressure ramping parameter helps ramping the pressure at the start of the co-simulation which is beneficial to avoid any numerical errors which may oc-

cur. One need to define a range of time between t_{zero}, t_{couple}. The pressure and shear stresses exported from STAR-CCM+ set to zero before t_{zero} and t_{couple} where the exported pressure and shear stresses from STAR-CCM reflects the actual ones in STAR-CCM+. The pressure and shear stresses between the aforementioned time interval are gradually ramped from zero to the actual values.

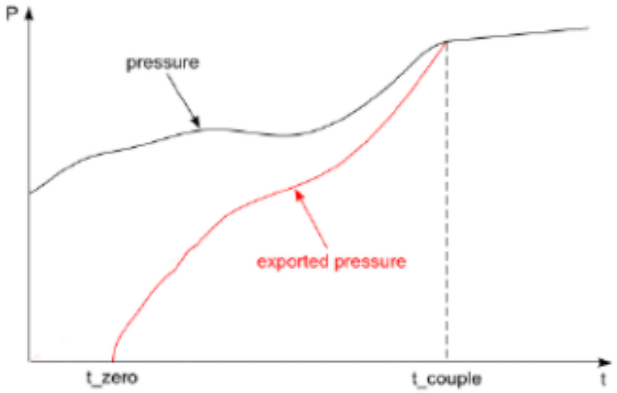

Figure E.1: Pressure Ramping methodology scheme Siemens, 2020

E.1.3 ABAQUS Setup

ABAQUS generates an input file containing all the information needed to calculate the FEA problem, such as the coordinates for the nodes, material properties, boundary conditions. The input file also specifies what type of simulation is to be carried out. In appendix E.2 an example of an input file presented. In this case, the geometry and load case in the example are arbitrary with a static moment. The input file needs to be modified to be used in a co-simulation using STAR-CCM+ and ABAQUS. In the following example, the end of the input file in the appendix has been modified and highlighted with colored text.

Modifications in inputfile

```
** ----------------------------------------------------------------
**
** STEP: Step-1
**
*Step, name=Step-1, nlgeom=YES, inc=1000000
Co-simulation step
*Dynamic,
APPLICATION=TRANSIENT FIDELITY
0.0001, 60, 1e-06, 0.007
**
** OUTPUT REQUESTS
**
*Restart, write, frequency=0
**
** FIELD OUTPUT: F-Output-1
**
*Output, field, variable=PRESELECT
**
** HISTORY OUTPUT: H-Output-1
**
*CO-SIMULATION, NAME=FSI_foil, PROGRAM=MULTIPHYSICS,
CONTROLS=Control
*CO-SIMULATION REGION, TYPE=SURFACE, EXPORT
FSI_foil, U
*CO-SIMULATION REGION, TYPE=SURFACE, IMPORT
FSI_foil, CF
*CO-SIMULATION CONTROLS, NAME=Control,
COUPLING SCHEME=GAUSS-SEIDEL, SCHEME MODIFIER=LEAD,
STEP SIZE=1E-4, TIME INCREMENTATION=SUBCYCLE,
TIME MARKS=YES
**
*End Step
```

The first modification in red specifies that it is a dynamic co-simulation and controls the initial time step, the maximum time step, and the smallest time step. The second modification in blue specifies the name of the surface that is a part of the co-simulation, parameters that are to be exported and imported, and the type of coupling preformed between the two softwares.

The input file is then specified in STAR-CCM+ together with the location of the ABAQUS software. Once the simulation is started, STAR-CCM+ initiates ABAQUS together with the input file and imports the results, in this case, displacement, from ABAQUS.

E.2 Input file

example of input file

```
*Heading
** Job name: Example Model name: Model-1
** Generated by: Abaqus/CAE 2020.HF3
*Preprint, echo=NO, model=NO, history=NO, contact=NO
**
** PARTS
**
*Part, name=Part-1
*Node
      1,          10.,          10.,          10.
      2,          10.,          7.5,          10.
      3,          10.,           5.,          10.
      4,          10.,          2.5,          10.
 ~~~~~~~~~~~~~~~~~~~~~~~~~~~~~~~~~~~~~~~~~~~~~~~~
*Element, type=C3D8R
 1,  26,  27,  32,  31,   1,   2,   7,   6
 2,  27,  28,  33,  32,   2,   3,   8,   7
 3,  28,  29,  34,  33,   3,   4,   9,   8
 4,  29,  30,  35,  34,   4,   5,  10,   9
 ~~~~~~~~~~~~~~~~~~~~~~~~~~~~~~~~~~~~~~~~~~~~~~~~
*Nset, nset=_PickedSet4, internal, generate
   1,  125,    1
*Elset, elset=_PickedSet4, internal, generate
  1,  64,   1
** Section: Section-1
*Solid Section, elset=_PickedSet4, material=Steel
,
*End Part
**
**
** ASSEMBLY
**
*Assembly, name=Assembly
**
*Instance, name=Part-1-1, part=Part-1
*End Instance
**
*Nset, nset=Set-1, instance=Part-1-1, generate
   5,  125,    5
*Elset, elset=Set-1, instance=Part-1-1, generate
  4,  64,   4
*Nset, nset=Set-2, instance=Part-1-1
   1, 101
*Elset, elset=__PickedSurf7_S6, internal, instance=Part-1-1, generate
  1,  61,   4
*Surface, type=ELEMENT, name=_PickedSurf7, internal
__PickedSurf7_S6, S6
*End Assembly
**
** MATERIALS
**
```

```
*Material, name=Steel
*Elastic
200000., 0.3
**
** BOUNDARY CONDITIONS
**
** Name: BC-1 Type: Displacement/Rotation
*Boundary
Set-1, 1, 1
Set-1, 2, 2
Set-1, 3, 3
Set-1, 4, 4
Set-1, 5, 5
Set-1, 6, 6
** ----------------------------------------------------------------
**
** STEP: Load
**
*Step, name=Load, nlgeom=NO
*Static
1., 1., 1e-05, 1.
**
** LOADS
**
** Name: Load-1   Type: Pressure
*Dsload
_PickedSurf7, P, 200.
**
** OUTPUT REQUESTS
**
*Restart, write, frequency=0
**
** FIELD OUTPUT: F-Output-1
**
*Output, field, variable=PRESELECT
**
** HISTORY OUTPUT: H-Output-1
**
*Output, history, variable=PRESELECT
*End Step
```